UNIVERSITY OF SHEFFIELD

DOCTORAL THESIS

Reconstruction of Soil Stress-Strain Response Using Optimisation

Author:
Jared A CHARLES

Supervisors:
Dr. Colin C SMITH
Dr. Jonathan A BLACK

A thesis submitted in fulfillment of the requirements for the degree of Doctor of Philosophy

Geotechnical Engineering Group
Department of Civil and Structural Engineering
Faculty of Engineering

July 8, 2020

Reconstruction of Soil Stress-Strain Response Using Optimisation

This work was typeset using the LaTeX template "Masters/Doctoral Thesis" as published by LaTeXTemplates.com. [2]

An electronic copy of this thesis is available online in the White Rose eThesis repository. [3]

The experimental data produced as part of this project is available online in the University of Sheffield ORDA data repository. [4]

[1] https://creativecommons.org/licenses/by-nc-nd/4.0/
[2] https://www.latextemplates.com/template/masters-doctoral-thesis
[3] https://etheses.whiterose.ac.uk/
[4] https://doi.org/10.15131/shef.data.14198681

Abstract

Reconstruction of Soil Stress-Strain Response Using Optimisation

by Jared A CHARLES

An Identification Method is a methodology by which the properties of a material can be recovered by back analysis of experimental data. In the context of geotechnics, the relevant data would be the displacement field of a body of soil undergoing deformation along with the loading data that is causing the deformation. The recovered properties for a geotechnical problem that would be most useful can be represented with a stress-strain curve.

Two Identification Methods are presented in this thesis. Both methods utilise optimisation such that a stress-strain curve can be recovered that minimises the gap between internal work, a function of the stress and strain fields, and external work, a function of loading and load displacement. The first method, an evolution of existing work, splits the unknown stress-strain curve into a number of segments, with the stress associated with each segment being optimised. The second method, novel for this project, defines the unknown curve with an arbitrary equation, the parameters of which are to be found through optimisation or alternatively a brute force approach.

To validate the methods, a series of artificial datasets were produced using FEA and were found to function very well. The datasets were subjected to a variety of artificial degradation strategies such as the addition of random noise with the finding that the peak stress is lowered proportionally to the addition of noise. Laboratory tests were also carried out for validation purposes. A series of footing tests were performed on undrained clay, with Digital Image Correlation (DIC) data recorded, and the recovered curves were compared with triaxial and shear vane data. Depending on the quality of the individual data sets, the methods were found to be promising. More flawed data sets of course produced worse recovered curves, but higher quality datasets resulted in recovered curves that were within the range suggested by triaxial testing.

Keywords: Back analysis; Identification Method; Stress-Strain Response; Particle Image Velocimetry (PIV); Physical Modelling; Optimisation

Declaration of Authorship

I, Jared A CHARLES, declare that this thesis titled, "Reconstruction of Soil Stress-Strain Response Using Optimisation" and the work presented in it are my own. I confirm that:

- This work was done wholly while in candidature for a research degree at the University of Sheffield.
- No part of this thesis has previously been submitted for a degree or any other qualification at the University of Sheffield or any other institution.
- Where I have consulted the published work of others, this is always clearly attributed.
- Where I have quoted from the work of others, the source is always given. With the exception of such quotations, this thesis is entirely my own work.
- I have acknowledged all main sources of help.
- Where the thesis is based on work done by myself jointly with others, I have made clear exactly what was done by others and what I have contributed myself.

Jared A CHARLES

July 8, 2020

Date

Publications

During the course of completing this thesis, a number of peer reviewed publications based on the work contained within were produced. The following, correct as of submission of this thesis, is an exhaustive list of such publications:

- J A Charles et al. (2019). "Automated reconstruction of soil stress-strain response from full field displacement measurements and loading data using optimisation". In: *Proceedings of the XVII ECSMGE-2019, Geotechnical Engineering foundation of the future*. IGS, pp. 1–8. DOI: 10.32075/17ECSMGE-2019-0343
- J A Charles et al. (2018b). "Identification of soil stress-strain response from full field displacement measurements in plane strain model tests". In: *Physical Modelling in Geotechnics, Volume 2: Proceedings of the 9th International Conference on Physical Modelling in Geotechnics (ICPMG 2018), July 17-20, 2018, London, United Kingdom*. CRC Press, pp. 835–840. DOI: 10.1201/9780429438646
- J A Charles et al. (2018a). "Evaluating the effects of noise on full field displacement data used for the identification of soil stress-strain response". In: *Numerical Methods in Geotechnical Engineering IX, Volume 1: Proceedings of the 9th European Conference on Numerical Methods in Geotechnical Engineering (NUMGE 2018), June 25-27, 2018, Porto, Portugal*. CRC Press, pp. 221–226. DOI: 10.1201/9780429446931

Acknowledgements

I would like to thank my supervisors, Dr. Colin C Smith and Dr. Jonathan A Black, for the support and advice they have provided throughout this project. I have had many useful conversations with Colin that helped me to understand and explain the inner workings of the methodologies that I have used. Jonathan taught me many of the laboratory techniques that I needed to successfully carry out the physical modelling portion of this project. The support of both of my supervisors was very helpful to me, not only in facilitating the completion this project, but also in gaining the skills and experiences that I will need to pursue an academic career.

I would also like to thank the technical support provided primarily by Mr. Alex Cargill, Mr. Mark Foster, and Mr. Paul Blackbourn. My Laboratory work simply wouldn't have been possible without the wide range of help the technician team provided, from manufacturing bespoke equipment to maintaining and providing training in existing apparatus. I would thank Dr. Irfan Khan for the help he provided with troubleshooting the 3D actuation robot and associated electronics.

Thanks also go to my examiners, Dr. Danny Smyl and Dr. Sam Stanier. I found the Viva to be an enjoyable experience and I greatly appreciate the discussions about potential directions I can take this project in the future.

Finally, I would like to thank my friends and colleagues in the Geotechnical Engineering Group. I had many interesting conversations at the weekly coffee mornings and learned much at the seminars that group members presented. I will give particular mention to some of my fellow PhD students, Alan, Fahed, Gabriella, Hang, Rowena, Rui, Shaymaa, Steven, and Xinyuan, who made this experience a lot less lonely. It takes more than academic or technical support to complete a PhD; having people there for me who would listen and understand was hugely important, not only for finishing this project, but being happy while doing so.

The work presented in this thesis was carried out as part of an EPSRC funded PhD studentship.

Contents

List of Figures

List of Tables

List of Symbols

Note that this list contains only the symbols that are likely to be of use to the reader throughout this thesis. Symbols that are locally defined and used have been omitted.

Symbol	Name	Unit
W	Work	J
W_{int}	Internal work	J
W_{ext}	External work	J
W_d	Energy density	$J \cdot m^{-3}$
W_{force}	Work imparted by a force	J
$W_{friction}$	Work expended due to friction	J
$W_{gravity}$	Work relating to gravity	J
P	Point force	N
μ	Coefficient of Friction	
M	Mass	kg
A	Area	m^2
V	Volume	m^3
u	Displacement	m
J	Joule	$kg \cdot m^2 \cdot s^{-2}$
N	Newton	$kg \cdot m \cdot s^{-2}$
$\underline{\sigma}$	Stress tensor	$N \cdot m^{-2}$
σ_x	Stress in x direction	$N \cdot m^{-2}$
σ_y	Stress in y direction	$N \cdot m^{-2}$
τ_{xy}	Shear stress	$N \cdot m^{-2}$
σ_1	Major principal stress	$N \cdot m^{-2}$
σ_2	Minor principal stress	$N \cdot m^{-2}$
θ_σ	Stress plane of reference	rad
$\theta_{p\sigma}$	Stress principal angle	rad
s	Mean stress	$N \cdot m^{-2}$
t	Maximum shear stress	$N \cdot m^{-2}$
c_u	Undrained soil strength	$N \cdot m^{-2}$
$\underline{\epsilon}$	Strain tensor	
ϵ_x	Strain in x direction	
ϵ_y	Strain in y direction	
γ_{xy}	Shear strain	
ϵ_1	Major principal strains	

ϵ_2	Minor principal strains	
θ_ϵ	Strain plane of reference	rad
$\theta_{p\epsilon}$	Strain principal angle	rad
ϵ_v	Volumetric strain	
ϵ_s	Maximum shear strain	
(x, y)	Pixel coordinates	$Pixels$
(X, Y, Z)	World coordinates	m
(x_0, y_0)	Principal point	$Pixels$
(f_x, f_y)	Scale factors	
F	Focal Length	m
s	Skew factor	
$\mathbf{K}$	Intrinsic Matrix	
$\mathbf{R}$	Extrinsic Matrix	
(θ, ϕ, ψ)	Yaw, pitch, and tilt	rad
K_n	The n^{th} tangential distortion coefficient	
P_n	The n^{th} radiall distortion coefficient	
λ	Refraction correction factor	
H	Camera to back of window distance	m
t	Window thickness	m
n	Window refractive index	m

Chapter 1

Introduction and Objectives

1.1 Background

In order for practising geotechnical engineers to design structures such as foundations, retaining walls, embankments, and cuttings, it is necessary to predict how the soil involved in the design will behave. As it is typically either not possible or not economical to build large scale prototypes in civil engineering, the behaviour of geotechnical structures must be predicted using analytical or numeric methods.

For very simple problems, analytical hand calculations such as Terzhagi's bearing capacity equation may be used whereas for complex problems, numerical solutions governed by constitutive models can be calculated in Finite Element Analysis (FEA) software.

Regardless of the complexity of the problem the practising geotechnical engineer faces, methods have been developed to predict the response of a soil. What all these methods have in common is the need for constitutive parameters as inputs. From the simplest linear elastic model, in which the stress-strain response is governed by Young's Modulus and Poisson's Ratio, to complex models governed by tens of parameters, the accuracy of the practising engineer's prediction is reliant on the accuracy of the constitutive parameters chosen.

Determining these constitutive parameters can be done by either obtaining them from references or literature, based on broad characteristics of the soil or by extracting them experimentally. Extracting the constitutive parameters of soils is typically done through a number of physical tests (1D compression tests, shear box tests, triaxial tests etc.) in which the stress-strain field is assumed to be simple and known. Depending on how many parameters are required, multiple tests may need to be run.

These methods of determining the constitutive parameters assume a uniform response throughout the soil and potentially provide limited or incomplete data. As the true representativeness of the data obtained is unknown, the use of conservative safety factors may be necessary to ensure any design is adequate. Having low confidence in the representativeness of the parameters used could result in economic or environmental inefficiencies due to overdesign.

An Identification Method, as described extensively by Avril et al. (2008a), is a method developed for testing solids in order to recover the constitutive parameters of a sample based on recorded loading data and PIV derived displacement data. Although numerous such methods are described in the aforementioned paper, with varying algorithms and data requirements, the principle is that constitutive parameters are to be found such that a modelled response, using said parameters, is similar to the physically measured response. Identification Methods have been used extensively in material science for a range of metallic objects.

The development of Particle Imaging Velocimetry (PIV), a subtype of Digital Image Correlation (DIC), first adapted for geotechnical usage by White et al. (2001) allows access to full-field displacement data of a sample undergoing testing. This process uses high resolution digital cameras to track the planar movement of specified patches of soil based on their texture. This texture can either be natural or artificially applied using floc seeding. PIV is a non-intrusive method that provides no further disturbance to the soil sample undergoing testing.

One Identification Method, the Virtual Fields Method (VFM), as described by Grédiac and Pierron (1998), requires full-field displacement data of a specimen undergoing testing, along with data relating to the applied loading scheme. The principles of the conservation of energy and of virtual work are then used to recover the parameters of a chosen constitutive model. This method has been used in the field of material science, typically to recover elastic parameters of metal dog bone specimens.

Preliminary work by Gueguin et al. (2015) demonstrated a geotechnical Identification Method based on the principle of conservation of energy that can be seen as a less robust simplification of VFM, with applications to limited soil types and stress-strain responses. The method, developed with the goal of recovering and reconstructing the stress-strain response bypasses the requirement of kinematically and statically admissible stress and strain fields required by VFM by presupposing the rough shape of the stress-strain response based on engineering judgement.

This preliminary work has the potential to serve as a good starting point from which further advancements of the methodology can be developed and tested. This will be the purpose of this project. The aims and objectives will be summarised in the following section.

1.2 Objectives

The primary aim of this project is to develop, test, and validate one or more Identification Method that is suitable for extracting the stress-strain response of geotechnical physical models using full field PIV-derived displacement data. The preliminary work done by Gueguin et al. (2015) serves as a starting point, however the existing implementation had a number of limitations and little validation, with much of the available code requiring significant revisions. As such, the following objectives were formulated.

1. Investigate existing Identification Methods developed in the field of material science in order to determine their applicability to geotechnical problems and understand the principles by which they operate. Factors to consider would relate to the methods ability to work with plane strain data, and capabilities regarding highly non-linear behaviour.

2. Carry out further review of literature relating to physical modelling techniques that will be necessary to utilise in order to properly validate any developed Identification Methods.

3. Analyse and assess the method proposed by Gueguin et al. (2015) and the associated codebase. Make required changes to the code to fix bugs and generalise functions to allow for future development. Significant work needed to be done on the algorithm related to calculation of internal work.

4. Develop one or more additional approaches to the Identification Method using a shared codebase such that existing pre and post processing functionality can be reused where appropriate.

5. Generate a suite of artificial datasets using FEA such that any proposed Identification Methods can be validated for a range of scenarios, varying both geometry of the problem and soil behaviour. Nonlinear stress-strain responses are of particular interest for testing. The datasets can be further utilised by artificially degrading them through the addition of noise to test the resilience of the proposed method or methods.

6. Design and carry out a series of laboratory physical model tests in order to build a set of real datasets that can be used to examine the capabilities of the proposed methods.

7. Validate the proposed Identification Methods using both the artificially generated dataset and the datasets derived via physical modelling. Discuss and solve any issues that arise and compare and contrast the benefits and drawbacks of any proposed Identification Methods.

8. Produce a user friendly piece of software implementing one or more of the proposed Identification Methods such that it would be useful for other researchers to use as a means of examining PIV datasets produced during physical modelling.

1.3 Format of this Document

This thesis is split into a number of chapters. The titles and descriptions of these chapters are as follows:

Chapter 1: Introduction and Objectives. This chapter contains a brief introduction and summary of the main motivations behind the project, as well as a description of the key aims and objectives. Finally, a summary of the content of each chapter is given.

Chapter 2: Literature Review. This chapter presents the literature review carried out as part of this project. Commentary is first given on the use of existing Identification Methods, primarily those used by material engineers but also on the preliminary work carried out in adapting the methodologies to geotechnical engineering. Next, the theory behind Particle Imaging Velocimetry is explained along with the associated photographic and photogrammetric techniques necessary to properly utilise the technique. Finally, a summary of the existing techniques geotechnical engineers use to obtain soil properties is provided along with the limitations and drawbacks of these methods. To conclude the chapter, any notable gaps in existing literature are identified along with explanation as to how these gaps relate to this project.

Chapter 3: Derivation and Calculation of the Energy Equilibrium Equation. This chapter derives from first principles the energy equilibrium equation that is at the heart of the Identification Methods proposed in this document. Key terminology will be defined in this chapter. Notes on the key assumptions and simplifications made are presented here along with justifications behind these decisions. The method by which strains were calculated from the displacement field is also explained.

Chapter 4: Programmatic Implementation of the Identification Method. This chapter provides a primer on optimisation for readers who are unfamiliar with the concept followed by a description of what optimisation means in the context of the problem at hand. Derivations and explanations for the two proposed Identification Methods can be found in this chapter. Flow charts and Diagrams are presented to aid in the illustration of the inner workings of each method. Commentary is given on the key similarities and differences between the two methods.

Chapter 5: Artificial Data Set Generation. This chapter explains the strategy by which "perfect" artificial datasets will be used to test the proposed Identification Methods. The selection of datasets is explained along with the methodology of their generation. The scheme by which the addition of artificial noise was used to further test the Identification Methods is also explained.

Chapter 6: Physical Modelling Data Set Generation. This chapter shows the laboratory scheme by which real datasets will be produced using physical modelling. A detailed and illustrated description of the required equipment is given along with the methodologies by which the samples was prepared, and testing will be carried out. Commentary on data processing, such as Particle Imaging Velocimetry is given and builds on the more theoretical discussion of these topics provided in the literature review.

Chapter 7: Analysis of Artificial Datasets. This chapter validates the proposed Identification Methods by testing them with the "perfect" artificial datasets presented in Chapter 5. Qualitative assessment of the datasets is first provided, followed by the results of validating the Identification Methods under optimal circumstances using the aforementioned datasets. The rest of the chapter deals with artificially degrading the data, not only to test the rigour of the methods to the limit, but also to gain insight that could be useful in diagnosing potential issues with real datasets.

Chapter 8: Analysis of Real Datasets. This chapter discusses the capabilities of the proposed Identification Methods when dealing with real datasets. Qualitative assessment of these datasets is first given, identifying any noteworthy flaws or potential issues. The methods are then tested using the datasets. Key parameters such as resolution of PIV patches will be varied with the effects explained. Discussion of the findings and the results of the validation process are presented.

Chapter 9: Conclusions and Future Work. This chapter summarises the key findings of this project. The objectives given in Chapter 1 will be discussed. Possibilities for future work in this field are also given.

Appendix A: Reformulating Internal Work to use "Geotechnical" Parameters. This appendix contains the derivation necessary to reformulate the internal work equation such that work can be calculated in terms of maximum shear stress and maximum shear strain, instead of the stress and strain tensors. This content is relevant to the derivation contained in Chapter 3.

Appendix B: Additional Data. This appendix contains investigations into parameter choice and raw sensor data that was produced from the physical modelling tests. This content is relevant to the analysis presented in Chapter 8.

Chapter 2

Literature Review

2.1 Introduction

This chapter consists of a review of existing literature relating to Identification Methods and processes by which constitutive parameters can be obtained from experimental data. Work on this topic has most prominently been carried out by researchers in the field of material science, on a range of materials, both structural and biological, with particular attention paid to metals. As the goal of this project is the application of an Identification Method to geotechnical engineering, a thorough background on a number of formerly proposed Identification Methods is essential.

Many Identification Methods notably take advantage of full field displacement measurements. This full field measurement is carried out using Digital Image Correlation (DIC), a method by which the movement of material is tracked via digital imaging. As such, DIC is of great importance to the project as it will be used to obtain and analyse physical data, with the output from the DIC process used as an input for any developed Identification Methods. Particle Imaging Velocimetry (PIV) is the form of DIC that is most applicable to geotechnics. This chapter contains a description of the DIC process at the heart of PIV, along with a brief account on how various authors have changed, improved, and implemented PIV over its history. Most importantly provided is a description of the practical considerations of using PIV, notably the need to calibrate the obtained image data, such that distortion is removed and the user may freely convert between image space and object space coordinate systems.

A summary of existing techniques that are used to recover soil properties will be given. This will include both laboratory and field tests that allow researchers or engineers to gain insight into soil behaviour. Any Identification Method developed during this project is not intended to supplant such techniques, but to complement them. An assessment of the benefits and drawbacks of the existing techniques will also be provided.

The final section in this chapter will be a summary of gaps in the literature, and how these gaps associate with the aims and objectives of this project.

2.2 Identification Methods

An Identification Method is a process by which the parameters of a constitutive model may be reconstructed from physical test data. Avril et al. (2008a) provide a detailed comparison of several prominent Identification Methods. These methods include: Finite Element Model Updating (FEMU), Constitutive Equation Gap Method (CEGM), Virtual Fields Method (VFM), Equilibrium Gap Method (EGM), and Reciprocity Gap Method (RGM). Avril et al. (2008a) further categorise these methods as either: Updating Methods, in which an initial guess for constitutive properties is used to numerically calculate the stress or displacement fields, which is compared to measured values in order to iteratively improve the constitutive properties; Non-Updating Methods, in which stress fields are to be calculated from measured displacements and the to-be-found constitutive properties, allowing the formation of equilibrium equations. Methods can be further described as requiring field measurements over the domain, field measurements over only the boundary, or able to function using either type of field measurements.

Each of the methods listed will be briefly described, with particular attention paid to the Virtual Fields Method as it is regarded in the literature to be used more frequently than the other methods, and appears to be the most applicable and promising method for geotechnical engineering. As such, a full derivation of VFM for elastic models will be provided, whereas other methods, which are of significantly less importance for this project, will be illustrated with either an abridged derivation or a description of the key equations. For all methods, comments will be made on their usage in literature, with a example papers listed for various problem types.

2.2.1 Finite Element Model Updating

FEMU consists of performing FEA simulations in order to find the constitutive properties that give a numerical result closest to the measured experimental results. The relationship between energy, displacement, and force in a discretised FEA system can be written as shown in Equation 2.1, (Pagnacco et al., 2005). Note that for simplicity a particularly basic FEA model is shown.

$$\Pi = \frac{1}{2} U_G^T K_G U_G - U_G^T F_g \tag{2.1}$$

in which Π is the potential energy of the system, typically 0, K_G represents the global stiffness matrix (the constitutive parameters are encoded in this matrix), F_g is the global external load vector, and U_G is the discretised displacement vector.

There are two forms of FEMU: the Force Method (FEMU-F) in which the measured full field displacement data is input into the FEA simulation in order to calculate force data, which can be compared to measured force data, and the Displacement Method (FEMU-U) which is the opposite, force data is input into the FEA simulation and displacement data is used for the comparison.

The Force Method (FEMU-F) minimises the residual force $R_F(p)$, where p represents the vector of unknown parameters, which is taken as the difference between simulated and measured force. Measured stiffness is used for the global stiffness matrix i.e. $U_G = U_{mes}$. The values for simulated force can be found by rearranging Equation 2.1. Thus, the following equation is to be minimised (Pagnacco et al., 2005):

$$R_F(p) = F_{sim} - F_{mes} = K_G(p).U_{mes} - F_{mes} \tag{2.2}$$

The Displacement Method (FEMU-U) similarly minimises the residual displacement $R_U(p)$, which is the difference between simulated and measured displacement. Simulated displacement can be found from the output of the FEA simulation. The equation to be minimised is as follows (Pagnacco et al., 2005):

$$R_U(p) = U_{sim} - U_{mes} = U_G(p) - U_{mes} \tag{2.3}$$

FEMU has been adapted for numerous problem types, including but not limited to, linear-elastic (Kavanagh and Clough, 1971), elasto-plastic (Meuwissen et al., 1998), and hyperplastic (Genovese et al., 2006). This method will function for any problem that can be expressed in a form suitable for FEA analysis.

2.2.2 Constitutive Equation Gap Method

The Constitutive Equation Gap Method (CEGM) was originally used for the validation of the results from FEA simulations, with the ability to calculate local and global errors, however Florentin and Lubineau (2010) formulated CEGM in such a way that it can be used for parameter identification.

The method calculates the Constitutive Equation Gap (CEG), which, for linear elastic models, is the difference between a known stress field τ and a stress field calculated through a

constitutive model, using elasticity tensor $\mathcal{A}$ and known displacement field v. The CEG can be expressed as follows:

$$\varepsilon(v,\tau,\mathcal{A}) = \frac{1}{2}\int_{\Omega}(\tau - \mathcal{A} : \epsilon[v]) : \mathcal{A}^{-1} : (\tau - \mathcal{A} : \epsilon[v])dV \tag{2.4}$$

The goal of the method is to find an elasticity tensor $\mathcal{A}$ such that the CEG is minimised, i.e. the measured (or analytically calculated) stress field is to be as close as possible to the stress field calculated using a constitutive model.

As stated in Avril et al. (2008a), there are two forms of CEGM. The first is in which kinematic measurements are enforced exactly, i.e. the measured displacement field $\hat{u}$ is introduced into Equation 2.4 directly, as such the minimisation function remains unchanged as:

$$\text{Min } \varepsilon(\hat{u},\tau,\mathcal{A}) \tag{2.5}$$

Whereas the second method enforces kinematic measurements using a penalty form. This is useful for cases with noise in which the measured displacement field may not be kinematically valid. For this form, the minimisation problem is formulated as:

$$\text{Min } \mathcal{F}(v,\tau,\mathcal{A}) = \alpha\varepsilon(v,\tau,\mathcal{A}) + \frac{\beta}{2}\|v-\hat{u}\|^2 \tag{2.6}$$

in which α and β are weighting factors.

CEGM has primarily been used for linear elastic problems, for example by Geymonat et al. (2002), but more recently nonlinear constitutive models have been used, for example by Latourte et al. (2009). In nonlinear cases, such as elasto-plastic, the CEGM as described in this section must be performed for each timestep.

2.2.3 Equilibrium Gap Method

The Equilibrium Gap Method is a method by which damage within an elastic medium can be located. First presented by Claire et al. (2004), the method assumes that full field displacement data is available in a regular grid, with each point on the grid then input into a finite element formulation as nodes between which elements will be constructed. To quantify damage, a damage parameter D_e is assigned to each element e and determines the relationship between the damaged elastic propertied and the reference undamaged elastic properties. This relationship can be seen in Equation 2.7, in which $\mathbf{K}_{me}$ and $\mathbf{K}_{me0}$ are the reference and damaged stiffness matrices for element e.

$$[\mathbf{K}_{me}](D_e) = (1 - D_e)[\mathbf{K}_{me0}] \tag{2.7}$$

Additionally, elastic strain energy E_{me} for element e can be expressed in terms of the damage parameter and reference stiffness matrix, as shown in Equation 2.8, in which $\{\mathbf{u}_e\}$ is the vector of nodal displacementd for element e.

$$E_{me}(D_e, \{\mathbf{u}_e\}) = \frac{1 - D_e}{2}\{\mathbf{u}_e\}^t[\mathbf{K}_{me0}]\{\mathbf{u}_e\} \tag{2.8}$$

With the known displacement field (and hence strain field), the damaged stiffness matrices (in terms of the damage parameter) equations relating to stress and energy equilibrium can be established such that the unknown damage parameters can be found. These equations are present in the work by Claire et al. and summarised in the review paper by Avril et al., but will not be reproduced here due to the EGM not being of particular relevance to geotechnical problems. The concept of automatically identifying damage could instead be applied to anomalous regions within a body of soil, however the limitation to elasticity and the need to know the reference parameters would make adapting this Identification Method to soils challenging.

2.2.4 Reciprocity Gap Method

The Reciprocity Gap Method (RGM) is considered by Avril et al. to be a varient of the VFM in which only the displacements along the boundaries are known. As such, this method is not as useful to problems that are relevant to geotechnical engineering in which for many tests the full field displacement data will be available.

Several authors have used RGM for automated identification of cracks. Andrieux et al. (1999) for example, uses the formulations derived originally by Calderón (2006) (note that this paper is a reprint of work done in 1980) to identify and locate planar cracks in an elastic material for static cases, provided boundary kinematics are overdetermined. Bui et al. (2004) expands on the aforementioned work to apply the principal to elastodynamic cases, with what Bui et al. terms the instantaneous reciprocity gap.

Although interesting, RGM appears to not be applicable to geotechnical problems that this project is concerned with, and as such the equations and derivations relating to it will not be presented. Plane strain problems are the focus of this research project. In such problems the primary dataset available will be the displacement field of a cross section through a body of soil (or a vertical surface in contact with a window). There is potential that the RGM could be adapted to solve geotechnical problems in which surface deformation is known,

potentially in the field, but this is beyond the scope of this work. The interested reader can find the key equations and derivations of the RGM in the cited papers, or in the previously cited review paper by Avril et al.

2.2.5 Virtual Fields Method

The Virtual Fields Method (VFM) uses the principle of virtual work along with full field displacement data to identify constitutive parameters. For linear elastic materials, the careful choice of one virtual field per parameter allows recovery of parameters by solving a system of linear equations. For elasto-plastic or other cases in which the parameters are nonlinear, an optimisation must be carried out (Avril et al., 2008a; Toussaint et al., 2006).

For a volume V with internal stress field σ_{ij}, measured internal strain field ϵ_{ij}, traction T_i on surface S, and based on the principle of virtual work, virtual displacement field u_i^* which is kinematically admissible, and virtual strain field ϵ_{ij}^* the following equation can be derived (Pierron, 2012; Kramer and Scherzinger, 2014):

$$W_{int}^* = W_{ext}^* \qquad \int_V \sigma_{ij}\epsilon_{ij}^* dV = \int_S T_i u_i^* dS \tag{2.9}$$

in which:

$$\epsilon_{ij}^* = \frac{1}{2}\left(u_{i,j}^* + u_{j,i}^*\right) \tag{2.10}$$

and in which kinematically admissible u_i^* refers to the displacement field being continuous, differentiable, and consistent with the problems boundary conditions. Any virtual field meeting these requirements may be used, an infinite number are possible, however some may be better suited to recovering the constitutive parameters than others (Pierron, 2012).

With the assumption of plane strain (i.e. $\sigma_{13} = \sigma_{23} = \sigma_{33} = 0$) specimen thickness t, and traction force T_i applied over a line L_f Equation 2.9 can be reformulated as:

$$t\int_S \left(\sigma_{11}\epsilon_{11}^* + \sigma_{22}\epsilon_{22}^* + \sigma_{12}\epsilon_{12}^*\right) dS = t\int_{L_f} T_i u_i^* dl \tag{2.11}$$

which written in Voigt notation, canceling t, is:

$$\int_S \left(\sigma_1\epsilon_1^* + \sigma_2\epsilon_2^* + \sigma_6\epsilon_6^*\right) dS = \int_{L_f} T_i u_i^* dl \tag{2.12}$$

Using an arbitrary constitutive model, linear-elasticity used in this example, the matrix Q relates stress to strain:

$$\begin{bmatrix} \sigma_1 \\ \sigma_2 \\ \sigma_6 \end{bmatrix} = \begin{bmatrix} Q_{11} & Q_{12} & 0 \\ Q_{12} & Q_{22} & 0 \\ 0 & 0 & Q_{66} \end{bmatrix} \begin{bmatrix} \epsilon_1 \\ \epsilon_2 \\ \epsilon_6 \end{bmatrix} \tag{2.13}$$

where:

$$Q_{11} = Q_{22} = \frac{E}{1-\nu^2} \qquad Q_{12} = \frac{\nu E}{1-\nu^2} \qquad Q_{66} = \frac{Q_{11} - Q_{12}}{2} = \frac{E}{2(1-\nu)} \tag{2.14}$$

allowing the expansion of Equation 2.12 into:

$$Q_{11} \int_S \left(\epsilon_1 \epsilon_1^* + \epsilon_2 \epsilon_2^* + \frac{1}{2} \epsilon_6 \epsilon_6^* \right) dS + Q_{12} \int_S \left(\epsilon_1 \epsilon_2^* + \epsilon_2 \epsilon_1^* - \frac{1}{2} \epsilon_6 \epsilon_6^* \right) dS = \int_{L_f} T_i u_i^* dl \tag{2.15}$$

In the above case there are two unknowns E and ν, and as such two kinematically admissible virtual fields are needed such that two linear simultaneous equations can be found. To illustrate this process, a simple example (adapted from Pierron (2012)) will be followed. Figure 2.1 shows a diametrically compressed disk.

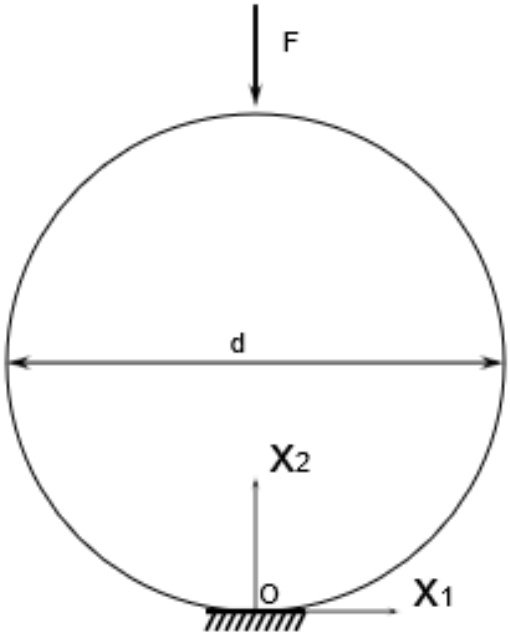

FIGURE 2.1: A diagram of a diametrically compressed disk, with diameter d applied force F, and a coordinate system (x_1, x_2) about origin O

$$\begin{bmatrix} u_1^{*(1)} \\ u_2^{*(1)} \end{bmatrix} = \begin{bmatrix} 0 \\ -k_1 x_2 \end{bmatrix} \qquad \begin{bmatrix} \epsilon_1^{*(1)} \\ \epsilon_2^{*(1)} \\ \epsilon_6^{*(1)} \end{bmatrix} = \begin{bmatrix} a \\ -k_1 \\ a \end{bmatrix} \tag{2.16}$$

$$\begin{bmatrix} u_1^{*(2)} \\ u_2^{*(2)} \end{bmatrix} = \begin{bmatrix} k_2 x_1 \\ 0 \end{bmatrix} \qquad \begin{bmatrix} \epsilon_1^{*(2)} \\ \epsilon_2^{*(2)} \\ \epsilon_6^{*(2)} \end{bmatrix} = \begin{bmatrix} k_2 \\ 0 \\ 0 \end{bmatrix} \tag{2.17}$$

The Equations 2.16 and 2.17 show the two chosen virtual fields in which k_1 and k_2 are arbitrary constants, the first virtual field is vertical compression and the second vertical field is horizontal swelling. Figure 2.2 shows a graphical representation of these fields. Note that kinematic admissability can be trivially checked by calculating the displacement at the fixed boundary to be 0.

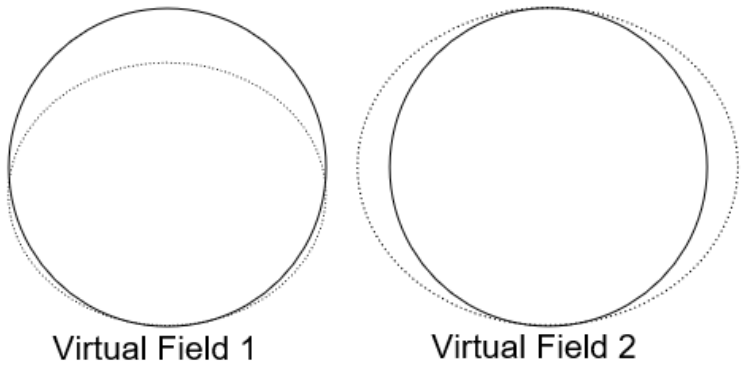

FIGURE 2.2: An illustration of the deformations imposed on the disc during each of the chosen virtual fields, the first being compression, and the second swelling.

These virtual fields can be substituted into the equilibrium Equation 2.15, in which the integral of traction is taken as a point force F, at location d from the origin in x_2 direction, giving the following:

$$\begin{aligned} &\text{Virtual Field 1} \quad -k_1 Q_{11} \int_S \epsilon_2 dS - k_1 Q_{12} \int_S \epsilon_1 dS = \frac{F k_1 d}{t} \\ &\text{Virtual Field 2} \quad -k_2 Q_{11} \int_S \epsilon_1 dS - k_2 Q_{12} \int_S \epsilon_2 dS = 0 \end{aligned} \tag{2.18}$$

with arbitrary constants cancelled:

$$\begin{aligned} &\text{Virtual Field 1} \quad -Q_{11}\int_S \epsilon_2 dS - Q_{12}\int_S \epsilon_1 dS = \frac{Fd}{t} \\ &\text{Virtual Field 2} \quad Q_{11}\int_S \epsilon_1 dS + Q_{12}\int_S \epsilon_2 dS = 0 \end{aligned} \tag{2.19}$$

which reformulated into the matrix form $\mathbf{AQ} = \mathbf{B}$ is:

$$\begin{bmatrix} \int_S \epsilon_2 dS & \int_S \epsilon_1 dS \\ \int_S \epsilon_1 dS & \int_S \epsilon_2 dS \end{bmatrix} \begin{bmatrix} Q_{11} \\ Q_{12} \end{bmatrix} = \begin{bmatrix} \frac{-Fd}{t} \\ 0 \end{bmatrix} \tag{2.20}$$

After integrating the strain fields, likely through summing discretised physically measured elements, Equation 2.20 can be solved to find Q_{11} and Q_{12} and hence E and ν.

Work has been carried out to determine the optimal virtual field choice. Special virtual fields, as developed by Grédiac et al. (2002), are virtual fields chosen such that the matrix $\mathbf{A}$ is the identity matrix. Although not always possible, this allows the trivial solution of $\mathbf{Q} = \mathbf{B}$ without the need to carry out a matrix inversion, an operation that becomes increasingly computationally expensive with matrix size.

The Virtual fields method has been applied to multiple problem types including in-plane linear elastic (Grédiac and Pierron, 1998; Avril and Pierron, 2007), visco-elastic (Giraudeau and Pierron, 2003), and elastic-plastic (Grédiac and Pierron, 2006; Avril et al., 2008b). In the case of nonlinear models (i.e. elasto-plastic), it is not possible to solve for the constitutive parameters, optimisation must instead be used to minimise the difference between internal and external energy (Pierron, 2012).

2.2.6 Identification Methods in Geotechnics

The Identification Methods described were primarily used and developed by researchers in the field of material science or mechanical engineering. The primary materials for which properties were identified were solid blocks of metal. Geotechnical materials behave very differently to metals such that the described methods would potentially require major modification, or at the very least novel methodologies for obtaining and processing data.

Prior to the commencement of this project, very little work has been carried out regarding the development and use of an Identification Method in geotechnical engineering. A single conference proceeding by Gueguin et al. (2015) is the only published work in this field. The work (in which the second author is a supervisor to this PhD Project) describes an

energy equilibrium based methodology which the author says is inspired by the VFM, CEG, and EGM methods. Based on the literature describing these methodologies (as discussed in the preceding sections), it appears that the proposed Identification Method cannot be categorised as any of the above options. Although VFM is the closest, the concept of virtual work is not used. Internal work based on the strain field and the unknown stress field is equilibrated with external work based on the load. An unknown segmented stress-strain curve is found using linear optimisation to find the closest match.

This work will form the foundations of this project. Three simple FEA models are shown to validate the method for an elastic-perfectly-plastic soil response, but no cases for either real data or more complex responses are shown.

As this work was carried out by researchers at the same institution as the author of this project, the codebase and several internal notes detailing its use were available. Much of this codebase is suitable for reuse. The changes and additions necessary to meet the objectives of this project will be discussed in detail in later chapters of this report.

2.3 Particle Imaging Velocimetry

Particle Imaging Velocimetry (PIV) is a subtype of the Digital Image Correlation (DIC) method by which the velocity field within a material can be found across a plane. In the case of fluids, as the method was originally developed for by Adrian (1991), this would be a laser illuminated plane within a liquid seeded with particles. In geotechnics however, the plane could simply be the surface of a block of soil.

Although numerous now less commonly used methods were developed to achieve this effect (the history of which is documented in the textbook Particle Image Velocimetry by Adrian and Westerweel (2011)), Particle Imaging Velocimetry focusses on tracking the movement of particles between a pair of images through computational analysis (Adrian, 1991).

The basis of PIV is to use a camera to record the movement of particles within the sample. The particles could take the form of natural variation in the material, or could be artificially added. In the case that the plane of interest is within a transparent material such as water or transparent soil, laser light can be used to illuminate the particles along the desired plane.

According to Prasad (2000) there are two commonly used forms of PIV:

- Particle Tracking Velocimetry, in which individual particles are matched between images such that their distance can be measured, originally by hand, and more recently algorithmically. A velocity vector would be found for each particle.

- Correlation Based PIV, in which instead of tracking individual particles patches of the image called "interrogation areas" are tracked by finding the best match for the new location of the interrogation area. A velocity vector would be found for each interrogation area, with areas typically arranged on a uniform grid, providing a full vector field across the image.

2.3.1 Digital Image Correlation Algorithm

The DIC algorithm upon which PIV is based is commonly used for tracking soils. It functions by splitting the image into "Interrogation areas" which contain multiple particles. The movement of these Interrogation areas is then calculated by finding the location in the next image that is most similar, usually requiring it to be within a specified "Search area" to minimise the portions of the image which must be searched (Huang et al., 1997).

Although higher order forumulations exist, the simplest forumulation allows the movement of the interrogation area to be found by calculating the best fit for its location in the next image. In a discretised pixel based input, as used in digital cameras, the following equation defines the cross-correlation function used to determine the "degree of match" (Westerweel, 1993; Westerweel, 1999).

$$C(x,y) = \frac{1}{U * V} \sum_{u=1}^{U} \sum_{v=1}^{V} [I(u,v) - \bar{I}][S(u+x, v+y) - \bar{S}] \tag{2.21}$$

In Equation 2.21 $C(x,y)$ represents the correlation or "degree of match" for points x and y, and in which x and y of zero indicates no movement. $I(u,v)$ represents the pixel intensity of the interrogation area within (u,v) space, $S(u+x, v+y)$ is the intensity of the search area, where x and y are the extensions outside of the interrogation area. U and V are the total number of pixel rows and columns in the images. $\bar{I}$ and $\bar{S}$ are the values for mean pixel intensity in areas $I(u,v)$ and $S(u+x, v+y)$ respectively.

Equation 2.21 is the simplest formulation of the DIC correlation function. Higher order methods that provided a significant advance in PIV accuracy involve the ability to reshape and rotate interrogation areas. Described by Florio et al. (2002), an iterative process in which after an initial run, interrogation areas are split, allows the resolution benefits of smaller interrogation areas without the corresponding loss of accuracy. Deformation of the interrogation area (such as rotation, shearing, or stretching) allows a much more accurate representation of what is going on. Methodologies such as this are likely to be implemented in popular commercial or open source DIC packages and not only would allow for improved patch displacement values but would potentially allow for the recovery of other values such as patch rotation.

There are two ways to calculate the correlation field $C(x, y)$: directly in the spatial domain, or using Fast Fourier Transform (FFT) in the frequency domain (Huang et al., 1997). The advantages and disadvantages for each are as follows (Thielicke and Stamhuis, 2014):

- Direct calculation allows for the interrogation and search area to be different sizes with no loss of accuracy but potentially uses excessive computational recourses as area sizes increase.
- FFT based calculation requires areas to be the same size but is much faster to calculate. It is additionally more susceptible to random noise.

Numerous techniques to improve the accuracy of correlation-based PIV have been developed. The most prominent of which is called sub-pixel interpolation. Willert and Gharib (1991) state that the technique allows the correlation peak and hence displacement for an interrogation area to be found to sub-pixel accuracy, resulting in a reduction of error caused during discretisation. The technique essentially takes the correlation field $C(x, y)$ and fits a curve to it, using some form of interpolation (spline or Gaussian being common methods) and then finds the peak of said curve. This allows the location of the peak to be found to a fraction of a pixel. A demonstration can be seen in Figure 2.3.

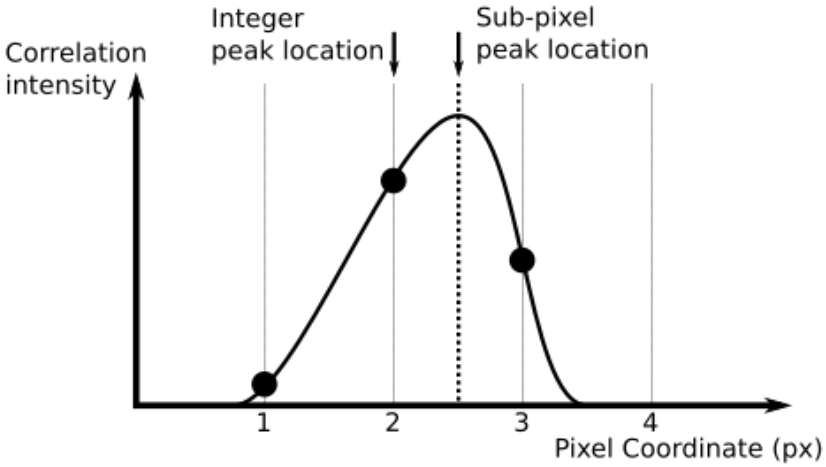

FIGURE 2.3: An diagram based on a similar figure from Thielicke and Stamhuis (2014) showing a 1D representation of sub-pixel interpolation.

Post Processing

Once the output vector field for the image is found, post-processing is often necessary to produce a valid output (Nogueira et al., 1997). The most common problem with data is so called "wild vectors", i.e. vectors corresponding to an interrogation area that by eye are anomalous compared to those around them and to what would be expected for the problem

type. Nogueira et al. (1997) propose that these wild vectors may be dealt with by removing them based on their deviance from the mean. Vectors outside of a specified number of standard deviations would be identified as anomalous and removed. Westerweel and Scarano (2005) recommend using a "normalised median" test, in which vectors are compared to the median of those immediately adjacent to them. Upon removing a vector, both papers propose replacing it with a value interpolated from its immediate neighbours.

2.3.2 PIV in Geotechnics

Geotechnical problems are fundamentally different from fluid dynamics problems. Fluid dymaics problems will typically model flow, will have relatively large displacements, and will tend to be transparent. Soils are typically not transparent, and under usual conditions, will undergo relatively small deformations. Soil displacement fields were first measured by burying lead shot within the sample such that xrays may be used to record the displacement of these targets (Gerber, 1929). This method was also used by Roscoe et al. (1963) to calculate strain fields within the soil sample.

Xray photography is somewhat unwieldily to use for testing, requiring specialist equipment and safety considerations. Chen et al. (1996) used digital video cameras to record the movement of targets added to a soil sample during a centrifuge test. This resulted in a similar output, i.e. a discretised vector field with a value corresponding to each target. This method utilised a computer algorithm to identify and track targets.

PIV software specifically for geotechnical problems was first developed by White and Take (2002) allowing for digital correlation to be carried out on the soil surface, using the methods developed for fluid dynamics, without the need for specific targets. Depending on the soil texture, floc may be added to ensure enough texture, as a flat colour will cause PIV software to fail.

2.3.3 Recent Advances in PIV

The work by Take (2014) describes advances in geotechnical PIV that have been developed since the original release of GeoPIV in 2002. The review paper by Take provides a much more exhaustive summary than what would be appropriate for this literature review, yet it was particularly useful for finding several relevant papers that will be discussed in this section. Of particular interest are the developments relating to quantifying and improving PIV accuracy.

Pan et al. (2008) and Pan et al. (2010) provide quantitative methods by which the quality of PIV patches and speckle patterns can be assessed. Pan et al. (2008) introduces the concept of

Sum of the square of subset intensity gradients (SSSIG), in which the suitability of a patch for DIC is assessed. To find the SSSIG, Equation 2.22 can be used, where $g_x(\mathbf{x}_{ij})$ and $g_x(\mathbf{x}_{ij})$ are the derivatives of grayscale intensities of the subset at pixel location $\mathbf{x}_{ij}$. N is the size of the subset, assuming a square shape. Pan et al. states that these gradients were calculated using the central difference of neighbouring points in the x and y directions.

$$sssig = \frac{1}{2}\left(\sum_{i=1}^{N}\sum_{j=1}^{N}[g_x(\mathbf{x}_{ij})]^2 + \sum_{i=1}^{W}\sum_{j=1}^{H}[g_y(\mathbf{x}_{ij})]^2\right) \tag{2.22}$$

Pan et al. additionally provide plots demonstrating a negative correlation with SSSIG and PIV error values.

In the later work by Pan et al. (2010), the concept of mean intensity gradient (MIG) is introduced. Increases in MIG correlate with reductions in PIV error. Instead of providing a value to assess each individual subset a single global parameter is provided. The methodology to calculate MIG, represented by δ_f, is as follows, in Equations 2.23 and 2.24:

$$\delta_g = \frac{\sum_{i=1}^{W}\sum_{j=1}^{H}|\nabla g(\mathbf{x}_{ij})|}{W \cdot H} \tag{2.23}$$

$$|\nabla g(\mathbf{x}_{ij})| = \sqrt{[g_x(\mathbf{x}_{ij})]^2 + [g_y(\mathbf{x}_{ij})]^2} \tag{2.24}$$

Unless specified, the notation is the same as the SSSIG equation, with the addition of W and H being the size in pixels of the entire image. Pan et al. also state that given a global MIG value, the SSSIG value of a subset can be estimated with Equation 2.25. Pan et al. state that the accuracy of such an estimation will increase with subset size.

$$SSSIG \approx N \cdot \delta_g \tag{2.25}$$

2.3.4 Available PIV Packages

Implementing PIV software from scratch would be very time consuming and largely unnecessary as many such packages have already been developed. Although paid commercial software exists, there are several free and/or open source options available. Three different PIV packages were examined for suitability. This section will detail the pros and cons as well as explain the selection of the most appropriate.

The freely available GeoPIV-RG (Stanier et al., 2015) is the package most commonly used by the geotechnical physical modelling community. This package was specifically designed for soil. Command line functionality exists to generate meshes and run the analysis. Automation is difficult due to some steps requiring manual input. Of particular note is the software's ability to manage control points. A centroiding algorithm exists such that control points can be located and tracked throughout the series of images. A built in calibration function exists however the data is stored in standard text documents so an alternate or bespoke methodology could be used for calibration. The main disadvantage of GeoPIV-RG is that it is closed source. It's Matlab functions are protected ".p" files, meaning they are highly obfuscated to the point that the internal workings are opaque and no modifications are possible. This means that manual inputs cannot be automated and methods cannot be verified. Finally, post processing is lacking, requiring spurious vectors to manually be clicked for removal.

Another PIV implementation is the open source PIVlab (Thielicke and Stamhuis, 2014). This software is available to download as an app via the Matlab app store and all code is freely examinable. A graphical interface makes setting up images and meshes painless. Image preprocessing functionality is also included allowing for improving contrast with methods such as a high pass filter and adaptive histogram equalisation. Post analysis visualisation also has several useful tools. For instance, an arbitrary line can be graphically selected across the data such that a cross sectional displacement plot can be made. The software has many settings allowing a choice of algorithms and allows for multiple passes with different mesh resolutions. Postprocessing capability allows for wild vectors to be filtered by standard deviation or local median, and includes an interpolation function to replace removed data. The downside of this package is that it is primarily designed for fluid dynamics in which significantly greater deformation is expected than in georechnics. Displacement is measured only for image pairs as opposed to relative to the start as in GeoPIV-RG. Additionally, there is no calibration function or means to identify control points.

The final package looked into is OpenPIV (Taylor et al., 2010). In terms of core functionality is is roughly equivalent to PIVlab however lacks finer control for many features. Again, there is a lack of calibration capability, providing means to only scale pixels to millimeters in the x and y direction. The authors of this software recommend it's use as a sanity check for commercial PIV software as opposed to a stand alone tool. It seems there is no functionality in OpenPIV that is not in PIVlab.

GeoPIV-RG would appear to be the most appropriate tool to use. Although lacking many of the extras, such as automatic outlier filtering and contrast correction, the core process is better suited to geotechnics. There is also the benefit that GeoPIV-RG is most commonly used within the geotechnical research community, making collaboration and data sharing easier.

2.3.5 Photography

Readers familiar with the use of DSLR cameras will no doubt have sufficient background knowledge on how cameras might be best used to obtain high quality images suitable for PIV, however, key points will be summarised in this section. Note that although this section is written based on the author's own knowledge, numerous resources can be found online by searching "beginners DSLR guide" or equivalent, for example the web article by Hook (2013).

When a photo is taken, the shutter in the camera will open and light will enter through the aperture via a lens and strike a sensor. After a predetermined time, the shutter will close.

An important concept is the exposure triangle. This is the relationship between three settings on cameras. Aperture, Shutter speed, and ISO.

Aperture, measured as F-stop determines the size of the hole through which light passes. This can be mechanically controlled within the camera lens. A high aperture allows for more light to enter but causes a reduction in depth of field. Depth of field represents how much of the image is in focus simultaneously. A smaller aperture will have an improved depth of field but allow less light.

Shutter speed, or exposure, represents how long the shutter will be open for. A fast shutter speed will let in less light than a longer shutter speed. However, with a longer shutter speed image quality can be reduced by movement of either the camera or the object being photographed. The use of a tripod or similar is necessary for particularly long exposures.

ISO, or exposure compensation, determines how sensitive the sensor is to light. It essentially allows the signal to be amplified. High ISO value allow images to be taken when less light is able to reach the sensor, either due to choices regarding aperture and exposure, or simply due to poor lighting conditions. Unfortunately, amplifying the signal received will also increase noise, potentially causing a grainy image.

The trade-offs between these three factors are a key part of photography. For PIV imaging there are a number of considerations. Firstly, in a controlled laboratory environment good quality lighting should not be an issue. LED lights can be set up and unhelpful natural lighting can be blocked out. Secondly, the area that needs to be in focus is a single plane. Depth of field can be short, allowing for a larger aperture. Shutter speed can therefore be faster, allowing for a high frame rate with little movement during each image. A final consideration is that many images are to be taken in the course of a laboratory test. It is of paramount importance that camera setting do not change in between images. If an off the shelf camera is to be used it must have the ability to disable any "auto" modes and allow for manual control.

2.3.6 Photogrammetry

The American Society for Photogrammetry and Remote Sensing, a scientific association founded in 1934, defines photogrammetry as "... the art, science and technology of obtaining reliable information about physical objects and the environment through processes of recording measuring and interpreting images and patterns of electromagnetic radiant energy and other phenomena." (ASPRS, 2019)

To paraphrase, photogrammetry is the means by which quantitative information can be determined about objects via photographs of them, particularly measurements and dimensions.

The term photogrammetry (or more precisely the german equivalent) was first used by Albrecht Meydenbauer, a Prussian architect and building surveyor, in 1867 (Albertz, 2001), however the foundations of such techniques go back much further. The work by Doyle (1964) provides a detailed history of the technique and it's development over the centuries, and includes an exert from the notebook of Leonardo da Vinci in which vision is described in a way that has much in common with the more recent pinhole camera model.

Uses of photogrammetry range from the relatively mundane building surveying as pioneered by Meydenbauer, to the more extraordinary use in aeriel reconnaissance. Pearse (1994) for example, in a formerly classified document released from the CIA's historical archives, describes the use and development of photogrammetry for military intelligence purposes. The ability to accurately measure Soviet equipment being an obvious improvement over simply having images.

In this project, photogrammetry will be used to facilitate the accurate measurement of planar soil displacement. PIV or other techniques, will provide a discretised displacement field that is measured in pixels. To properly calculate the internal energy expenditure of a specimen undergoing deformation, it is not only necessary to accurately convert pixel coordinates into more appropriate units, but to do so taking into account various aberrations or distortions that may be present in the photographs taken.

Whereas the previous section about photography briefly summarised the considerations regarding taking "good" photographs, this section will examine the considerations regarding obtaining accurate measurements from said photographs. The pinhole camera model will be introduced, as will lens distortion and refraction. Finally, a number of preexisting software tools to process image data will be evaluated.

Intrinsic and Extrinsic Parameters

Intrinsic and Extrinsic parameters refer to properties of the pinhole camera model. This simplified model assumes light travels in straight lines from the object being observed, through an infinitesimally small hole, and strikes a flat plane behind. A simple diagram of the pinhole camera model can be seen in Figure 2.4.

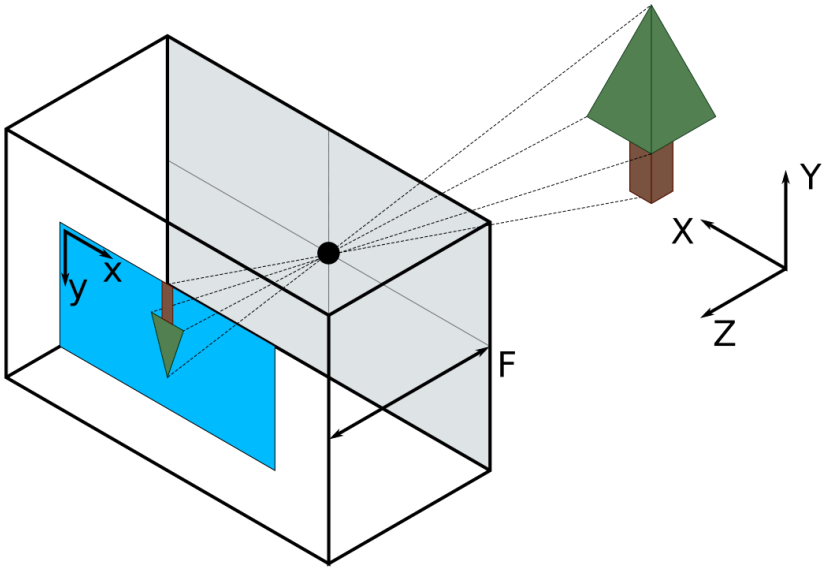

FIGURE 2.4: A sketch representing the pinhole camera model. Light from the 3D tree travels through the pinhole resulting in a 2D image.

As all light paths are straight, and all intercept at a single point, trigonometry can be used to relate the location of the object with the location on the image plane. In other words, the pinhole camera model allows conversion between object space coordinates (X, Y, Z) and image space coordinates (x, y). It should be noted that lens or other distortions or abberations are not included in the pinhole camera model, and as such must be taken into account separately (Davies, 2012; Forsyth, 2012). Also consulted was the web resource by Simek (2013) in which a clear tutorial for programmatically implementing a pinhole camera model is given.

Intrinsic parameters, as per the previously cited resources, allow for 2D transformation of object coordinates into pixel coordinates. World objects are assumed to exist on a single plane, and are projected onto a smaller plane within the camera via the pinhole. Three different transformations are needed. Note that these transformations relate to the position of the film or sensor behind the pinhole. The location of the pinhole is fixed.

First, translation to correct for the location of the sensor. The principle point of the image (the center) is needed for this and has coordinates (x_0, y_0), measured in pixels. Second, the world coordinates need to be scaled. The focal length F which is the distance from the

pinhole to the sensor, measured in world coordinates, is needed but must first be converted into pixel coordinates using factors in the x and y directions: f_x and f_y, where $f_x = F \cdot p_x$ and$f_y = F \cdot p_y$ with p_x and p_y being the dimensions of a pixel measured in world units. The final transformation is shear correction. It is unlikely, but possible, that the pixel sensor array within a camera may not be perpendicular in the x and y direction. Shear can be removed with a skew factor s.

The intrinsic matrix is labelled **K** and is made up of the aforementioned translations. Multiplying them together as shown in Equation 2.26 allows for construction of the intrinsic matrix, with the final formulation shown in Equation 2.27. Note that for ease of later use an additional column of zeros can be added, transforming the **K** into a four by three matrix.

$$\mathbf{K} = \underbrace{\begin{bmatrix} 1 & 0 & x_0 \\ 0 & 1 & y_0 \\ 0 & 0 & 1 \end{bmatrix}}_{Translation} \cdot \underbrace{\begin{bmatrix} f_x & 0 & 0 \\ 0 & f_y & 0 \\ 0 & 0 & 1 \end{bmatrix}}_{Scaling} \cdot \underbrace{\begin{bmatrix} 1 & s/f_x & 0 \\ 0 & 1 & 0 \\ 0 & 0 & 1 \end{bmatrix}}_{Shear} \tag{2.26}$$

$$\mathbf{K} = \begin{bmatrix} f_x & s & x_0 \\ 0 & f_y & y_0 \\ 0 & 0 & 1 \end{bmatrix} \rightarrow \begin{bmatrix} f_x & s & x_0 & 0 \\ 0 & f_y & y_0 & 0 \\ 0 & 0 & 1 & 0 \end{bmatrix} \tag{2.27}$$

The Intrinsic parameters, also called internal parameters, only control what is going on inside the camera. The location of the camera relative to the object being photographed is not included. The location and positioning of the camera is instead determined by the Extrinsic, or eternal parameters.

Extrinsic parameters have two components. A rotation matrix **R** and a translation vector **t**. The rotation matrix contains nine terms relating to the alignment of the camera, each of which is a trigonometric function of yaw θ, pitch ϕ, and tilt ψ. The translation vector contains three values representing the spatial location of the camera in the X, Y, and Z directions. The rotation matrix **R** is shown in Equation 2.28 with the expanded trigonometric terms shown in Equation 2.29 and the translation vector is shown in Equation 2.30.

$$\mathbf{R} = \begin{bmatrix} r_1 & r_2 & r_3 \\ r_4 & r_5 & r_6 \\ r_7 & r_8 & r_9 \end{bmatrix} \tag{2.28}$$

$$\mathbf{R} = \begin{bmatrix} cos\psi cos\theta & sin\psi cos\theta & -sin\theta \\ -sin\psi cos\phi + cos\psi sin\theta cos\phi & cos\psi cos\phi + sin\psi sin\theta sin\phi & cos\theta sin\phi \\ sin\psi cos\phi + cos\psi sin\theta cos\phi & -cos\psi cos\phi + sin\psi sin\theta sin\phi & cos\theta sin\phi \end{bmatrix} \tag{2.29}$$

$$\mathbf{t} = \begin{bmatrix} t_x \\ t_y \\ t_z \end{bmatrix} \tag{2.30}$$

The rotation matrix and translation vector can then be assembled into the extrinsic matrix. Equation 2.31 shows the assembled matrix. Adding additional rows to **R** and **t** also allows for a formulation in which the two translations are multiplicative and can be done as separate steps. This is shown in Equations 2.32 and 2.33, where **I** is the identity matrix. Simply assembling the extrinsic matrix is equivalent to the multiplication formulation, however there may be programmatic reasons to favor one over the other.

$$\mathbf{E} = \begin{bmatrix} \mathbf{R} & \mathbf{t} \\ 0 & 1 \end{bmatrix} = \begin{bmatrix} r_1 & r_2 & r_3 & t_x \\ r_4 & r_5 & r_6 & t_y \\ r_7 & r_8 & r_9 & t_z \\ 0 & 0 & 0 & 1 \end{bmatrix} \tag{2.31}$$

$$\mathbf{E} = \begin{bmatrix} \mathbf{R} & \mathbf{t} \\ 0 & 1 \end{bmatrix} = \begin{bmatrix} \mathbf{I} & \mathbf{t} \\ 0 & 1 \end{bmatrix} \cdot \begin{bmatrix} \mathbf{R} & 0 \\ 0 & 1 \end{bmatrix} \tag{2.32}$$

$$\mathbf{E} = \begin{bmatrix} 1 & 0 & 0 & t_x \\ 0 & 1 & 0 & t_y \\ 0 & 0 & 1 & t_z \\ 0 & 0 & 0 & 1 \end{bmatrix} \cdot \begin{bmatrix} r_1 & r_2 & r_3 & 0 \\ r_4 & r_5 & r_6 & 0 \\ r_7 & r_8 & r_9 & 0 \\ 0 & 0 & 0 & 1 \end{bmatrix} \tag{2.33}$$

The intrinsic matrix **K** and the extrinsic matrix **E** can then be used together for the complete pinhole camera model. Note that the four by three form of the intrinsic matrix must be used to allow for matrix multiplication. Equation 2.34 shows the full model. A previously undefined term has been introduced, w, which is a scale factor.

$$w \begin{bmatrix} x \\ y \\ 1 \end{bmatrix} = \mathbf{K} \cdot \mathbf{E} \begin{bmatrix} X \\ Y \\ Z \\ 1 \end{bmatrix} = \begin{bmatrix} f_x & s & x_0 & 0 \\ 0 & f_y & y_0 & 0 \\ 0 & 0 & 1 & 0 \end{bmatrix} \cdot \begin{bmatrix} r_1 & r_2 & r_3 & t_x \\ r_4 & r_5 & r_6 & t_y \\ r_7 & r_8 & r_9 & t_z \\ 0 & 0 & 0 & 1 \end{bmatrix} \cdot \begin{bmatrix} X \\ Y \\ Z \\ 1 \end{bmatrix} \tag{2.34}$$

Having assembled the pinhole camera equation, it is now possible to convert between object space and image space coordinates. There are however many unknowns. How these unknowns might be recovered will be discussed later. The next section however, will discuss the addition of lenses to the model.

Lenses

Lenses cause light to bend due to having a different refractive index, however unlike windows which are a uniform flat plane (the optics of which will be described in the following section) lenses are curved. The thickness of glass light must travel through, and hence how much it bends, will vary depending on which part of the lens is passed through. A more complex model was required to represent this phenomena (Slama, 1980). A commonly used lens distortion model is Brown (1966), in which lens distortion can be split into tangential and radial.

Tangential distortion takes place when the lens is not parallel to the image sensor and radial distortion is caused by the lens curvature. Radial distortion increases in severity the further from the center of the image, and tangential distortion changes linearly from one edge of the image to the other. Each effect is modelled with an infinite series. J. de Villiers et al. (2008) provide equations based on this model formulated for the removal of such distortion. Equations 2.35, 2.36, and 2.37 for the aforementioned removal technique are shown below.

$$\begin{aligned} x_u = x_d + (x_d - x_0)(K_1 r^2 + K_2 r^4 + \ldots) + \\ (P_1(r^2 + 2(x_d - x_0)^2) + 2P_2(x_d - x_0)(y_d - y_0))(1 + P_3 r^2 + \ldots) \end{aligned} \tag{2.35}$$

$$\begin{aligned} y_u = y_d + (y_d - y_0)(K_1 r^2 + K_2 r^4 + \ldots) \\ +(2P_1(x_d - x_0)(y_d - y_0) + P_2(r^2 + 2(y_d - y_0)^2))(1 + P_3 r^2 + \ldots) \end{aligned} \tag{2.36}$$

$$r = \sqrt{(x_d - x_0)^2 + (y_d - y_0)^2} \tag{2.37}$$

Definitions for terms are as follows: (x_d, y_d) represents a pixel location in a distorted image, (x_0, y_0) are the coordinates for the optical center in pixels, (x_u, y_u) represent a pixel location in an undistorted image, as if it were taken using a perfect pinhole camera, K_n is the n^{th} tangential distortion coefficient, P_n is the n^{th} radial distortion coefficient, and r is the distance from a distorted location to the centre of the image.

The two most commonly occurring types of radial distortion are barrel and pin-cushion. Barrel distortion, in which the centre of the image appears magnified, and pin-cushion distortion, in which the edges appear magnified, are inverses of each other. This property, along with the Brown models ability to model both types of radial distortion, is the justification J. de Villiers et al. (2008) provide for their adaption allowing removal of distortion.

Recovery of Camera Parameters

Having demonstrated the models necessary to model both a pinhole camera and lens distortion, it is now possible to convert between image space coordinates and object space coordinates for a real camera provided the relevant parameters are known. These parameters can be found through a process called camera calibration.

The intrinsic parameters and lens parameters should remain constant for a camera provided settings are not adjusted between images and and such need only be found once. Some of these parameters may be provided by the manufacturer of the camera of lens. The extrinsic parameters, based on camera location and orientation, will by definition be different for every image taken.

Efficient and accurate means by which these parameters can be recovered is an area of active research that is beyond the scope of this project. As such, a summary of the key concepts will be presented, along with an illustrative selection of some of the more noteworthy methods. The methods themselves are not of particular importance to this project as preexisting tools (discusses in a following section) exist to solve the calibration parameters.

The kernel of all calibration processes is having a set of points in which both image space and object space coordinates are known. This allows the suitability of a set of parameters to be assessed. A good set of camera parameters will allow the image space coordinates to be converted to object space coordinates that closely match the known values, whereas a poor set of parameters may produce large errors.

Heikkila and Silven (1997) discusses how traditionally the intrinsic and extrinsic parameters were estimated linearly through the process of direct linear transformation. The paper explains that this linear approach ignores nonlinear lens distortion and is susceptible to noisy data, but can still be used as an initial estimate to seed more robust methods.

Further work by Heikkilä (2000) demonstrates a practical methodology in which a 3D array of circular control points are processed. An iterative algorithm is used to obtain the nonlinear parameters, presenting an evolution over earlier least-squares based approached. Additionally, the parameters for the reverse camera model are found, allowing coordinate conversion in both direction.

Zhengyou (2000) splits prior methods into "Three-dimensional reference object-based calibration" such as the method described by Heikkilä (2000), and "Self-calibration" in which a moving camera can observe an arbitrary rigid scene. Zhengyou presents an alternative in which a 2D array or points can be photographed from multiple (a minimum of two) angles in order to have enough constraints to recover the parameters.

Camera calibration is a field with extensive ongoing research, however this review will limit the papers discussed to these few foundational papers describing the key points. The cutting edge is far beyond what is necessary for this project but these papers, with over ten thousand citations between them, should provide the reader with sufficient understanding of the calibration procedure.

Refraction

In PIV testing, the soil will typically be behind at least one layer of glass or perspex relative to the camera. Control points for photogrammetry likewise could be behind one or more layers (or potentially zero if they are on the front of the window). One possible arrangement would be two windows with the control points sandwiched in between.

Refraction is the bending of light due to entering a medium with a differing refractive index, for instance light that was travelling through air, now travelling through perspex. This bending will result in distortion changing the apparent location of objects photographed through a refractive medium. For laboratory testing using PIV, this could be the location of soil patches, the location of control points, or both, potentially to differing degrees.

Refraction is modelled with Snell's Law and the degree of refraction will increase with distance from the principal point (assuming the camera is perpendicular to the glass). Snell's law is shown in Equation 2.38 in which α is the angle of incidence, β is the angle of refraction, and n is the refractive index of the medium.

$$\sin\alpha = n \cdot \sin\beta \tag{2.38}$$

Other researchers (Effendi, 2007; Stanier, 2011) carrying out PIV testing have used and validated a set of equations derived by White (2002). The equations presented by White are as follows, with Equation 2.39 providing the correction mechanism, Equation 2.40 providing the refraction factor for a single layer of material, and Equations 2.41 and 2.42 define the refraction factor for cases with two layers of material.

For the following equations $\vec{R}_{actual}$, $\vec{R}_{apparent}$, and $\vec{R}_0$ are position vectors representing the actual and apparent position of a point, allowing with the position of the principle point. Each vector contains the corresponding x and y coordinates. λ is the refraction correction factor, H is the distance from the camera to the back of the window/s, t and n represent the thickness and refractive index for a single window, whereas t_1,t_2,n_1, and n_2 are the equivalent values for a pair of windows. The final term β_1 is the angle of refraction for the first window.

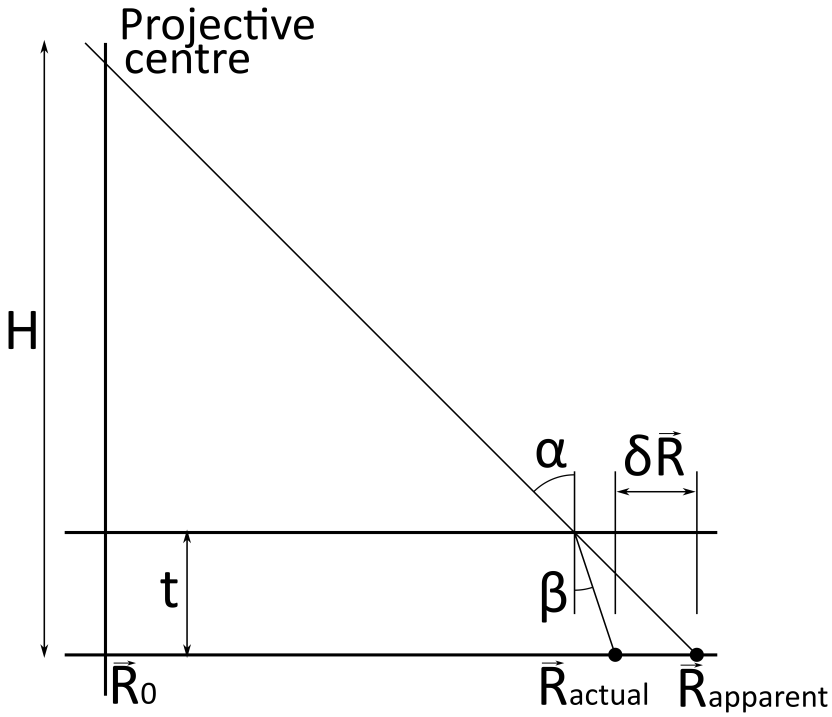

FIGURE 2.5: The geometry of a single window refraction case.

$$\begin{bmatrix} x_{actual} \\ y_{actual} \end{bmatrix} = \begin{bmatrix} x_{apparent} \\ y_{apparent} \end{bmatrix} - \lambda \begin{bmatrix} x_{apparent} - x_0 \\ y_{apparent} - y_0 \end{bmatrix} \tag{2.39}$$
$$\vec{R}_{actual} \qquad \vec{R}_{apparent} \qquad \vec{R}_{apparent} - \vec{R}_0$$

$$\lambda = -\frac{t}{H} + \frac{t}{\sqrt{n^2(H^2 + |\vec{R}_{apparent} - \vec{R}_0|^2) - |\vec{R}_{apparent} - \vec{R}_0|^2}} \tag{2.40}$$

$$\lambda = -\frac{t_1 + t_2}{H} + \frac{t_1}{|\vec{R}_{apparent} - \vec{R}_0| \cot\beta_1} + \frac{t_2}{|\vec{R}_{apparent} - \vec{R}_0| \sqrt{{n_2}^2(\cot^2\beta_1 + 1) - 1}} \tag{2.41}$$

$$\cot\beta_1 = \sqrt{{n_1}^2 \left(\frac{H^2}{|\vec{R}_{apparent} - \vec{R}_0|^2} + 1 \right) - 1} \tag{2.42}$$

The meaning behind the above equations and terms are best shown in a diagram. Figures 2.5 and 2.6, reproduced based on the equivalent diagrams in White (2002), shows the geometry for one and two window refraction problems respectively. Note the new term $\delta\vec{R}$ which represents the total difference, i.e. $\delta\vec{R} = \lambda(\vec{R}_{apparent} - \vec{R}_0)$.

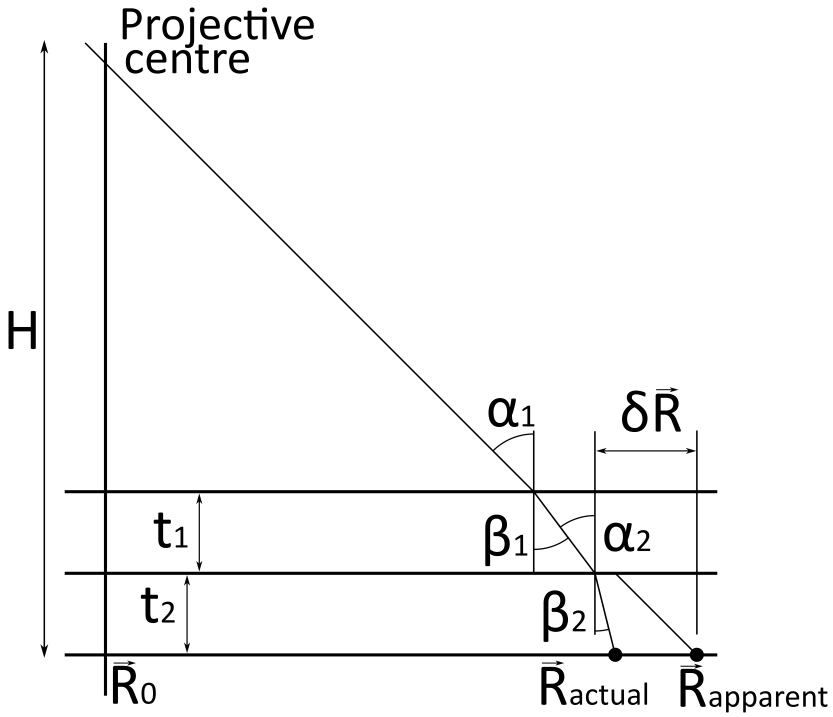

FIGURE 2.6: The geometry of a two window refraction case.

Validation

After obtaining the camera, lens, and refraction parameters, a validation step should be carried out. This consists of calibrating an image containing a known object, such as a distortion target, example manufactured by AppliedImage (2017) shown in Figure 2.7, and measuring the known distances within. The distortion target contains an array of very accurately drawn dots. By measuring the distances between them in a calibrated image, the validity of data may be ensured.

Available Tools

Several tools exist which could be of use for photogrammetry. This section will discuss the pros and cons of each.

Perhaps the simplest is the built in GeoPIV-RG calibration function. This uses a pinhole camera model and lens model to calculate object space coordinates of locations within an image (Stanier et al., 2015). There are a number of drawbacks. The assumption that the control points are in the same plane as the soil is not necessarily true depending on how laboratory equipment is set up. Having control points, e.g. in front of a window for instance would invalidate the pinhole camera model. The assumption of coplanarity also allows for

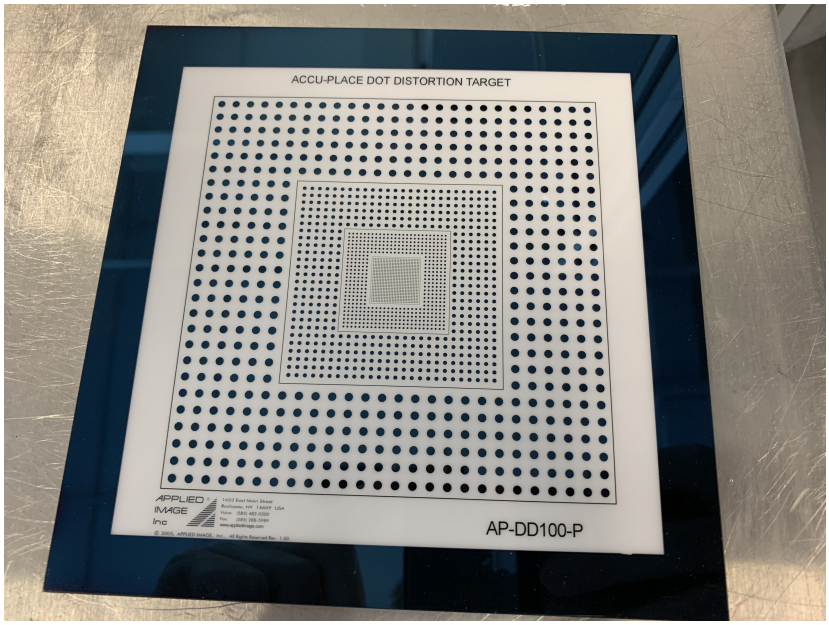

FIGURE 2.7: An example of a distortion target.

refraction to be ignored, an such the function will not be able to deal with laboratory models where this is not the case. It is also unclear how the lens model has been implemented. As stated in previous sections, solving lens parameters requires either control points in a 3D array for a single image, or coplanar control points in multiple images from multiple angles. The GeoPIV-RG calibration function has no capability for a 3D control point array and as the camera is stationary during a PIV there will be negligible difference in camera location between images. As the software is closed source, it is not possible to verify how GeoPIV-RG is able to solve the lens model. It is possible that small camera movement is enough, or assumptions have been made to allow a solution, but there is no documentation explaining this.

Heikkilä, as referenced several times in the theory sections of this literature review, has published a Matlab toolbox capable of recovering camera parameters (Heikkilä, 2000). This toolbox features the capability to solve the pinhole and lens models with either one 3D control point array or several coplanar array images. Additional functions are provided, including the ability to remove distortion from image coordinates, find the camera location (extrinsic parameters) for a single calibrated image, and is additionally able to solve the inverse model (i.e. going from world coordinates to image coordinates). The code is also able to be examined freely to ensure it is functioning as expected and has ample documentation and papers describing it. This is a general purpose tool that is not specific to PIV, as such it should be seen as building blocks that must be assembled to provide PIV calibration capabilities. Again, there is no refraction functionality, so this would have to be added as an additional

step.

The final tool of potential use is the Matlab Computer Vision toolbox (MathWorks, 2017). This is a very extensive toolbox with many features beyond the scope of this project. It also has a license fee to use, which may make it unsuitable for implementation in any software that isn't intended as a research tool. Of particular note is the camera calibration app. This app provides a graphical interface to allow for the selection of images with coplanar arrays and then solves both the pinhole and lens models, with many settings to allow the user to select assumptions etc. A graphical output showing the extrinsic locations of each image is also provided. The camera calibration app is very user friendly and is able to automatically detect control points (in the form of a chessboard pattern). After obtaining the camera and lens parameters, a number of functions are provided for processing PIV data. Lens distortion can be removed with the "undistortPoints" function. Extrinsic parameters for a single image can be found with the "extrinsics" function, and the "pointsToWorld" function is able to find the world coordinates for a set of given image coordinates for a set camera location. Many easy to use functions are provided that could be assembled into a PIV calibration script.

It seems likely that the Matlab computer vision toolbox is the best solution due to it's extensive capabilities and ease of use. None of the examined software packages have capability for dealing with refraction, so bespoke scripts will have to be written. It is not anticipated that this will be particularly difficult.

2.4 Traditional Laboratory and Field Methodologies

As obtaining soil properties has been necessary for engineering design for many years, multiple methods exist to categorise and quantify soil as an engineering material. These methodologies are commonly used either in the lab or in the field.

This section will list some of the available methods that have overlap with the properties and parameters obtainable via an Identification Method, along with several others that are useful for understanding broader soil behaviour. The intention of this section is to identify tests that can be used to validate a geotechnical Identification Method during future laboratory testing. It is unlikely that these methods would be replaced by an identification based approach, but that they could potentially coexist alongside one.

2.4.1 Triaxial shear test

A triaxial test allows for a soil specimen to be loaded differently in 3 axes. A true triaxial test allows this loading to be mechanically controlled in each direction whereas more standard test apparatus allow only mechanically controlled loading in one (typically the vertical) direction with the two other axis being loaded uniformly by water pressure. As the specimen is loaded the normal stress applied and displacement can be recorded Head (1986).

There are several variations including Consolidated Drained (CD), and Consolidated Undrained (CU), however the most applicable to this project is the Unconsolidated Undrained (UU) test in which a specimen is loaded under a strain controlled regimen at a rate fast enough to disallow consolidation. In a UU test, the specimen will be loaded until it fails by either a shear band forming or by barrelling.

The output of a UU triaxial test will be a plot of axial strain against axial stress. This is not equivalent to shear strain vs shear stress but a comparison is possible through empiric factoring.

Detailed guidance on how UU triaxial tests (or indeed other variants) can be read in British standards 1377-8:1990 (British Standards Institution, 1990d). Exact details for factors such as sample preparation and size, confining pressure, loading rate, etc. will not be discussed in the literature review but instead in the later physical modelling chapter (Chapter 6).

Although a commonly carried out test, samples must be extracted causing a potential for disturbance. Even perfectly following the process specified in the standards specify, there is no guarantee that the results will be truly representative.

2.4.2 Direct shear test

Volume seven of the BSI standard for soil testing described the process by which direct shear testing is to be carried out British Standards Institution (1990c). The test involves placing soils or rocks in a split shear box in which both parts can be slid past each other. The test can be carried out for both frictional soils (i.e. sands) and cohesive soils (i.e. clays). Testing on rocks is limited to weak rocks unless there are suitable discontinuities. Additional guidance on carrying out a direct shear test is given by Head (1994)

Multiple confining pressures are used to record peak shear stresses. These values are then plotted and a line of best fit is found. The y intercept is cohesion c and the slope is the angle of friction θ. For cohesive soils, this line should be horizontal.

These found values can be compared directly to a stress-strain curve found by other means. For cohesive undrained soil, cohesion will be equal to the peak shear stress at the plateau of the stress-strain curve.

2.4.3 Shear vane test

The procedure to carry out shear vane testing is described in BS 1377-9:1990 (British Standards Institution, 1990d). This is a field test that is carried out in situ. The method is carried out by inserting a vane into the ground and rotating it until the soil immediately surrounding the vane shears in a circular pattern. The handle of the vane will have a spring mechanism by which the required torque is measured and recorded.

The test can be used only for cohesive soils and recovers the peak shear stress. When comparing to stress-strain curve data, this would be the value of the horizontal plateau. The standards describe the specification of the vane and the correct procedure which is relatively simple.

It should be noted that this test is designed to be carried out in the field. Using it to test a sample in a laboratory would not be compliant with BS 1377-9:1990, but may be able to provide useful comparison data provided any considerations e.g. boundary conditions, are taken into account.

2.4.4 Cone penetrometer test

A cone penetrometer test (CPT) is a test in which a rod with an angled tip is driven into the ground. The force on the angled tip is recorded, along with the force on a sleeve around the tip. The piezocone penetration test (CPTU) additionally records pore water pressure from integral sensors around the cone. BS EN ISO 22476-1:2012 describes the apparatus and procedure for carrying out a CPT (British Standards Institution, 2012).

The raw outputs for a CPT or CPTU provide insight into changes in soil behaviour with depth. Several authors describe the ability to use CPT data to empirically obtain bearing capacity (Meyerhof, 1956) and undrained shear strength (Rémai, 2013). Undrained shear strength can be compared directly to the plateau of the stress-strain curve or peak shear values from other tests, and bearing capacity can be used to estimate cohesion via Terzaghi's equation. CPT tests are traditionally carried out in situ, however smaller models may be suitable for laboratory use.

2.4.5 Oedometer test

Oedemeter tests are used to determine how a soil will behave during consolidation. BS 1377-5: 1990 which details compressibility, permeability and durability tests explains how to prepare for and carry out one dimensional consolidation tests British Standards Institution (1990b). The oedemeter is apparatus in which a circular disc of soil is placed within a consolidation cell and sandwiched between two porus plates. Vertical loading can be applied with displacement recorded. Loading is incrementally increased, either by manually adding weights to a lever arm, or pneumatically.

After completing the test, a number of parameters relating to the consolidation of the soil will be found. Although none of these are useful for direct comparison with the output of an Identification Method, they may provide useful clues for cases where soil behaves differently at different depths for example. These parameters can also be used to aid in the consolidation of a specimen from slurry, or for determining whether a loading test will be drained or undrained.

2.4.6 Water content test

Measurement of soil water content is useful for understanding behaviour, and a quick and easy method for identifying differential soil properties thoughout a sample or accross a site.

Guidance on several possible procedures can be found in Head (1984). One particular test, in which samples are weighed before and after oven drying is detailed by British Standards Institution (1990a). Exceptable sample sizes and oven temperatures are given allong with a step by step process.

The moisture content can be found with Equation 2.43, in which w is the moisture content, m_1 is the mass of the container, m_2 is the mass of the container containing wet soil, and m_3 is the mass of the container containing dry soil.

$$w = \frac{m_2 - m_3}{m_3 - m_1} \cdot 100 \tag{2.43}$$

2.4.7 Soil classification

Although not a way of directly obtaining properties, classifying the soil can allow for a range of values to be taken from literature, either directly (perhaps not suitable for detailed

design), or as a sanity check on values obtained by other means. Knowing the broad behavioural properties based on classification will also allow for better selection of more detailed tests.

Head (1984) provides guidance on soil classification through the use of identification charts. Visual descriptions are provided for broad classification (e.g. gravels, sands, peats) with simple field tests for estimating compactness, strength, and structure. For example, a soft or loose silt is "Easily moulded or crushed in the fingers" whereas a firm or dense silt "Can be moulded or crushed by strong pressure in the fingers".

The cited manual provides numerous other tests including chemical analysis, particle size distribution and specific gravity.

2.4.8 A note on "true" soil response

Despite there being numerous different means by which soil properties can be recovered, it is worth considering whether any one model can be said to obtain the "true" soil response. Every test mentioned above measures the soil in a slightly different manner with different drawbacks. Most of the presented methodologies involve some form of disturbance that bring into question the representativeness of the test.

It is likely that, for instance, a direct shear test would recover a different undrained strength than a triaxial test. Several triaxial cores from the same body of soil are also likely to produce different stress-strain responses. After performing a range of tests it is likely that some could be discounted as anomalous, with many of the remaining tests being roughly, but not exactly, similar in terms of the indicative soil response. There is ultimately no way of telling which result would be truly representative of the soils behaviour. Instead, there would be a range of possibilities, with the confidence in this range increasing as more tests are performed.

An Identification Method would be an additional means by which a soil response can be recovered. As with any method it is unlikely that the recovered response is exactly representative of the soils behaviour. As with the other methods, this does not imply that an Identification Method would be without use. Having an additional data point that is generated in a completely separate way has potential to increase confidence that the range of soil responses recovered through various testing methodologies are approximately representative of the "true" response.

2.5 Identified Gaps in Literature

There are a number of gaps in existing literature that can be filled during this project. The most significant of which is the lack of Identification Methods that have been applied to geotechnical problems.

Of the Identification Methods used in materials science, the majority of work has been carried out on simple linear elastic constitutive models. Geotechnical problems are typically highly nonlinear and as such methods focused on elastic behaviour will either be unsuitable or require modification. Frictional soil in particular is in no way analogous to the work done using metals.

2.6 Conclusion

This chapter has described a number of commonly used Identification Methods and assessed their suitability for use with geotechnical problems. PIV and photogrammetry have been discussed with practical considerations and relevent equations shown, and finally a brief summary of commonly used laboratory and field tests used to recover soil properties has been given.

All relevent information to understand, develop, and validate a geotechnical Identification Method has been presented, along with a summary of the main challenges that are not covered by existing literature.

Chapter 3

Derivation and Calculation of the Energy Equilibrium Equation

3.1 Introduction

As stated in the Literature Review, the principle behind Identification Methods is typically that of energy equilibrium. Although there are wide ranges of implementations, work acting upon a specimen is assumed to be equal to work dissipated via deformation.

This chapter will therefore provide the derivation from first principles for the energy equilibrium equation to be used with the methods presented in this thesis. Of particular note is the formulation of the equilibrium equation in terms of common geotechnical parameters: mean stress s, maximum shear stress t, volumetric strain ϵ_v, and shear strain ϵ_s. Using such parameters allows for uniformity with common geotechnical constitutive models and sample testing methodologies.

The chapter will contain several sections to achieve this aim. First, a derivation of work done in terms of stress and strain will be presented. This will be followed by the definitions of the stress and strain parameters listed in the previous paragraph, along with their graphical representations in the form of Mohr's circles. Finally, the derivation and proof for the energy equilibrium will make up the remainder of the chapter.

At first glance, some of the content covered in this chapter may seem trivial, after all, most readers could quote the definition of work if asked. However, in the course of writing this thesis, it was found that there is a great deal of nuance involved, particularly when generalising otherwise trivial cases. This chapter serves to show the foundations on which the methodology presented in this thesis is built, along with what simplifications and assumptions can be made. The following sections will err on the side of completeness, with detail given in places most relevant to this thesis. The intention of this chapter is that interested

reader will be able to follow the presented derivations and proofs and have confidence in the later methodology, without needing to piece together sections from multiple textbooks.

It should be noted that this derivation, and thesis, assumes a purely mechanical case in which heat or sound production or other effects are assumed to be negligible and as such are not included in energy equilibrium. Although such terms may be present in general and rigorous continuum mechanics textbooks, these terms are almost universally discounted in geotechnical engineering. An additional and important assumption is the use of infinitesimal strain theory as opposed to finite strain theory. This is valid on the assumption that deformations dealt with are small compared to the size of the material in question.

Additionally, it should be noted that this project is only concerned with plane strain cases, and as such, unless otherwise stated, it should be assumed that the derivations, assumptions, and other presented work is valid only in plane strain. There is no reason that the methodologies presented couldn't be adapted to 3D problems, but doing so is beyond the scope of this thesis.

3.2 Work

3.2.1 Work due to Forces

Mechanical work is commonly known to be calculated by multiplying a force P by a corresponding displacement u, i.e. $W_{force} = P \cdot u$. Although this is true, it is a simplification based on the assumptions of a constant load applied to a single point. A more generalised form, again for a point load, is as follows:

$$W_{force} = \int P \, du \tag{3.1}$$

Equation 3.1 describes work due to a force as the integral of force with respect to displacement, or the area under the force-displacement curve. This is sufficient to describe movement of a rigid object, for example a footing foundation, in which a solid block of concrete moves by a measurable amount under the influence of a measurable force. In 2D (or indeed 3D) cases, it will likely be necessary to split both force and displacement into x and y components, as the angles of the magnitudes will not necessarily be equal.

There are several cases worth mentioning. The first is work done due to gravity. This would be non negligible and worth considering in any models with net vertical movement. In this

case, the applied loading is the product of the mass of an object and gravitational acceleration (9.81 $m \cdot s^{-1}$), resulting in a total work as shown in Equation 3.2, were M is mass and g is gravitational acceleration and u_y is vertical distance moved.

$$W_{gravity} = \int M \cdot g \, du_y \tag{3.2}$$

In some situations, work done by gravity may in fact be negative, i.e. adding energy to the system. Scenarios such as a failing embankment or retaining wall are good examples, whereas other systems such as an anchor pullout may involve gravity removing energy from the system. Horizontal movement has no effect on work done due to gravity.

Work done against friction is also of note. In this case, a resisting force F can be taken as the coefficient of friction multiplied by a normal force N, which is then multiplied by the distance moved against this friction. This case is worth mentioning as a geotchnical plane strain tests are often carried out in glass or perspex fronted boxes and energy is expended moving the soil against the glass. This will indeed be the case for the laboratory work that will be presented in later chapters. Equation 3.3 shows work expended due to friction, in which μ is the coefficient of friction and u is the distance moved against friction. It should be noted that in some scenarios this concept would better be represented with adhesion rather than friction. Although friction will be present in nearly all laboratory tests it will in many cases be negligible. For the experimentation carried out as part of this project (described in Chapter 5) it was found to be of little importance but is nonetheless included in this section for completeness. Appendix B contains supplementary laboratory data demonstrating the relatively minor influence of friction.

$$W_{friction} = \int N \cdot \mu \, du \tag{3.3}$$

It is possible that gravity could add work to the system such as in cases where material is moving downwards. In such a case the work done due to gravity would be negative. Work due to friction will instead always be positive regardless of movement direction.

Figure 3.1 provides an example of the concepts discussed in this section. Note that in this example, force P is now acting along the angle of the resulting movement due to the effects of gravity, and would need to be split into x and y components. Friction however, always acts opposite to the resultant movement angle.

The units for work are Joules J, or alternatively $kg \cdot m^2 \cdot s^{-2}$. This term derives from the multiplication of force measured in newtons N (which in SI units is $kg \cdot m \cdot s^{-2}$) with distance measured in metres m.

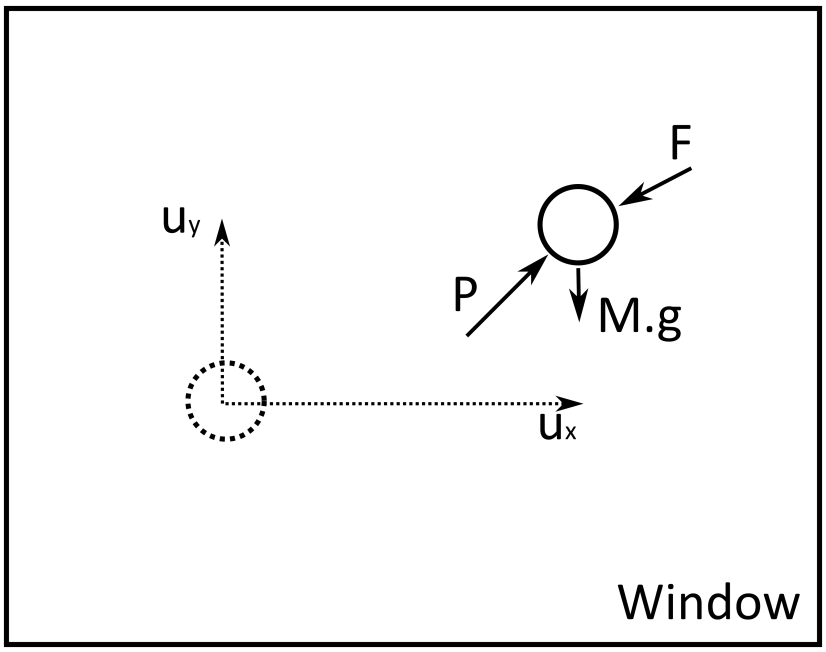

FIGURE 3.1: An Infinitesimal particle moving u_x and u_y distance due to force P, gravity, and friction

3.2.2 Work due to Stress and Strain

Simply considering work in terms of force and displacement cannot describe the work taking place in the soil beneath the footing. Even discretizing the soil doesn't solve the issue, as the soil isn't simply moving, but instead is deforming. Work must therefore be described in terms of stress and strain.

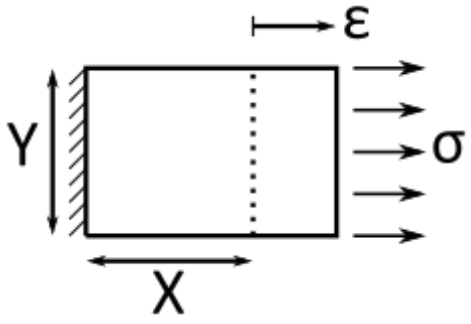

FIGURE 3.2: A block of sides X and Y undergoing a strain of ϵ due to a stress of σ.

Figure 3.2 shows a simple 2D example of a block of material undergoing extension due to a uniform distributed load. The dimensions are Xm by Ym with a depth of 1m into the page, and a 2D area of Am ^{2} , where $A = X \cdot Y$. A constant stress of σ (measured in $kg \cdot m^{-1} \cdot s^{-2}$) causes a strain of ϵ (measured in $m \cdot m^{-1}$). Dimensional analysis of these terms shows that

multiplication of stress and strain does not result in work, but instead energy density W_d i.e. work per unit volume. Equation 3.4 shows this multiplication, along with the associated SI units.

$$W_d = \sigma \cdot \epsilon \qquad J \cdot m^{-3} = kg \cdot m^{-1} \cdot s^{-2} \cdot m \cdot m^{-1} \tag{3.4}$$

It is clear that simply multiplying this value by the corresponding volume will provide the work done. Examining the meanings behind stress and strain also intuitively shows this. Stress is a force divided by an area, and strain is an extension over the original length. Volume is a product of both the aforementioned area and depth. As such, the final equation for work is as follows, where V is volume:

$$W = \sigma \cdot \epsilon \cdot V \tag{3.5}$$

Again, it should be noted that Equations 3.4 and 3.5 are valid in trivial cases with constant stress, or where constant stress is a reasonable assumption. The more generalised form involves the integral of the stress-strain curve. It is typically assumed that stress is a function of strain and as such, the previous equations can be rewritten as shown in Equations 3.6 and 3.7:

$$W_d = \int \sigma \ d\epsilon \tag{3.6}$$

$$W = \int \sigma \ d\epsilon \cdot V \tag{3.7}$$

Similarly, the above process can be repeated for shear strain γ and shear stress τ. Figure 3.3 shows a block of material of dimensions Xm by Ym with a depth of 1m into the page, and again a 2D area of Am ^{2} undergoing deformation due to shear force. Note that the same shear strain can be presented in two equivalent ways, as shown in Figure 3.3, in which γ is equal to $\alpha + \beta$.

It should be noted that shear strain is not a distance over original length as normal strain is, but instead is an angle. However for small shear strains (less than 0.2 radians), the small angle approximation accurate to an acceptable tolerance, allowing for $\tan(\alpha) \approx \alpha$. As such, $\alpha = \frac{\Delta X}{Y}$ and $\beta = \frac{\Delta Y}{X}$ with the sum of these equalling total shear strain $\gamma = \frac{\Delta X}{Y} + \frac{\Delta Y}{X}$. It should be noted that the shear strain γ is twice the tensor notation shear strain ϵ_{xy}. As before, multiplying shear stress by shear strain gives energy density, and multiplying energy density by volume provides work done. The following equations demonstrate:

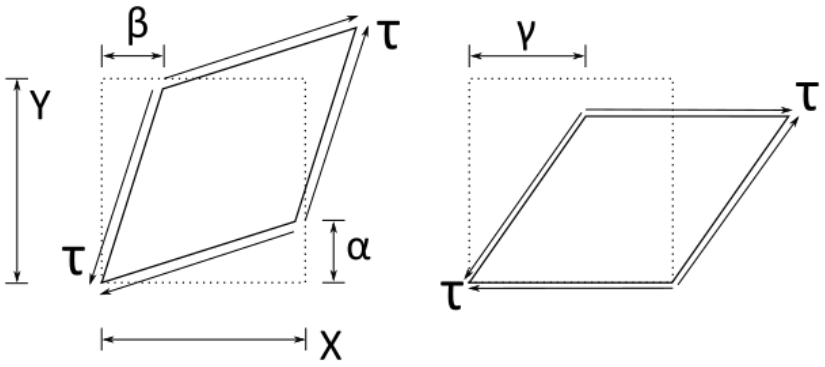

FIGURE 3.3: A block of sides X and Y undergoing a shear strain of γ due to a shear stress of τ.

$$W_d = \tau \cdot \gamma \tag{3.8}$$

$$W = \tau \cdot \gamma \cdot V \tag{3.9}$$

Or in the more generalised case allowing for changes in τ:

$$W_d = \int \tau \ d\gamma \tag{3.10}$$

$$W = \int \tau \ d\gamma \cdot V \tag{3.11}$$

The final factor to consider with regards to work due to stress and strain, is that objects could undergo multiple stresses and strains simultaneously. Normal stresses and strains at 90 degrees to each other , as well as shear stress and strain. Fortunately, these different stress and strain energy calculations do not interact with each other, and as such, the terms for work and energy density discussed above can simply be added and are shown in Equations 3.12 and 3.13.

$$W_d = \int \sigma_x \ d\epsilon_x + \int \sigma_y \ d\epsilon_y + \int \tau_{xy} \ d\gamma_{xy} \tag{3.12}$$

$$W = \left(\int \sigma_x \ d\epsilon_x + \int \sigma_y \ d\epsilon_y + \int \tau_{xy} \ d\gamma_{xy} \right) \cdot V \tag{3.13}$$

Or simplified based on the assumption of constant stress:

$$W_d = \sigma_x \cdot \epsilon_x + \sigma_y \cdot \epsilon_y + \tau_{xy} \cdot \gamma_{xy} \tag{3.14}$$

$$W = \left(\sigma_x \cdot \epsilon_x + \sigma_y \cdot \epsilon_y + \tau_{xy} \cdot \gamma_{xy}\right) \cdot V \tag{3.15}$$

In tensor notation, this can be expressed as the double dot product of the stress tensor and the strain tensor, multiplied by volume:

$$W = [\underline{\sigma} : \underline{\epsilon}] \cdot V = \begin{pmatrix} \sigma_x & \tau_{xy} \\ \tau_{xy} & \sigma_y \end{pmatrix} : \begin{pmatrix} \epsilon_x & \frac{\gamma_{xy}}{2} \\ \frac{\gamma_{xy}}{2} & \epsilon_y \end{pmatrix} \cdot V = \begin{pmatrix} \sigma_x & \tau_{xy} \\ \tau_{xy} & \sigma_y \end{pmatrix} : \begin{pmatrix} \epsilon_x & \epsilon_{xy} \\ \epsilon_{xy} & \epsilon_y \end{pmatrix} \cdot V \tag{3.16}$$

3.3 Stress and Strain

This section will show definitions of various stress-strain terms with reference to Mohr's circles.

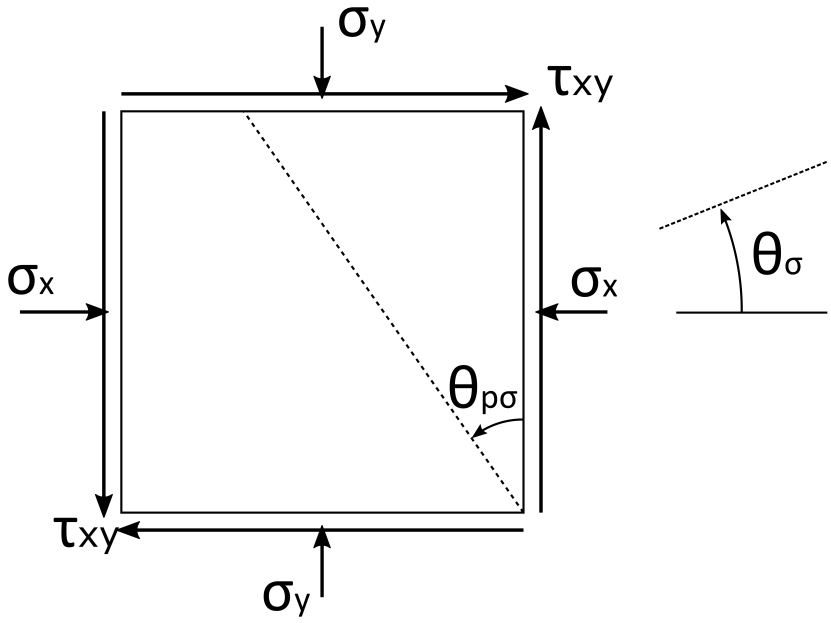

FIGURE 3.4: A block of material subject to normal stresses σ_x and σ_y and shear stress τ_{xy}. $\theta_{p\sigma}$ represents the principal angle for stress, and θ_σ represents an arbitrary rotation of the frame of reference

Figure 3.4 shows a diagram of an infinitesimal block of soil subject to various stresses. Normal stresses σ_x and σ_y are at right angles to each other and as such change in one has no

effect on the change in the other. Shear stress τ_{xy} likewise is independent. The plane of reference by which these stresses is measured is arbitrary. Rotating the plane of reference by θ_σ will change the stresses, but is equally valid. Should the plane of reference be rotated by the principal angle $\theta_{p\sigma}$, no shear stress will be recorded, and the stresses the block is subjected to can be described purely with normal stresses, in this case referred to by principal stresses σ_1 and σ_3. It should be noted that there are two principal angles, 90° apart, that will achieve this effect. This is because the plane of reference can be rotated in either direction. Either of these angles can be used but for simplicity the smaller angle will be assumed for the diagrams given in this section. Figure 3.5 shows a Mohr's circle, a visual representation of this changing plane of reference. The circle allows for identification of the aforementioned principal stresses geometrically, or through the following equations:

$$\sigma_1 = \frac{\sigma_x + \sigma_y}{2} + \sqrt{\left(\frac{\sigma_x - \sigma_y}{2}\right)^2 + \tau_{xy}^2} \tag{3.17}$$

$$\sigma_3 = \frac{\sigma_x + \sigma_y}{2} - \sqrt{\left(\frac{\sigma_x - \sigma_y}{2}\right)^2 + \tau_{xy}^2} \tag{3.18}$$

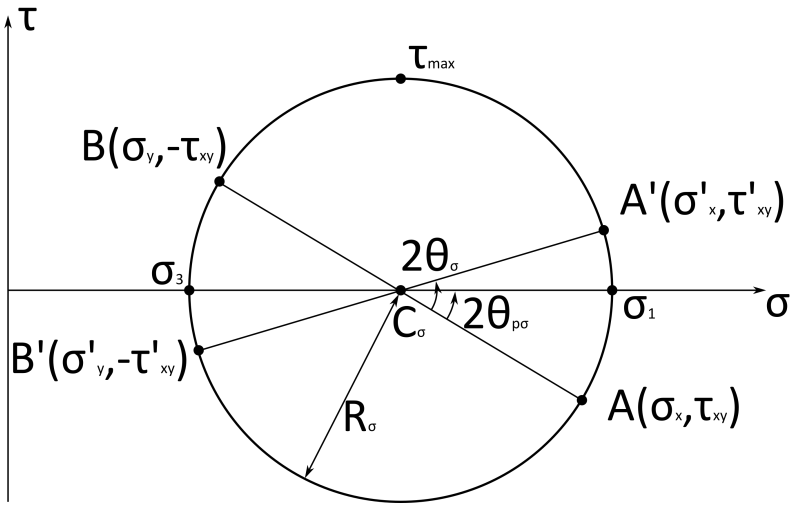

FIGURE 3.5: A stress Mohr's circle presenting the forces shown in Figure 3.4.

The Mohr's circle allows the definition of several additional terms, described in the following equations:

$$s = \frac{\sigma_1 + \sigma_3}{2} = \frac{\sigma_x + \sigma_y}{2} \tag{3.19}$$

$$t = R_\sigma = \frac{\sigma_1 - \sigma_3}{2} = \sqrt{\left(\frac{\sigma_x - \sigma_y}{2}\right)^2 + \tau_{xy}^2} \tag{3.20}$$

Equation 3.19 shows mean stress. This is the hydrostatic component of stress, i.e. a uniform component that is applied equally in all directions. Geometrically, the value can be found at the centre of the circle, at point C_σ. The value can be found by averaging the normal stresses regardless of the plane of reference used.

Equation 3.20 shows maximum shear stress. This is the non hydrostatic component of stress, i.e. it is applied differently in different directions. Geometrically, maximum shear stress is equivalent in magnitude to the radius, and the max shear stress (which is the point at the very top of the circle). As the value is equivalent to the radius, it can be found trivialy in cases of principal stresses, or using the Pythagorean theorem for any other reference plane. Maximum shear stress is half of deviatoric stress.

The following set of equations relate to rotating the plane of reference by θ_σ. Stress terms such as σ_x will be converted to σ'_x as shown geometrically in the Mohr's circle.

$$\tau'_{xy} = (\sigma_y - \sigma_x) \cdot \cos(\theta_\sigma) \cdot \sin(\theta_\sigma) + \tau_{xy} \cdot (\cos^2(\theta_\sigma) - \sin^2(\theta_\sigma)) \tag{3.21}$$

$$\sigma'_x = \sigma_x \cdot \cos^2(\theta_\sigma) + \sigma_y \cdot \sin^2(\theta_\sigma) + \tau_{xy} \cdot \cos(\theta_\sigma) \cdot \sin(\theta_\sigma) \tag{3.22}$$

$$\sigma'_y = \sigma_x \cdot \sin^2(\theta_\sigma) + \sigma_y \cdot \cos^2(\theta_\sigma) - \tau_{xy} \cdot \cos(\theta_\sigma) \cdot \sin(\theta_\sigma) \tag{3.23}$$

The above equations can be combined as the rotation matrix R_σ, resulting in Equation 3.24, which can be more concisely expressed as Equation 3.25. Note that in cases were θ_σ is equal to the principal angle $\theta_{p\sigma}$ the τ'_{xy} terms should work out to zero.

$$\begin{pmatrix} \sigma'_x & \tau'_{xy} \\ \tau'_{xy} & \sigma'_y \end{pmatrix} = \begin{pmatrix} \cos\theta_\sigma & \sin\theta_\sigma \\ -\sin\theta_\sigma & \cos\theta_\sigma \end{pmatrix} \begin{pmatrix} \sigma_x & \tau_{xy} \\ \tau_{xy} & \sigma_y \end{pmatrix} \begin{pmatrix} \cos\theta_\sigma & -\sin\theta_\sigma \\ \sin\theta_\sigma & \cos\theta_\sigma \end{pmatrix} \tag{3.24}$$

$$\underline{\sigma'} = R_\sigma \cdot \underline{\sigma} \cdot R_\sigma^T \tag{3.25}$$

Equivalent diagrams and equations exist for strain.

Similarly to the stress diagram shown in Figure 3.4, Figure 3.6 shows an infinitesimal block of material undergoing strains ϵ_x and ϵ_y at right angles to each other with shear strain ϵ_{xy} applied along the edges. The plane of reference can be rotated by θ_ϵ with a rotation of the principal angle $\theta_{p\epsilon}$ resulting in a plane of reference with no shear strain. Figure 3.7 shows the corresponding Mohr's circle representing this plane of reference rotation. The following equations define the principal strains:

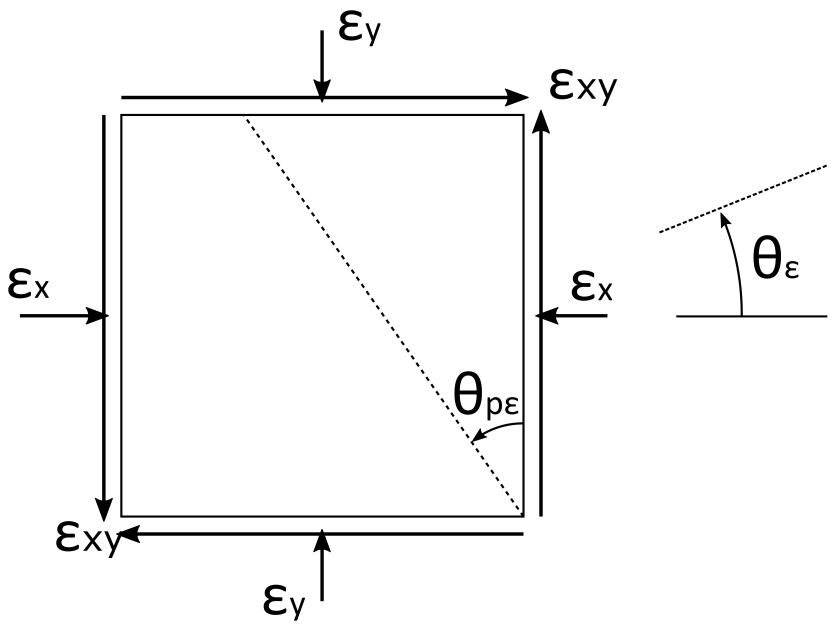

FIGURE 3.6: A block of material undergoing normal strains ϵ_x and ϵ_y and shear strain ϵ_{xy}. $\theta_{p\epsilon}$ represents the principal angle for strain, and θ_ϵ represents an arbitrary rotation of the frame of reference

$$\epsilon_1 = \frac{\epsilon_x + \epsilon_y}{2} + \sqrt{\left(\frac{\epsilon_x - \epsilon_y}{2}\right)^2 + \epsilon_{xy}^2} \tag{3.26}$$

$$\epsilon_3 = \frac{\epsilon_x + \epsilon_y}{2} - \sqrt{\left(\frac{\epsilon_x - \epsilon_y}{2}\right)^2 + \epsilon_{xy}^2} \tag{3.27}$$

Several additional terms can be described based on the Mohr's circle shown in Figure 3.7:

$$\epsilon_v = \epsilon_1 + \epsilon_3 = \epsilon_x + \epsilon_y \tag{3.28}$$

$$\epsilon_s = R_\epsilon = \frac{\epsilon_1 - \epsilon_3}{2} = \sqrt{\left(\frac{\epsilon_x - \epsilon_y}{2}\right)^2 + \epsilon_{xy}^2} \tag{3.29}$$

Equation 3.28 shows volumetric strain. This represents the change in volume for an object undergoing deformation. In cases where this is zero, ϵ_1 will equal $-\epsilon_3$, i.e. any length extension is equal and opposite to a width reduction, with no overall volume change. Any pair of perpendicular normal strains can be used to calculate this value.

Equation 3.29 shows maximum shear strain, ϵ_s. The magnitude of ϵ_s is equivalent to the radius of the circle, and geometrically is represented by the point at the very top. Maximum shear strain represents deformation that doesn't cause a volume change. As this value is

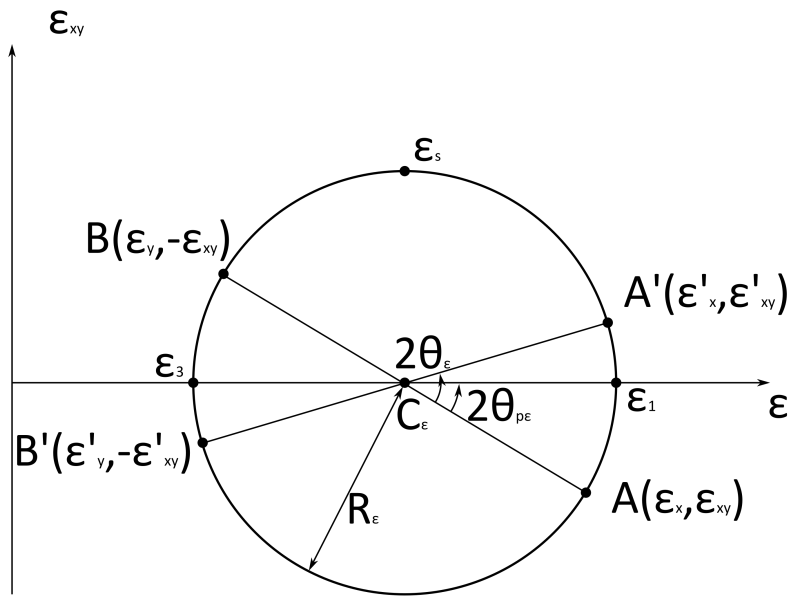

FIGURE 3.7: A strain Mohr's circle presenting the strains shown in Figure 3.6.

the radius, it is trivial to find using the principal strains, or slightly more complicated when calculating it from arbitrary strains via the Pythagorean theorem. Maximum shear strain is half of deviatoric strain.

Similar to those presented for strains, the following set of equations relate to rotating the plane of reference by θ_ϵ. Stress terms such as ϵ_x will be converted to ϵ'_x as shown geometrically in the Mohr's circle.

$$\epsilon'_{xy} = (\epsilon_y - \epsilon_x) \cdot \cos(\theta_\epsilon) \cdot \sin(\theta_\epsilon) + \epsilon_{xy} \cdot (\cos^2(\theta_\epsilon) - \sin^2(\theta_\epsilon)) \tag{3.30}$$

$$\epsilon'_x = \epsilon_x \cdot \cos^2(\theta_\epsilon) + \epsilon_y \cdot \sin^2(\theta_\epsilon) + \epsilon_{xy} \cdot \cos(\theta_\epsilon) \cdot \sin(\theta_\epsilon) \tag{3.31}$$

$$\epsilon'_y = \epsilon_x \cdot \sin^2(\theta_\epsilon) + \epsilon_y \cdot \cos^2(\theta_\epsilon) - \epsilon_{xy} \cdot \cos(\theta_\epsilon) \cdot \sin(\theta_\epsilon) \tag{3.32}$$

The above equations can be combined as the rotation matrix R_ϵ, resulting in Equation 3.33, which can be more concisely expressed as Equation 3.34. Note that in cases were θ_ϵ is equal to the principal angle $\theta_{p\epsilon}$ the ϵ'_{xy} terms should work out to zero.

$$\begin{pmatrix} \epsilon'_x & \epsilon'_{xy} \\ \epsilon'_{xy} & \epsilon'_y \end{pmatrix} = \begin{pmatrix} \cos\theta_\epsilon & \sin\theta_\epsilon \\ -\sin\theta_\epsilon & \cos\theta_\epsilon \end{pmatrix} \begin{pmatrix} \epsilon_x & \epsilon_{xy} \\ \epsilon_{xy} & \epsilon_y \end{pmatrix} \begin{pmatrix} \cos\theta_\epsilon & -\sin\theta_\epsilon \\ \sin\theta_\epsilon & \cos\theta_\epsilon \end{pmatrix} \tag{3.33}$$

$$\underline{\epsilon}' = R_\epsilon \cdot \underline{\epsilon} \cdot R_\epsilon^T \tag{3.34}$$

3.4 Discretisation and Equilibrium

The previous sections in this chapter have demonstrated how stress and strain can be used to calculate work due to deformation along with how an externally applied load with a corresponding displacement also represents work. Equation 3.16 provided an internal work equation in terms of the stress componants σ_x, σ_y, τ_{xy}, and the strain componants ϵ_x, ϵ_y, γ_{xy}. It is however much more useful to express internal work due to deformation with terms such as maximum shear stress and maximum shear strain, as these are more commonly used in constitutive models and found as the result of laboratory testing. Appendix A provides the full derivation for this conversion. The final formulation for internal work can be examined in Equation 3.35, which for simplicity is written assuming constant stress.

$$W_{\text{int}} = \left[s\epsilon_v + 2t\epsilon_s(1 - 2\sin^2(\theta_\sigma - \theta_\epsilon)) \right] \cdot V \tag{3.35}$$

This section will discuss discretisations, in terms of both space and time, to allow the work equations to be applied to real data, rather than an idealised infinitesimal block. The full equilibrium equation will be presented, and finally, simplifications and assumptions that can be made will be listed, along with justifications and situations for use.

As stated previously, external work must equal internal work. As constant stress is currently being assumed, it shall first be assumed that the equivalent terms for external work are constant (i.e. no integrals), however the more general form will shortly be provided. As such, equilibrium can be expressed as follows for cases where forces and stresses are constant:

$$W_{ext} = W_{int} + W_{gravity} + W_{friction} \tag{3.36}$$

$$F \cdot u = \left[s\epsilon_v + 2t\epsilon_s(1 - 2\sin^2(\theta_\sigma - \theta_\epsilon)) \right] \cdot V + M \cdot g \cdot u_y + N \cdot \mu \cdot u \tag{3.37}$$

Equation 3.37 contains external work in the form of a load multiplied by a corresponding displacement which is equal to internal work in terms of the "geotechnical" stress and strain parameters, allowing for varying principle angles, a term for work expended by movement against gravity and a term for work expended by movement against friction.

Discretisation in time is relatively straight forward and will most likely be determined based on available data. Force, displacement, and strain data will not be a continuum but a list of values associated with a timestep. Previous sections have shown integrals for cases where stress or force is not assumed to be uniform. These equations will be summated below. In practical applications, simple methods such as the trapezium rule will be able to be used for integration. Equation 3.38 shows the equilibrium equation for timestep j.

$$\begin{aligned}\int_{u^{j-1}}^{u^j} P\,du = \left[\int_{\epsilon_v^{j-1}}^{\epsilon_v^j} s\,d\epsilon_v + 2(1-2\sin^2(\theta_\sigma-\theta_\epsilon))\cdot\int_{\epsilon_s^{j-1}}^{\epsilon_s^j} t\,d\epsilon_s\right]\cdot V \\ + \int_{u_y^{j-1}}^{u_y^j} M\cdot g\,du_y + \int_{u^{j-1}}^{u^j} N\cdot\mu\,du\end{aligned} \tag{3.38}$$

Dicretisation in the spatial dimension essentially consists of splitting a continuous domain into a series of elements. Overall applied force will be unchanged, but each element will have its own distortion, and displacement (and hence gravity and friction) data. Simply summing the work expended in each element will give the overall work, and be equal to work done by the applied loading. Equation 3.39 shows this, for a case with E elements, in which e is the element reference and V_e refers to the volume of element e.

$$\begin{aligned}\int_{u^{j-1}}^{u^j} P\,du = \sum_{e=1}^{E}\Bigg(\left[\int_{\epsilon_v^{j-1,e}}^{\epsilon_v^{j,e}} s\,d\epsilon_v + 2(1-2\sin^2(\theta_\sigma-\theta_\epsilon))\cdot\int_{\epsilon_s^{j-1,e}}^{\epsilon_s^{j,e}} t\,d\epsilon_s\right]\cdot V_e \\ + \int_{u_y^{j-1,e}}^{u_y^{j,e}} M\cdot g\,du_y + \int_{u^{j-1,e}}^{u^{j,e}} N\cdot\mu\,du\Bigg)\end{aligned} \tag{3.39}$$

For cases with large datasets that are flawed through noise or other phenomena, there is likely no possible soil behaviour that will achieve balance between internal and external work. Many terms contained in Equation 3.39 will be different for each element and timestep. Maximum shear stress, for example, will vary depending on shear strain, so the unknown is the relation between the two values. This could be rephrased as saying that stress is some function of strain, where this function is currently unknown. Depending on how the soil is assumed to behave, the unknown relationships may be highly nonlinear and require solving via an optimiser. Even optimal parameters will likely have a gap between internal and external work, as such, the best answer is the one in which this energy gap is minimised. Equation 4.3 shows how the relationship between internal and external work for timestep j can be formulated with the addition of an energy gap term.

$$W_{ext}^j = W_{int}^j + W_{gravity}^j + W_{friction}^j + localgap^j \tag{3.40}$$

Depending on the exact soil used, or the constitutive equations assumed to model its behaviour, a number of assumptions can be made to simplify Equation 3.39. For ease of reading, each simplification will be applied in turn, however in reality any number of combination of these assumptions could be made. Firstly, the assumption of associative flow, that is the principal stress and principal strain angles being equal, allows for the $\sin^2$ term to be cancelled. The resulting equation is as follows:

$$\int_{u^{j-1}}^{u^j} P\, du = \sum_{e=1}^{E} \left(\left[\int_{\epsilon_v^{j-1,e}}^{\epsilon_v^{j,e}} s\, d\epsilon_v + 2 \cdot \int_{\epsilon_s^{j-1,e}}^{\epsilon_s^{j,e}} t\, d\epsilon_s \right] \cdot V_e + \int_{u_y^{j-1,e}}^{u_y^{j,e}} M \cdot g\, du_y + \int_{u^{j-1,e}}^{u^{j,e}} N \cdot \mu\, du \right) \tag{3.41}$$

The second assumption to be discussed is taking volumetric strain as nil. This would be valid in cases where the soil volume, and density, is constant. For linear elastic cases, this would happen when Poisson's ratio is 0.5. The equilibrium equation after this assumption can be expressed as:

$$\int_{u^{j-1}}^{u^j} P\, du = \sum_{e=1}^{E} \left(2 \cdot \int_{\epsilon_s^{j-1,e}}^{\epsilon_s^{j,e}} t\, d\epsilon_s \cdot V_e + \int_{u_y^{j-1,e}}^{u_y^{j,e}} M \cdot g\, du_y + \int_{u^{j-1,e}}^{u^{j,e}} N \cdot \mu\, du \right) \tag{3.42}$$

Next, cases in which work done by gravity is assumed to be zero. This would be valid in computer simulated datasets in which the soil is specified to be weightless. Some real test data, for example footing tests with zero volumetric strain, will have no net soil height change. In these cases an equal amount of soil will move down as will move up, giving no overall change in gravitational energy. With the term relating to gravity removed, the equation is as follows:

$$\int_{u^{j-1}}^{u^j} P\, du = \sum_{e=1}^{E} \left(2 \cdot \int_{\epsilon_s^{j-1,e}}^{\epsilon_s^{j,e}} t\, d\epsilon_s \cdot V_e + \int_{u^{j-1,e}}^{u^{j,e}} N \cdot \mu\, du \right) \tag{3.43}$$

The final term that can be removed is the frictional work term. This is unlikely to be achievable in physical tests, however the influence of the term relative to work due to distortion will vary, in some cases it may have negligible effect on the final solution. Simulated datasets will be able to trivially discount friction. Having made all the aforementioned simplifications, the final work equilibrium equation is:

$$\int_{u^{j-1}}^{u^j} P\, du = \sum_{e=1}^{E} \left(2 \cdot \int_{\epsilon_s^{j-1,e}}^{\epsilon_s^{j,e}} t\, d\epsilon_s \cdot V_e \right) \tag{3.44}$$

3.5 Practical calculation of strain data

It had been stated that the measured strain field is not a continuum but discretised into a number of elements. Although in simulated FEA datasets, it is possible to directly obtain strain data, for physical testing only displacement data will be obtained via PIV and strains must be calculated.

Although existing software exists to convert a displacement field to a strain field, the following section will demonstrate the key equations of the Constant Strain Triangle (CST) formulation. As the full derivation exists in numerous text books it will not be included in this document. What is presented is essentially an abridged version. The aptly named textbook "Finite Element Analysis" (Bhavikatti, 2005) was consulted while writing this section, although readers will be able to find many other similar resources online. This CST is an FEA element by which a three node triangular element can be used to find strains from the displacement data in each node. This technique is implemented in the Identification Method code used for this thesis.

There are benefits and drawbacks of using CSTs, significant advantages are simplicity and ease of use with PIV data. Triangulating an arbitrary arrangement of points is easy, so any PIV data can be processed this way. Disadvantages include no compatibility between neighbouring elements. This is not currently important as energy is calculated in each element separately.

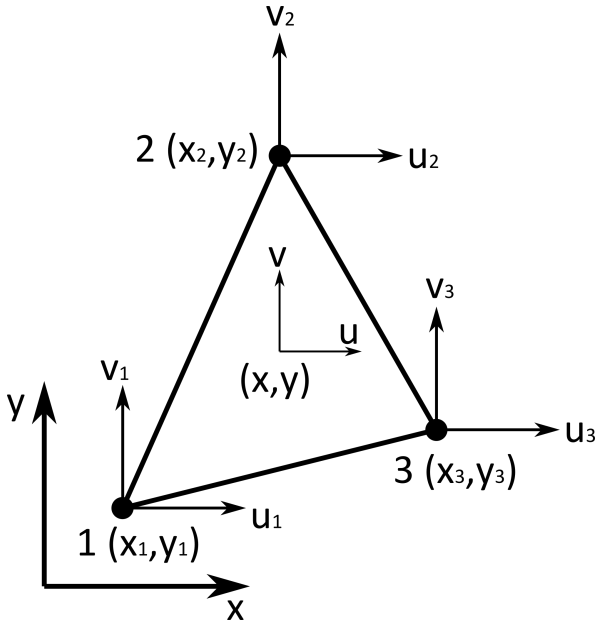

FIGURE 3.8: An arbitrary triangular element.

Figure 3.8 shows a triangular element. It contains three nodes 1, 2, and 3. Each of these points has a location (x_i, y_i) and a displacement (u_i, v_i) in the x and y directions respectively. Shown in the middle of the triangle is an arbitrary point with coordinates (x, y) and displacements (u, v).

If displacement points are available on a regular grid, it is trivial to arrange points into a series of triangular elements from which strain can be calculated. It is likely that the grid of displacement points would be irregular, either due to photogrammetric corrections or removal of anomalous points. Delaunay triangulation (Delaunay et al., 1934) can be used to generate a set of triangular elements from an arbitrary grid of points. There is a built in Matlab function that can perform the triangulation procedure.

The equation describing the displacement of an arbitrary point is shown as follows, as per Bhavikatti (2005):

$$\begin{pmatrix} u(x,y) \\ v(x,y) \end{pmatrix} = \begin{pmatrix} N_1 & N_2 & N_3 & 0 & 0 & 0 \\ 0 & 0 & 0 & N_1 & N_2 & N_3 \end{pmatrix} \begin{pmatrix} u_1 \\ u_2 \\ u_3 \\ v_1 \\ v_2 \\ v_3 \end{pmatrix} \tag{3.45}$$

The terms N_1, N_2, and N_3 are shape functions, and are described in Equations 3.46, 3.46, and 3.46.

$$N_1 = \frac{a_1 + b_1 x + c_1 y}{2A} \tag{3.46}$$

$$N_2 = \frac{a_2 + b_2 x + c_2 y}{2A} \tag{3.47}$$

$$N_3 = \frac{a_3 + b_3 x + c_3 y}{2A} \tag{3.48}$$

The value of each shape function can be found by substituting in the x and y terms. One property of note is that each shape function must equal one at its corresponding node, i.e. $N_1 = 1$ at node 1, and equal zero at the other nodes. A number of terms have been introduced, a_1 to c_3, are defined in Equation 3.49. The interested reader will be able to consult any finite element analysis textbook for the derivation of these terms.

$$\begin{array}{lll} a_1 = x_2y_3 - x_3y_2 & a_2 = x_3y_1 - x_1y_3 & a_3 = x_1y_2 - x_2y_1 \\ b_1 = y_2 - y_3 & b_2 = y_3 - y_1 & b_3 = y_1 - y_2 \\ c_1 = x_3 - x_2 & c_2 = x_1 - x_3 & c_3 = x_2 - x_1 \end{array} \tag{3.49}$$

The final term from the shape function equations to define is area. This could be calculated in numerous ways, however the most convenient is via the determinate of the coordinates. This is a common mathematical method and as such the derivation is not included in this document. The equation for area is as follows:

$$A = \frac{1}{2} det \begin{pmatrix} 1 & 1 & 1 \\ x_1 & x_2 & x_3 \\ y_1 & y_2 & y_3 \end{pmatrix} \tag{3.50}$$

It is now possible to calculate displacement at any point within the triangle. One point of particular interest may be the centroid. This can either be obtained by averaging the displacements of the nodes, or alternatively by taking each shape factor as one third.

The next stage is the process is the calculation of strains. The general definition of strains within an element is given in Equation 3.51.

$$\epsilon = \begin{pmatrix} \epsilon_x \\ \epsilon_y \\ \gamma_{xy} \end{pmatrix} = \begin{pmatrix} \frac{\delta u}{\delta x} \\ \frac{\delta v}{\delta y} \\ \frac{\delta u}{\delta y} + \frac{\delta v}{\delta x} \end{pmatrix} \tag{3.51}$$

Equation 3.52 together with the generalised displacement Equation 3.45 allow for strain to be described with the following equation:

$$\epsilon = \begin{pmatrix} \epsilon_x \\ \epsilon_y \\ \gamma_{xy} \end{pmatrix} = \begin{bmatrix} \frac{\delta N_1}{\delta x} & \frac{\delta N_2}{\delta x} & \frac{\delta N_3}{\delta x} & 0 & 0 & 0 \\ 0 & 0 & 0 & \frac{\delta N_1}{\delta y} & \frac{\delta N_2}{\delta y} & \frac{\delta N_3}{\delta y} \\ \frac{\delta N_1}{\delta y} & \frac{\delta N_2}{\delta y} & \frac{\delta N_3}{\delta y} & \frac{\delta N_1}{\delta x} & \frac{\delta N_2}{\delta x} & \frac{\delta N_3}{\delta x} \end{bmatrix} \begin{pmatrix} u_1 \\ u_2 \\ u_3 \\ v_1 \\ v_2 \\ v_3 \end{pmatrix} \tag{3.52}$$

The Equations for the shape functions, 3.46, 3.47, and 3.48 are very easy to differentiate in terms of x or y, allowing Equation 3.52 to be reformulated as shown in Equation 3.53

$$\epsilon = \begin{pmatrix} \epsilon_x \\ \epsilon_y \\ \gamma_{xy} \end{pmatrix} = \frac{1}{2A} \begin{bmatrix} b_1 & b_2 & b_3 & 0 & 0 & 0 \\ 0 & 0 & 0 & c_1 & c_2 & c_3 \\ c_1 & c_2 & c_3 & b_1 & b_2 & b_3 \end{bmatrix} \begin{pmatrix} u_1 \\ u_2 \\ u_3 \\ v_1 \\ v_2 \\ v_3 \end{pmatrix} \tag{3.53}$$

Or in a more concise form, where $[\underline{B}]$ is the strain displacement matrix, and (δ) is the vector of displacements:

$$\epsilon = [\underline{B}](\delta) \tag{3.54}$$

In which:

$$[\underline{B}] = \frac{1}{2A} \begin{bmatrix} b_1 & b_2 & b_3 & 0 & 0 & 0 \\ 0 & 0 & 0 & c_1 & c_2 & c_3 \\ c_1 & c_2 & c_3 & b_1 & b_2 & b_3 \end{bmatrix} \tag{3.55}$$

With the given equations, it is now possible to calculate both a central displacement value for a triangular equation, as well as all components of strain. These components can be used along with the methodologies presented earlier in this chapter to generate the necessary formulations for internal energy within an element.

3.6 A note on anisotropic soils

Isotropy is the property of being the same in all directions. In the context of geotechnics, this means the soil will behave the same way no matter what direction it is loaded from. The equilibrium equation (before the assumption of associative flow is made), contains terms for the principal angles of stress and strain. Within Equation 3.37 for instance, differences in these angles are taken into account when calculating internal work done. Even in such a case, there is no term to determine isotropy.

What does determine isotropy is the stress-strain response. Isotropic soils will have a single response regardless of the principal angles. An anisotropic soil will have a different response depending on the principal angle. Stress will not simply be a function of strain, but instead a function of strain and one or both of the principal angles.

For simplicity, the work presented in this thesis (most notably in Chapter 4 in which the programmatic implementation is derived) will assume soil is isotropic. Anisotropic behaviour could be included in the future by implementing a constitutive relationship able to deal with it.

3.7 Conclusion

This chapter has demonstrated the derivation of the energy equilibrium equation that forms the basis of the methodology presented in this thesis. Simplifications and assumptions to this equation have been discussed, along with how it might be discretised for use with real data. The final equation, Equation 3.44, shows the energy equilibrium in its most simplified form.

The aforementioned equation, although the heart of the methodology in this thesis, is on its own insufficient to recover the soil stress-strain behaviour. It cannot simply be solved, some commentary has been provided on the concept of "Energy Gap", the idea that the physical realities of data prevent true equilibrium between internal and external work, let alone a simple solution via a matrix inversion or other trivial method. The following chapter will demonstrate programmatic methods by which Equation 3.44 can be used, and how the "Energy Gap" can be satisfactorily dealt with, along with all relevant data processing and optimisation procedures.

Chapter 4

Programmatic Implementation of the Identification Method

4.1 Introduction

This chapter will focus on the derivation for two different Identification Method formulations along with discussion as to how they can be implemented programmatically.

Whereas the previous chapter derived the mathematical equilibrium equation, it was pointed out that with realistic datasets it is unlikely that internal work and external work will exactly match. The concept of an energy gap was introduced, with the stated goal that the "best" soil properties are to be found, with "best" being defined as the properties that will cause this energy gap to be as small as possible. As discussed in the preceding chapter, stress is assumed to be an unknown function of strain, and as such the parameters to be found are those that describe this function.

Therefore, to begin the chapter, a brief overview of optimisation will be given. A full derivation of the techniques used for this project would be long and unnecessary as such methods have existed for decades and are used in this project via a pre-existing commercial software package. The content presented is instead a short guide to optimisation designed such that readers without experience in this area will understand the key concepts sufficiently to aid in understanding later sections and chapters.

Next, the chapter will introduce what is being termed the "Equation based" Identification Method, in which the soil stress-strain response is presupposed to follow the shape of an equation defined by a small number of parameters. For example, if the stress-strain response was assumed to follow the form of a quadratic equation $t = a \cdot \epsilon_s^2 + b \cdot \epsilon_s + c$, the variables a, b, and c, could be optimized such that the energy gap is as small as possible.

Although the quadratic equation serves as an easy example that many readers will be familiar with, it however would be an exceedingly poor approximation of soil behaviour. Other equations taken from literature will be significantly more relevant, and would typically be termed constitutive equations. Some will be trivially simple such as elasticity, or elastic-perfectly-plastic behaviour, but others may be significantly more complex.

This chapter will therefor present a generalised framework in which the parameters of arbitrary constitutive equations can be optimised for. The implementation of a small number of these constitutive equations will be presented, along with considerations and difficulties of their application, along with a generalised discussion that would be of use should reader attempt to implement their own choice of equations.

The second of the two proposed formulations will then be introduced. The "Segment based" Identification Method uses a different approach. The unknown stress-strain curve will be split into an arbitrary number of segments, the stiffness of each as variables to be found. This is the methodology that was initially developed by Gueguin et al. (2015), however the means by which internal work is summated in terms of the arbitrary segments was completely reformulated for this project.

A number of additional ways of constraining the curve will be discussed, along with how they are implemented. It will be shown how this second approach allows for significantly more freedom in the shape of the curve and will discuss whether that is a benefit or a drawback.

For ease of reading, detailed diagrams and flowcharts of each methodology will be provided.

Finally, differences and similarities between the two methods will be discussed. Commentary will be given on how such differences might effect the outcome of the usage of each method.

4.2 Background

In previous chapters the concept of energy equilibrium has been introduced. The key takeaway is that work done to a soil sample by loading is equal to the work expended within the sample by deformation. Other optional terms relating to gravity of friction can be added as appropriate. This can be summarised with Equation 4.1.

$$W_{ext} = W_{int} + W_{gravity} + W_{friction} \tag{4.1}$$

For simplicity, a number of assumptions will be made for the time being, firstly that strain will be purely deviatoric with no volumetric strain, secondly, that flow is associative during plastic deformation, and finally that friction and gravity are negligible. As such, the energy equilibrium equation can be stated as follows where P represents force, u^j represents displacement u for timestep j, the domain is split into E elements, each referenced with e, where t and ϵ_s are maximum shear stress and maximum shear strain respectively, and finally V_e is the volume of element e.

$$\int_{u^{j-1}}^{u^j} P\, du = \sum_{e=1}^{E} \left(2 \cdot \int_{\epsilon_s^{j-1,e}}^{\epsilon_s^{j,e}} t\, d\epsilon_s \cdot V_e \right) \tag{4.2}$$

For non trivial datasets, it is unlikely that internal and external energy will exactly match due to measurement errors etc. as such the concept of an energy gap was introduced, the difference between internal and external work for each timestep j, out of a total J, as shown in Equation 4.3, with a goal of minimising the sum of these energy gaps, as shown in Equation 4.4.

$$W_{ext}^j = W_{int}^j + localgap^j \tag{4.3}$$

$$Minimise \sqrt{\left(\sum_{j=1}^{J} (localgap^j)^2 \right)} \tag{4.4}$$

Maximum shear strain ϵ_s is measurable via PIV, so in order to calculate internal work, maximum shear stress t must be found. The means through which t will be found is by the reconstruction of a stress-strain curve. This chapter will detail two methodologies by which this unknown stress-strain curve can be found.

4.3 A brief primer on optimisation

Optimisation is the process by which the best possible solution to a problem can be selected. Optimisation is used in many fields including finance, logistics, and engineering. Examples of problems in which optimisation can be used include finding the shortest route a delivery driver could take to visit multiple locations, finding the truss structure requiring the lowest amount of material to support a given load, or to find the allocation of shares in an investment portfolio providing the highest return for a specified risk level.

Many categories of optimisation exist with multiple algorithms and many software packages, both commercial and open source, have been developed to facilitate solving them.

Linear optimisation is perhaps the simplest algorithm conceptually. An objective function which is dependent on a set of variables is to be minimised or maximised by choosing values for the variables. The possible values for these variables are restricted by a set of constraints. Both the constraints and objective function are linear, i.e. none of the variables have an exponent. The above paragraph can be condensed into the standard mathematical notation for a linear optimisation problem, as shown in Equation 4.5. Although this generalised form exists in multiple sources, the MOSEK optimiser documentation was consulted (MOSEK, 2020).

$$\begin{array}{cc} \text{Minimise} & \mathbf{c}^T\mathbf{x} + c^f \\ \text{Subject to} & \mathbf{l}^c \leq \mathbf{A}\mathbf{x} \leq \mathbf{u}^c \\ \text{And} & \mathbf{l}^x \leq \mathbf{x} \leq \mathbf{u}^x \end{array} \tag{4.5}$$

Vector $\mathbf{c}$ is the known coefficients relating to the objective function with c^f representing an arbitrary fixed constant, $\mathbf{A}$ is the matrix of known constraints, and $\mathbf{x}$ is the vector of unknown variables, which are to be found. Vectors $\mathbf{l}^c$ and $\mathbf{u}^c$ represent the lower and upper bounds for the constraints with vectors $\mathbf{l}^x$ and $\mathbf{u}^x$ representing the equivalent values for the variables.

A simple example will now be presented in Equation 4.6.

$$\begin{array}{cc} \text{Minimise} & \begin{pmatrix} 2 & 1 \end{pmatrix} \begin{pmatrix} x \\ y \end{pmatrix} \\ \text{Subject to} & \begin{pmatrix} -1 & -1 \\ -2 & 1 \\ 0.8 & 1 \\ 0.75 & -1 \end{pmatrix} \begin{pmatrix} x \\ y \end{pmatrix} \leq \begin{pmatrix} -3 \\ 2 \\ 10 \\ 4.5 \end{pmatrix} \\ \text{And} & \begin{pmatrix} x \\ y \end{pmatrix} \geq \begin{pmatrix} 0 \\ 0 \end{pmatrix} \end{array} \tag{4.6}$$

The objective function $2x + y$ must be minimised. Values of x and y should be chosen that do not violate the constraints whilst providing the lowest value objective function. There are several algorithms that would be suitable for solving this problem, however due to there only being two variables, this problem can be solved graphically. Figure 4.1 shows the above problem.

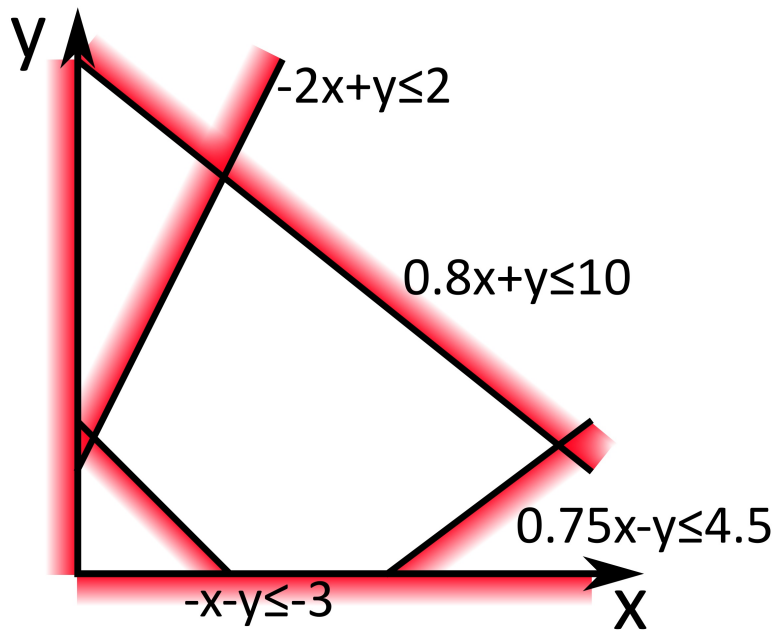

FIGURE 4.1: A graphical representation of an example optimisation problem.

The constraints are plotted with a red gradient indicating the forbidden side. The permitted values of x and y are therefor contained within the central polygon. Examining the vertices allows for x and y values of $\frac{1}{3}$ and $2\frac{2}{3}$ respectively, giving the objective function a value of $3\frac{1}{3}$. The interested reader will be able to test that these values meet all the constraints.

The given example was particularly simple, allowing for a representation in two dimensions. It would perhaps be possible to use the graphical method in three dimensions, but a problem with ten thousand variables for instance would require a much more robust methodology.

The Simplex algorithm is perhaps the most well known, however it is inefficient when compared with more recent developments. The interior point algorithm was used for the work carried out for this thesis. Although theoretically possible for several decades prior, the first practical interior point algorithm was presented by Karmarkar (1984). Extensive work has been carried out on the interior point algorithm but a full review would be far beyond the scope of this thesis, as would a derivation of the algorithm. All that is required is the knowledge that such algorithms exist and are able to solve large and complex problems in relatively short time frames.

The interior point algorithm provides one additional piece of functionality of note: the ability to solve nonlinear problems. The simple example given has only linear constraints, however there are problems in which the constraints could be curves, or in higher dimensions,

cones. Conic optimisation will be used for the Identification Methods presented in this thesis. Solving a conic optimisation by hand in the manner that the linear optimisation was presented would not be possible. The standard conic optimisation form, however, will be given in Equation 4.7. As before, the MOSEK optimiser documentation was consulted when reproducing this standard form (MOSEK, 2020).

$$\begin{aligned} \text{Minimise} \quad & \mathbf{c}^T\mathbf{x} + c^f \\ \text{Subject to} \quad & \mathbf{l}^c \leq \mathbf{A}\mathbf{x} \leq \mathbf{u}^c \\ & \mathbf{l}^x \leq \mathbf{x} \leq \mathbf{u}^x \\ & \mathbf{x} \in \mathcal{K} \end{aligned} \tag{4.7}$$

Many of the terms in the above equation are defined identically as in the general form of the linear optimisation formulation, with the addition of $\mathcal{K}$ which represents a compound conic constraint. The final term in the general form uses a compound conic constraint to represent any number of individually defined conic constraints with one term. If a subset of variables $\mathbf{x}^t$ are constrained to be within the convex cone $\mathcal{K}^t$, and all variables $\mathbf{x}$ are contained in the set of real numbers $\mathbb{R}^n$, which is also a convex cone, it can be said that all variables are contained within at least one convex cone. Smaller conic constraints can simply be multiplied together allowing for a single complex conic constraint term to be used.

There are multiple types of cones that could be used as constraints in optimisation problems. The type that is most applicable to this project is the quadratic cone. The general form for a quadratic cone is given in Equation 4.8, as per MOSEK (2020).

$$\mathcal{Q}^n = \left\{ \mathbf{x} \in \mathbb{R}^n : x_0 \geq \sqrt{\sum_{j=1}^{n-1} x_j^2} \right\} \tag{4.8}$$

Quadratic cones are essentially a constraint saying that one variable x_0 must be greater than or equal to the square root of the sum of squared values for a set of $n-1$ additional variables. An example use for this would be minimising the root mean square for a set of values for curve fitting or similar usage. By including x_0 in a minimisation objective function, the RMS of other variables within the cone will be minimised.

Implementing an optimisation algorithm would be very time consuming and difficult. As such the commercial MOSEK package was used. This software features many algorithms including interior point and has programming interfaces for a range of languages including Matlab and C++. At the time of writing this thesis licenses were available for free for academic or educational usage (MOSEK, 2020).

4.3.1 The existence of an optimal stress-strain response

Thought was given to what it means for there to be an optimal stress-strain curve. Although the optimal curve is the curve resulting in the lowest energy gap between internal and external work, what can be deduced about the nature of this curve? Is there one single curve that is obviously optimal, or are there a range of suitable curves that by eye could be quite different?

Assume there exists a single pair of images; displacement is measured between them giving a single set of strain data. Each element within the pair will have different strains corresponding to different parts of the stress-strain curve. There will also be a single value of external work. For such a simple case the reader may assume it is simple to find the correct stress-strain response. In actual fact the curve can be any arbitrary shape.

For any arbitrary curve, in which the internal work is different to the external work for a single pair of images, the curve can simply be scaled up or down in the y axis until the work matches, the shape of the curve is irrelevant. Figure 4.2 demonstrates this. If, for example, the calculated internal work was 10% lower than the external work, the curve can simply be scaled by 10%.

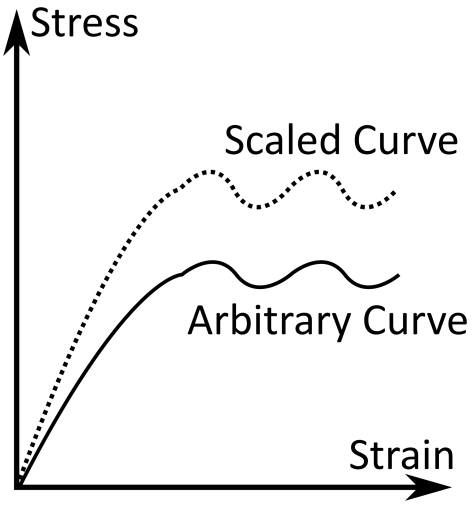

FIGURE 4.2: The relationship between an arbitrary and scaled curve.

For a case in which there are two pairs of images, with two sets of strain data and corresponding external work, it is possible to scale the arbitrary curve to be perfect for each pair separately, but not such that it is a perfect match for both at once. There exists a compromise scale factor such that the energy gap for each image pair is minimised when internal work is calculated using this compromise curve. Figure 4.3 shows a graphical representation of this concept.

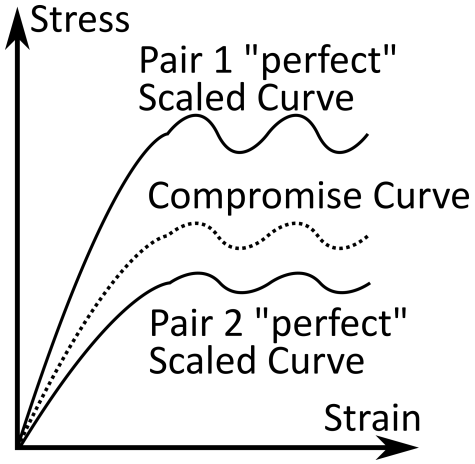

FIGURE 4.3: The relationship between scaled curves and a compromise curve.

The above process can be carried out for any number of arbitrary curves. Each curve can be scaled separately to match energy for an individual pair, but a compromise must be made to give the best match for two or more pairs. Trying many such curves and finding their compromise location will give a range of energy gaps, some will be lower than others. Figure 4.4 shows an additional set of curves to illustrate this point.

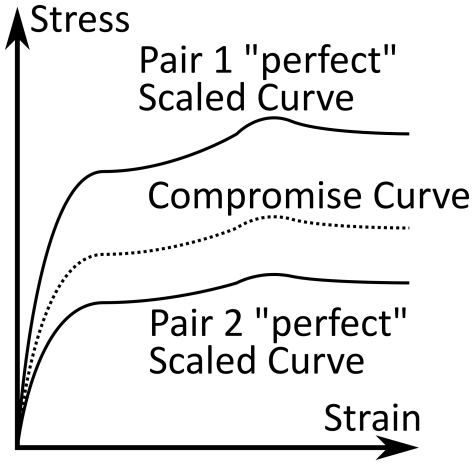

FIGURE 4.4: An additional set of arbitrarily chosen curves.

This thought experiment raises a number of points regarding optimisation of stress-strain response. A lack of data will make it harder if not impossible to find a global minimum energy gap. As demonstrated, a single pair of images can have its internal work and external work matched with any arbitrary shape curve. It is also possible that synthetic datasets could be chosen to achieve this effect with many image pairs.

Actual datasets are unlikely to have this issue, as data will be from tens or hundreds of images with significant overlap with regards to observed strains. In the event a dataset

does allow for arbitrary curves, this could be found by examining the energy gap. If it is zero, or alternatively within the margin of error for the optimiser, there is a chance there is insignificant data to properly constrain the curve.

4.4 Principals of the Equation Based Identification Method

As stated, a means by which maximum shear stress can be calculated is necessary to find internal work. The so called Equation Method, assumes that maximum shear stress is a function of maximum shear strain, as shown in Equation 4.9. An additional assumption that stress and strain start at zero across the entire field is also made. There are scenarios such as soil that has been preloaded or disturbed in which this assumption would not be valid, but for simplicity a zero start shall be assumed and validation testing discussed in later chapters will be designed with the aim to make this assumption valid.

$$t = f(\epsilon_s) \tag{4.9}$$

The exact equation is unimportant provided that the relationship can be described with a small number of variables that can be optimised for. Later in the chapter a set of suitable equations will be presented and discussed, but for now three particularly simple cases will be used for demonstrative purposes.

The first equation to be examined is the trivially easy case of a fixed value of t. In this case, the stress-strain curve is a horizontal line, and work is the area under it. Such a model could be referred to as perfectly plastic. The only unknown in this model would be the value t_{max}. Figure 4.5 shows an example of such a stress-strain curve.

Regardless of ϵ_s value, t is always constant. The constant t value has been defined as t_{max}. The diagram shows four data points, labelled j_0 to j_3, representing measured strain values for a single element. Where data is derived by PIV, each data point would represent a single element within a single image. $\delta\epsilon_{s1}$ etc. represent the change in maximum shear strain between data points. As stated, the diagram is representative of a single element and total internal work would require the area under a similar curve for every element.

It is trivial to see that the area under the curve for each image pair is simply the difference in maximum shear strain values multiplied by t_{max}. Internal work for each element can then be calculated by multiplying this value by $2 \cdot V_e$. To express this sentiment mathematically, solving the integral in Equation 4.2 results in the following equation:

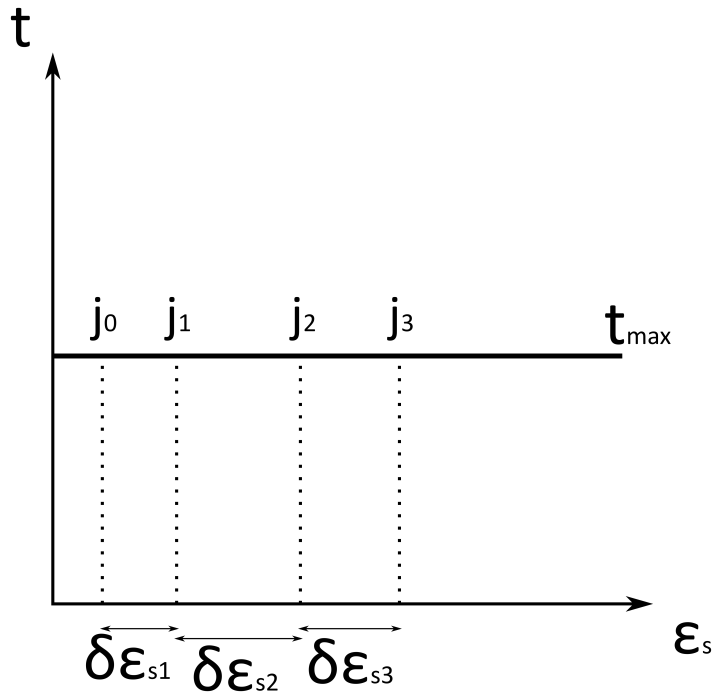

FIGURE 4.5: A stress-strain curve in which the soil response is modelled as perfectly plastic and represented by a horizontal line. j represents strain data points.

$$\int_{u^{j-1}}^{u^{j}} P\, du = \sum_{e=1}^{E} \left(2 \cdot V_e \cdot t_{max} \cdot [\epsilon_s^{j,e} - \epsilon_s^{j-1,e}] \right) \tag{4.10}$$

Assuming a soil sample undergoing testing is recorded using PIV, nearly every term within Equation 4.10 is known. Force P and load displacement u can be recorded using a load cell and LVDT respectively, the strain data ϵ_s is known via PIV, and element volume V_e is specified based on PIV mesh size. The only unknown value is t_{max}, which is assumed to be constant regardless of timestep. Splitting the equilibrium equation into matrices is a useful next step. For illustrative purposes, four images resulting in three timesteps will be assumed with the first image $j = 0$ having no strain, force, or displacement. Equation 4.3 can be formulated as follows:

$$\begin{pmatrix} W_{ext}^1 \\ W_{ext}^2 \\ W_{ext}^3 \end{pmatrix} = \begin{pmatrix} W_{int}^1 \\ W_{int}^2 \\ W_{int}^3 \end{pmatrix} + \begin{pmatrix} localgap^1 \\ localgap^2 \\ localgap^3 \end{pmatrix} \tag{4.11}$$

Substituting in the relevant terms results in Equation 4.12.

$$\begin{pmatrix} \int_{u^0}^{u^1} P\,du \\ \int_{u^1}^{u^2} P\,du \\ \int_{u^2}^{u^3} P\,du \end{pmatrix} = \begin{pmatrix} \sum_{e=1}^{E}[(\epsilon_s^{1,e} - \epsilon_s^{0,e}) \cdot 2 \cdot V_e] \\ \sum_{e=1}^{E}[(\epsilon_s^{2,e} - \epsilon_s^{1,e}) \cdot 2 \cdot V_e] \\ \sum_{e=1}^{E}[(\epsilon_s^{3,e} - \epsilon_s^{2,e}) \cdot 2 \cdot V_e] \end{pmatrix} \cdot \begin{pmatrix} t_{max} \end{pmatrix} + \begin{pmatrix} localgap^1 \\ localgap^2 \\ localgap^3 \end{pmatrix} \tag{4.12}$$

With the above equation, it is clear to see how changing the value of t_{max} will vary the value of the local energy gaps, and in turn the global energy gap. It follows that there is a value of t_{max} in which the global energy gap is minimised. This can be found through linear optimisation or, for a trivial case such as this, a brute force approach.

The perfectly-plastic response is as simple as can be. A single variable is all that is required to describe the soil response. A linear elastic case, if not any more realistic, is slighlty more complex with two variables. The equation for a straight line is $y = mx + c$ with the variable m representing the slope and the variable c representing the intercept in the y axis.

In terms of the stress-strain curve used in geotechnical problems, the slope can be labelled G for shear modulus, and y intercept c will be labelled t_i. Typically the intercept would be zero, however in cases in which there has been an unknown amount of loading prior to beginning measurements for instance, the more genreal case may be appropriate and will be used in the following derivation. The elastic equation for maximum shear stress is shown in Equation 4.13.

$$t = G \cdot \epsilon_s + t_i \tag{4.13}$$

A diagram showing such an elastic curve is shown in Figure 4.6. As for the perfectly plastic example, the diagram shows four data points, labelled j_0 to j_3, representing measured strain values for a single element.

As before, to find the internal work done by an element, the area under the curve must be found and multiplied by two and the volume of the element. 4.14 shows how the internal work for a series of elements can be found in this way and summed to equal external work.

$$\int_{u^{j-1}}^{u^j} P\,du = \sum_{e=1}^{E}\left(2 \cdot V_e \cdot \left(\frac{1}{2} \cdot G \cdot [(\epsilon_s^{j,e})^2 - (\epsilon_s^{j-1,e})^2] + t_i \cdot [(\epsilon_s^{j,e}) - (\epsilon_s^{j-1,e})]\right)\right) \tag{4.14}$$

Again, in order to facilitate use with optimisation software, separating the known values from the unknown parameters is necessary. The unknown parameters G and t_i will be moved into a separate vector as shown in Equation 4.15. The example given has 3 timesteps.

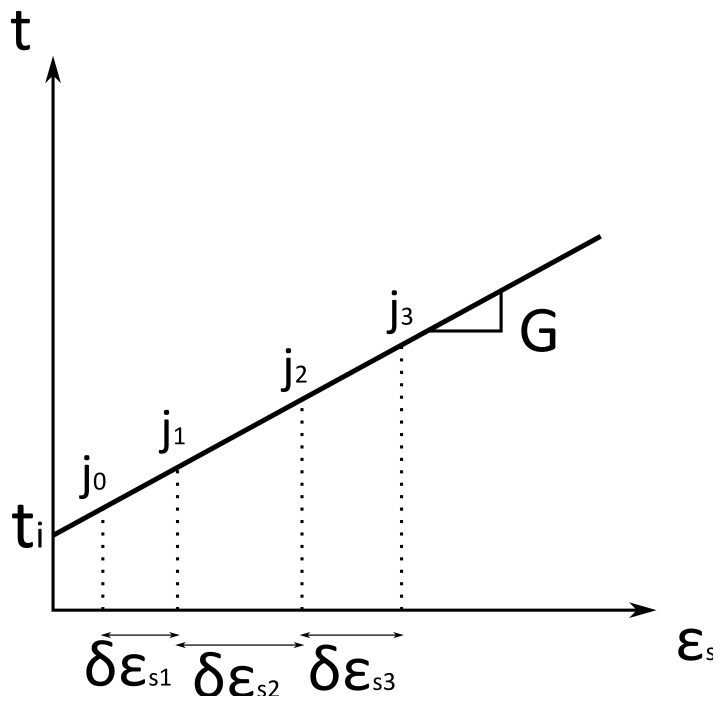

FIGURE 4.6: A stress-strain curve in which the soil response is modelled as elastic and represented by a straight angled line. j represents strain data points.

$$\begin{pmatrix} \int_{u^0}^{u^1} P\,du \\ \int_{u^1}^{u^2} P\,du \\ \int_{u^2}^{u^3} P\,du \end{pmatrix} = \begin{pmatrix} \sum_{e=1}^{E}(\frac{1}{2}\cdot[(\epsilon_s^{1,e})^2-(\epsilon_s^{0,e})^2]\cdot 2\cdot V_e) & \sum_{e=1}^{E}([(\epsilon_s^{1,e})-(\epsilon_s^{0,e})]\cdot 2\cdot V_e) \\ \sum_{e=1}^{E}(\frac{1}{2}\cdot[(\epsilon_s^{2,e})^2-(\epsilon_s^{1,e})^2]\cdot 2\cdot V_e) & \sum_{e=1}^{E}([(\epsilon_s^{2,e})-(\epsilon_s^{1,e})]\cdot 2\cdot V_e) \\ \sum_{e=1}^{E}(\frac{1}{2}\cdot[(\epsilon_s^{3,e})^2-(\epsilon_s^{2,e})^2]\cdot 2\cdot V_e) & \sum_{e=1}^{E}([(\epsilon_s^{3,e})-(\epsilon_s^{2,e})]\cdot 2\cdot V_e) \end{pmatrix} \cdot \begin{pmatrix} G \\ t_i \end{pmatrix} + \begin{pmatrix} localgap^1 \\ localgap^2 \\ localgap^3 \end{pmatrix} \tag{4.15}$$

Finally, a more complex response will be described in the following paragraphs. Although an extremely poor representation of soil behaviour (or any other mechanical behavior for that matter), the quadratic equation $t = a \cdot \epsilon_s^2 + b \cdot \epsilon_s + c$ will be used. This equation has multiple variables and requires the strain data to be used multiple times. Figure 4.7 shows a diagram of a quadratic curve.

For this slightly more complex case, the area under the curve can be found by integration.

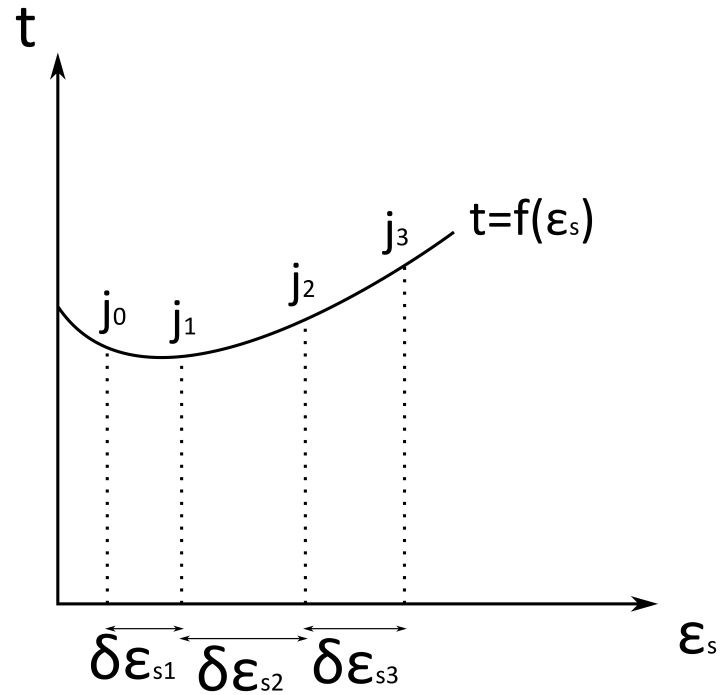

FIGURE 4.7: A stress-strain curve in which the soil response is modelled as a polynomial equation. j represents strain data points.

Equations 4.16 and 4.17 demonstrates this process. The difference between the two aforementioned equations is that Equation 4.17 has been factorised such that the parameters a, b, and c have been separated from the other terms, such that they could be moved into a vector.

$$\int_{\epsilon_s^{j-1}}^{\epsilon_s^j} t \ d\epsilon_s = \int_{\epsilon_s^{j-1}}^{\epsilon_s^j} a \cdot (\epsilon_s)^2 + b \cdot \epsilon_s + c \ d\epsilon_s = \frac{a}{3} \cdot (\epsilon_s^j)^3 + \frac{b}{2} \cdot (\epsilon_s^j)^2 + c \cdot (\epsilon_s^j) + d - \frac{a}{3} \cdot (\epsilon_s^{j-1})^3 - \frac{b}{2} \cdot (\epsilon_s^{j-1})^2 - c \cdot (\epsilon_s^{j-1}) - d \tag{4.16}$$

$$\int_{\epsilon_s^{j-1}}^{\epsilon_s^j} t \ d\epsilon_s = \int_{\epsilon_s^{j-1}}^{\epsilon_s^j} a \cdot (\epsilon_s)^2 + b \cdot \epsilon_s + c \ d\epsilon_s = \frac{a}{3} \cdot [(\epsilon_s^j)^3 - (\epsilon_s^{j-1})^3] + \frac{b}{2} \cdot [(\epsilon_s^j)^2 - (\epsilon_s^{j-1})^2] + c \cdot [(\epsilon_s^j) - (\epsilon_s^{j-1})] \tag{4.17}$$

With the integral solved, the area under the curve can be substituted into the work equilibrium Equation 4.2 to produce the following:

$$\int_{u^{j-1}}^{u^j} P\,du = \sum_{e=1}^{E}\left(2\cdot V_e\cdot\left(\frac{a}{3}\cdot[(\epsilon_s^{j,e})^3-(\epsilon_s^{j-1,e})^3]+\right.\right.$$
$$\left.\left.\frac{b}{2}\cdot[(\epsilon_s^{j,e})^2-(\epsilon_s^{j-1,e})^2]+c\cdot[(\epsilon_s^{j,e})-(\epsilon_s^{j-1,e})]\right)\right) \tag{4.18}$$

As with the perfectly plastic case, every term except for a,b, and c are known. Using a simple case in which three timesteps are specified, the problem can be formulated as a matrix of known values multiplied by a vector of unknowns as shown below in Equation 4.19. It should be noted that this equation would be prohibitively large to fit on a page and as such temporary labels have been defined. The definitions for these labels can be seen in Equation 4.20.

$$\begin{pmatrix}\int_{u^0}^{u^1} P\,du\\ \int_{u^1}^{u^2} P\,du\\ \int_{u^2}^{u^3} P\,du\end{pmatrix}=\begin{pmatrix}l_{1,3} & l_{1,2} & l_{1,1}\\ l_{2,3} & l_{2,2} & l_{2,1}\\ l_{3,3} & l_{3,2} & l_{3,1}\end{pmatrix}\cdot\begin{pmatrix}a\\ b\\ c\end{pmatrix}+\begin{pmatrix}localgap^1\\ localgap^2\\ localgap^3\end{pmatrix} \tag{4.19}$$

$$\begin{pmatrix}l_{1,3}\\ l_{1,2}\\ l_{1,1}\\ l_{2,3}\\ l_{2,2}\\ l_{2,1}\\ l_{3,3}\\ l_{3,2}\\ l_{3,1}\end{pmatrix}=\begin{pmatrix}\sum_{e=1}^{E}(\frac{1}{3}\cdot[(\epsilon_s^{1,e})^3-(\epsilon_s^{0,e})^3]\cdot 2\cdot V_e)\\ \sum_{e=1}^{E}(\frac{1}{2}\cdot[(\epsilon_s^{1,e})^2-(\epsilon_s^{0,e})^2]\cdot 2\cdot V_e)\\ \sum_{e=1}^{E}([(\epsilon_s^{1,e})-(\epsilon_s^{0,e})]\cdot 2\cdot V_e)\\ \sum_{e=1}^{E}(\frac{1}{3}\cdot[(\epsilon_s^{2,e})^3-(\epsilon_s^{1,e})^3]\cdot 2\cdot V_e)\\ \sum_{e=1}^{E}(\frac{1}{2}\cdot[(\epsilon_s^{2,e})^2-(\epsilon_s^{1,e})^2]\cdot 2\cdot V_e)\\ \sum_{e=1}^{E}([(\epsilon_s^{2,e})-(\epsilon_s^{1,e})]\cdot 2\cdot V_e)\\ \sum_{e=1}^{E}(\frac{1}{3}\cdot[(\epsilon_s^{3,e})^3-(\epsilon_s^{2,e})^3]\cdot 2\cdot V_e)\\ \sum_{e=1}^{E}(\frac{1}{2}\cdot[(\epsilon_s^{3,e})^2-(\epsilon_s^{2,e})^2]\cdot 2\cdot V_e)\\ \sum_{e=1}^{E}([(\epsilon_s^{3,e})-(\epsilon_s^{2,e})]\cdot 2\cdot V_e)\end{pmatrix} \tag{4.20}$$

Again, the equation has been formulated such that it is clear how a small number of variables effect the energy gap. Three variables will be possible to solve using a brute force search depending on how fine the search and size of the search area, but it is likely to be much easier to use optimisation.

Through these two simple examples the principles of the Equation based Identification Method have been shown. To summarise, an equation representing t as a function of ϵ_s must be chosen. This equation must then be integrated to find the area under the stress-strain curve. After multiplying this by the volume of the element and 2, the equation can be rearranged such that the unknown variables are moved to a vector.

Although the examples shown are unrealistic for soil behaviour, they make demonstrating the process significantly easier. Derivations for more realistic equations will be covered in

later sections of this chapter.

4.4.1 An alternative "Brute Force" approach

The Equation based Identification Method allows for optimisation of the stress-strain response curve shape using relatively few parameters. Although purpose built optimisation software such as MOSEK is the most appropriate way of solving this problem, it is also possible to attempt a brute force approach in which all possible combinations are attempted.

The time taken to solve the problem will of course be much greater, potentially orders of magnitude so depending on how many variables are used to describe the curve, but provides a number of advantages. Firstly, any bugs or flaws in the prebuilt optimiser can be eliminated during any diagnostic process. Secondly, the optimal curve can be guaranteed to be the global optimal as all possibilities are tested. Thirdly, a plot such as a contour map or similar can be used to visualise how changing the parameters effects the energy gap. An example of what such a plot may look like is given in Figure 4.8. It should be noted that this plot does not use the previously described polynomial equation but instead the more complex "Vardanega and Bolton" curve that will be discussed in the following section. And finally, with the use of the aforementioned contour map insight can be gained into the nature of the optimal solution. Is the solution part of a plateau of similarly good possibilities, or are there other local optimal that would also be a reasonable if sub optimal answer.

To some extent, the issue of computational time can be reduced using a tiered brute force approach. An initial coarse search of the parameter space could be carried out to gain a rough initial estimate of the optimal parameter selection after which a finer search is carried out on a subset of the parameter space immediately adjacent to the initial course estimate. This approach has the downside of not guaranteeing that the global optimal can be found. If the "zoomed in" fine search was of a sufficiently small area that did not contain the global optimal solution, it would never be found. Nonetheless, this approach was ultimately implemented in order to ensure that practical computational times were achieved.

There may be some equations in which linear optimisation is not possible. The approach described for the perfectly plastic case and the quadratic equation case allow for easy separation of the known strain field from the unknown equation parameters. For cases where the equation parameter is an exponent ($3x^a$ rather than ax^3 for instance) it is not possible to separate the parameters in this way. Nonlinear optimisation approaches may be possible but will not be considered in this thesis. These equations however can be optimised for using a brute force approach. Although the brute force approach is in many ways worse in terms of its functionality as a practical tool, the diagnostic benefits it brings make it useful as a diagnostic tool during the validation of the Equation based Identification Method.

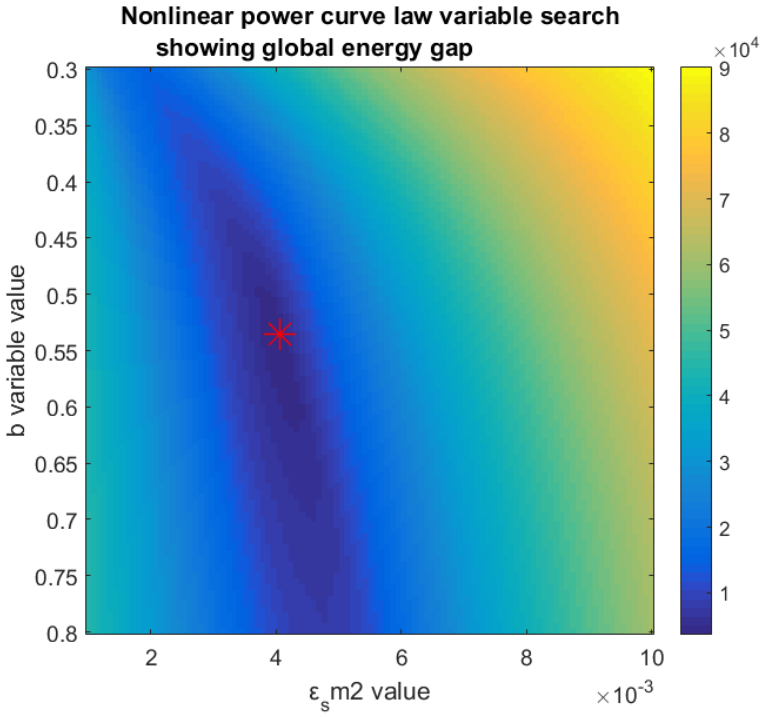

FIGURE 4.8: A plot taken from Charles et al. (2019) showing an example contour plot generated using a brute force approach.

4.4.2 Choice of Equations

Two somewhat realistic equations will be implemented and presented in this thesis.

The first is the elastic-perfectly-plastic curve, in which there is a fully elastic section followed by a horizontal fully plastic section. This is a composite model in which there are two sections in which internal work is calculated differently. Delta strain values for an element and timestep may be contained within a single phase or may spread across two. There will be 4 parameters: G and t_i for the elastic phase, t_{max} for the plastic phase and the strain at the interface between the phases ϵ_p. Equation 4.21 shows the equations determining maximum shear stress as a function of shear strain.

$$\underset{for\ 0 \leq \epsilon_s \leq \epsilon_p}{t = G \cdot \epsilon_s + t_i} \qquad \underset{for\ \epsilon_p < \epsilon_s}{t = t_{max}} \tag{4.21}$$

When using linear optimisation, G, t_i, and t_{max} can be found trivially by assembling a matrix with one row per timestep and one column per variable which can then by multiplied by the vector of variables. An element that travels across the boundary can have its contribution to each phase calculated and summed into the matrix separately. One complication is that the fourth variable, ϵ_p, cannot be solved linearly. It is not a value that can simply be multiplied

by to find internal work. The value of ϵ_p determines which phase an elements delta strain will fall in to. The easiest way to find the optimal value is to try a range of values of ϵ_p and carry out the optimisation for each possible value.

It should also be noted that the general form discussed above would allow for a non continuous curve, in which the elastic phase is not connected to the plastic phase. To eliminate this problem, one variable can be replaced. t_{max} for instance, can be calculated with $t_{max} = G \cdot \epsilon_p + t_i$, with the problem then formulated to calculate internal work using this new t_{max} value. Alternatively, G could be eliminated as a variable.

The location of the interface between the two phases must be found. Although more efficient search processes exist, due to the simplicity of this equation, a brute force approach can be used with an acceptable computational time penalty.

The second equation to be implemented is the "Vardanega and Bolton" curve as described by Vardanega and Bolton (2011). This curve will similarly feature two phases, the "Vardanega and Bolton" part, followed by a perfectly plastic phase. The "Vardanega and Bolton" curve formula is shown in Equation 4.22. It should be noted that Vardanega and Bolton recommended this curve only between 20% and 80% of yield strain. For the purposes of defining an unknown curve, the simplification of extending this range has been taken.

$$t = \frac{t_{max}}{2} \epsilon_s^b \epsilon_{s_{m2}}^{-b} \tag{4.22}$$

There are three terms in this equation t_{max}, which is the peak maximum shear stress, $\epsilon_{s_{m2}}$ which is the shear strain at which half the peak maximum shear stress is achieved, and b which is a dimensionless exponent governing the shape of the curve. No additional parameters are needed to describe the plastic phase. t_{max} is the same, and ϵ_p at the interface can be determined with Equation 4.22 and the value for $\epsilon_{s_{m2}}$. By setting $t = t_{max}$ and rearranging the equation it can be shown that $\epsilon_p = 2^{\frac{1}{b}} \cdot \epsilon_{s_{m2}}$. The equation defining t across the full domain can thus be described as shown in Equation 4.23.

$$\underset{for\ 0 \leq \epsilon_s \leq 2^{\frac{1}{b}} \cdot \epsilon_{s_{m2}}}{t = \frac{t_{max}}{2} \epsilon_s^b \epsilon_{s_{m2}}^{-b}} \qquad \underset{for\ 2^{\frac{1}{b}} \cdot \epsilon_{s_{m2}} < \epsilon_s}{t = t_{max}} \tag{4.23}$$

The area under the "Vardanega and Bolton" phase can be found by integration as demonstrated before. Equation 4.24 shows the internal work expended on a set of E elements for a timestep j.

$$W_{int}^{j} = \sum_{e=1}^{E} \left[\int_{\epsilon_s^{j-1}}^{\epsilon_s^{j}} \frac{t_{max}}{2} \epsilon_s^{b} \epsilon_{s_{m2}}^{-b} d\epsilon_s \cdot 2 \cdot V_e \right] \tag{4.24}$$

Completing the integration yields the following, shown in Equation 4.25.

$$W_{int}^{j} = \sum_{e=1}^{E} \left[\frac{t_{max}}{2(b+1)} \cdot \left(\epsilon_{s_{(j,e)}}^{b+1} - \epsilon_{s_{(j-1,e)}}^{b+1} \right) \cdot 2 \cdot V_e \right] \tag{4.25}$$

The above equation contains many nonlinear terms preventing optimisation using a linear optimiser. A brute force approach is most appropriate for this curve. It should be noted that the values for b are typically between 0.3 and 0.9 and the values for t_{max} and $\epsilon_{s_{m2}}$ can be estimated by running a simpler case (for instance elastic-perfectly-plastic) and varying the values found up and down by a certain percentage.

The two sets of equations given provide relatively realistic responses by each using two different phases governed by their own equation. Unfortunately, the interface between these phases, as well as some terms in the "Vardanega and Bolton" are nonlinear, resulting in the need to use the less efficient brute force approach to recover parameters.

4.4.3 Flow chart of the equation method

A flow chart illustrating the algorith at the heart of the Equation based approach is given in Figure 4.9.

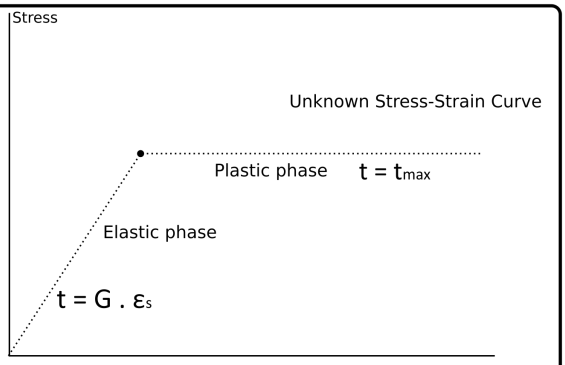

Step 1: Choose one or more equations.
E.g. elastic and plastic

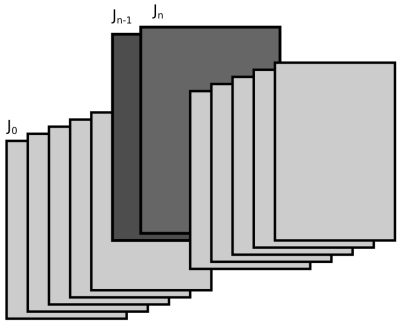

Step 2: Cycle through images, selecting 2 at a time.
Calculate external work corresponding to each image pair:

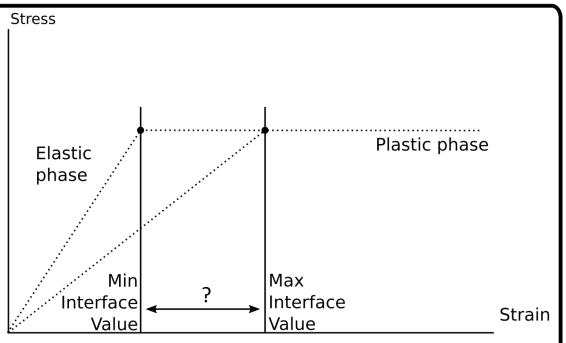

Step 3: Try a range of values for any non linear variables.
E.g. Interface location between planes.
A loop can be programmed for this step.

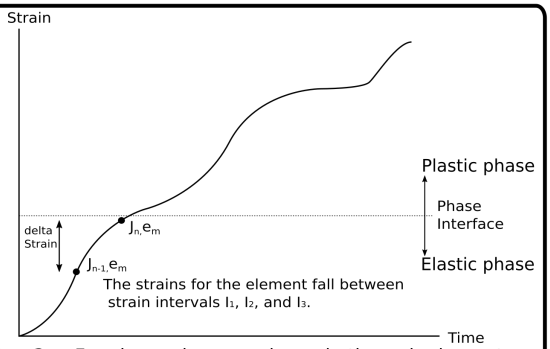

Step 3.a: For chosen image pair, cycle through elements.
Find where the start and end strain is with respect to the chosen equations.

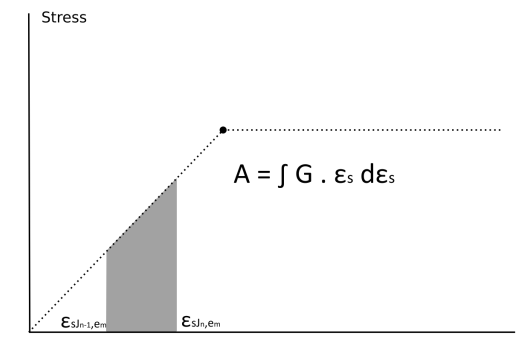

Step 3.b: Integrate the equation for the curve and find the area under the curve for each element in terms of the unknown curve parameters.

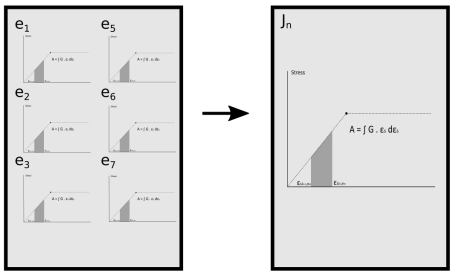

Step 3.c: Sum the calculated area for each element and multiply by twice the element volume. Repeat for the next image pair.

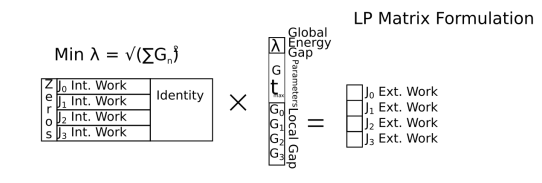

Step 4: Internal work for each image can be expressed in as a row vector with strain data and a column vector of unknown equation parameters. Assemble LP matrix with 1 row per image, to minimise gap between internal and external work. λ is the value to be minimised and Conic optimisation is used.
A brute force approach could also be used

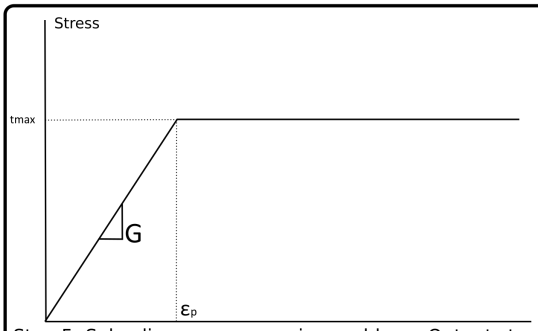

Step 5: Solve linear programming problem. Output stress strain curve can be plotted using equation parameters.
Quality of fit can be found using the global energy gap.

FIGURE 4.9: A flow chart explaining the algorithm for carrying out the Equation based Identification Method.

4.5 Principals of the Segment Based Identification Method

The Segment based method divides the unknown curve into a series of segments. Each segment will be represented by a start and an end maximum shear stress value. These values will be shared with the segment before and after respectively, resulting in a continuous curve. The curve being split in such a way allows for trivial integration using the trapezium method. Figure 4.10 shows how the unknown stress-strain response will be represented with the aforementioned segments.

It should be noted that the concepts of the Segment based approach are based on pre-existing work that was completed prior to the commencement of this project and was presented by Gueguin et al. (2015). Significant work has been carried out to improve and generalise the methodology, particularly the work presented in this section regarding the calculation of area under an unknown stress-strain curve.

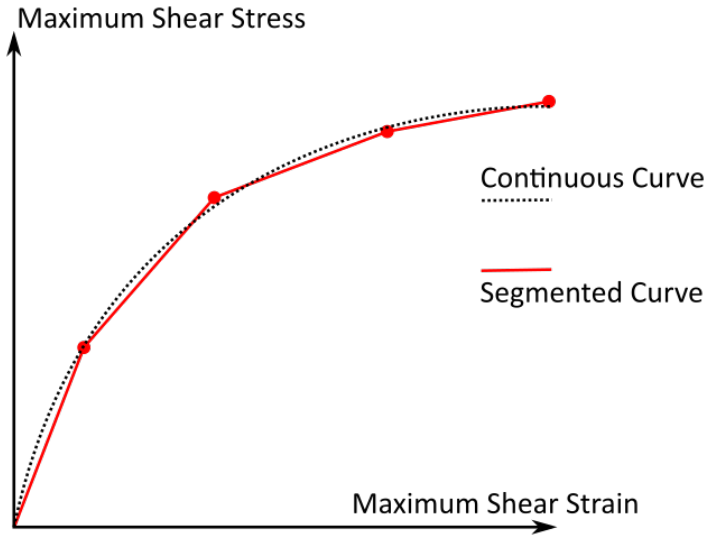

FIGURE 4.10: The relationship between a continuous stress-strain response and a segmented response.

An important consideration is that the number of segments is unrelated to the number of images, the number of patches, or any other parameter. It can be set to whatever the user deems fit. As such, the delta strain value for a given patch within a given image pair could be represented by a fraction of a single segment or it could span across several. A robust method for keeping track of where each patch is on the stress-strain curve, along with the means to efficiently sum the internal work must therefore be derived.

As with the previous presented methodology, the measured strain field will be split into a grid of triangular elements. Each element will have a fixed area and a strain value that changes with each timestep (there is one timestep per image). Examining timesteps one

at a time, it must be determined which segment (or segments) each element delta strain occupies. Examining each element in turn, the start and end strains can be compared to the strains allocated to each segment. If a segment is fully contained within the elements delta strain, one multiplied by the element area can be added to its tally. If only part of a segment is contained, the inclusion fraction can be multiplied by the area and tallied. This can be repeated for every element within the timestep.

Figure 4.11 shows a case in which the contributions of three elements are to be found for a single timestep. Element A, in which the measured maximum shear strain starts at $\epsilon_{s,A1}$ and ends at $\epsilon_{s,A2}$ with the change represented by $\delta\epsilon_{s,A}$. Similarly element B has the start, end, and delta values as $\epsilon_{s,B1}$, $\epsilon_{s,B2}$, $\delta\epsilon_{s,B}$ and for element C: $\epsilon_{s,C1}$, $\epsilon_{s,C2}$, $\delta\epsilon_{s,C}$. The diagram also has segments on the stress-strain curve labelled 1 to 11.

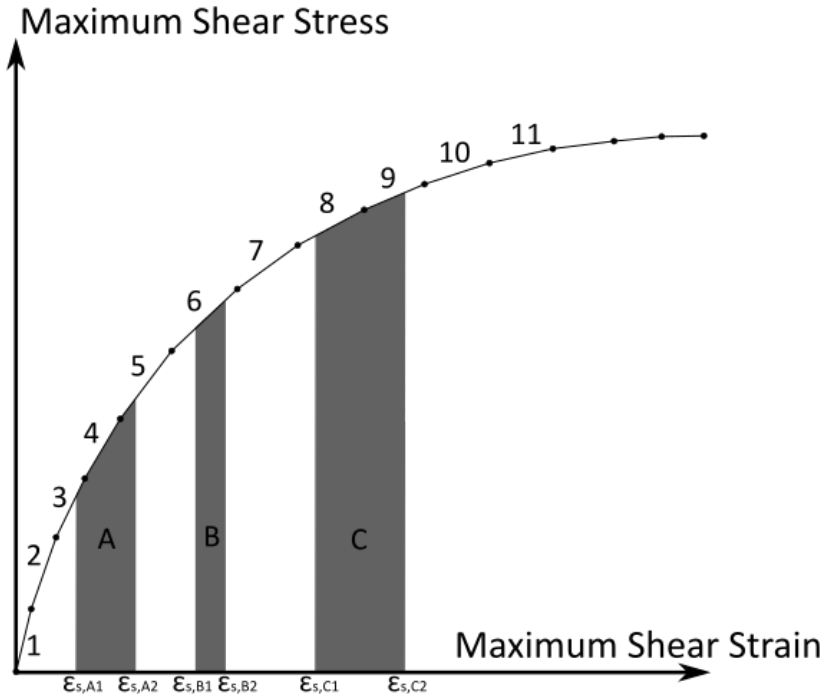

FIGURE 4.11: The relationship between a series of stress-strain segments and the area under the curve for a set of elements.

It can be seen that element A spreads across several segments. Segment 4 for instance is fully contained within the strain increment, whereas segments 3 and 5 are only partially contained. Element B contains only part of segment 6 and element C contains parts of 8 and 9. For each segment it would be possible to calculate an inclusion factor F and a location factor L representing with numbers between 0 and 1 the percentage of inclusion for a segment and the percentage through the segment were the measured data starts. If a segment is fully contained the location factor would be 0 and the inclusion factor 1.

To work out the area under the curve which can be multiplied by two to find internal work, values for maximum shear stress at the beginning and end of each segment are needed. As the stress values at the start and end of each segment are the unknowns to be found, the area under the curve must be formulated in a way to facilitate easy inclusion of these unknown parameters. A matrix of the strain components of work will be multiplied by the vector of stresses. In order to determine how this matrix should be arranged it is necessary to examine how the trapezium rule equation will be used to deal with partial inclusion of segments. Figure 4.12 shows the most general case, a segment with start and end strains $\epsilon_{s,1}$ and $\epsilon_{s,2}$ with (unknown) start and end stresses t_1 and t_2. The increment for the element (i.e. the area to be calculated) has start and end strains $\epsilon_{s,s}$ and $\epsilon_{s,e}$ with (unknown) start and end stresses t_s and t_e.

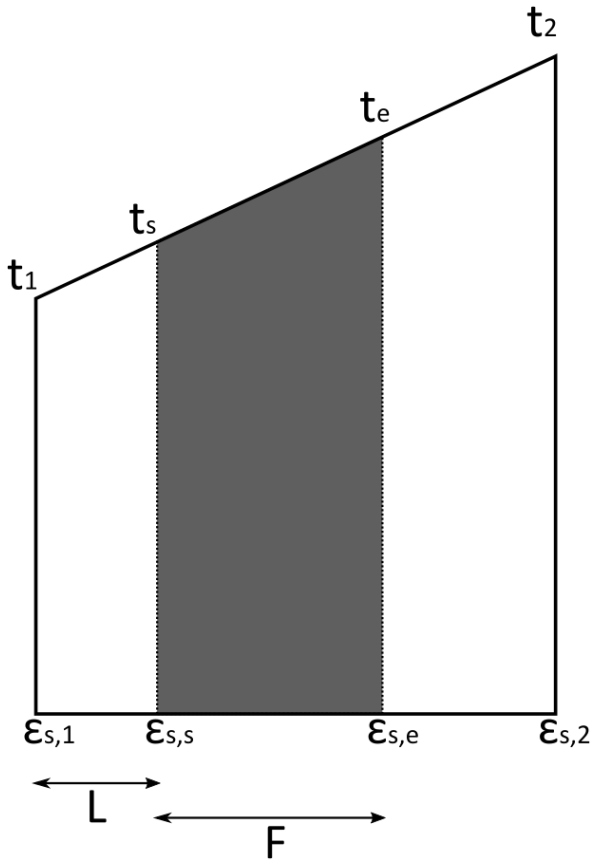

FIGURE 4.12: A diagram illustrating how the area of under the curve for an elements increment within one timestep relates to a predefined stress-strain curve segment.

The area under the entire segment, A_s, is trivially shown in Equation 4.26 and similarly the area under the element increment, A_{ei}, is shown in Equation 4.27. Unfortunately, the area for the element increment must be written in terms of t_1 and t_2 as these are the parameters that will be optimised for and in which internal work must be expressed.

$$A_s = 0.5 \cdot (t_1 + t_2) \cdot (\epsilon_{s,2} - \epsilon_{s,1}) \tag{4.26}$$

$$A_{ei} = 0.5 \cdot (t_s + t_e) \cdot (\epsilon_{s,e} - \epsilon_{s,s}) \tag{4.27}$$

The values of $\epsilon_{s,s}$ and $\epsilon_{s,e}$ are already known as these are derived from the measured dataset. The difference between them will be labelled $\delta\epsilon_s$. The unknown t_s and t_e can be written in terms of the (also unknown) t_1 and t_2 via similar triangles. Equation 4.28 shows these relationships, with Equations 4.29 and 4.30 showing the area under the curve for an element increment in terms of t_1 and t_2.

$$t_s = (t_2 - t_1) \cdot L + t_1 \qquad t_e = (t_2 - t_1) \cdot (L + F) + t_1 \tag{4.28}$$

$$A_{ei} = 0.5 \cdot ((t_2 - t_1) \cdot L + t_1 + (t_2 - t_1) \cdot (L + F) + t_1) \cdot \delta\epsilon_s \tag{4.29}$$

$$A_{ei} = 0.5 \cdot (t_1 \cdot (2 - 2L - F) + t_2 \cdot (2L + F)) \cdot \delta\epsilon_s \tag{4.30}$$

The next step is to extract the t_1 and t_2 into a vector. The result of this is shown in Equation 4.31

$$A_{ei} = \begin{bmatrix} 0.5 \cdot \delta\epsilon_s \cdot (2 - 2L - F) & 0.5 \cdot \delta\epsilon_s \cdot (2L + F) \end{bmatrix} \cdot \begin{bmatrix} t_1 \\ t_2 \end{bmatrix} \tag{4.31}$$

The above demonstrates how the area under the stress-strain curve (to find internal work multiply by 2, see Equation 4.2) will be calculated for a case with a single element (with unit area) and a stress-strain curve made up of a single segment. It is fairly easy to apply the demonstrated principles to more complex cases. For an element increment that covers multiple segments, a 1×2 matrix as shown in Equation 4.31 will be calculated for each segment. These matrices can be added to a global matrix at the correct locations. Each row in the matrix will represent a timestep and each column represents a strain segment. Similarly, the areas under the curve for each element can be calculated and added to this global matrix. In cases where the area of an element is not 1, simply multiply the 1×2 matrix by the area before adding it to the global matrix.

The Segment based approach results in a discretised stress-strain response. The curve will not be smooth but instead split into a number of linear segments. For some cases, e.g. where

the stress-strain response is assumed to be elastic or elastic-perfectly-plastic, it would be satisfactory to describe the curve with only a handful of segments. For more complex cases, tens or even hundreds of segments may be necessary.

The effects of the number of segments on the accuracy of the output curve is to be determined. It is obviously apparent that too few segments would cause issues but other questions arise. For instance, is it possible to have too many segments, or how would the optimisation process be affected if there were segments that have no corresponding data?

As stated, the presented algorithm represents a significant evolution over the methodologies that were found in the inherited codebase and were used in the cited publication (Gueguin et al., 2015). Major modifications were put in place during the course of this project to allow for improvements in the distribution of element strain data. The algorithm based on the trapezium rule was implemented and energy gap calculations were changed to be incremental rather than cumulative. The improved methodology presented here is adaptable and could be used for cumulative energy calculation if necessary.

4.5.1 Curve Constraints

By default, the shape of the curve of the Segment based Identification Method is unconstrained. Every segment is independent of all others, save for its immediate neighbours with which a node is shared. Although this freedom is in some ways a benefit in that arbitrarily complex soil responses could be recovered, there could be issues with unexpected outputs. The optimiser could for instance find that the curve with the lowest energy gap contains negative maximum shear stresses, or stresses that fluctuate wildly as strain increases. Sections of the curve with relatively low amounts of data constraining them may behave in unusual ways, or noisy data could result in unpredictable curves.

The optimiser has no knowledge of geotechnical engineering. By asking it to recover the best fit stress-strain response, that it exactly what it will give. What is actually needed is to ask the optimiser to recover the best fit *realistic* stress-strain response. Constraints can be added to limit the possible shape of the output curve in ways that force it to look somewhat like a stress-strain response should. Although it would be possible to limit the shape of the curve to a high degree based on the expected response, over constraining the curve could limit identification of the true response, should there be some reason it doesn't meet the expectations. As such, as few common sense constraints will be listed and briefly discussed. It should be noted that this thesis deals with monotonically loaded cohesive undrained soils and these constraints are tailored as such. Other soil responses for e.g. granular soils or dynamic loading will require a different approach.

The simplest constraint is the requirement that the stress-strain curve is positive. MOSEK allows the input of allowable ranges to optimisation variables so each maximum shear stress value can be specified to be ≥ 0. This constraint prevents the optimiser artificially reducing internal work by having sections of the curve below the x axis.

The next constraint is the requirement that maximum shear stress increases as shear strain increases. This requires the curve to move in an upwards direction from the origin and prevents a zig-zag shaped curve. Constraining the curve in this way prevents the need to carry out any post-processing or smoothing. Implementation of this constraint is simple. Subtract the variable for maximum shear stress at $j-1$ from the maximum shear stress at j and constrain the difference to be ≥ 0.

The third constraint will require the final segment or segments of the curve to be a flat plateau. Segments beyond a user specified value of shear strain can be identified and forced to be horizontal, or simply the final segment. This constraint can be added in the same way as the "always increasing maximum shear stress" constraint, with the difference between stresses at j and $j-1$ fixed at exactly zero.

The final and most complex constraint to be implemented will force the slope of the curve to gradually decrease. This constraint will ensure a curve that starts steep and smoothly reduces in gradient until the plateau is reached. Implementing this requires the difference in gradients between two segments to be greater than zero. The gradient however is not an optimisation variable so this constraint must be formulated in terms of the maximum shear stresses at the beginning and end of each segment. Figure 4.13 shows an illustration of the geometry of this problem. Stresses at $j-1$, j, and $j+1$ are the optimisation variables, and the delta strain values for the two segments, $\delta\epsilon_{sj}$ and $\delta\epsilon_{sj+1}$, are known values.

The gradient for a segment is the change in maximum shear stress divided by the change in shear strain. The gradient for the first segment minus the gradient for the second segment must be greater than zero. The following Equations 4.32, 4.33, 4.34, and 4.35 show how this concept can be rearranged such that it can be added to an optimisation matrix.

$$\frac{t_j - t_{j-1}}{\delta\epsilon_{sj}} - \frac{t_{j+1} - t_j}{\delta\epsilon_{sj+1}} \geq 0 \tag{4.32}$$

$$\delta\epsilon_{sj+1} \cdot (t_j - t_{j-1}) - \delta\epsilon_{sj} \cdot (t_{j+1} - t_j) \geq 0 \tag{4.33}$$

$$t_{j-1} \cdot -\delta\epsilon_{sj+1} + t_j \cdot (\delta\epsilon_{sj} + \delta\epsilon_{sj+1}) + t_{j+1} \cdot -\delta\epsilon_{sj} \geq 0 \tag{4.34}$$

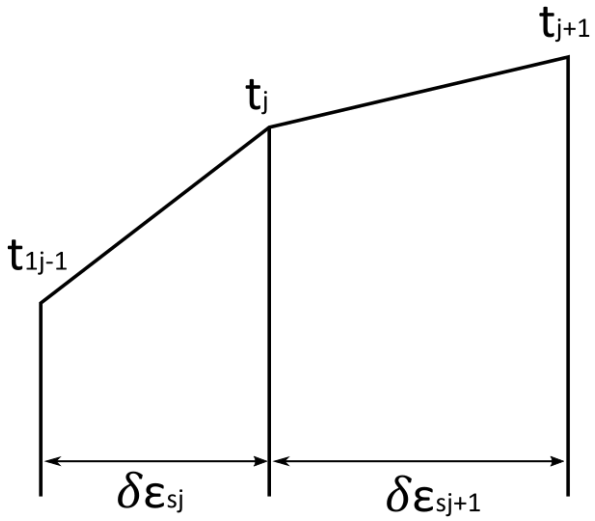

FIGURE 4.13: A diagram illustrating the geometry of constraining the stress-strain response such that the gradient gradually decreases.

$$\begin{pmatrix} -\delta\epsilon_{sj+1} & (\delta\epsilon_{sj} + \delta\epsilon_{sj+1}) & -\delta\epsilon_{sj} \end{pmatrix} \cdot \begin{pmatrix} t_{j-1} \\ t_j \\ t_{j+1} \end{pmatrix} \geq 0 \tag{4.35}$$

The formulation shown in Equation 4.35 can be easily expanded for curves with many segments. A global matrix can be assembled with one row per segment with the three terms placed in the correct columns, forming a diagonal pattern.

As stated, these constraints are designed to allow for realistic stress-strain responses to be found for monotonically loaded undrained soils. These constraints will be used during testing and validation of the Segment based Identification Method, which will be presented in Chapter 7 for testing with artificial datasets and in Chapter 8 for testing with real datasets. These constraints were chosen as they closely represent the expected soil behaviour. Should it turn out that the behaviour observed in later chapters poorly matches these constrains, commentary will be given as to why.

4.5.2 Construction of Optimisation matrix

Optimisation problems consist of an equality matrix generated from strain data and constraints (as discussed above) multiplied by a vector of variables which are to be optimised. The number of rows in the vector of variables must equal the number of columns in the equality matrix. The result of this multiplication will be constrained. Two constraint vectors will be used for this role, one with lower bound values and one with upper bound values.

These vectors will have the same number of rows as the equality matrix. The results of the multiplication must be within the upper and lower values.

The objective function is the goal which the optimiser will aim to achieve. The objective function will be given as an equation in terms of a subset of the variables with the goal of minimising the value of this equation while ensuring no constraints are violated. The equation to be minimised is given at the start of this chapter in Equation 4.4. The goal is to minimise the global energy gap, which is the square root of the sum of the squared values of local increment energy gaps. Conic optimisation will be used for this. An additional global energy gap variable, λ, will be used, which is defined as the square root of the sum of the squared local energy gaps, with the objective function then simply being to minimise λ.

The introduction of energy gaps into the formulation is simple. A vector of incremental internal works can be calculated by multiplying the matrix generated from strain data by the vector of maximum shear stresses. As internal work plus local energy gap must equal external work, the local energy gaps can be added to the vector of variables, which will be multiplied by the identity matrix. The upper and lower bound constraints can both be set to the vector of incremental external work terms.

The specification of the optimisation problem can be examined in Equation 4.36. Terminology is the same as previously used with the addition of $\mathbf{t}$ which is the vector of maximum shear stresses and G_j representing the gradient of the curve between t_j and t_{j+1}. A description of what each line represents is also included. A more detailed discussion of how these constraints are implemented can be found in the preceding subsection.

$$\begin{array}{lcl} \text{Minimise} & \lambda & \text{Objective function} \\ \text{Subject to} & Wint_j + localgap_j = Wext_j & \text{Energy equilibrium} \\ & G_{j+1} - G_j \leq 0 & \text{Reducing gradient} \\ & t_{j+1} - t_j \geq 0 & \text{Increasing stress} \\ & \mathbf{t} \geq 0 & \text{All stresses positive} \\ \text{And} & \lambda = \sqrt{\sum_{j=1}^{n_{images}} (localgap_j)} & \text{Conic constraint} \end{array} \tag{4.36}$$

A diagram showing the layout of the optimisation problem is given in Figure 4.14. The matrix and vectors are split to show what each section relates to with dimensions given, where N_{im} is the number of images (and hence strain and external work increments) and N_{seg} is the number of strain segments in the unknown stress-strain curve.

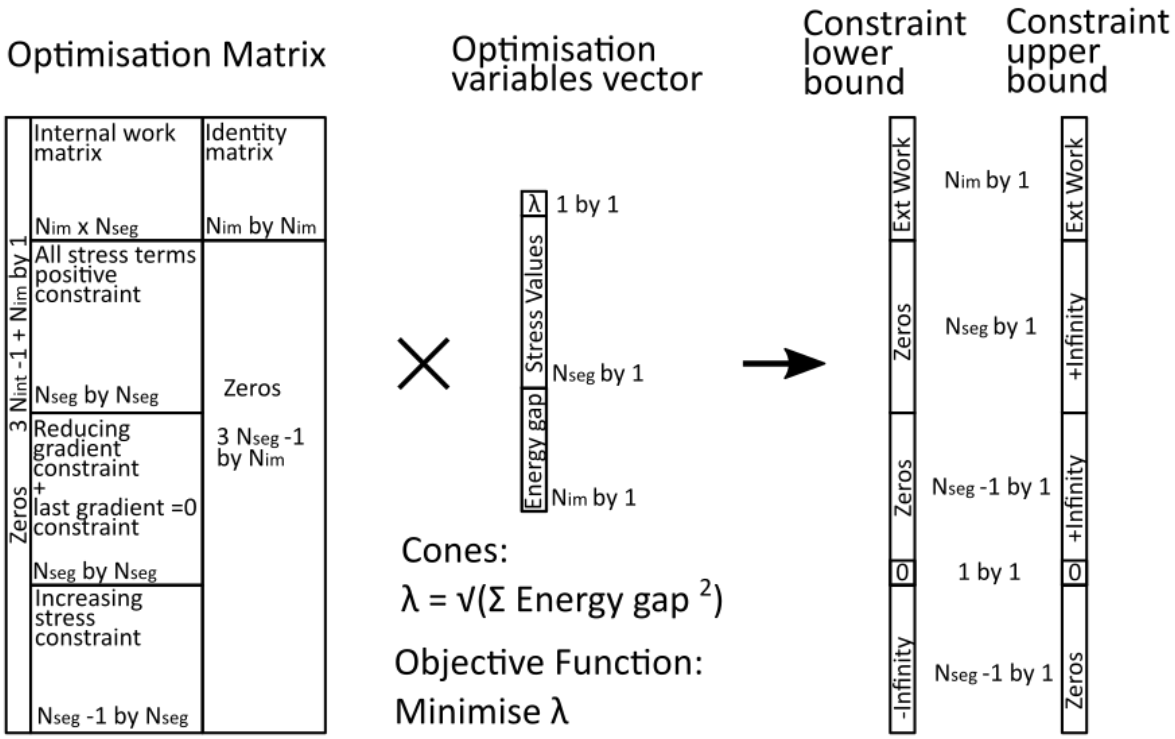

FIGURE 4.14: The layout of the Segment Method optimisation problem.

4.5.3 Flow chart of the segment method

A flow chart illustrating the algorithm at the heart of the Segment based approach is given in Figure 4.15.

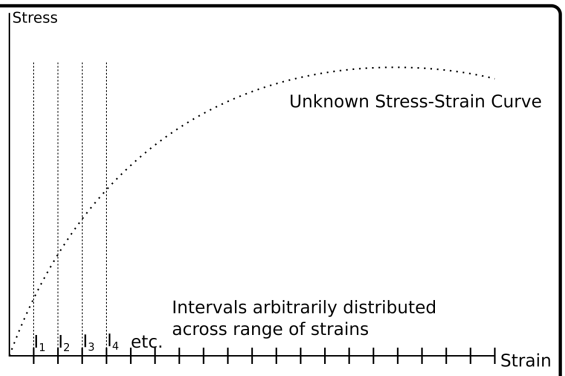

Step 1: Generate desired strain intervals.

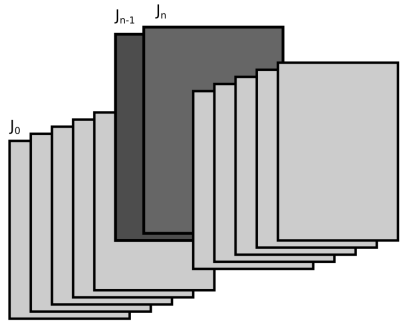

Step 2: Cycle through images, selecting 2 at a time. Calculate external work corresponding to each image pair:

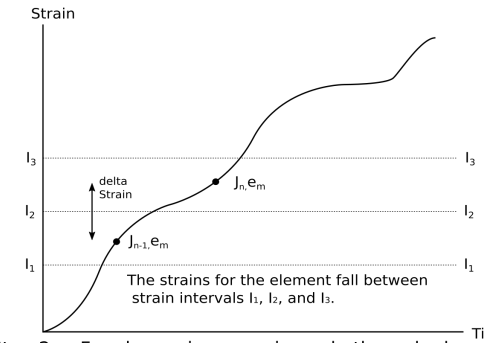

Step 2.a: For chosen image pair, cycle through elements. Find where the start and end strain is with respect to the strain intervals.

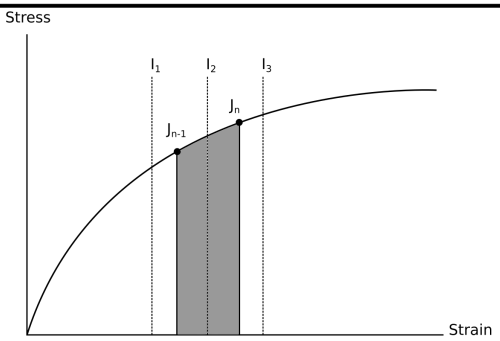

Step 2.b: Find the area under the stress-strain curve for each element, in terms of unknown shear for each strain interval.

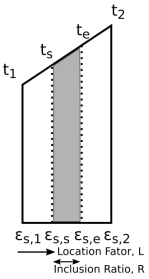

Let $t_s = (t_2-t_1) * L + t_1$ and $t_e = (t_2 - t_1) * (L+R) + t_1$

And let $\delta\varepsilon = \varepsilon_e - \varepsilon_s$

The desired shaded area A can then be derived:

$A = 0.5 * (t_s - t_e) * \delta\varepsilon$

Step 2.c: Area must be found in terms of strain intervals and corresponding stress values. Strain intervals likely don't match exactly with element values so modified trapezium rule allowing interpolation used.

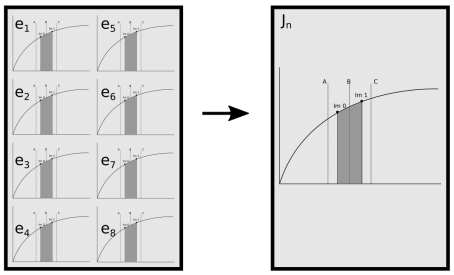

Step 2.d: Sum the calculated area for each element and multiply by twice the element volume. Repeat for the next image pair.

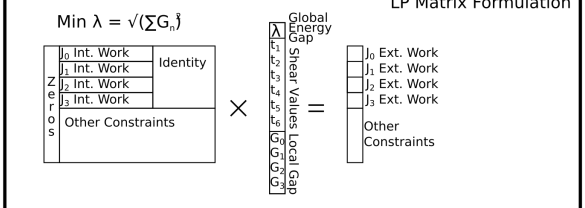

Step 3: Internal work for each image can be expressed in as a row vector with strain data and a column vector of unknown stress data. Assemble LP matrix with one row per image, to minimise gap between internal and external work. There will be one stress value per strain interval, and one energy gap value per Image. λ is the value to be minimised and Conic optimisation is used.

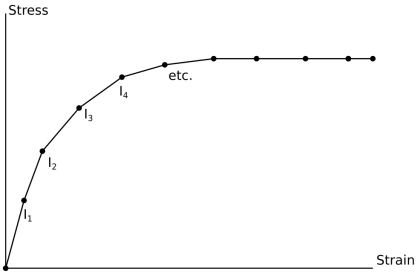

Step 4: Solve linear programming problem. Output stress strain curve can be plotted using strain intervals and newly found corresponding shear values. Quality of fit can be found using the global energy gap.

FIGURE 4.15: A flow chart explaining the algorithm for carrying out the Segment based Identification Method.

4.6 Comparison of the two approaches

The two proposed Identification Methods, the Equation based approach and the Segment based approach, at their core aim to achieve the same goal. A stress-strain response curve is to be found such that the gap between internal and external work is as low as possible. The two methods differ in how the unknown curve is described, with various practicalities, drawbacks, and benefits.

The Equation based approach results in a significantly simpler optimisation problem with only a few variables. The shape of the curve is very limited. If for instance the equation for a perfectly elastic case was used, the only variation to the curve shape would be the angle and the intercept of the straight line. Should the soil in actual fact respond in some other way, the curve may in fact be a very poor fit. The Equation based approach also has the additional drawback of some equations, particularly more realistic options, requiring nonlinear optimisation. This requires more complex programming, or the use of a brute force approach.

The Segment based approach is much more free. The curve is split into many segments, the arrangement of which can be whatever the optimiser sees fit. Constraints can be added to force the curve into shapes that are judged to be more likely and to eliminate artefacts that would not be possible in reality. There are many more optimisation variables in the Segment based approach than there are in the Equation based approach. Distributing the strain data between the segments is also a relatively time consuming process, taking several times as long as the final optimisation stage.

For this project, the goal is development and validation of the methods. As such, computational complexity and run time are not factors that will be used to judge the capabilities of either method. Qualitative commentary will be given but there will not be a systematic study. These factors may be of concern should an attempt to be made to implement one or both methods in a commercial or research tool destined for public release in the future.

If time and computational complexity are discounted, the main difference between the methods is the degree of constraint. The Equation based approach will result in a highly constrained curve with very few degrees of freedom whereas the Segment based approach is by default unconstrained, with optional constraints added as appropriate. The effects of this difference will be an area of examination in later chapters. Questions such as whether the optimiser produces more accurate curves with or without constraints will be answered.

4.7 Conclusion

Two different Identification Method implementations have been derived and presented. Each method builds upon the work equilibrium equation derived in Chapter 3 to provide a practical means by which the unknown stress-strain response can be recovered such that the energy gap between internal and external work is minimised. The first of the two methods requires the curve to be defined by one or more equations, the parameters for which are to be recovered. The second method splits the curve into a large number of segments of which the arrangement is to be optimised.

The full derivation for each method has been presented along with commentary on use and a flow chart illustrating the key steps in the algorithm for each method.

Chapter 5

Artificial Data Set Generation

5.1 Introduction

In order to verify that the proposed Identification Methods are functioning as they are supposed to, it is necessary to test them with datasets and compare the output with a known correct answer. Although the end goal is to do this with real laboratory data (as will be discussed in Chapter 6), there are a number of complications with using such datasets. Noise, experimental error, and even not knowing for sure if the known correct answer is truly representative could make it difficult to identify the source of any errors of discrepancies.

To provide initial validation a small number of "handmade" datasets will be produced using Matlab. Two slightly differing simple shear cases will be presented each of which will consist of a grid of nodes displacing over time, with the required force to produce the specified movement.

To provide for more complex and realistic test cases a suite of finite element models will be developed and ran. A FEA analysis allows for the discounting of noise, gravity, and any other factor that is not explicitly modelled. There is no need to take lens distortion into account and it can be guaranteed that the simulated models will behave exactly as specified. The Abaqus FEA software (Dassault Systèmes, 2014) package will be used.

Several FEA models will be run. The simplest will be a simple shear case, which should match the "handmade" simple shear case and serve as validation for the FEA modelling process. Aditionally a rotating wall case will be produced, and a rectangular footing case, the observed peak loading of which can be validated with Terzaghi's bearing capacity equation. For each FEA model two different input curves tested (elastic perfectly-plastic, and the "Vardanega and Bolton" curve as described by Vardanega and Bolton (2011)). From each model, loading and displacement will be recorded for the external action carried out, and nodal displacement for the soil mesh will be recorded to allow for computation of internal work.

Although noise can be neglected in FEA models, it is reality for datasets produced by actual laboratory experimentation. As such, any Identification Method that is to be of use must be able to function with reasonable levels of nose present. To test resilience to noise, the "handmade" and FEA datasets will be artificially degraded to determine how this affects recovery of soil properties and to what degree.

This chapter will first describe the input stress-strain responses to be used with the artificial datasets, the process by which the "handmade" datasets are generated, followed by the FEA modelling methodologies, and finally the scheme by which the models can be artificially degraded. Discussion of these generated datasets along with the results of using them with the proposed Identification Methods will be found in Chapter 7.

5.2 Input stress-strain Curves

Two different soil responses were modelled to provide a range of material properties to attempt to recover. Elastic Perfectly-Plastic was chosen as it is a particularly simple response, and the "Vardanega and Bolton" curve was chosen to provide a more complex response. The chosen curves are described in the following sections.

5.2.1 Elastic Perfectly-Plastic

The Elastic Perfectly-Plastic consists of a linear elastic section, between strains between strains of 0 and 0.015 followed by a perfectly plastic plateau at shear stress of $90kPa$. In order to ensure the assumptions made during the derivation and implementation of the Identification Methods are valid, Poisson's Ratio would ideally be set to 0.5. This value however causes issues due to the limitations inherent to FEA and as such Poisson's Ratio was set to 0.499 potentially allowing for a small amount of spurious volumetric strain.

Figure 5.1 shows the specified stress-strain response.

5.2.2 "Vardanega and Bolton" Curve

The "Vardanega and Bolton" curve, as described by Vardanega and Bolton (2011), can be plotted using the equation shown below in Equation 5.1. This equation was originally developed by finding the empiric best fit to a large quantity of experimental data and as such should be reasonably representative of real soil. The exact curve used is largely unimportant as the goal is to match the input used for the FEA model with the output from the

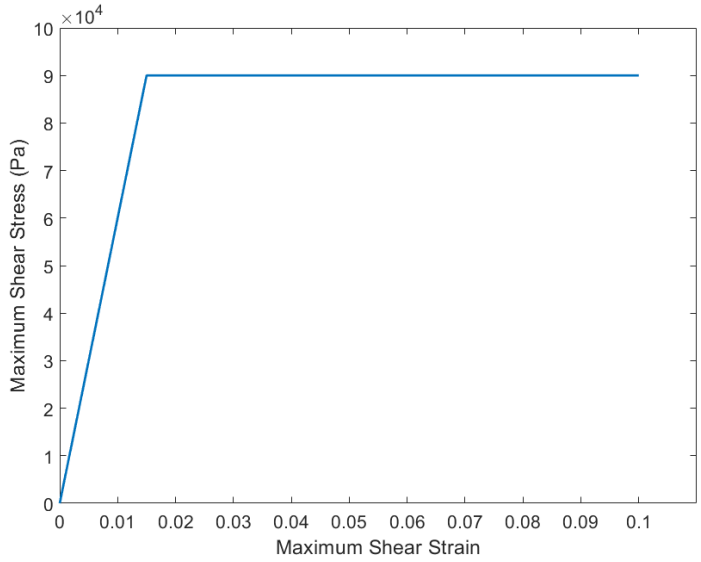

FIGURE 5.1: The stress-strain response used for modelling the Elastic-Perfectly-Plastic case.

Identification Methods, but it seems more appropriate to use a curve with some geotechnical relevance rather than generate a curve based on a generic equation such as $y = \sqrt{x}$ or similar.

$$t = \frac{c_u}{2} \epsilon_s^b \epsilon_{s_{m2}}^{-b} \tag{5.1}$$

This equation is used with the parameter set shown in Table 5.1.

c_u	$100kPa$
b	0.5
$\epsilon_{s_{m2}}$	0.005

TABLE 5.1: Parameters used with the "Vardanega and Bolton" equation to generate an artificial stress-strain response

The equation will be used only up to c_u, after which a perfectly plastic response will be assumed. The stress-strain response is reproduced in Figure 5.2.

5.3 "Handmade" datasets

Perhaps the simplest dataset to make is simple shear. This could be done with very simple hand calculations. Shear strain can be calculated with $\gamma_{xy} = 2 \cdot \epsilon_{xy} = \frac{\delta u}{\delta y} + \frac{\delta v}{\delta x}$. More information on the calculation of strains can be found in Chapter 3. For a block of material

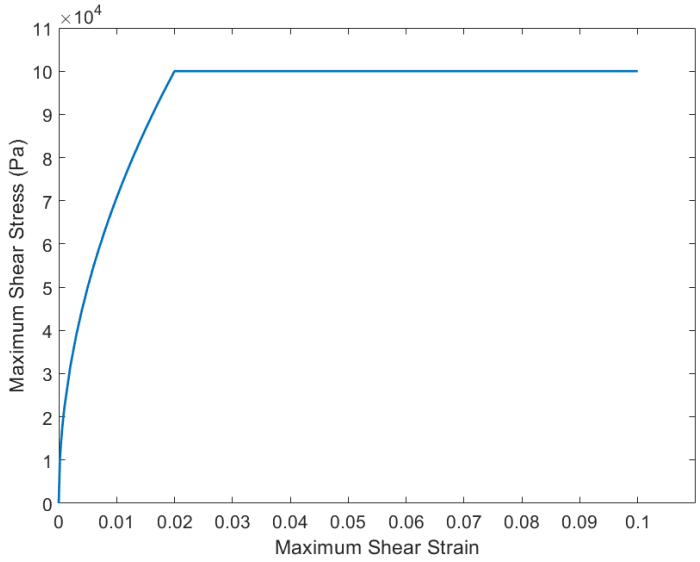

FIGURE 5.2: The stress-strain response used for modelling the "Vardanega and Bolton" case.

undergoing simple shear as shown in Figure 5.3, shear stress is equal to the movement in the x direction divided by the height.

By arbitrarily choosing a set of time values, a corresponding set of displacement and strain values can be chosen. For simplicity, a linear increase in shear strain was used but any scheme would function for this purpose. Maximum shear strain ϵ_s can be calculated based using the equations derived from Mohr's circle (see Chapter 3). For this case in which ϵ_x and ϵ_y are zero, this will simply be equivalent to ϵ_{xy} At this stage the shear strain values are known for each timestep but the load displacement values still need to be calculated. The displacement component is known as it is by definition the same as the displacement of the soil. To find the load component maximum shear stress t must be found as an intermediary stage.

As the stress-strain curves that will govern the behaviour of the simple "handmade" model are already specified, finding maximum shear stress is as easy as reading it off the curve. A known value of maximum shear strain will allow the corresponding value of maximum shear stress to be found. The force required to produce such a stress can be found by multiplying the maximum shear stress value by the x dimension of the block of material. This can be completed for every timestep allowing for plots of load, displacement, and maximum shear strain against time. This is all the data required to carry out the Identification Method process.

The hand calculations above however produce only a single element. If the goal is to have a dataset that is representative of what would be produced by PIV then many elements will

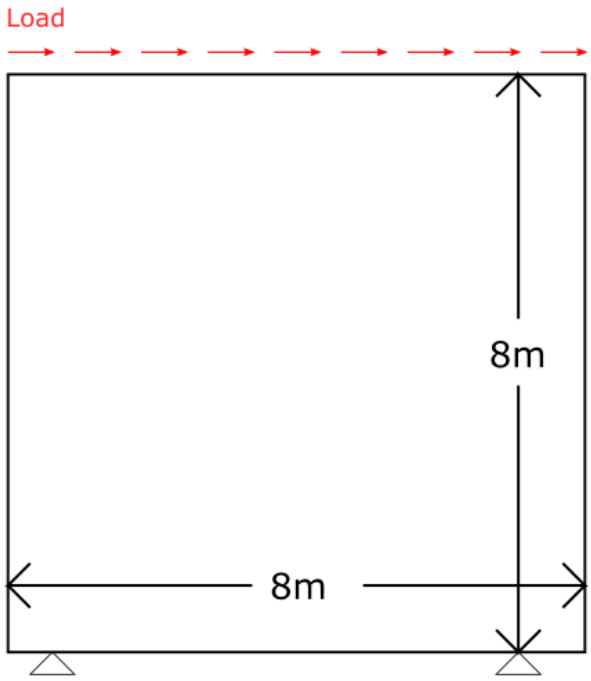

FIGURE 5.3: The geometry of the Simple Shear model, as previously published in (Charles et al., 2018a)

be needed. The reason "handmade" is in quotation marks is that the actual datasets were produced using Matlab. A set of nodes were generated in a uniform grid with the nodes at the top displacing the full amount as calculated by hand and he nodes at the bottom being fixed. Nodes in the middle will displace proportionally to their location. This grid of displacing nodes provides a good approximation of PIV data and can be processed as such. Strains can be calculated from the displacement field followed by, in turn, stress and force.

The exact model created was a block of soil with dimensions 8m by 8m with a grid of 33 by 33 displacement nodes. 50 timesteps were used and evenly distributed over 10 seconds. The final horizontal displacement of the top row of nodes will be 0.96m, resulting in $\gamma_{xy} = 0.12$ or $\epsilon_{xy} = 0.06$.

An additionally and slightly more complex scenario that can be generated in this manner is a split simple shear case. A diagram for this scenario can be seen in Figure 5.4. For this model both the top and bottom of the soil specimen is fixed with loading applied to a slightly off-centre horizontal section through the soil. This could perhaps represent the pull-out of a geomembrane. The scheme regarding overall size, node numbers, and timesteps as used for the simple shear case will be reused here with the geomembrane at 5m from the top.

Nodal displacements were calculated such that they linearly increase from zero to the peak value at the geomembrane in each direction. Due to the asymmetry in the model, differing

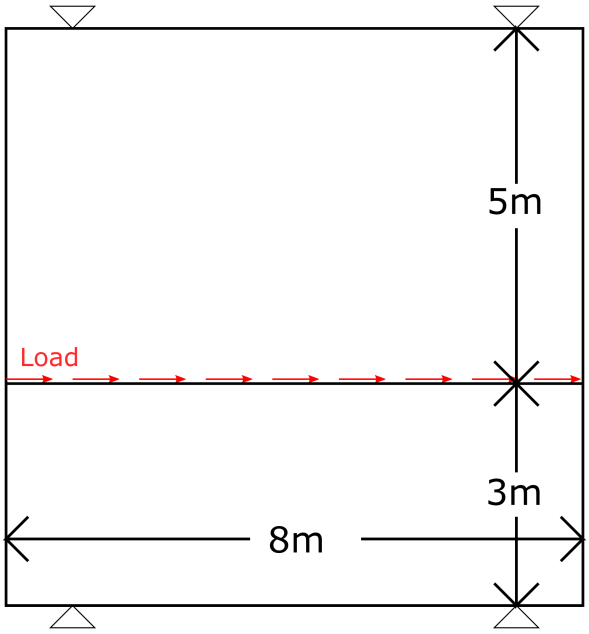

FIGURE 5.4: The geometry of the Split Simple Shear model

shear strain values will be found in the top and the bottom with differing maximum shear stress values obtained via the stress-strain curve for each part of the model. The force will be the sum of each of these maximum shear stress values multiplied by the x dimension.

The split simple shear case represents a slight increase in complexity over the standard simple shear case. Simple shear produces a uniform strain field with one value across all elements, whereas the split case has two separate areas with their own uniform strain field across all elements. More realistic cases will likely have strain fields that are completely non uniform but this would be prohibitively difficult to calculate by hand and as such FEA will be used to produce more complex models.

5.4 FEA Modelling

ABAQUS was used to generate a series of artificial datasets generated via FEA. Each FEA model was relatively simple, consisting of a two dimensional square of soil constructed using a uniform mesh. The dimensions of both the soil block and the mesh will vary between the individual models and will be discussed in the following sections.

The two generated soil responses were input using an elasticity model followed by a plasticity model. This was done by first generating a list of strains and calculating the associated deviatoric stres corresponding to each strain value. The first increment was assumed to be elastic, with following increments plastic. It should be noted that ABAQUS requires the list

of stresses and strain to be input as true stress and plastic strain. True stress was found by multiplying the maximum shear stress values by $\sqrt{3}$, as per the von Mises yield criterion, and plastic strains were calculated by subtracting true stress over Young's Modulus from the original strain value. Finally, Poisson's ratio was set to 0.499.

This procedure was carried out to allow for direct comparison between an input stress-strain response and the equivalent output curve recovered using the Identification Method. There is the possibility that the soil model as input is not fully representative of what was intended, either due to assumptions in the conversion between different kinds of stress and strain, or other behaviour that is not defined in such a simple model. Initial experimentation however indicates that the original input curve can be recovered successfully after using ABAQUS in this manner. Additionally, a simple shear case was produced using both hand calculations and FEA, allowing for validation of this process.

The Elastic Perfectly-Plastic response was modelled with only the three values at the beginning, end, and vertex included whereas the "Vardanega and Bolton" response used 25 points to describe the curve.

5.4.1 FEA Simple Shear Model

As in the "handmade" Simple Shear case, for the FEA Simple Shear case a block of soil is fixed at the base and loading is applied parallel to the top edge. The block is loaded purely and uniformly in shear by an amount that is trivial to calculate by hand. A Simple Shear model was created using ABAQUS for both of the stress-strain responses specified in section 5.2. Figure 5.3 shows the layout of this model. It should be noted that this model should produce funtionally the same output as the simple shear "hand" calculation. It has been completed as a FEA model in order to demonstrate the validity of the FEA process in producing artificial datasets.

To accurately represent the model within ABAQUS, a fixed boundary condition was placed along the base, and a constraint requiring uniform movement in the x direction was applied to the top edge, along with a boundary preventing vertical movement. The mesh used hybrid 3 node triangular elements, with the mesh having 16 elements in each direction.

Due to the horizontal movement of the nodes along the top edge being constrained to be uniform, the traditional shear stress for a simple shear case can be modelled with a single point of actuation. Thus, the node in the top left was programmed to move a total of 0.96m over 10 seconds. As this is strain based actuation, the forces are unknown and will be calculated by the software based on the material response. ABAQUS was allowed to determine how best to split this period into timesteps with an upper limit of 100 with the software ultimately deciding on 11 for both soil responses.

Two variations on the simple shear case were produced. First the true simple shear case in which every node had its movement in the y direction fixed as zero. This is the case that is functionally the same as the "hand" calculation. The second variation is without this constraint of y direction movement. Both the loaded edge is still rigid and unable to move in the y direction, however a more complex displacement field is produced within the middle of the model. The timesteps were chosen in the same way, with ABAQUS deciding on 21 for the "Vardanega and Bolton" response and 14 for the elastic perfectly-plastic response.

5.4.2 Rotating Wall Model

The second model that was implemented in ABAQUS is slightly more complicated. A block of soil is supported along the base and right hand side, with the left hand side rotating about a fixed point on the base. The soil is squashed by this wall rotating inwards and is forced to move upwards. This model will result in significantly more complex stress and strain fields than the simple shear case. Again, the model was implemented in ABAQUS for both of the previously defined stress-strain responses. Figure 5.5 shows the layout of this model.

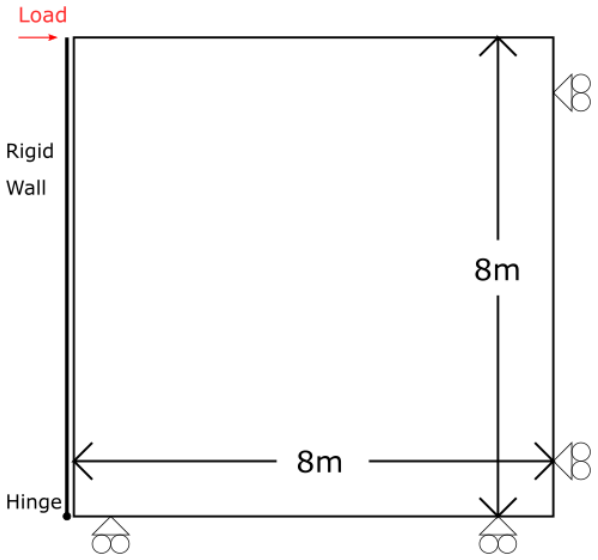

FIGURE 5.5: The geometry of the Rotating Wall model, as previously published in (Charles et al., 2018a)

Again, the mesh used 16 triangular elements to a side. Unlike the simple shear case, hybrid 6-node triangles were used in place of 3-node triangles. Although it is ultimately unimportant as the goal is not to accurately model a rotating wall, but to simply get an internally consistent dataset, it was decided that the more complex deformation pattern provided by the higher order elements would be more interesting and useful for testing the Identification Methods.

The right hand boundary, as well as the base were implemented using simple supports, with the base allowed to move horizontally and the right hand side allowed to move vertically. The wall was modelled as a beam element, in which each node was fixed relative to its neighbours. As these nodes formed the boundary of the soil, this had the side effect of modelling the wall as fully rough.

For this model, load based actuation was used. Loading was applied as a horizontal point load to the node at the very top of the rotating wall. As before, the load increases linearly from 0 to 1MN for the "Vardanega and Bolton" curve and from 0 to 750kN for the elastic perfectly-plastic curve. The loading was applied over 10 seconds with ABAQUS deciding to use 21 timesteps for the "Vardanega and Bolton" response and 11 timesteps for the elastic perfectly-plastic response.

5.4.3 Strip Footing Model

Perhaps the most complex of the three datasets generated is the strip footing. In this case, a footing is pressed into a large area of soil resulting in downwards movement under the footing, sideways movement going away from it, and upwards soil movement to the sides of the footing. This model is also representing the same mechanism that will be used in the laboratory to generate datasets from physical modelling (see Chapter 6). The mesh features 20 hybrid 6-node triangles to an edge. The model was implemented in ABAQUS and a diagram showing the geometry can be examined in Figure 5.6.

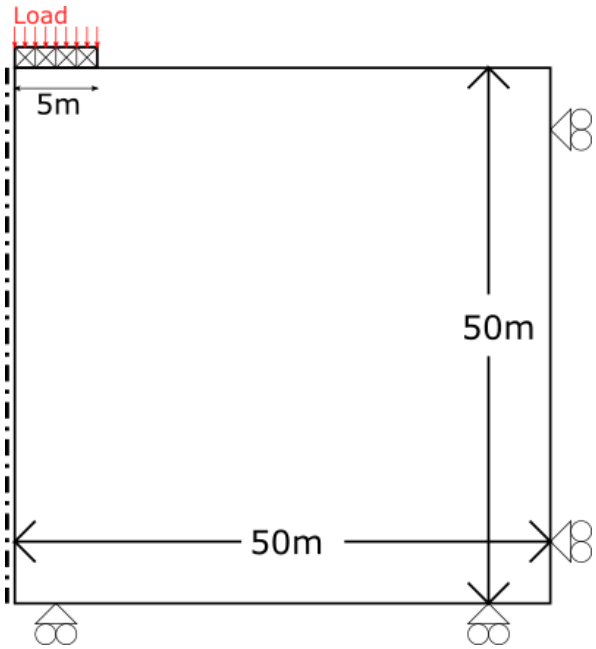

FIGURE 5.6: The geometry of the Rectangular Footing model.

The boundaries on the base and right hand side are simple supports, allowing sliding along the boundary but not past it. The left hand edge is a symmetry boundary. This prevents movement in the x direction as well as rotations around the z axis (the z axis being into the page), but allows all other relevant degrees of freedom. The nodes representing the footing are, as with the previous models, constrained to move as a single rigid object.

Loading was applied as a point load to the node directly above the mirror line. The mirror does not affect energy equilibrium as doubling the soil area via the mirror would also double the load, so for the purposes of the Identification Method process, the mirror can be ignored and the method applied to just the single half. A strain based actuation was applied to the footing node on the mirror line and displacment was increased linearly from zero, to 2m for both the "Vardanega and Bolton" soil response and the elastic perfectly-plastic response. The resultant load on this node will be calculated based on the soil rsponse. ABAQUS chose to use 30 timesteps for the "Vardanega and Bolton" response and 14 for the elastic perfectly-plastic response spread over 10 seconds.

5.5 Artificial Noise Generation

Datasets obtained during physical modelling will not be perfect. Many such sources of noise exist that will adversely affect the quality of the recorded data.

The camera image is a potential source of noise. Although measures can be taken such as ensuring good lighting will help to mitigate this, the issue is likely to persist to some degree. The PIV process will additionally have potential to introduce noise. The DIC process as discussed in Chapter 2 is used to track the movement of patches of soil by finding a new location in future images that matches best. Although the methodology is good, there is an upper degree of precision possible, and there is also the possibility for anomalous wild vectors.

To more realistically simulate datasets derived from physical modelling, the artificial datasets described in this chapter will be purposely degraded with the intention to assess the effects of noise both qualitatively and quantitatively.

This section will first describe the methodology by which noise will be applied and then discuss what effects noise is expected to have on internal energy calculations.

5.5.1 Noise Generation Methodology

Noise is random and unwanted variations in a signal, which in terms of this project ultimately means random variations to the measured displacement field. As such, to artificially

degrade the FEA datasets with noise, the recorded nodal displacements must be altered by a random value. The noise will be applied to the displacement values for each node in each timestep separately in the x and y direction.

It is necessary to give thought to how best to do this, not only to be representative to real data, but to allow for a systematic quantitative study of the effects of noise. The amount of noise added will also be varied. A trivially small addition to the dataset will likely have no effect, but if the random variations are equivalent to or greater than the actual nodal displacements, the data will likely be unusable. The signal to noise ratio will be a key factor to consider.

The meaning of randomness is also a factor of consideration. If a random addition of x axis movement between -10mm and 10mm were to be added to an arbitrarily large set of nodal displacements, a decision would have to be made as to whether the random numbers are to be distributed evenly as per a uniform distribution, or instead distributed such that most nodes are near the middle (0mm in this case) with few near ± 10mm as per a normal distribution. Figure 5.7 shows a representation of these distributions.

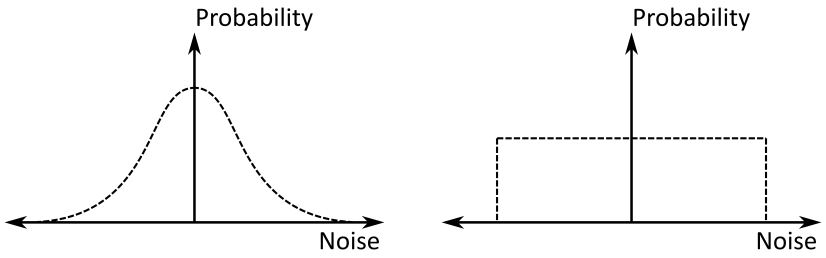

FIGURE 5.7: A diagram showing a normal distribution (left) and a uniform distribution (right).

It is most likely that normal distribution is most representative of the noise generated during physical modelling, however both distributions will be trialled.

Now that the type of noise has been examined, the point raised regarding the amount of noise can be addressed. As any noise generating function will be implemented in Matlab, the functions available for each kind of noise will determine how this is to be specified. For a uniform distribution, the "rand" function will be used, returning a random number between 0 and 1, which can be used in the equation $r = r_{lim} * 2 * (rand - 0.5)$ to give a random number between $\pm r_{lim}$.

For a normal distribution the function "normrnd" will be used. This function takes a mean value and a standard deviation value as an input. Mean will be zero, whereas standard deviation will be $\frac{1}{3} \cdot r_{lim}$. Standard deviation is a statistical term determining variance in a set of data, and for a normal distribution, 99.7% $\approx$ 100% of values are found within 3 standard deviations of the mean. Using the aforementioned Matlab functions in this way

allows for the direct comparison between the two random distributions, with noise between $\pm r_{lim}$ for each method with only the distribution changing.

The value for r_{lim} can be adjusted to vary the amount of noise added. To link this to the concept of signal to noise ratio, the mean observed change in displacement within an FEA dataset can be calculated, and a ratio of this value can be used as r_{lim}. A ratio of 0 would be no noise added, and a ratio of 1 would be a case in which the magnitude of random noise is equivalent to the actual observed displacements, however the datasets are likely to cease to be meaningful much before a ratio of 1 is reached.

5.5.2 Prediction of the Effects of Noise

With either of the two noise addition methodologies, the mean noise added to a large number of nodes would be 0. This would also be the case for noise from physical datasets, note however that this is different for systematic error which is not considered in this section in which the average error is likely to not be 0.

The mean added displacement due to noise being zero does not imply that the overall effect on the calculated internal energy will also cancel out. As per the equations regarding strain calculation from a triangular element in Chapter 3, strains can be calculated from displacements using Equation 5.2, in which the LHS contains the strain terms in the x, y, and shear directions and the RHS contains the strain-displacement matrix $[\underline{B}]$ and the displacement vector for points 1 to 3. The contents of $[\underline{B}]$ are discussed in depth in Chapter 3 and relate to the original dimensions of the undistorted triangle but are unimportant for the current discussion.

$$\epsilon = \begin{pmatrix} \epsilon_x \\ \epsilon_y \\ \gamma_{xy} \end{pmatrix} = [\underline{B}] \begin{pmatrix} u_1 \\ u_2 \\ u_3 \\ v_1 \\ v_2 \\ v_3 \end{pmatrix} \tag{5.2}$$

An important point to raise is that total strain due to actual displacement and noise displacement can be found by either summing both displacement values and calculating strain in one step, or by calculating actual strains and noise strains and summing these. Equation 5.3 shows this relationship, where ϵ_{xt}, ϵ_{xa}, and ϵ_{xn} for instance represent the total, actual, and noise values of ϵ_x

$$\epsilon_t = \begin{pmatrix} \epsilon_{xt} \\ \epsilon_{y_t} \\ \gamma_{xy_t} \end{pmatrix} = \begin{pmatrix} \epsilon_{xa} \\ \epsilon_{y_a} \\ \gamma_{xy_a} \end{pmatrix} + \begin{pmatrix} \epsilon_{xn} \\ \epsilon_{y_n} \\ \gamma_{xy_n} \end{pmatrix} = [\underline{\mathrm{B}}] \begin{pmatrix} u_{1a} \\ u_{2a} \\ u_{3a} \\ v_{1a} \\ v_{2a} \\ v_{3a} \end{pmatrix} + [\underline{\mathrm{B}}] \begin{pmatrix} u_{1n} \\ u_{2n} \\ u_{3n} \\ v_{1n} \\ v_{2n} \\ v_{3n} \end{pmatrix} = [\underline{\mathrm{B}}] \begin{pmatrix} u_{1a} + u_{1n} \\ u_{2a} + u_{2n} \\ u_{3a} + u_{3n} \\ v_{1a} + v_{1n} \\ v_{2a} + v_{2n} \\ v_{3a} + v_{3n} \end{pmatrix} \tag{5.3}$$

Equations 5.2 and 5.3 demonstrate that the noisy strain field is in fact the "actual" strain field with an extra noise field added on. The noise field can be examined separately.

As stated previously, the average displacement added due to noise is 0 in both the x and y directions. It would follow that the average values for ϵ_{xn}, ϵ_{y_n}, and γ_{xy_n} are also 0, with the distributions of these terms being the same as the distributions for the displacements.

Internal work was formulated in Chapter 3 not in terms of ϵ_x, ϵ_y, and γ_{xy} but instead in terms of ϵ_v and ϵ_s, volumetric strain and maximum shear strain. The equations for these terms, reproduced here for ease of readability are shown in Equation 5.4 and 5.5.

$$\epsilon_v = \epsilon_x + \epsilon_y \tag{5.4}$$

$$\epsilon_s = \sqrt{\left(\frac{\epsilon_x - \epsilon_y}{2}\right)^2 + \epsilon_{xy}^2} \tag{5.5}$$

Of note is that should the mean strain in the x and y direction be zero, the mean volumetric strain should also be zero. This makes intuitive sense as displacement nodes are shared by several triangles. Movement of a node may increase the size of one triangle while shrinking another, with the overall volume for the whole arrangement being relatively unchanged should there be a sufficiently high number of points. Figure 5.8 illustrates this point.

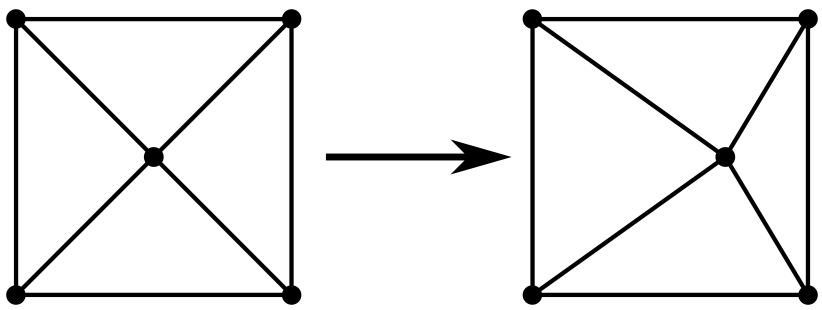

FIGURE 5.8: A diagram illustrating how the addition of noise to a displacement node could cause no overall volume change.

Although the total volumetric change due to noise is zero, the energy is not necessarily zero and will depend on which constitutive behaviour has been modelled. If, for instance, it takes more energy to compress one triangular element than is recovered by the decompression of another, there may still be a net spurious expenditure of energy due to noise with regard to volumetric strain. For this project, the simplification of ignoring volumetric strain has been taken as soil behaviour is assumed to be cohesive and undrained. Although elemental volumetric strain due to noise will be present, it is currently not particularly important. Should a different model be used for the Identification Method procedure in the future dealing with this strain may become relevant.

Maximum shear strain however is an entirely different situation. In Equation 5.5, ϵ_x, ϵ_y, and ϵ_{xy} are raised to the power of 2 before being square rooted. This means the value of maximum shear strain will always be positive. It will typically be larger should the noise be added via the uniform distribution rather than the normal distribution method as a higher percentage of noise is further from the mean of zero. Even in the case shown in Figure 5.8 in which no volumetric strain takes place, every triangular element would see additional positive shear strain due to the added noise.

Again, the effects on energy will depend on how exactly the Identification Method is modelling the soil behaviour. Elements that are being loaded, and moving along the stress-strain curve due to actual strains will move further along due to "noise" strains and elements being unloaded, should the model count this as negative energy, will move back less than they otherwise would. Noise will always result in higher maximum shear strains being observer than what is in reality happening.

As the goal of the Identification Methods developed during this project is to recover the stress-strain curve, the effect of noise on the recovered curve is an important factor to consider. The equation for work equilibrium, with terms cancelled due to assumptions about the principal angles and nil volumetric strain (see Chapter 3 for details), is reproduced as shown in Equation 5.6. External work is on the RHS which is twice the integral of the force (P) displacement (u) curve for timestep j, and Internal work is on the LHS which is the integral of the maximum shear stress (t) maximum shear strain (ϵ_s) curve for timestep j multiplied by element volume V_e and summed for all elements E.

$$\int_{u^{j-1}}^{u^j} P \, du = \sum_{e=1}^{E} \left(2 \cdot \int_{\epsilon_s^{j-1,e}}^{\epsilon_s^{j,e}} t \, d\epsilon_s \cdot V_e \right) \tag{5.6}$$

As demonstrated, for elements being loaded noise will increase measured maximum shear strain by some degree. The start and end of the stress-strain integral in Equation 5.6 will be increased. Although the exact stress-strain curve shape, and random chance must be taken

into account, this will typically increase the area under the curve for any curve where stress increases with strain. A sketch showing how such a movement would increase the area under the curve for a timestep is shown in Figure 5.9.

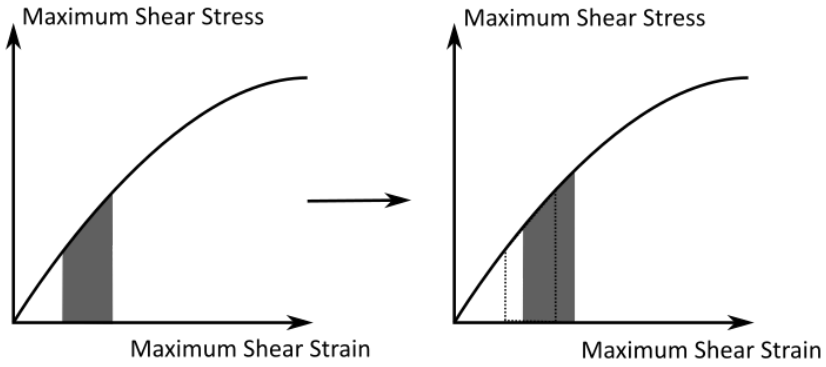

FIGURE 5.9: A diagram illustrating how the addition of noise could increase the area found by integrating the stress-strain curve.

As internal work for a timestep is the area under the curve summed for each element, such a change due to noise would result in an increase in internal work. As energy equilibrium is enforced, and external work is unaffected by this manner of noise, internal work must also not change. As maximum shear strain is increasing, shear stress must decrease. The addition of noise will cause the curve, and ultimately its c_u value to be lower in order for the Identification Method to enforce energy equilibrium.

It would also follow that the higher amounts of noise added to the displacement field will result in greater reductions of c_u and the height of the stress-strain curve. Experimentation with the FEA derived artificial datasets described in this chapter will be used to determine the validity of this statement. Understanding the effects of noise will also be of use with diagnosing any issues with real physical modelling derived datasets.

5.6 Conclusion

This chapter has demonstrated the methodology by which a range of FEA models have been used to generate artificial datasets with which the proposed Identification Methods can be tested and validated. Additionally, a methodology by which noise can be added to artificially degrade these datasets to better resemble real data has been developed, with thought given to allowing for systematic application and measurement of this phenomenon.

Finally, an informal proof has been given that increasing the amount of noise in a dataset will lower the recovered stress-strain response. Testing this hypothesis will take place in Chapters 7 and 8.

Chapter 6

Physical Modelling Data Set Generation

6.1 Introduction

To validate the Identification Methods specified in Chapter 4 in a realistic manner, it is necessary to obtain high quality physical model test data through laboratory experimentation.

Whereas perfect FEA derived data will, by definition, be perfect, physical model data will suffer from noise, friction, calibration issues, and numerous other factors that would not be apparent in artificial data.

It would follow that the physical modelling test data that would produce the best results using the Identification Methods would be as close to perfect as possible, however the methods ability to cope with less than perfect data is something worth assessing. A method that only works with extremely high quality data is still of value, but of less value than a method able to robustly deal with noise etc.

As such, the laboratory schemes presented in this chapter will aim for high quality data based on the best practices within the field for obtaining PIV data from physical modelling. I.e. every piece of equipment and method will be commonly used for physical modelling with no special alterations to facilitate the Identification Methods.

The end goal of such an approach is that researchers would be able to implement an Identification Method as an additional stage in arbitrary physical testing with little to no change to the approach they would otherwise take.

To acquire the required datasets, a number of plane strain footing tests will be carried out at 1g, with digital cameras in place for PIV data acquisition. The Identification Methods will be used to recover a stress-strain response, which will be compared to soil properties obtained through a series of more traditional element tests.

The purpose of the laboratory testing can be summarised as follows:

1. Obtain high quality PIV data from 1g plane strain footing tests on fine-grained soil, loaded at a constant rate of strain at an undrained loading rate.
2. Determine the material properties, undrained shear strength and stiffness, and the stress-strain curve such that they may be compared with the software output.

The rest of this chapter will describe in detail the equipment and methodologies required to achieve these aims.

6.2 Equipment

The following sections provide a detailed description of all the equipment used, along with commentary of the decisions made, benefits and drawbacks, and necessary compromises. Where appropriate, calibration data will be provided, and images of apparatus will be given.

6.2.1 Box

The testing box consists of a modular aluminium frame of dimension 600 by 400 by 200mm. The box is attached to a baseplate allowing for movement by forklift and is rated for centrifuge testing, although current testing will be limited to 1g.

The modularity of the frame allows for the larger 600 by 400mm faces to be replaced depending on current usage. During consolidation, these faces will be aluminium, whereas during testing they will be perspex windows to allow for acquisition of imaging data from both sides of the box.

The windows will be manufactured out of perspex of approximate thickness 55mm, with additional sacrificial targeting windows of 3mm thick. Sacrificial windows will allow for the addition of target calibration markers without causing damage to the larger and more expensive structural windows.

The box features integrated draining channels and outlets to allow flow during consolidation. To further enhance the box during consolidation, an aluminium extension can be securely fastened to the top of the box to allow for an additional 200mm in height. A top plate used during consolidation with further drainage channels is also available.

The horizontal size of the box allows for two tests to be run side by side, with each being given half the area. This allows for twice as many datasets to be produced per consolidation

than if only one central test were carried out, as well as allowing identification of any natural variation across the specimen.

The base plate on which the box is mounted features numerous additional mounting points to allow other equipment such as cameras and lighting to be securely fastened.

6.2.2 Targeting Windows

As mentioned in the previous section, the box is designed to accommodate non-structural sacrificial targeting windows. The purpose of PIV targets is twofold:

1. Allow for conversion between pixel and world displacements by means of knowing the world distance between fixed points within the image.
2. Filter global errors from displacement, i.e. if all targets are measured to displace by a uniform amount, it is likely due to camera movement and can be subtracted from soil displacement. Target points are assumed to be fixed.

Some thought was given to the arrangement of the target array. Many examples from literature have used a uniform grid of target points, however points in the way of "interesting" parts of the soil will result in a loss of data. In cases of purely qualitative analysis, this is no problem, however for this project the data is needed for further processing. As such, the target points were arranged in a double layered square around the edge of the area of interest. Although somewhat arbitrary, the layout was chosen to ensure there were plenty of points without obstructing the area adjacent to the footing. The number of points, 88 per footing, is high, but it is better to have too many than not enough. In the event the large number of control points causes issues, e.g. slows computational times, it is possible to discount some of them and use a smaller subset for calibration and analysis.

The target window was laser etched with location markings upon which targeting stickers were stuck. The stickers were purchased from a 3D imaging supplier and featured a white circle within a black ring of diameter 4mm. The stickers were slightly asymmetrical (in that the circles were not centered on the sticker center) and very hard to place perfectly by hand. Fortunately, it is possible to calculate their exact locations using photogrammetry; this will be discussed in later sections.

A total of four target arrays were prepared across two targeting windows. As mentioned previously, images will be taken from both sides of the box, with space for two side by side tests.

6.2.3 Consolidation Rig

Soil will be consolidated within a large hydraulic press. The equipment, custom built for the laboratory in which testing takes place provides sufficient force to prepare the samples needed for this series of tests (Hakhamaneshi et al., 2016).

Control of the applied force is manual, with a lever to move the press up and down, and a dial to control the force. This process is somewhat difficult due to the only feedback being from the load cell, so it is important to alter loading slowly and conservatively, particularly for the earlier stages.

6.2.4 Loading Rig

Loading will be applied using a 1g 3 axis robot. The robot is a bespoke piece of equipment already available prior to starting this project. Primarily used for automated sand pluviation, the robot features linear actuators in 3 dimensions and hydraulic loading. It is fully digitally controllable via LabView programming and has ample space for the large sample boxes used with sufficient clearance for all imaging apparatus.

Although the loading capacity of the robot exceeds the required amounts, the robot is not bolted to the floor. The upper limit of soil strength able to be tested is therefore the weight of the robotic actuator. Although this weight is not known to the author, it is sufficiently high that it should be inconsequential.

A shroud was constructed around the robotic actuator in order to allow precise lighting control. The laboratory in which the testing will take place has many large windows and high ceilings. Not only would natural lighting cause reflections in the sample box windows, but would be highly inconsistent depending on the time of day and the weather outside. By blocking natural lighting with the shroud, made of black plastic sheeting, the sample will be illuminated only by artificial LED lighting.

One factor of importance is the speed at which loading is applied. The robotic actuator allows it's operator to specify an actuation speed. The choice of actuation speed should be chosen to ensure undrained conditions are achieved. Randolph (2004), proposed the following equation to determine the soils drainage status using a dimensionless velocity value:

$$V = \frac{v_f \cdot D}{c_v} \tag{6.1}$$

In which V is the dimensionless velocity value, v_f is the actual displacement value, D is the diameter, and c_v is the coefficient of consolidation. It should be noted that diameter D was designed for use with circular objects penetrating soil. For the footings used in this laboratory experiment, width will be used in place of diameter.

The dimensionless velocity value V required for drained or undrained behavior has been experimentally derived by multiple authors. Lehane et al. (2008) found drained conditions for $V \leq 0.01$ and undrained conditions for $V \geq 10$. House et al. (2001) quotes several values from literature: drained at $V < 0.01$ with undrained at $V > 30$, and drained at $V < 0.2$ and undrained at $V > 20$. Stanier (2011) used values of $V < 0.01$ and $V > 20$ for drained and undrained conditions respectively to ensure undrained behavior of helical pile tests.

The range of dimensionless velocities that could mean undrained conditions vary by a reasonable amount, literature indicates that the value may be specific not only to the soil in question but also the exact test carried out. It would be a significant undertaking to empirically find the V resulting in undrained conditions for rectangular footing tests on clay, so the best way to ensure undrained conditions is to take a value, and ensure it is exceeded by a reasonable safety margin.

As actuation velocity is otherwise arbitrary, values would ideally taken such that there is no danger of drained conditions even with the most conservative estimates of the required V. This however must be balanced with the desire to obtain high quality imaging data. Slower footing displacements will give more camera frames per unit of movement. Based on the values from literature, it was therefore decided that V must exceed 20. As there are two footings of different sizes, differing drive speeds could be chosen for each, however for simplicity a single drive speed will be selected that meets the requirement for both footings.

6.2.5 Footings

Two footings have been manufactured from 20mm thick aluminium. Each will have a length of 200mm, equivalent to the full depth of the box to simulate plane strain. The first footing will have a width of 20mm and the second footing will be of width 40mm. These widths correspond to areas of 4000mm^2 and 8000mm^2 respectively. Care will have to be taken to ensure the actuator loading, footing areas, and soil strength are suitably matched.

The relatively small widths of the footings ensure there is ample room within the box such that edge effects can be minimised, even if multiple tests are run on the same soil sample.

Each footing features an $M10$ threaded connection at the centre point to allow attachment to loading apparatus. Two additional $M5$ threaded connectors were milled at the ends of the footings to provide utility in case additional equipment is to be added in future testing.

The edges that will contact the perspex window were trimmed immediately prior to testing to allow the footings to fit, as a very small tolerance was specified. Additionally, rubber "wipers" were added to the edges to minimise the chances of soil moving between the footings and the wall. A photograph of the two footings can be examined in Figure 6.1.

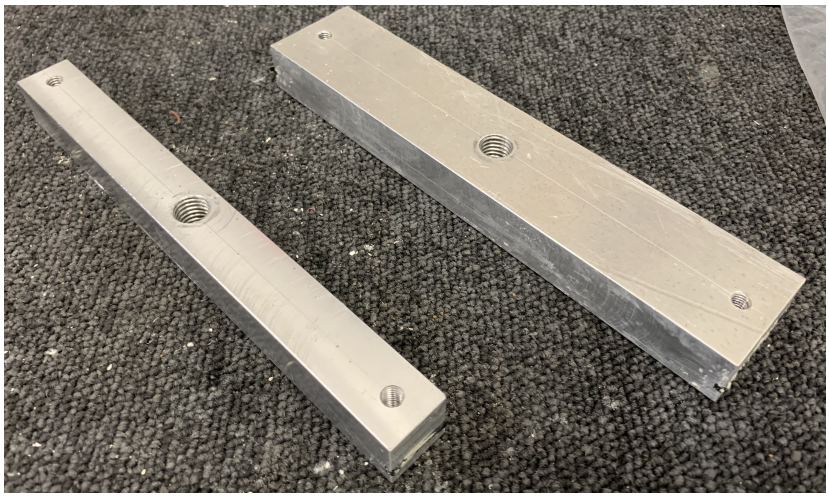

FIGURE 6.1: The two footings that will be used during testing.

6.2.6 Measurement Devices

A number of measurement devices were used throughout both the consolidation and testing phases. This section will summarise the equipment used.

During consolidation the following devices were used:

- 25 ton load cell. This load cell was chosen based on availability of equipment. Its capacity far exceeds what is necessary for consolidation, with loading unlikely to reach 10-20% of the maximum measurable amount. This is unfortunate as signal noise will be significantly higher than what would be observed with a more suitably specced device. As it is used for consolidation, a process taking place over a timescale in the order of a week, this should have little effect in later stages as the noise will be small compared to the applied load, however for earlier stages, extra care must be taken to not apply excessive loading and squeeze the soil slurry out of the box. Calibration data for the load cell can be examined in Figure 6.2.
- A draw string LVDT will be used to measure consolidation displacement. This choice is standard and has but a few points of discussion to mention. The LVDT was securely clamped to the consolidation rig with the end of the draw string screwed to the consolidation plate within the soil box. It is important to ensure there is enough capacity as it would be disastrous for the length of the draw string to be exceeded. Calibration

was carried out by extending the draw string to a known amount against a metre rule and recording the output voltage. Accuracy is limited as a metre ruler cannot accurately measure less than a millimetre, however due to the long draw length, significant number of readings, and the accuracy of the consolidation displacement data not being particularly important (to the nearest millimetre is fine), the method was deemed sufficient. Figure 6.3 shows the graph of the calibration data recorded for the draw string LVDT

Additionally, during the consolidation phase, manual readings of displacement are to be taken several times a day with a tape measure. Although significantly less useful than data recorded on the order of seconds, this serves as a backup incase the PC recording the consolidation data were to suffer from a crash or data corruption. This measure is particularly prudent to take as the consolidation process will take in excess of one week.

During testing the following devices were used:

- A 2kN in-line load cell will be used used to measure force between the actuator and the footing. The capacity of the loacell is ideal for the footing sizes and desired soil strengths, with enough headroom that it should be reused should further testing with stronger soil or larger footings be required. The threading on the load cell is M10 which matches the specified threading in the centre of the footings and the actuator, allowing for easy assembly. The load cell was calibrated using a Budenberg hydraulic dead weight tester. In this apparatus, a known set of metal disc weights is suspended by hydraulic pressure which is equally applied to the load cell, with voltage then recorded. It should be mentioned that this methodology doesn't allow for the recording of calibration data while the load cell is in tension. Although tension is likely of little importance during testing (the exception being during pullout of the footing from the ground), the assumption that tension voltages follow the same trendline as compression will have to be made. A photograph of the Bundenburg hydraulic dead weight tester can be seen in Figure 6.4. The recorded calibration data for the 2kN load cell can be seen plotted in Figure 6.5.

- Three LVDT sensors are to be used to record displacements. Two will be mounted to an extruded aluminium frame above the footing to record displacement at each end, allowing for the identification of differential displacement. The third LVDT will be attached directly to the actuator. Although the actuator robots movement will be specified, this LVDT will serve to record the actual movement, which may or may not be equal to the input value. Each LVDT will have a range of over 20mm. It may be necessary to reposition them in between testing such that there is enough stroke for each test. The LVDT measuring actuation for instance, will not be able to be put in place until the actuator is in position at the top of the soil. Calibration for the LVDTs

was carried out using a micrometer screw gauge. The LVDT is securely fastened in a jig such that turning the screw gauge will depress the sensor. A digital dial is used to record true displacements accurate to a hundredth of a millimetre, with output voltage from the LVDT also recorded. Although identical models, each of the three LVDTs will be calibrated separately, as they are almost certain to require different calibration values. A photograph of an LVDT within the micrometer screw gauge can be seen in Figure 6.6. Plots of the calibration data for the three LVDTs (labelled LVDT 0, LVDT 1, and LVDT 2) can be seen in Figures 6.7, 6.8, and 6.9.

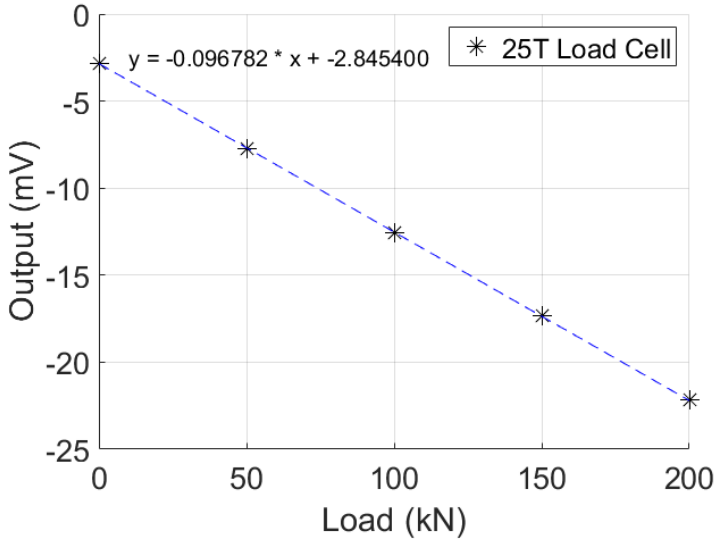

FIGURE 6.2: Calibration data for the large 25 ton load cell.

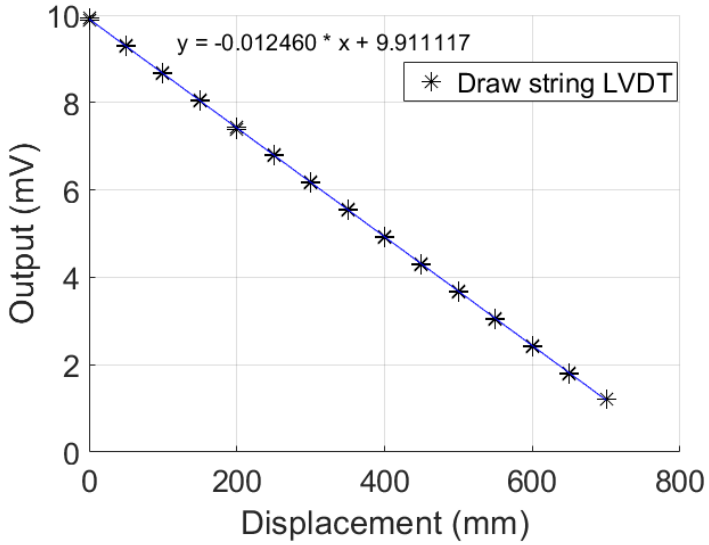

FIGURE 6.3: Calibration data for the draw string LVDT.

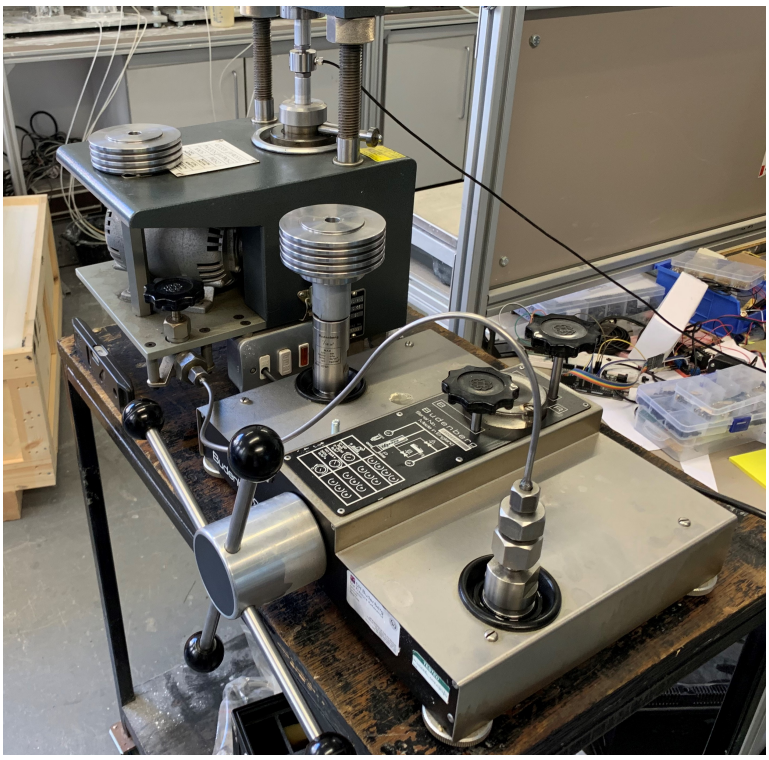

FIGURE 6.4: Bundenberg hydraulic dead weight tester. The weight discs can be seen in the centre of the image.

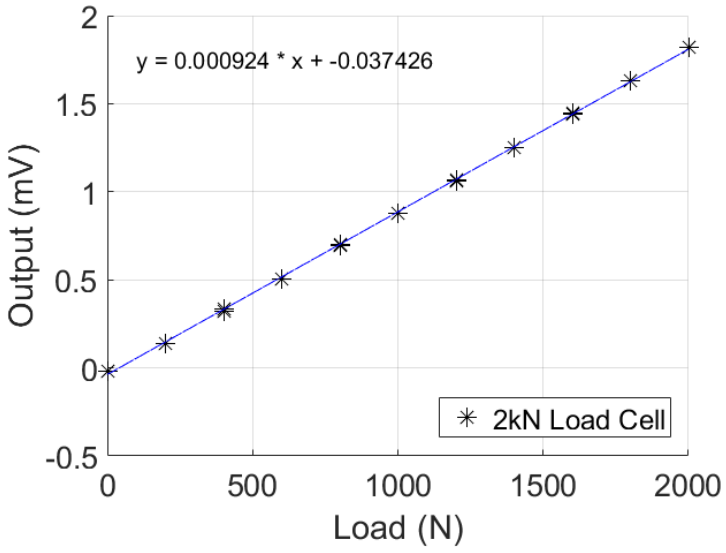

FIGURE 6.5: Calibration data for the 2kN load cell.

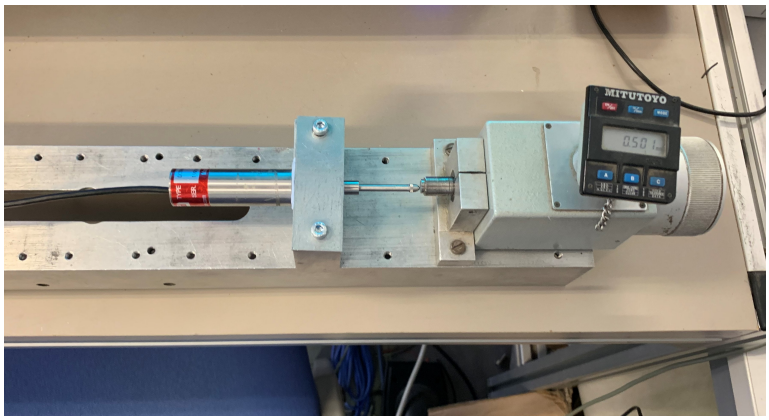

FIGURE 6.6: The micrometer screw gauge used to accurately measure displacement during LVDT calibration.

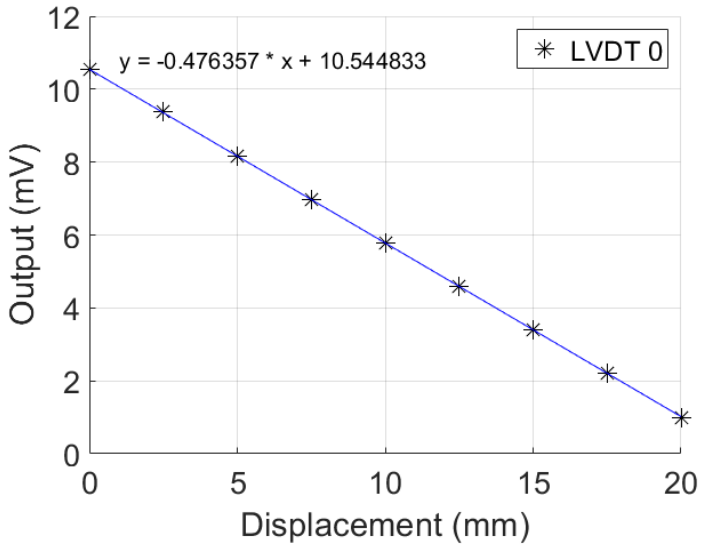

FIGURE 6.7: Calibration data for LVDT 0.

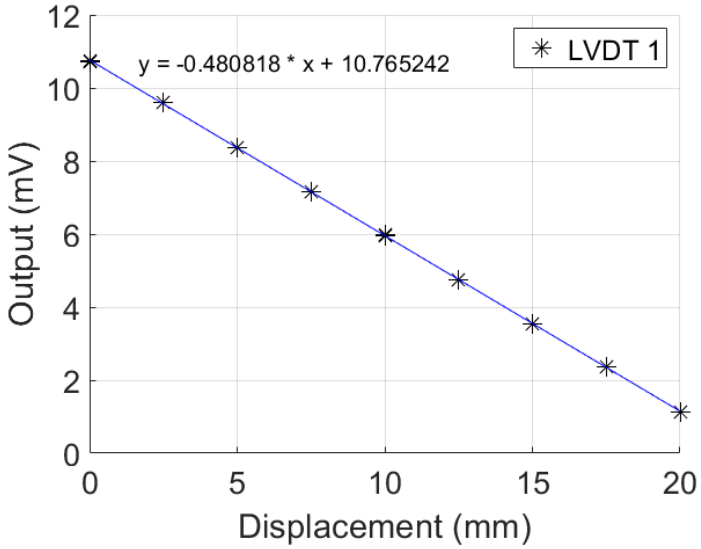

FIGURE 6.8: Calibration data for LVDT 1.

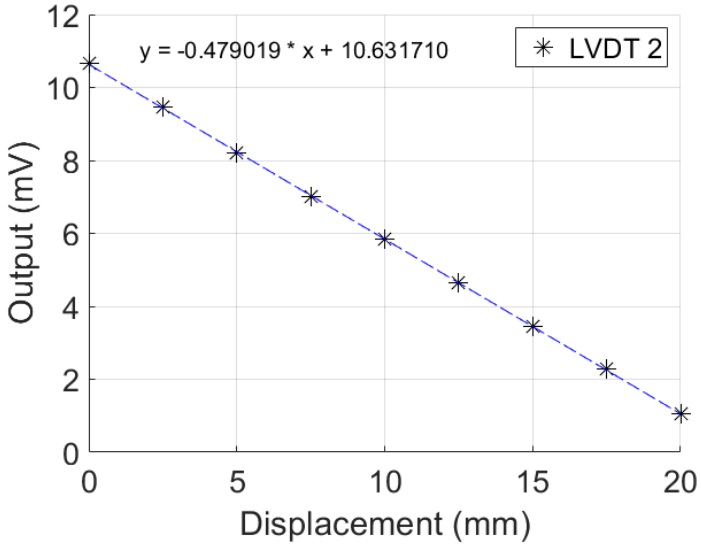

FIGURE 6.9: Calibration data for LVDT 2.

6.2.7 Camera and Lighting Setup

Two industrial cameras will be used simultaneously to image each side of the box. The chosen camera system is the Basler Pilot piA2400-17gc. Table 6.1 provides an abridged summary of the camera specifications as provided in the marketing material. The data is taken from the website of a distributor (SodaVision, 2018):

Resolution (H x V pixels)	2454 px x 2056 px
Pixel Size horizontal/vertical	3.45 μm x 3.45 μm
Frame Rate	17 fps
Interface	GigE
Sensor Vendor	Sony
Sensor	ICX625
Sensor Type	CCD
Sensor Size (mm)	8.47mm x 7.10mm
Max. Image Circle	2/3 inch
Lens Mount	C-mount

TABLE 6.1: Camera specifications for Basler piA2400-17gc

The camera was selected from those available within the laboratory stores due to its high resolution and frame rate. Another advantageous feature is the GigE ethernet connection allowing the camera to be easily linked with a computer, either directly or in the case of a multi camera setup, via a network switch or router.

The C-mount lens mount allows for any compatible lens to be used regardless of lens manufacturer.

The lens chosen was the Ricoh FL-CC0614A-2M. Table 6.2 provides an abridged summary of the lens specifications as provided in the marketing material. The data is taken from the website of the manufacturer (Ricoh, 2018):

Format size	2/3 inch format
Focal length	6mm
Maximum aperture ratio	1:1.4
Iris range	1.4-16
Lens Mount	C-mount
Horizontal angle of view (2/3 inch format)	71.2 °

TABLE 6.2: Lens specifications for Ricoh FL-CC0614A-2M

The chosen lens has a fixed focal length and rings to adjust the focus and iris. The adjustment rings features screws to securely lock the settings in place, this is particularly useful the ensuring all photos taken will be uniform.

The camera and lens setup will be fixed to an extruded aluminium frame that in turn is fastened to the baseplate. This allows for the camera location and rotation to be fixed throughout testing as changes would be adverse to the collection of high quality PIV data. Some small movements due to vibration are still possible but should be minimised.

The camera frames will allow for the cameras to be moved in the horizontal direction. As the box has room for two tests to be performed side by side, the camera position will be adjusted between tests such that the second test can be carried out.

Lighting will be provided by two LED lighting panels powered wired into a variable voltage power supply. Limitations in available equipment means only one light will be used on each side of the sample, two would have been better, but this will be mitigated by use of a reflective surface to increase uniformity of lighting. As the tests are carried out at 1g, no structural assembly is needed to secure the lighting. The exact locations, along with power setting will be determined by trial and error prior to the test beginning. Figure 6.10 shows a photograph of one of the identical pairs of cameras that will be used to collect image data.

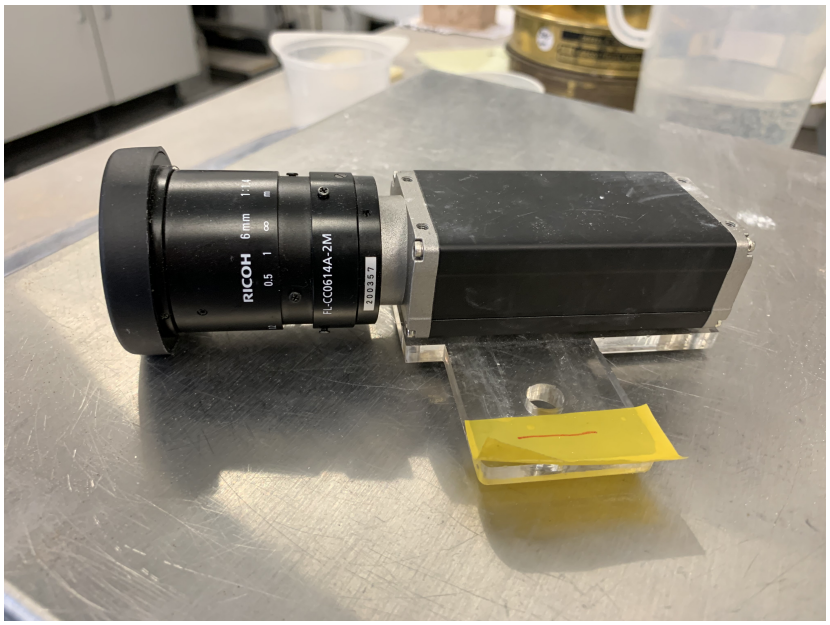

FIGURE 6.10: One of the cameras used during testing.

Testing the camera setup indicates that when both cameras are taking photos simultaneously a frame rate of approximately 1 FPS is achievable.

6.2.8 Computing and Networking equipment

The computer used for data acquisition was a Dell manufactured desktop featuring an Intel i7-3770 processor, 8gb of ram, a gigabit ethernet port, and two 1tb mechanical hard disk

drives in a RAID 1 array.

The exact specifications are not important in terms of experimental method and/or repeatability but a few factors stand out as worth mentioning. Firstly, a significant amount of image data will be produced at a fairly fast rate. A processor and hard drive with the speed to keep up is essential. A solid state drive would have been desirable to allow for faster data read and write but was not present in the system controlling the actuator. The gigabit network port is also essential to allow for the camera data to be obtained. In an ideal world the computer would have multiple ports, as the data stream from a single camera could saturate a gigabit link, and two cameras are to be used. The frame rate will therefore be lower than it could have been but is still acceptable.

It was decided that due to the large number of ethernet devices being used a local network would be created rather than use the university campus wide network. This allowed for full admin level access to the network devices that otherwise would not have been available. A cheap TP-link router was used along with an 8 port gigabit unmanaged switch produced by Netgear.

6.2.9 Data Acquisition

Data from the sensors was acquired using National Instruments data acquisition equipment.

A NI cDAQ-9188XT chassis was used, featuring hot swappable slots for up to 8 I/O modules and an Ethernet port allowing for communication with the control computer via an IP network.

Several I/O modules were used. For load cells, both during consolidation and testing, a NI-9205 C Series Voltage Input Module was used. This module allows for measurements between ± 10 V. It features a D-sub socket allowing pre wired sensors to be swapped out. The module has an aggregate sample rate of 250000 samples per second.

LVDT output was measured using the NI-9237 C Series Strain/Bridge Input Module. This device measures between ± 25 mV. The module has four channels and such the three LVDTs were wired to the D-sub socket. The sample rate is 50000 samples per second for each channel.

6.2.10 Control Software

LabView was used to manage both the consolidation and main test procedure.

During consolidation displacement and loading were recorded and plot in real time in calibrated units so it was clear what was going on. As the consolidation rig required manual control this was the only feedback available to determine the correct loading amount.

Testing required two instances of LabView to run simultaneously. The first was the pre-existing control panel for the three axis robot used for actuation. Relative or absolute movement could be specified with a given velocity, and manual movement was also possible. A nudge function allowing movement of a single millimetre was used for final alignment. The second LabView instance recorded sensor data and controlled the cameras. This LabView was ran for around a minute prior to commencing actuation to ensure no data is lost (i.e. from attempting a simultaneous start) and also to allow for a baseline dataset with no expected movement.

6.3 Sample Preparation

Clay powder was mixed at a one to one ratio with water by mass. Imerys Speswhite was the brand and product chosen, which the manufacturer, Imerys (2018), describes as "... a highly refined kaolin of ultrafine particle size and high brightness from deposits in the South West of England." The resulting slurry required further processing as detailed below to ensure it is both representative and usable for PIV.

6.3.1 Consolidation

As specified, the soil used initially consists of powder mixed with water. In order to build a representative model, this slurry must be consolidated. In this process an increasing distributed load is applied to the slurry within the sample box.

The sample box and the top plate used for consolidation feature drainage holes and tubing to allow water to escape. Permeable Vyon filters are placed at the base of the sample box and on top of the soil to minimise the amount of kaolin that will escape. The ends of the tubes are submerged in a bucket of water to prevent air getting into the sample.

The consolidation press is used along with a large load cell and draw string LVDT. These pieces of equipment have been described in previous sections.

After filling the box with soil slurry and assembling the top plate, the sample is left for 24h to consolidate under its own self weight. The following day, a small load is applied which will be doubled every 24 hours until the desired consolidation pressure is reached. After this final pressure is achieved, the sample will be unloaded and allowed to rest for 24 hours. In this phase the sample will reabsorb water so it is important to ensure the drainage tubes are

submerged. Next, the metal walls of the sample box can be removed, the sample trimmed and flocced (see following section), and the perspex windows put in place. A final 24 hours of consolidation at the peak pressure will now be undertaken, after which the specimen is ready for testing.

Variations on such a schedule are acceptable (i.e. timing to ensure testing takes place on a certain day), provided the sample is not allowed to dry out. Additional time under the press should cause negligible further displacement, whereas a prepared sample will dry out if left long enough. A final consolidation pressure of $200kPa$ was used for all specimens. The consolidation scheme is given in Table 6.3.

Day	**Consolidation Pressure**
0	Self Weight
1	6kPa
2	12kPa
3	25kPa
4	50kPa
5	100kPa
6	200kPa
7	Unload
8	Trim, Flock, then 200kPa
9	Test

TABLE 6.3: A table showing the sheme by which specimens were consolidated.

6.3.2 Floc

After trimming the specimen, floc was applied to provide texture that the PIV process is able to identify or track. Floc most resembles the artificial grass powder that is commonly used with model railways, indeed this or any similar substance would function adequately.

The exact floc used was 07206 Flock, dark green, manufactured by Noch.

To apply floc to the specimen, the aluminium side plates used during consolidation must be removed from the box. Unfortunately as specimen could be only be tilted sideways to around 30°sprinkling floc roughly uniformly more challenging, particularly if the centrifuge in the laboratory was in use as there would be a substantial breeze. Floccing was achieved by lightly sprinkling floc whilst gently fanning it onto the angled soil surface where much will stick to the damp clay. This will be carried out on both sides of the specimen.

After floccing, the targeting windows and structural windows will be bolted in place. Another round of consolidation will be carried out to ensure uniformity along the freshly prepared top and sides of the specimen.

A photograph of the flocced sample can be seen in Figure 6.11

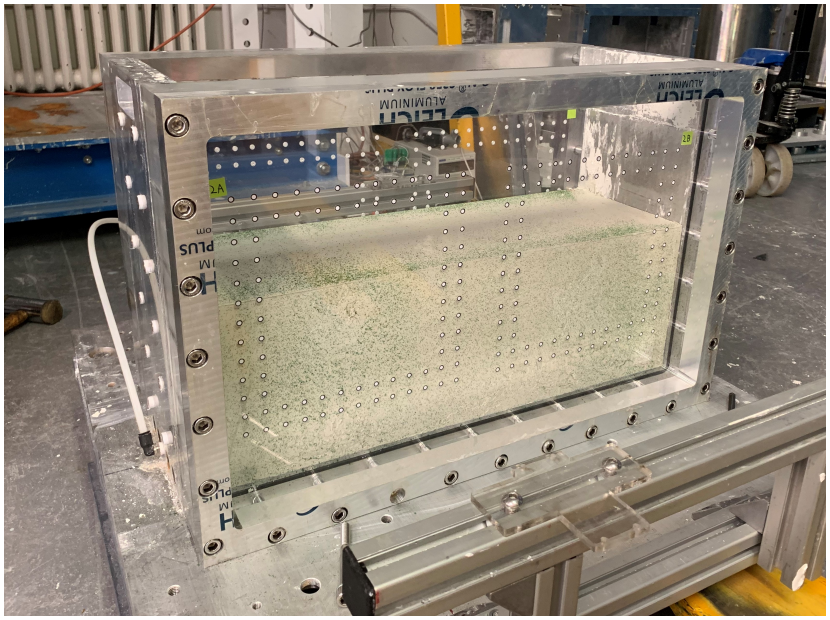

FIGURE 6.11: A soil sample after floccing with perspex windows in place.

6.4 Main Test Procedure

Testing will be carried out using the equipment and techniques described in this chapter. This section will assume the equipment had been assembled and is filled with a prepared soil specimen. The main test procedure is as follows:

1. Move box of consolidated soil into place within the actuation rig using a manual forklift. Placement should be square to the rig as much as possible. Spacing washers or similar miscellanea can be used to level the soil box along with a spirit level.
2. Attach the required footing via a load cell to the actuation rig. Put LVDTs in place at either end of the footing, and an additional one to measure displacement of the actuation rig.
3. Use LabView controls to move footing into place at the top of the box above the location of the first footing site.
4. Measure friction between the footing and window by recording force and displacement as the footing is moved into contact with the soil.
5. For the final approach and touchdown, images should be recorded incase of accidental soil displacement. The goal of the touchdown stage is to have the footing flat and fully

in contact with the soil. The load should stop either when the footing is visually in contact or immediately when a non-negligible load is recorded.

6. With the shroud closed, and all cameras and sensors recording, wait for approximately one minute of no movement such that there is data to use as a reference point, then instruct the actuation rig to displace the footing by the desired amount into the soil. It is important for the operator and any bystanders to not move near the experiment in order to avoid vibrations travelling though the floor and causing camera movement. Although this is likely to only be a minor effect, better safe than sorry.
7. Pullout data can similarly be recorded. Although there are no planned uses at this time, this data could potentially allow for a more complete picture should future work be carried out. Repeat step 6 with the actuator set to move the footing upwards and out of the soil. The load cell may record negative load due to suction forces.
8. Use LabView to move the actuator into place above the location for the second footing test. If necessary, replace the attached footing with the footing required for the second test.
9. Repeat steps 4 to 7 for the second footing test.
10. Carry out supplementary tests, or alternatively wrap the soil in clingfilm in order to preserve it for supplementary testing at a later date. Shear vane testing can be performed immediately, whereas supplementary tests requiring cores or samples to be taken can wait a small number of days provided the soil is suitably preserved.
11. After all testing is complete and samples taken, the soil box can be disassembled and cleaned, the soil removed, before being reassembled for future testing.

6.5 Particle Imaging Velocimetry

Particle Imaging Velocimetry (PIV) is the process by the movement of patches of soil can be identified via Digital Image Correlation (DIC). The history and workings of such a method are described in the literature review (Chapter 2), along with a detailed guide to the mathematics behind photogrammetry. This section will therefore not re-tread ground already covered and instead focus on how PIV and photogrammetry are utilised in the generation of physical model dataset generation.

6.5.1 GeoPIV-RG

GeoPIV-RG (Stanier et al., 2015) is the most commonly used PIV implementation used in the geotechnical physical modelling community, and was selected for use in this project for the reasons described in Chapter 2. As stated, it allows for tracking of soil patches and automated identification and tracking of control points.

A number of considerations for how the software is used exist, mostly relating to exactly how much (and how detailed) the dataset should be. The size and spacing of the patches are the primary settings. Larger patches should provide more accurate displacement data at the cost of lower resolution. Spacing allows for patches to overlap each other, or to have gaps between. For qualitative PIV analysis these decisions are less important as nearly any setup will allow a researcher to plot displacement vectors over images of the soil, however for quantitative analysis choices regarding patch size and spacing could have a large effect.

It is unclear exactly what patch density would allow for the best results when the data is used for an Identification Method process. A sparser density would be less computationally expensive but could potentially miss finer distortions. A range of possible values will be used (more discussion on this topic will be presented in Chapter 8).

PIV is a non-destructive process. It doesn't affect the sample being photographed, and once the photos exist they can be copied an infinite number of times. A single test can be analysed via PIV as many times as necessary and any number of combinations for settings can be examined.

6.5.2 Photogrammetry

Photogrammetry is the process by which image space coordinates can be converted to object space coordinates. In PIV this consists of converting the pixel coordinate displacement field output from the PIV process into a world unit displacement field. As stated in Chapter 2 the built in functions or GeoPIV-RG are insufficient for the goal for the exact use case in this project and as such a bespoke methodology utilising the Matlab Computer Vision toolbox (MathWorks, 2017) was developed.

Many parts of the photogrammetry process are trivial with pre-existing software. The camera parameters (intrinsic, extrinsic, radial distortion, and tangential distortion) can be recovered through the camera calibration app provided in the Matlab toolbox. Lens distortion can be removed with a single function. However, there are a number of challenges to overcome in order to carry out the photogrammetry process for the particular setup:

1. Identify both object space and image space control point coordinates.

2. Deal with different levels of refraction for control points and patch data.
3. Find the exact position of each camera for every frame.
4. Recover world patch locations when control points are not coplanar with patch data.

The first point raised refers to the necessity of knowing both image and object space coordinates for a set of control points. Image space coordinates are obtained through the GeoPIV-RG centroiding process however object space coordinates require discussion. Laser cut markings were etched into the sacrificial targeting windows, and the control points are small stickers affixed at these locations. It would be possible to use the known locations of the etchings, however the stickers had slight asymmetry and although care was taken to accurately place them, this was done by hand so some inaccuracy is to be expected.

The exact world coordinates for the points can be found using the following process. The targeting window should be placed flat with a chessboard pattern generated by the aforementioned Matlab library printed and placed coplanar with the control points. The camera pose (provided the intrinsic and lens parameters are already known) can be found from a single image with a set of known points (the chessboard pattern in this case). With the camera pose (also called the extrinsic parameters) known, the Matlab "pointsToWorld" function can be used to find the exact world coordinates for each control point sticker.

The second point raised is relevant due to the control points having only the depth of the thick structural window between themselves and the camera, whereas soil patches additionally have the thickness of the sacrificial targeting window. This factor is the primary reason the built in GeoPIV-RG calibration function was unsuitable for use.

This can be dealt with relatively easily. Each control points image space coordinate can be corrected for a single layer of refraction and the patches can be corrected with two layers. The equations to carry this out, based on the work by White (2002) are shown and discussed in the literature review.

The third consideration, finding the exact location of the camera for each image, is a necessary but straightforward process. The Matlab computer image toolbox allows for camera pose to be found for a single image with a set of known points provided the other parameters are already known. Both of these requirements are met. The control points will be used to estimate pose. Although the camera assembly will seek to minimise camera movement, this cannot be guaranteed. Knowing the pose for each individual frame allows for error caused by relative camera movement to be trivially removed.

The final consideration raised refers to the complication of the control points not being coplanar to the soil patches. As the control points were used to find the camera pose for

each image, simply using the "pointsToWorld" function would not work as it assumes coplanarity. The extrinsic parameters must therefore be manually adjusted by the thickness of the sacrificial targeting window. Although the difference is likely to be small, this will prevent any distance related scaling affecting the results.

With these key difficulties solved the entire photogrammetry process will be summarised in the following enumeration:

1. Use the Matlab Computer Vision toolbox (MathWorks, 2017) camera calibration app to recover the parameters that do not change between images (intrinsic, and lens distortion parameters).
2. Recover the true world locations of the control points, should the estimated values be deemed insufficiently accurate.
3. Carry out laboratory testing and obtain PIV data. See rest of this chapter for details!
4. Remove lens distortion from the PIV patch and control point image space locations.
5. Remove refraction errors from data. One layer for control points and two layers for patch data.
6. Find extrinsic (also called camera pose) parameters for every frame.
7. Recover object space coordinates using recovered parameters, camera pose, and corrected image space data.
8. Perform sanity check on output values (i.e. do found coordinates match well with known values such as footing width).

6.5.3 Camera Parameters

The Matlab Computer Vision toolbox (MathWorks, 2017) camera calibration app was used to recover the intrinsic and lens parameters for each of the two cameras. Many photographs were taken of a chessboard pattern at varying distances and angles to provide a set of data that the camera calibration app could use to find the optimal camera parameters. Figure 6.12 shows a screenshot in which the camera calibration app correctly identifies the vertices of the chessboard.

The images were taken with no perspex in between the camera and the chessboard. On the given image, the chessboard is on top of the sacrificial target window such that it is in the same plane as the target dots. This would allow for photogrammetric principles to be used to find the locations of the targets.

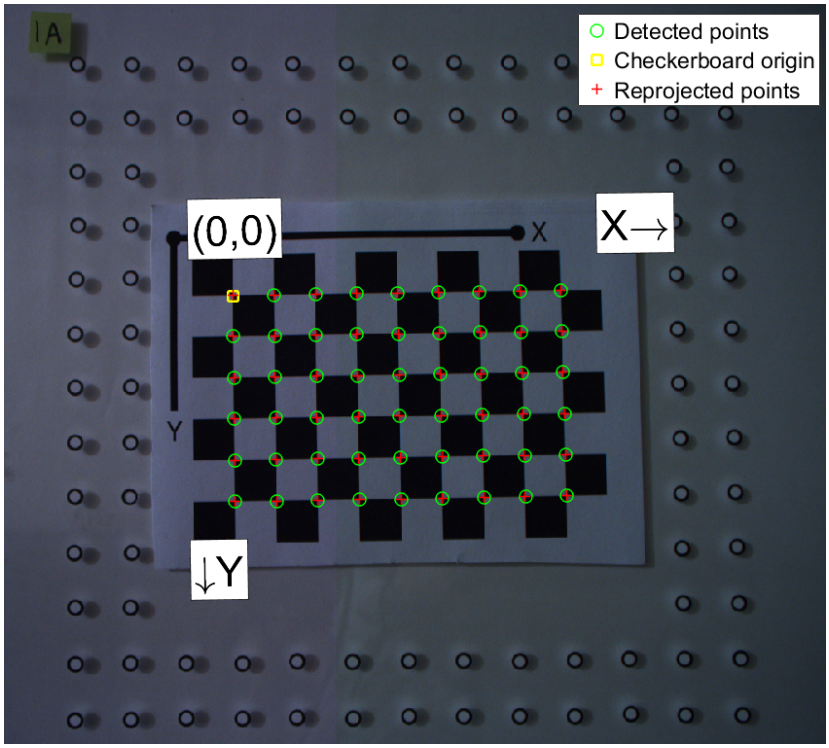

FIGURE 6.12: A screenshot of the Matlab camera calibration app.

$$\mathbf{K}_{cam1} = \begin{bmatrix} 1795 & -1.0302 & 1266 \\ 0 & 1795 & 1017 \\ 0 & 0 & 1 \end{bmatrix} \qquad \mathbf{K}_{cam2} = \begin{bmatrix} 1814 & -0.2189 & 1254 \\ 0 & 1814 & 985.9 \\ 0 & 0 & 1 \end{bmatrix} \tag{6.2}$$

Coefficient	**Camera 1**	**Camera 2**
P_1	-0.0619	-0.0578
P_2	0.1141	0.1209
P_3	-0.0453	-0.0716
K_1	-5.775×10^{-4}	-2.235×10^{-3}
K_2	8.328×10^{-4}	1.916×10^{-4}

TABLE 6.4: Lens Coefficients recovered using Matlab camera calibration toolbox.

Equation 6.2 shows the intrinsic matrices for each of the two cameras. As the cameras are identical models it would be expected that the matrices would contain approximately the same values, allowing for some variations due to manufacturing tolerances. This is indeed the case, with all parameters reasonably close to the corresponding value for the other camera. The one exception is skew. Camera 2 had an issue in that the lens attachment mechanism was slightly loose resulting in the lens drooping under its own weight a small amount.

This is likely the reason behind the differing values for otherwise identical camera setups.

Table 6.4 shows the lens coefficients for each of the two lenses. Coefficients P_n represent radial distortion and coefficients K_n represent tangential distortion. The lenses used were identical. Radial coefficients seem to be fairly similar whereas there is a notable difference in tangential coefficients between the cameras.

6.5.4 Validation of Photogrammetric Process

The photogrammetry process can be validated through use of a dot distortion target. This is a metal plate that has an array of dots precisely drawn on it at distances specified by the manufacturer. A test image can be taken with the target in place of the soil which will then be calibrated and the locations of the dots can be compared to the expected values. An image of the dot distortion target being used to validate the calibration of one of the cameras can be seen in Figure 6.13.

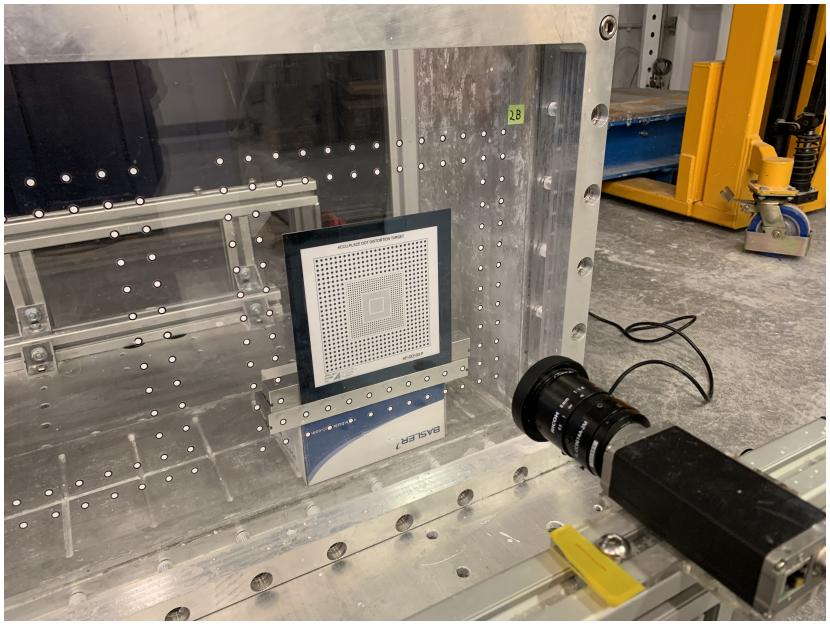

FIGURE 6.13: A photograph showing the validation of the calibration process.

Validating the photogrammetry process in this way is important for several reasons. Firstly, bespoke code was developed to carry out the photogrammetric process and proving it works will add confidence to the process. Secondly, ensuring the PIV displacements recorded are accurate requires the photogrammetric process to function correctly with errors here potentially reducing the quality of the stress-strain responses recovered by the proposed Identification Methods. Error in the photogrammetric process could not only result in incorrect strain calculations but also incorrect area calculations. As per Chapter 3 internal work is

integrated across area so errors in scaling in the photogrammetric process will scale the recovered stress-strain curve by the inverse amount.

Two tests will be performed to validate each of the cameras. The first will be a plot of a subset of the true and photogrammetrically recovered world coordinates of the dot displacement targets. This direct comparison will demonstrate that the recovered world coordinates are approximately equal to the true values. The second validation test will be a comparison between the total area of the dot displacement target for the known world coordinates and the recovered world coordinates.

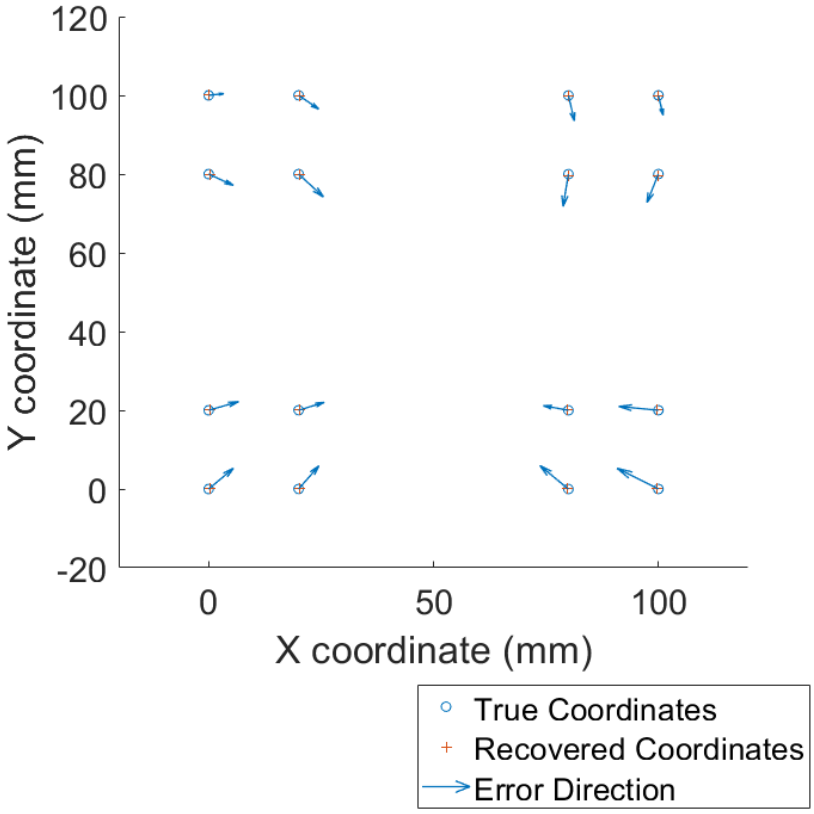

FIGURE 6.14: Photogrammetric error for camera 1. Note that vectors are illustrative and not to scale.

Figures 6.14 and 6.15 show the error for the validation process for cameras 1 and 2 respectively. The circular markings show the true world coordinates for the dot target points and the plus markings are the photogrammetrically recovered world coordinates. It can be seen that these markings are extremely close, and by eye cannot be distinguished. For this reason scaled arrows have been added to the plot showing the direction of the errors identified. Of note is that the recovered world coordinates tend to be more towards the centre of the target indicating scaling is slightly incorrect.

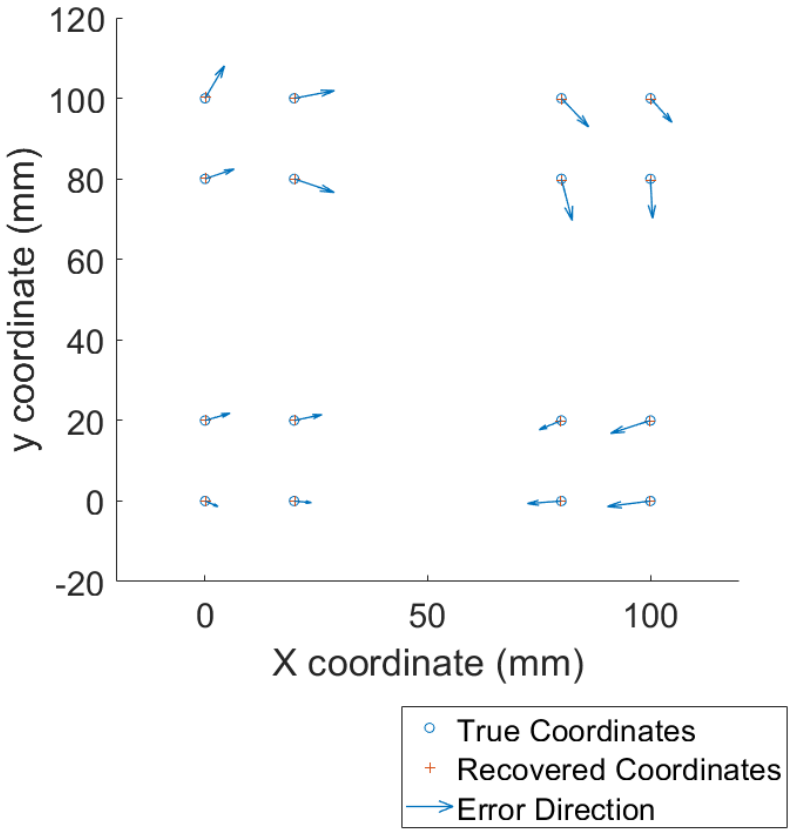

FIGURE 6.15: Photogrammetric error for camera 2. Note that vectors are illustrative and not to scale.

There are two potential causes for this discrepancy. The first is that the refraction correction process assumes that the camera is perpendicular to the plane of the image. Although the camera is fixed to an extruded aluminium frame there is the possibility that this assumption has not been met in practice. The second is the use of the Matlab function "extrinsics". This function is essentially a black box that recovers the camera location and rotation relative to the control points, of which both world and pixel coordinates are known. The "extrinsics" function is intended for use when the points it is given are unobstructed. Refraction correction was carried out such that the control points could be treated in this way but the effects of this on the function are unknown.

Although the errors are systemic in that the recovered points are always closer to the center than they should be the difference is relatively small, with the arrow plot being required to identify it. The second validation check, comparing areas of the dot distortion target illustrate this point. Area error percentages of -0.86% and -0.22% were found for cameras 1 and 2 respectively. This indicates that the photogrammetric process will result in element areas from triangulated PIV data that are smaller than they should be by $< 1\%$. This will

result in the recovered stress-strain curves being scaled in the y axis by a corresponding amount. This is not ideal but is something that will be taken into account when judging the accuracy of the proposed Identification Methods.

Although the area underestimation is a negative factor, scaling the world coordinates in this way will not effect the strain field. Scaling a triangular element undergoing straining up or down will not effect the strains calculated. It would be possible to add a manual correction factor, but as each camera would need a different factor and more validation images to be sure it is correct, this will not be done at the current time and the photogrammetric process will be assumed to be valid with the caveat regarding the likely effect on the recovered stress-strain responses.

6.6 Supplementary Testing

6.6.1 Triaxial

The primary test carried out for comparison with the stress-strain response will be an unconsolidated undrained (UU) triaxial test. Cores will be taken from the soil specimens after the footing tests have been carried out and immediately preserved with cling film such that moisture loss is minimised in the short time before triaxial testing will be carried out. Tests will be carried out at cell pressures of 100kPa and 200kPa.

The results of the triaxial testing will be unavoidably compromised as the cores will be taken from soil that has been loaded during the footing test. Although the samples will be taken away from the footing sites, there will be additional disturbance due to the coring and triaxial sample preparation process. These considerations are standard for triaxial tests and represent the limitations of the method. Despite these factors, triaxial testing will allow for a reasonably representative soil response to be recorded that will be comparable with the outputs of the proposed Identification Methods. Values for c_u obtained through the other supplementary tests will not only allow for comparison with the outputs of the proposed Identification Methods but will also allow for commentary on the quality of the triaxial test results.

A single triaxial test is likely to be unrepresentative of the true soil behaviour for the reasons discussed and as such a number of triaxial tests will be carried out. Four cores will be taken near the four corners of the specimen, with each core long enough that two triaxial samples can be prepared resulting in a total of eight triaxial tests per box. Eight tests will provide a range of soil responses rather than a single curve such that an acceptable output of the

proposed Identification Methods is likely to be within the range. Eight triaxial tests also allows for redundancy in the case of experimental error.

There would be the possibility of using the triaxial tests to study variability of the soil either across the specimen or with depth, however this is not the aim behind the triaxial testing and the relatively small number of samples taken will likely mean the inherent variations in the triaxial results prevent any meaningful conclusions. It will therefore be assumed that the entire specimen has approximately uniform behaviour that is within the range of behaviours recovered from multiple triaxial tests.

A photograph of a specimen undergoing triaxial testing can be examined in Figure 6.16.

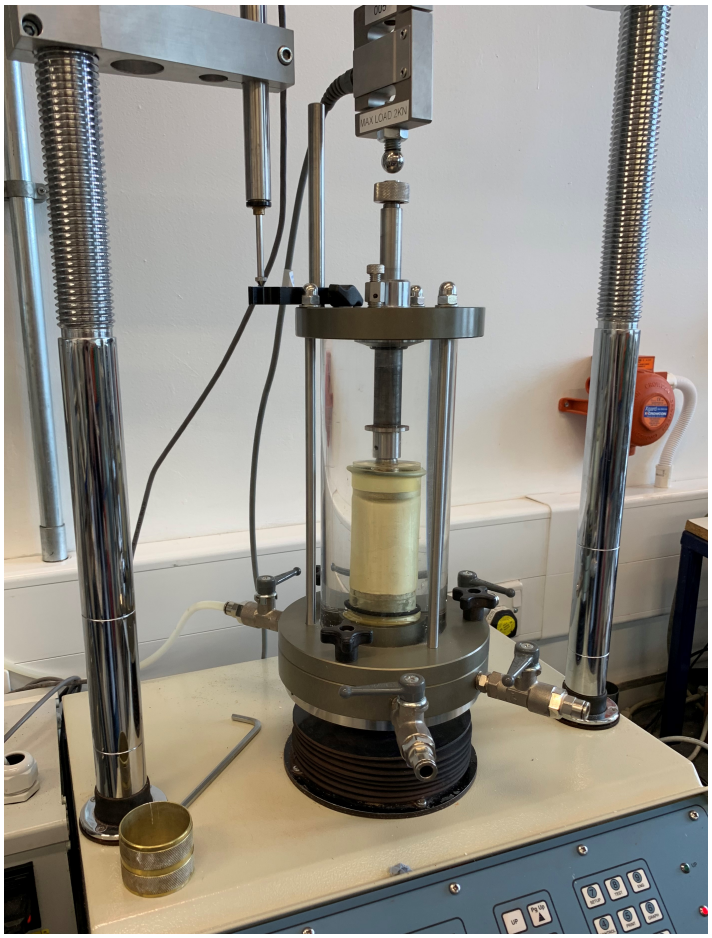

FIGURE 6.16: A soil sample within triaxial testing apparatus.

6.6.2 Back analysis using Terzaghi's bearing capacity equation

As the tests being carried out are footing tests, an additional means by which soil properties can be carried out is by back analysis using Terzaghi's bearing capacity equation. Given in

Equation 6.3, the bearing capacity equation provides the bearing capacity q_{ult} where c' is soil cohesion, σ'_{zD} is effective stress at the depth of the footing, γ is soil density, B is footing width, and N_c, N_q, and N_γ are parameters. Simplifications can be made as the footing as purely cohesive with zero friction, is at the surface resulting in the simplified equation shown in Equation 6.4. As the bearing capacity will be known (the peak recorded load during each test) c_u can be calculated trivially and used as an additional means of validation for any recovered stress-strain response.

$$q_{ult} = c'N_c + \sigma'_{zD}N_q + 0.5\gamma' BN_\gamma \tag{6.3}$$

$$q_{ult} = 5.142 \cdot c' \tag{6.4}$$

Although carrying out back analysis in this way results only in the c_u value as opposed to the full stress-strain response it still provides useful information for validation purposes. As two footing tests are carried out per box two values of c_u will be recovered using this method.

Unlike the other supplementary tests, using Terzaghi's equation for back analysis does not result in any further soil disturbance and is effectively carried out simultaneously with the footing tests so has potential to be representative of the soil behaviour during the actual test.

6.6.3 Shear Vane

Shear vane testing will be carried out on samples in order to recover the peak shear stress. Testing was carried out according to the procedure described in BS 1377-9:1990 (British Standards Institution, 1990d).

The apparatus used was a hand shear vane manufactured by Edeco Pilcon with a blade diameter of 33mm and blade height of 50mm. According to manufacturer instructions, the strength shown on the dial, measured in kPa, was multiplied by a factor of 1.145 in order to conform to the aforementioned standard. This value was printed on the shear vane dial during manufacture to account for differences in the springs between individual vanes.

Four shear vane tests will be carried out per specimen in the four corners of the box. As with the triaxial samples taken, the shear vane tests will be performed after the footings have been driven into the soil so some degree of disturbance will be present. Shear vane tests will be carried out immediately after the driven tests have been carried out such that there will be negligible change in moisture content.

6.7 Conclusion

This chapter has detailed the equipment and processes required to allow for the generation of datasets that can be used for the validation of the proposed Identification Methods. Whereas FEA can be used to make "perfect" artificial datasets, the data obtained through physical modelling will be flawed in that noise and measurement error will be present. This is not a problem, but the point behind carrying out physical modelling. The purpose of the proposed Identification Methods is to provide a practical tool that can be used as an additional step when researchers use physical modelling and as such testing the suitability of the methods with real datasets is essential.

Chapter 7

Analysis of Artificial Datasets

7.1 Introduction

In Chapter 5 the methodology by which a number of artificial datasets were produced was described. The end goal of the production of such data is the validation of the Identification Methods proposed in Chapter 4. The data produced, both from the simple "hand" calculations and the FEA analysis was designed to mimic displacement field datasets produced via PIV during physical modelling along with corresponding load displacement plots.

Each dataset can be input into both proposed Identification Methods and the output stress-strain curve will be compared with the curve used to generate the datasets. Similarities and differences will be identified and discussed, giving reference to theoretical points in Chapters 4 and 5 where appropriate.

As well as testing the raw data, two different schemes of degradation will be applied to the datasets to better simulate real data. Firstly, noise will be added to the displacement field in the manner described in Chapter 4 to simulate a flawed PIV dataset. Next, strains will be calculated using only a subset of the available displacement nodes to simulate the effects of a coarser displacement field. Additionally, an investigation into timestep spacing will be presented. Note that not all datasets will have all effects applied to them as doing so would result in many redundant figures showing almost the same thing, the graphs shown will be the ones that are best able to illustrate points or which have interesting considerations.

Using "perfect" artificial data in this way allows for a starting point that is known to have no issues. Proving that the software implementations work for perfect data is a key first step, after which gradual artificial degradation of the datasets in a variety of ways will allow for the rigour of the methods to be identified. Understanding the effects of dataset degradation will allow useful clues when it comes time to analyse real datasets in Chapter 8.

This chapter will first provide qualitative description and discussion of the artificial datasets, particularly in terms of the obtained displacement and strain fields. Although the parameters of the datasets are largely arbitrary and not intended to represent any particular scenario, simple hand calculations will be performed to demonstrate the validity of the FEA analysis where appropriate. Next, the output curves of all datasets will be given and compared with the expected curve used to generate the data, and finally the effects of the aforementioned degradation strategies will be demonstrated and discussed.

7.2 Qualitative analysis of datasets

The datasets will be qualitatively analysed. Plots showing the deformed shape have been produced to allow for comparison between models and colour maps of the strain field will also be given. The load displacement plots will also be examined.

7.2.1 "Handmade" artificial datasets

First to be examined is the simple "handmade" data. These models were simple shear and split simple shear cases. Each model was produced for both the "Vardanega and Bolton" curve and the elastic-perfectly-plastic curve. The displacement and strain data will not change with curve choice as it was the starting point from which stress and force data was derived. To allow for the calculation of strain, three node triangular elements were mapped on to the displacement grid through Delaunay triangulation, however for this uniform grid a less robust triangulation methodology would also have worked. Additionally, there is no issue of nodes moving out of the initial area. The location of every node is recorded for each timestep regardless of how later values relate to the initial position.

Figure 7.1 shows the final deformed shape for both stress-strain responses undergoing simple shear. Every node has moved in the y direction an amount proportional to its distance from the fixed edge. Peak displacement was 0.96m and the block of soil is 8m by 8m resulting in each element having a shear strain $\epsilon_{xy} = \frac{1}{2}\gamma_{xy}$ of 0.06. As all strain components other than shear are zero for the simple shear case, maximum shear strain ϵ_s is also the same value. Figure 7.2 shows a plot of this. Note that due to rounding in the triangulation process some elements have very slightly differing values, however all are correct to over 10 significant figures. Slight rounding errors such as this will have no effect but will be present in all datasets.

The final deformation of the split case can be seen in Figure 7.3. Again, the same displacement and strain field was used as the starting point for both stress-strain responses.

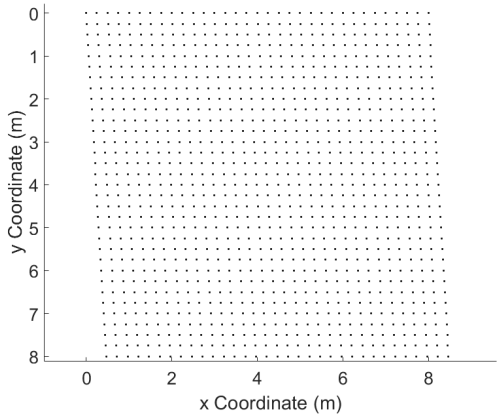

FIGURE 7.1: The final deformed shape of the Simple Shear case for both input curves.

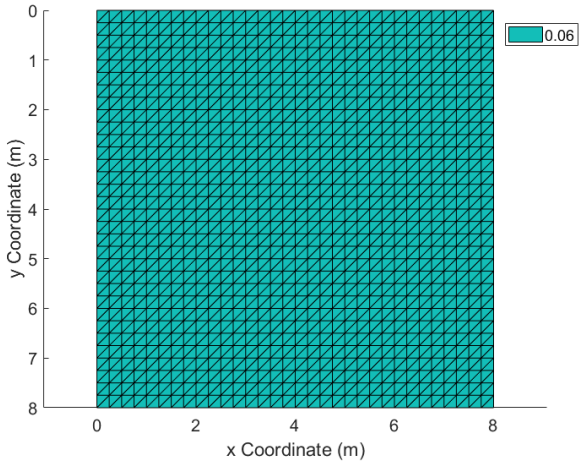

FIGURE 7.2: The final maximum shear strain field of the Simple Shear case for both input curves.

The strain field for the split case can be seen in Figure 7.4 which shows the strain field for the final frame. As the loading is applied to a horizontal cross section that is off centre, two distinct regions of strain are present. A peak displacement of 0.6m is observed, and with distance to the fixed edges being 3m and 5m the resulting shear strains $\epsilon_{xy} = \epsilon_s$ can be hand calculated to be 0.1 and 0.6.

Plots of the force-displacement curves for both the standard simple shear case and the split simple shear case are shown in Figures 7.5 and 7.6 respectively. For each geometry, a model was run using both stress-strain responses that were described in Chapter 5. The two responses are the "Vardanega and Bolton" curve and the elastic-perfectly-plastic curve.

Due to the uniform and linearly increasing strain values, it would be expected that the shape

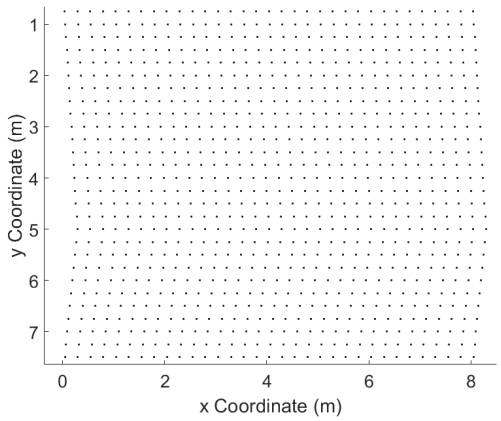

FIGURE 7.3: The final deformed shape of the split Simple Shear case for both input curves.

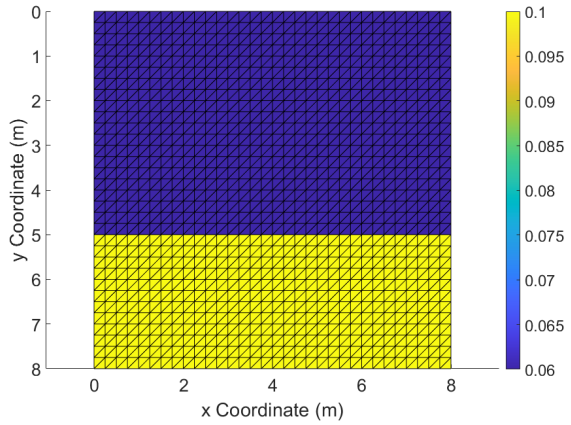

FIGURE 7.4: The final maximum shear strain field of the split Simple Shear case for both input curves.

of the force-displacement curves in Figure 7.5 would match that of the stress-strain curve, the values simply being scaled based on the sizes of the block of soil and this is indeed the case when resolution of the curves is taken into account. No curve fitting has been applied and the plots simply have connected the dots for each of the 50 timesteps used which leads to the force-displacement curves being somewhat less smooth that if they were continuous. Of particular note is is point in which plasticity is reached during the elastic-perfectly-plastic case. During one timestep every element of soil is undergoing elastic deformation whereas in the next timestep every element is in the plastic part of the stress-strain curve.

The force-displacement plots in Figure 7.6 for the split cases look rather less like a scaled version of the stress-strain curves than for the true simple shear cases. The split case is essentially two simple shear cases added together, with each section having the same displacement-time curve but differing strain, and hence stress and force values for each timestep. Plotting

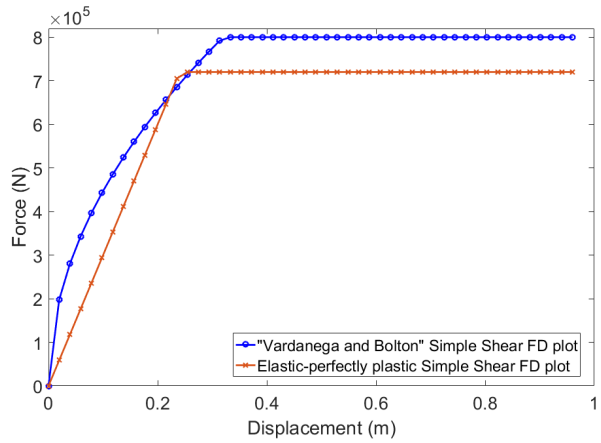

FIGURE 7.5: The force-displacement curves for the true simple shear "hand-made" artificial dataset.

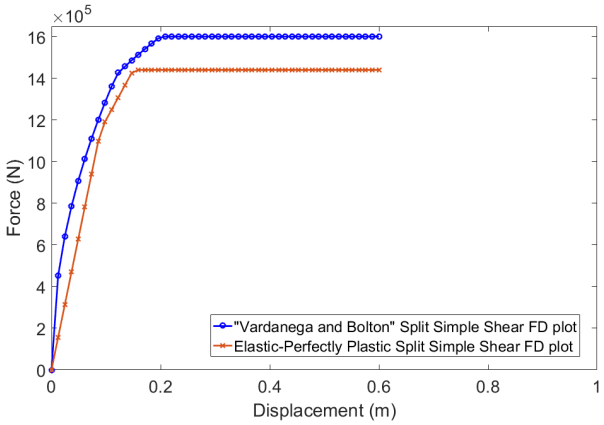

FIGURE 7.6: The force-displacement curves for the split simple shear "hand-made" artificial dataset.

the force-displacement curve for both the upper and lower section of the split models separately would produce curves looking similar to those in Figure 7.5, but when these curves are added to produce the global force-displacement curve they become less and less similar. Generating models with increasing numbers of dissimilar simple shear areas would likely result in force-displacement curves that are wildly different not only from the shape of the stress-strain curve but also from each other. For more realistic data in which every element is largely independent in the amount of strain it has this effect is likely to be more pronounced.

7.2.2 Simple Shear FEA datasets

To allow for the modelling of more realistic and complex cases ABAQUS FEA software was used to generate a number of artificial datasets. The first to be examined will be simple shear. As stated in Chapter 5 two variations of simple shear have been used to generate datasets. The first in which y movement is set to zero, i.e. functionally the same as the hand calculations, and the second in which y movement is unrestrained resulting in a much more complex mechanism. For both possibilities a total of two models were generated, representing both input stress-strain curves. As each model used strain based actuation with the same final displacement, plots of final strain or displacement fields will be largely the same by eye so a subset of data will be presented to illustrate any points without including multiple redundant graphs.

For this FEA model (and the following models), the nodal displacement data is extracted from ABAQUS and used as if each node were a PIV displacement point. Delaunay triangulation is used to generate an array of triangular elements from which strains can be calculated. As with the handmade models, there is no concept of nodes or elements leaving the area of interest, displacement points are simply tracked wherever they happen to go.

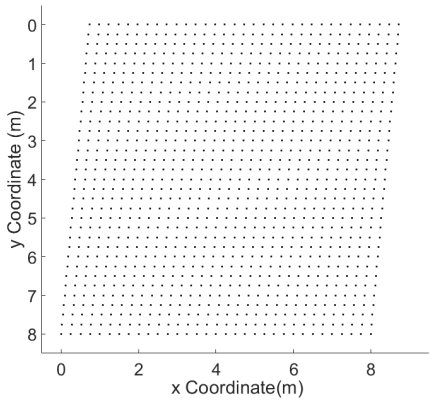

FIGURE 7.7: The final deformed shape of the FEA Simple Shear case using the "Vardanega and Bolton" input curve.

Figures 7.7 and 7.8 show the distorted shape and the strain field of the simple shear model generated using FEA. The shown plots are taken from the "Vardanega and Bolton" dataset but would be the same for the elastic-perfectly-plastic model. As with the "handmade" datasets, this is due to the model using strain based actuation and having a uniform strain field.

This particularly simple FEA model produces an identical final frame as the "handmade" simple shear datasets have. This indicates that the FEA model is functioning as expected. It should be noted that as ABAQUS was allowed to choose its own timesteps that only the final

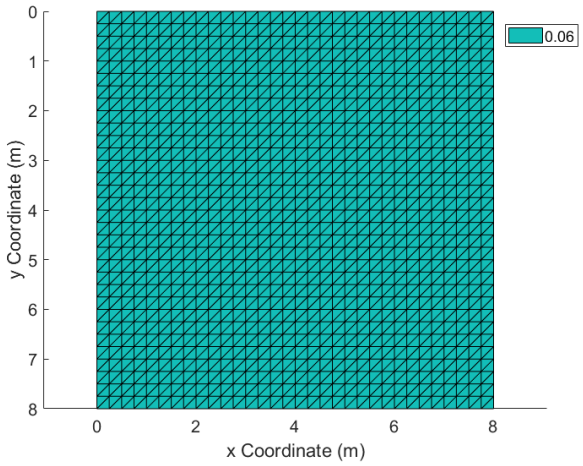

FIGURE 7.8: The final maximum shear strain field of the FEA Simple Shear case for the "Vardanega and Bolton" input curve.

frame is identical. The strain based actuation does of course increase linearly with time but timesteps are not uniformly distributed. Figure 7.9 shows plots of the force-displacement curves for the models for both stress-strain curves. Of note is that the same peak force is observed as in the corresponding "handmade" dataset force-displacement curves.

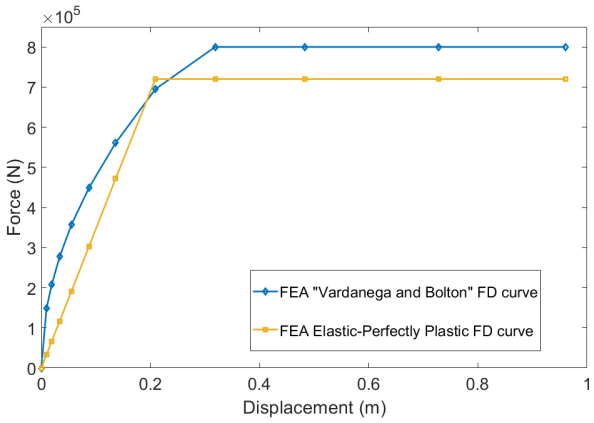

FIGURE 7.9: The Force-Displacement curves for the FEA Simple Shear case for both stress-strain responses.

For the cases in which movement is unfixed in the y direction (other than the top edge which is rigid and fixed in y) a completely different displacement and strain field is produced. Figures 7.10 and 7.11 show the distorted shape and the strain field of the shear model with y movement allowed, generated using FEA.

As shown in Figure 7.10 allowing for movement in the y direction results in a slightly different mechanism. Soil is now able to move up and down. This change means that the modelled mechanism is not simple shear, and indeed there are other strains than shear.

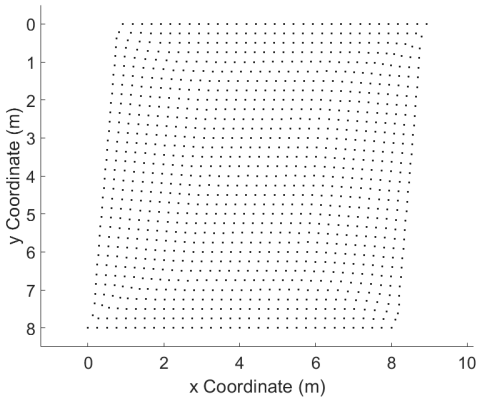

FIGURE 7.10: The final deformed shape of the FEA Unfixed Shear case for the "Vardanega and Bolton" input curve.

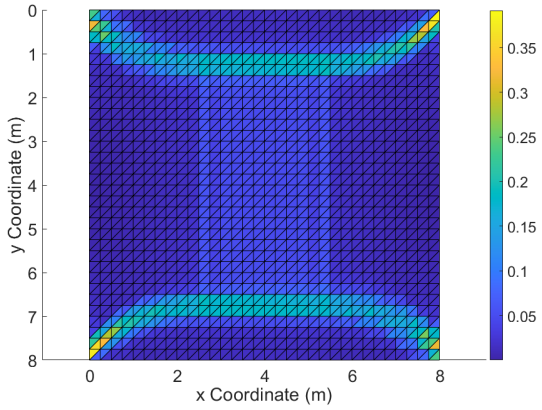

FIGURE 7.11: The final maximum shear strain field of the FEA Unfixed Shear case for the "Vardanega and Bolton" input curve.

Whereas in the true simple shear case only ϵ_{xy} had non zero values with ϵ_x and ϵ_y being nil, the unfixed shear case has non zero values for all strain components. This means that there are volumetric strains present.

Examining the displacement field, it is easy to see that some elements have indeed became smaller whereas some have grown, and that there is rotational symmetry in the displacement field. As a key assumption with the current Identification Method formulations is that volumetric strain is nil, the effects of this will be discussed later in this chapter. The sum of all volumetric strains is very small with a value of -5.7640×10^{-5} compared to the sum of maximum shear strains of 999.2995. Effectively zero total volumetric strain is to be expected as no soil was created or destroyed and Poisson's ratio was set at 0.499.

It should be noted that the sum of the absolute values of volumetric strain is 99.2890, or approximately 10% of the sum of the maximum shear strains. It can clearly be seen in the

deformed shape plot that there is visible element size change, although every element expansion is matched by an equivalent compression. The current assumption is that energy expenditure due to volumetric strain is nil, and although the sum of volumetric strain is approximately zero, if a different soil model were to be used in which compression takes more work than is returned by expansion then this would have to be taken into account. However, as the displacement field was generated in ABAQUS using 6-node triangles, it is possible that this volumetric effect is an artefact due to later triangulating the nodal displacement field with 3-node triangles in order to calculate strain.

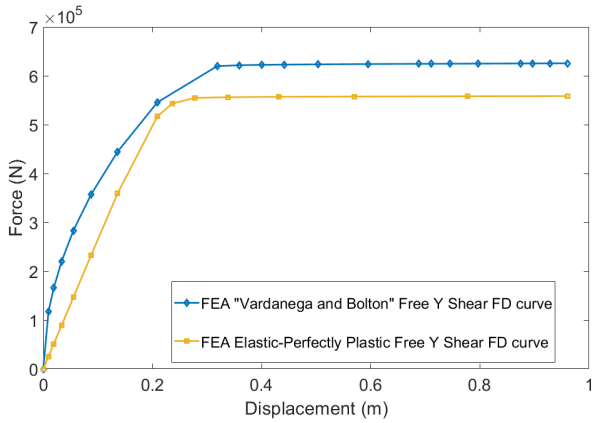

FIGURE 7.12: The Force-Displacement curves for the FEA Unfixed Shear case for both input stress-strain responses.

Figure 7.12 shows the force-displacement curves for models using both the "Vardanega and Bolton" and elastic-perfectly-plastic stress-strain curves. A key differences is aparent when comparing this figure to the equivalent for the true simple shear case (Figure 7.9): There is a differing peak force.

Lower peak force is to be expected. The unfixed shear model is a superset of the true simple shear model, anything simple shear can do, unfixed shear can also do. The mechanism returned by the FEA software will be the one requiring the lowest force and with new avenues of soil movement available, it seems apparent that it takes less energy to shear a block of soil in this manner than compared to the true simple shear case.

7.2.3 Rotating Wall FEA datasets

The next set of models represents an increase in complexity. The rotating wall model as described in Chapter 5 features a 2D square of soil of edge 8m, with the edge on the left hand side rotating into the block of soil about a fixed point on the base. Unlike other models these used a force based actuation scheme, in which applied loading increases linearly and displacement is a function of load. As with the simple shear cases, a model was produced

for each of the two soil responses defined in Chapter 5. Figures 7.13 and 7.14 show the distorted shape and the strain field of the rotating wall FEA model for the "Vardanega and Bolton" input curve.

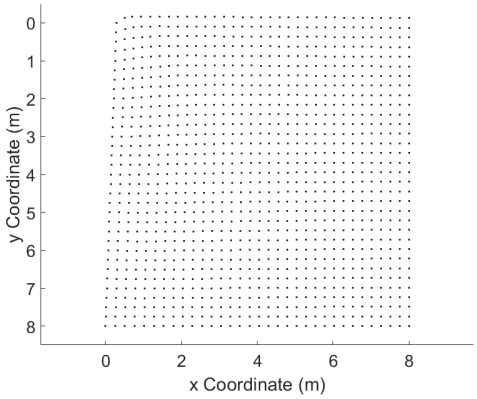

FIGURE 7.13: The final deformed shape of the FEA Rotating Wall case for the "Vardanega and Bolton" input curve.

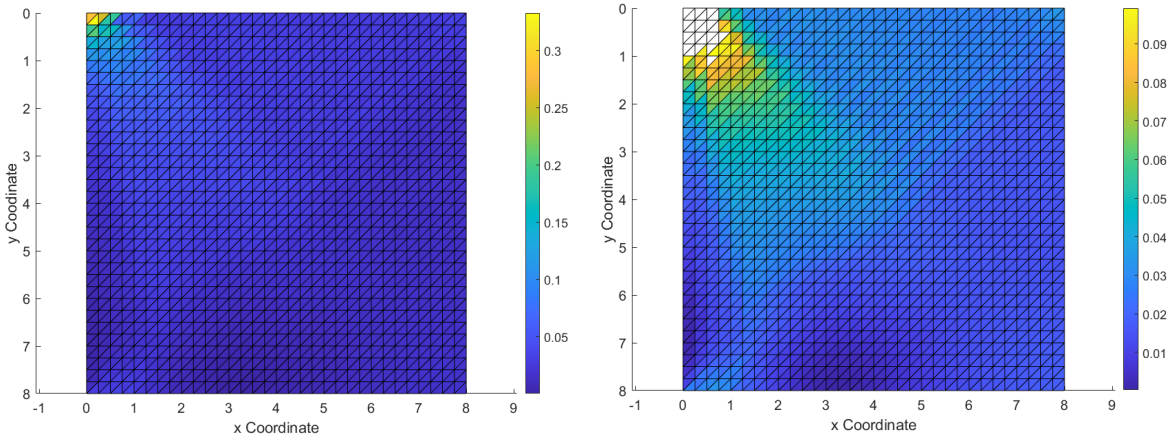

FIGURE 7.14: The final maximum shear strain field of the FEA Rotating Wall case for the "Vardanega and Bolton" input curve. The second plot has strains above 0.1 trimmed.

Analysis of Figures 7.13 and 7.14 allow for some insight into the behaviour of the model. Of note is the fact that relatively large areas of the model are undergoing little to no deformation or strain. This differs from the simple shear case, for both fixed and unfixed y direction movement, in which every element was undergoing some degree of displacement and deformation. Whether significant regions of negligible strain effect the usage of Identification Methods is something that will be discussed later in this chapter.

The sum of volumetric strain is again negligible with a value of -6.8464×10^{-5} with the sum of absolute volumetric strain as 27.7853 and the sum of maximum shear strain being

408.3933. The ratio of absolute volumetric strain to maximum shear strain is approximately 7%, slightly lower than the unfixed simple shear case. Unlike in the simple shear cases in which the solid "bounding box" stays the same size, the soil is squeezed such that upward movement on the free edge is observed. In this case the soil was modelled as weightless so considerations such as the effects of gravity need not be made. Should this scenario have been modelled with a soil with mass a non negligible amount of work would be expended moving the soil against gravity.

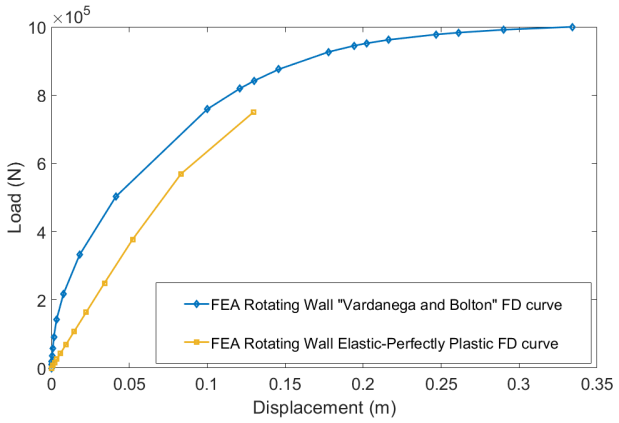

FIGURE 7.15: The Force-Displacement curves for the FEA Rotating Wall case for both input stress-strain responses.

As stated previously, the rotating wall scenarios were modelled using load actuation. This was done for two reasons. Firstly, for variety: although the change to load actuation should have no impact on calculation of either internal or external work, it is still worth confirming this. Secondly, for ease of modelling: the rigid tie used to allow for rotation of the left had side did not allow for a specified displacement to be applied to one end. It is possible that the model could have been adjusted to allow for this but seeing as there are benefits to generating datasets using load based actuation this was deemed to be low priority.

Figure 7.15 shows the force-displacement curves for the two variations on the rotating wall model that were generated. As load actuation was used each model was loaded linearly with time until the specified load was reached. For the “Vardanega and Bolton" curve this was $1MN$ and for the elastic-perfectly-plastic curve it was $0.75MN$ these values were chosen by trial and error as ABAQUS was unable to solve the model with excessively high loading applied. As the model ended when the chosen loading value was reached, the curves end at differing displacement values.

The force-displacement curve for the "Vardanega and Bolton" model looks similar to what has been presented in the sections regarding simple shear cases, a plateau has been reached indicating a significant part of the soil is undergoing plastic deformation. The force-displacement curve for the elastic-perfectly-plastic model does not look nearly as good. It has not reached

the expected plateau indicating much of the soil is still in the elastic phase. The effects of this on the recovery of stress-strain responses will be considered in later sections of this chapter.

7.2.4 Simple Footing FEA datasets

The next set of FEA models to be examined is the pair of simple footing models. A simple footing test was carried out on a 50m square block of soil. Symmetry was used in the FEA model, with 5m of footing modelled with another 5m on the other side of the line of symmetry. The simple footing datasets are perhaps the most interesting as they are most similar to the physical modelling derived datasets. Two scenarios were modelled, again using both the "Vardanega and Bolton" input curve and the elastic-perfectly-plastic input curve. As with the previously shown models, the displacement and strain fields presented will be for only one of these models.

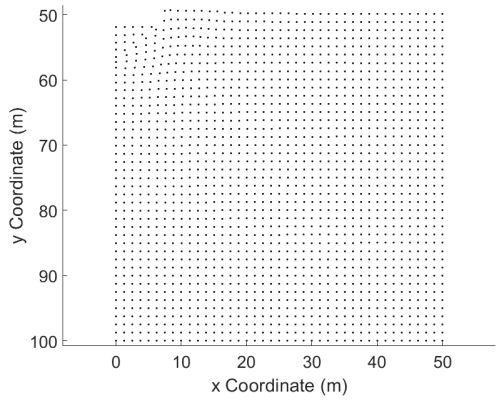

FIGURE 7.16: The final deformed shape of the FEA Simple Footing case for the "Vardanega and Bolton" input curve.

Figures 7.16 and 7.17 show the distorted shape and the strain field for the simple footing case modelled with the "Vardanega and Bolton" soil response. Examining these figures, it is clear to see a triangle of soil directly under the footing with relatively little internal distortion with a shear band between it and the rest of the soil. Of particular note is the element in the corner of the footing. A maximum shear strain of 1 is observed indicating distortion of approximately the same size as the element its' self. Singularities such as these are not uncommon during FEA modelling and although not particularly representative of reality, it shouldn't affect the Identification Method procedures from recovering the soil response. Also of note is the large region of relatively negligible strains, in this case it is even more pronounced than in the rotating wall scenario. The effects of this will be discussed in the following section.

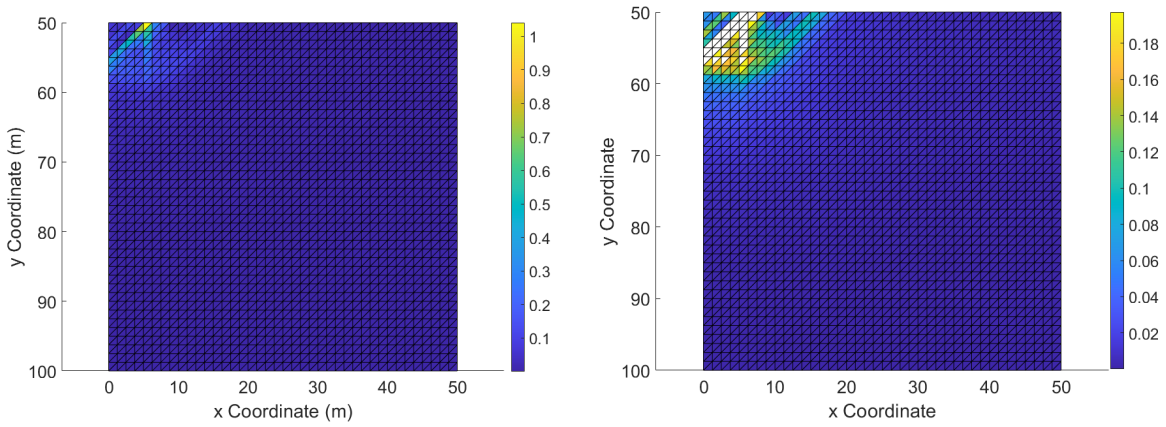

FIGURE 7.17: The final maximum shear strain field of the FEA Simple Footing case for the "Vardanega and Bolton" input curve. The second plot has strains above 0.2 trimmed.

Volumetric strain was observed in individual elements with the overall sum being approximately zero. The sum of volumetric strain for the presented case was 6.4300×10^{-5} with the sum of absolute values being 79.8694. For comparison the sum of maximum shear strains was 748.9798.

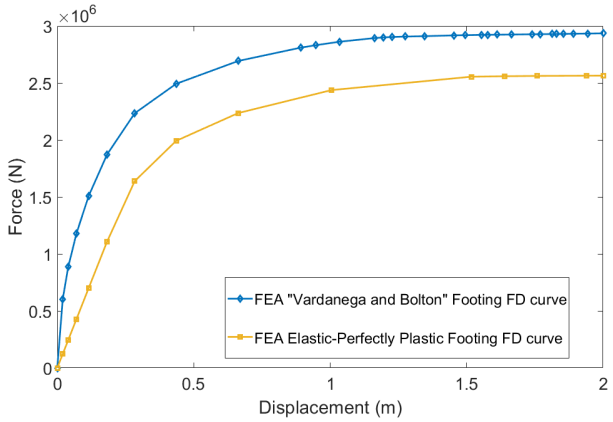

FIGURE 7.18: The Force-Displacement curves for the FEA Simple Footing case for both input stress-strain responses.

Figure 7.18 shows the force-displacement response for each of the aforementioned models. For simple footing cases Terzaghi's Bearing Capacity Theorem can be used for comparison.

Using the values of cohesion from the input stress-strain curves (100000 for the "Vardanega and Bolton" soil response and 90000 for the elastic-perfectly-plastic soil response) bearing capacity values of $257000N$ and $231000N$ can be found for the "Vardanega and Bolton" and the elastic-perfectly-plastic soil responses respectively. These are both lower than the measured values. As the observed bearing capacity reduces with increased mesh density it is likely

that further refinement would move the modelled values closer to the "true" values but this is beyond the scope of this project. The FEA models are internally consistent, ABAQUS enforces energy equilibrium so the Identification Method processes should be able to find a soil response to match internal and external work even if the data used is not particularly representative of a real life case.

7.3 Verification using "perfect" datasets

This section will consist of verification of both the Segment based and Equation based Identification Methods for each of the models described in the previous section. Comparisons between the recovered stress-strain curve and the expected curve will be given and any discrepancies identified and discussed. The previously presented datasets will be used in this section using both the "Vardanega and Bolton" and the elastic-perfectly-plastic input soil responses. It should be noted that all curves recovered using the Segment based approach are formed from 100 segments. An investigation into the impact of segment number will be provided later in the chapter.

7.3.1 Simple Shear "Handmade" dataset

The "Handmade" simple shear dataset is the simplest model generated. Figures 7.19 and 7.20 show comparisons between the input stress-strain response and the output stress-strain responses recovered via the two proposed Identification Methods.

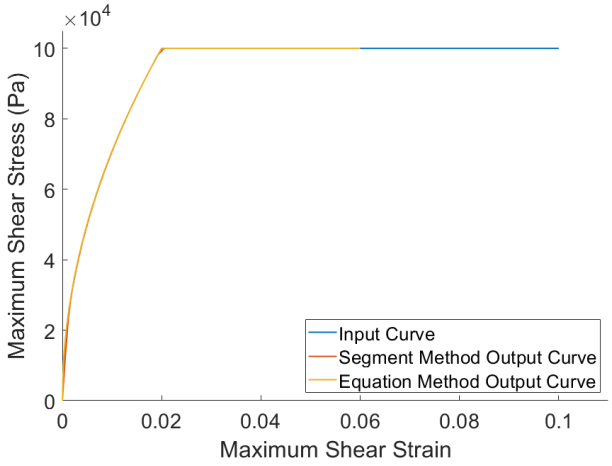

FIGURE 7.19: The input and output stress-strain curves for the "Handmade" Simple Shear case modelled with the "Vardanega and Bolton" soil response.

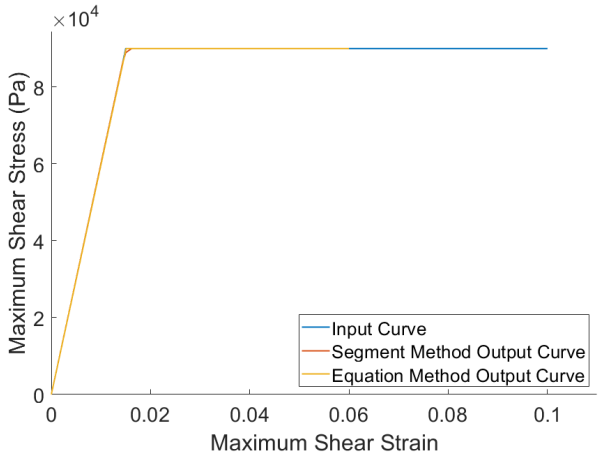

FIGURE 7.20: The input and output stress-strain curves for the "Handmade" Simple Shear case modelled with the elastic-perfectly-plastic soil response.

For both figures, it is clear that both the Equation based and Segment based Identification Methods have been able to recover the curves nearly exactly as expected. For the "Vardanega and Bolton" cases the global energy gap as a percentage of total external energy expenditure was 5.5×10^{-5}% and 1.6×10^{-3}% for the Segment based and equation Identification Methods respectively. For the Elastic-perfectly-plastic case these values were 1.6×10^{-3}% and 7.9×10^{-4}%. The energy gaps found are extremely low, indicating that the optimiser is able to find a very good fit. It should be noted that this is a particularly simple case so this is to be expected, with more complex cases likely having curves that not only do not match the input curve by eye but also have a larger energy gap found. Of note is the very slight discrepancy with the segment method curves for both soil responses, with the curve appearing to have cut the corner at the transition to plasticity. This is likely due to the segment resolution forcing the optimiser to connect the dots.

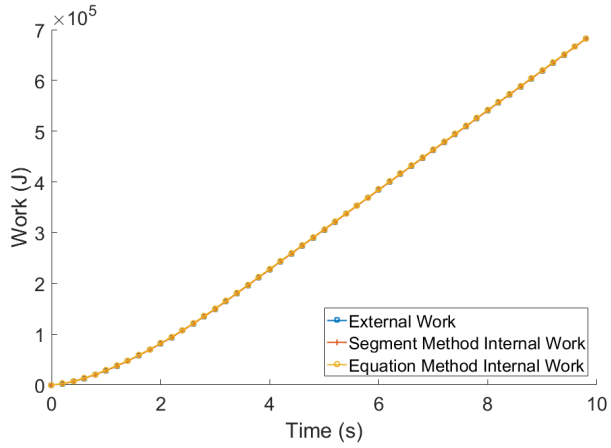

FIGURE 7.21: The cumulative internal and external work for the "Handmade" Simple Shear case modelled with the "Vardanega and Bolton" soil response.

Figure 7.21 shows a plot of the cumulative internal and external work. The given plot is for the "Vardanega and Bolton" soil response, however the equivalent plot for the elastic-perfectly-plastic response is by eye identical. Of note in this plot is the energy for the three lines plot (external work, segment method internal work, and equation method internal work) are almost completely on top of each other. This is to be expected due to the incredibly small energy gap. The distribution of timesteps can be seen in the markers on the plot, with 50 timesteps evenly distributed across the 10 seconds. Although this plot in and of itself is not overly interesting, it will be useful to have for purposes of comparison with the models discussed in later sections.

7.3.2 Split Shear "Handmade" dataset

The spit shear "Handmade" dataset differs from the simple shear handmade dataset in that instead of there being one region with uniform strain, their are now two differing regions of uniform strain. Loading and displacement are otherwise the same. Figures 7.22 and 7.23 show the comparison between input and output stress-strain curves for the two specified soil responses.

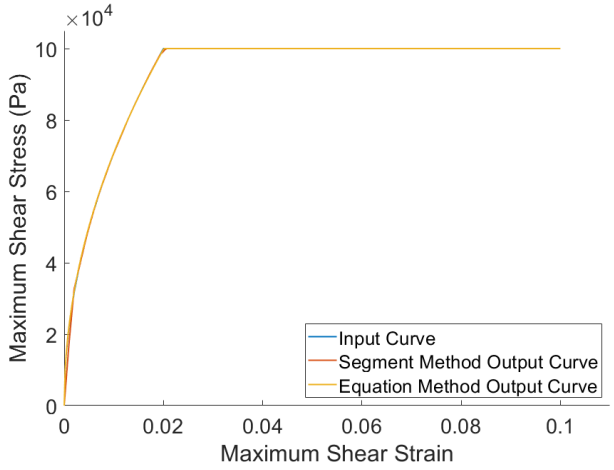

FIGURE 7.22: The input and output stress-strain curves for the "Handmade" Split Shear case modelled with the "Vardanega and Bolton" soil response.

As with the "handmade" simple shear models, the stress-strain responses output from both the "Vardanega and Bolton" and elastic-perfectly-plastic scenarios are a near perfect match. As before the Segment method output appears to have slightly cut the corner at the start of the plastic parts of both curves for presumably the same reasons as before.

Global errors for the "Vardanega and Bolton" curves are 1.1×10^{-3}% and 1.6×10^{-3}% for the segment and equation methods respectively and the errors for the elastic-perfectly-plastic curves are 3.3×10^{-3}% and 6.5×10^{-4}%. These error gap percentages are similarly low to

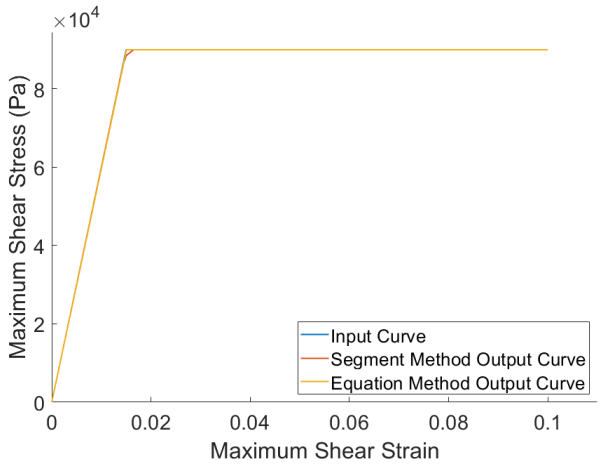

FIGURE 7.23: The input and output stress-strain curves for the "Handmade" Split Shear case modelled with the elastic-perfectly-plastic soil response.

those found for the "handmade" simple shear case. For the Segment method, direct comparisons between the numeric values are not applicable for these simple cases as the MOSEK optimiser reaches its tolerance values and can only say the given results are near optimal, so seemingly meaningful differences in these error percentages could in fact be largely meaningless. For the Equation based method there is no such limitation; as a brute force approach is used it can be guarenteed that the found values are optimal provided the true values are within the search area. As with the "handmade" Simple Shear case, the energy gap is lower for the elastic-perfectly-plastic scenario but there is negligible difference between the split shear and simple shear case.

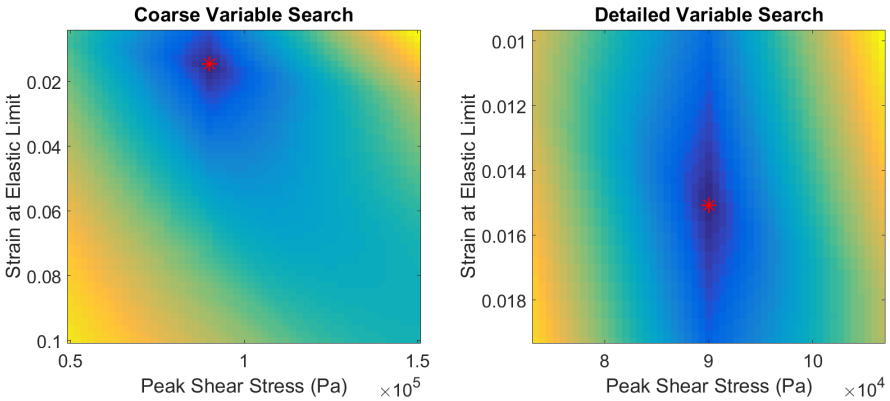

FIGURE 7.24: A set of plots showing the search area the Equation Method used for the "Handmade" Split Shear case modelled with the elastic-perfectly-plastic soil response.

Figure 7.24 shows the contour plots for the c_u and ϵ_{lim} variables for the elastic-perfectly-plastic stress-strain response that is output by the Equation based Identification Method. It

is clear that the outputs found using this method are the optimal solution. Although there is a plateau of almost as good outputs, the chosen value is truly optimal.

A plot comparing the internal and external works will not be presented for this scenario as it is identical by eye to the one presented for the "handmade" simple shear case. Lines for external work, and internal works for both the Equation based and Segment based methods are on top of each other with any differences too small to see in a plot.

7.3.3 Simple Shear FEA dataset

The simple shear FEA dataset is theoretically the same as the "handmade" simple shear dataset in terms of force, displacement, and strain against time, with the exception that timesteps are now irregular. The "handmade" datasets have 50 timesteps of length 0.2 seconds. The FEA datasets (including the datasets to be discussed in following sections) have both the number and spacing of their timesteps chosen by ABAQUS. The FEA software presumably seeks to balance accuracy with computational efficiency and chooses the timestep arrangement that allows for the lowest number of steps without introducing unacceptable errors. Both Identification Methods are able to handle arbitrarily spaced timesteps, the effects of which will be discussed shortly.

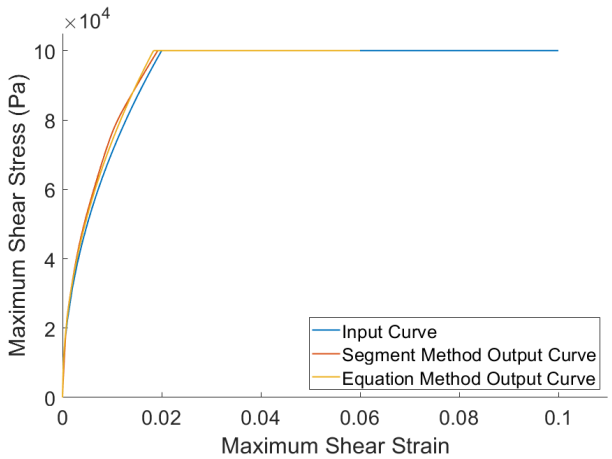

FIGURE 7.25: The input and output stress-strain curves for the FEA Simple Shear case modelled with the "Vardanega and Bolton" soil response.

Figures 7.25 and 7.26 show the comparisons in input and output stress-strain curves. It is clear that the output curves do not match quite as well as in the "handmade" case, with both the "Vardanega and Bolton" and elastic-perfectly-plastic responses being too steep at the start. In both cases the correct c_u value is obtained regardless of which Identification Method is used. Having the correct c_u value even with slightly incorrect curve shapes is promising if not ideal, as c_u would be the parameter most relevant to engineering design.

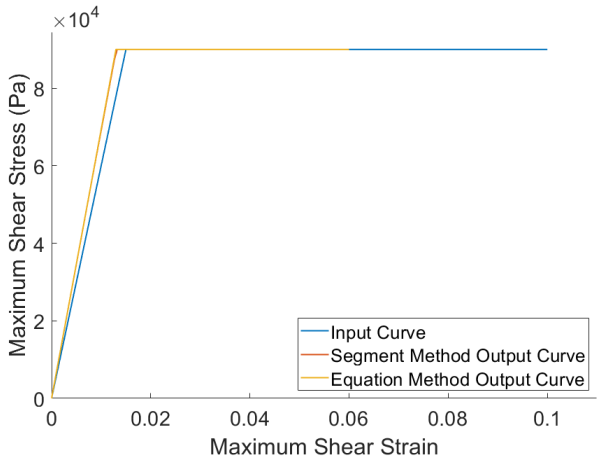

FIGURE 7.26: The input and output stress-strain curves for the FEA Simple Shear case modelled with the elastic-perfectly-plastic soil response.

The energy gap for the segment method are extremely low for the "Vardanega and Bolton", of the order of 1×10^{-13}%. MOSEK indicates that the curve found is optimal. The gap for the Segment based elastic-perfectly-plastic curve is 1.3×10^{-3}% which is also optimal. The values for energy gap percentage found for the Equation based approach are 4.2×10^{-3}% and 3.5×10^{-4}% for the two soil responses, values comparable to those found with the previously discussed models.

There are two possibilities for the reason for the mismatch in stress-strain curve that can be considered and discounted. First, optimiser issues. This is unlikely as the optimiser is reporting that everything is OK and the Segment based curve is very close to the Equation based curve which doesn't use the optimiser, especially for the elastic-perfectly-plastic case. Second, pre-processing errors. This is unlikely as the exact same pre-processing is used as in the "handmade" calculations in which the stress-strain curves recovered are all but perfect. The final possibility to be discussed is the distribution of timesteps.

Figure 7.27 shows the comparison between internal and external work. As before the curves are directly on top of each other. stress-strain responses have been found with very low energy gaps. Of note however is the distribution of timesteps. ABAQUS used 11 timesteps distributed irregularly throughout the 10 seconds the model ran for. Of these timesteps, 7 can be found before the 2 second mark and 6 are before the 1.5 second mark. As the model is a simple shear case in which shear increases linearly with time, it is clear that a significant percentage of data can be found in the earlier parts of the stress-strain curve. 2 and 1.5 seconds are the times at which full plasticity is reached for the two soil responses.

As the only difference between this scenario and the "handmade" simple shear model is

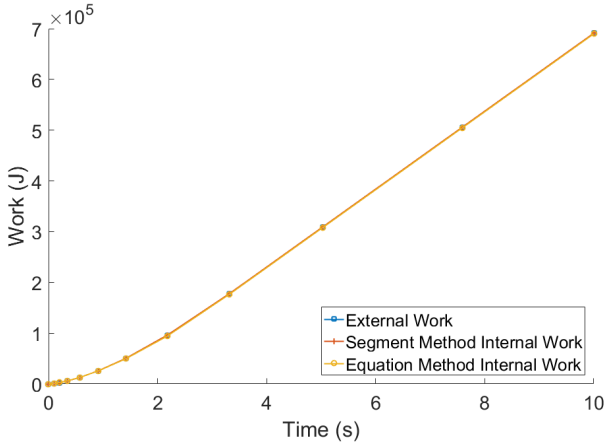

FIGURE 7.27: The cumulative internal and external work for the FEA Simple Shear case modelled with the "Vardanega and Bolton" soil response.

the number and arrangement of timesteps this seems to be the logical reason for a discrepancy. Although real physical modelling data is likely to have uniform timesteps, further investigation into this phenomenon using the simple shear case will be provided later in the chapter.

7.3.4 Unfixed y Shear FEA dataset

The next set of models to examine is the Unfixed "y" simple shear scenario that was modelled using FEA. As per the qualitative analysis sections these models have a much more complex strain field. Each timestep will have elements at various places across the stress-strain curve. Again, ABAQUS was allowed to choose its own timesteps and due to the increased complexity, slightly more were necessary with the "Vardanega and Bolton" case using 22 timesteps that were much more evenly distributed, although still with an overrepresentation at the start, that the simple shear case.

Figures 7.28 and 7.29 show the comparisons in input and output stress-strain curves. As with the simple shear case the output curves are very close to the input curves, certainly close enough that they could be used for design with appropriate safety factoring. A notable difference to the simple shear case is that the c_u values are very slightly lower for the elastic-perfectly-plastic case, with values of $89.3kPa$ found rather than the expected $90kPa$.

Energy gaps are still similarly low with percentage gaps of $2.1 \times 10^{-2}\%$ and $6.4 \times 10^{-3}\%$ for the segment and Equation based methods for the "Vardanega and Bolton" soil response and $4.2 \times 10^{-3}\%$ and $1.5 \times 10^{-3}\%$ for the segment and Equation based methods for the elastic-perfectly-plastic soil response. The segment method results were reported as optimal by the MOSEK optimiser as opposed to the near optimal reported for the very simple "handmade"

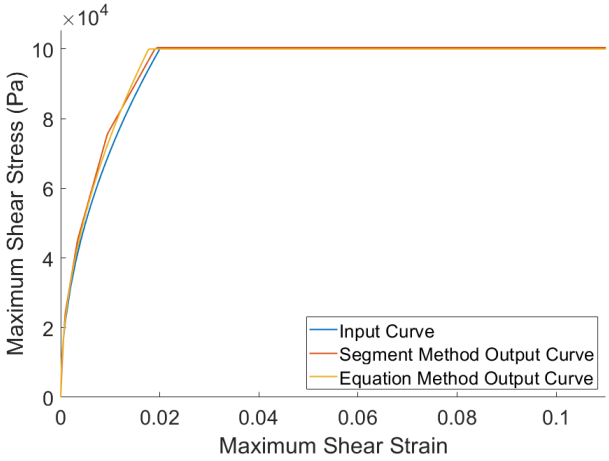

FIGURE 7.28: The input and output stress-strain curves for the FEA Unfixed y Shear case modelled with the "Vardanega and Bolton" soil response.

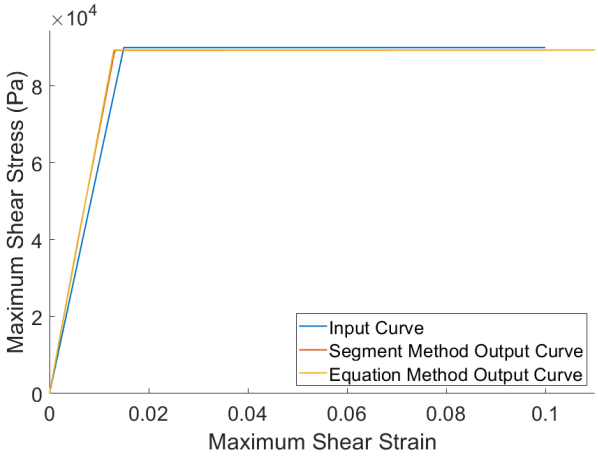

FIGURE 7.29: The input and output stress-strain curves for the FEA Unfixed y Shear case modelled with the elastic-perfectly-plastic soil response.

simple shear cases. Although the percentage energy gaps are still only fractions of a percentage, they do seem to be increasing in general, particularly the Segment based method for the "Vardanega and Bolton" soil response which is now an order of magnitude higher than the highest previously observed values.

Figure 7.30 shows the work comparison for the "Vardanega and Bolton" soil response. As stated earlier the higher number of timesteps and their arrangement can be seen. The energy gaps are still too negligible to see any daylight between the curves plotted.

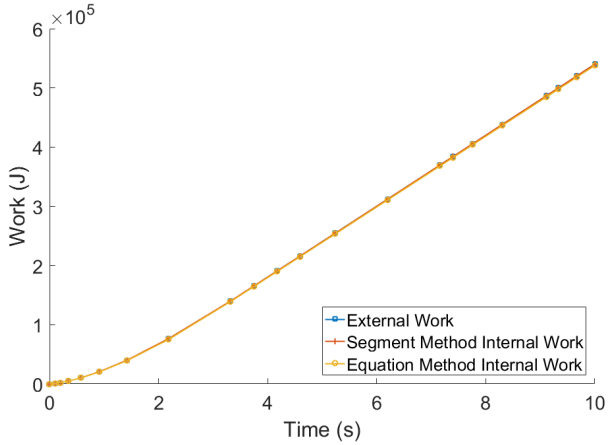

FIGURE 7.30: The cumulative internal and external work for the FEA Unfixed y Shear case modelled with the "Vardanega and Bolton" soil response.

7.3.5 Rotating Wall FEA dataset

The rotating wall datasets represent the next increase in complexity for analysis. As before ABAQUS decided how many timesteps to use for the modelling with 21 being chosen for the "Vardanega and Bolton" soil response and 12 for the elastic-perfectly-plastic. The rotating wall datasets have a significant difference to the other datasets in that load actuation was used rather than strain actuation. For the "Vardanega and Bolton" datasets this is unlikely to have much impact as plasticity was reached, the force-displacement plot can be seen to plateau as expected. The elastic-perfectly-plastic dataset however does not reach this plateau indicating that a significant number of elements are still in the elastic part of the curve with only a few deforming plastically.

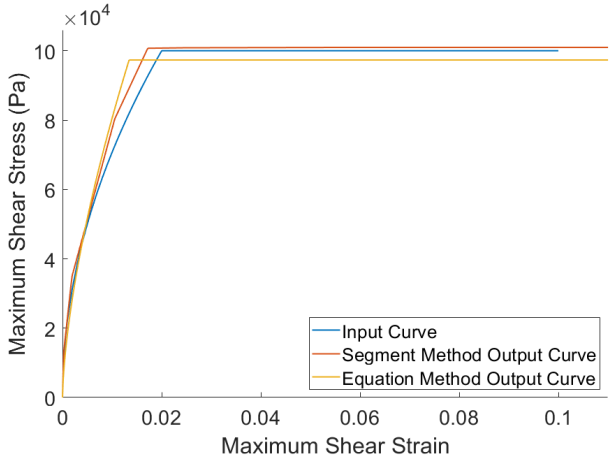

FIGURE 7.31: The input and output stress-strain curves for the FEA Rotating Wall case modelled with the "Vardanega and Bolton" soil response.

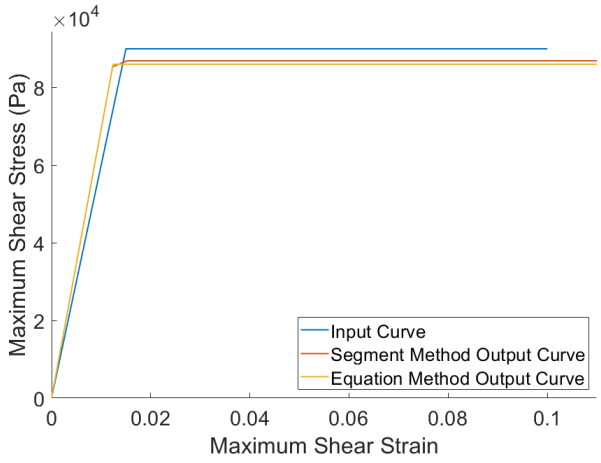

FIGURE 7.32: The input and output stress-strain curves for the FEA Rotating Wall case modelled with the elastic-perfectly-plastic soil response.

Figures 7.31 and 7.32 show the comparisons in input and output stress-strain curves. The quality of the outputs is reduced compared to the simpler datasets. c_u values differ for both stress-strain responses. The "Vardanega and Bolton" soil response has an input c_u value of $100kPa$ and has output values of $101kPa$ and $97.3kPa$ for the Segment based and Equation based approaches respectively. For the elastic-perfectly-plastic soil response which has an input c_u of $90kPa$ outputs for the two methodologies were found as $86.9kPa$ and $86kPa$ respectively. The elastic-perfectly-plastic c_u values are further from the actual value than those of the "Vardanega and Bolton" soil response, with the values for both methodologies being lower. As there is significantly lower data available to constrain the elastic-perfectly-plastic curve in the plastic section it would follow that this part of the curve would be less representative of actual behaviour. Later in this chapter the effects of trimming data at the start and end of a dataset will be investigated in order to provide insight to confirm the cause of this effect.

Despite the lower quality output the energy gaps are still very low with MOSEK indicating that an optimal solution was found. For the "Vardanega and Bolton" soil response gaps of $9.5 \times 10^{-3}\%$ and $2.3 \times 10^{-2}\%$ were found for the two methods and of $1.4 \times 10^{-2}\%$ and $2.3 \times 10^{-3}\%$ for the elastic-perfectly-plastic response. The plot comparing internal and external work is not presented for this dataset as it is extremely similar to the equivalent plots in previous sections, in which internal and external work has no visible difference.

Figure 7.33 shows the Equation based Identification Methods plots of search area for the parameters of the "Vardanega and Bolton" soil response. Note that the value of c_u is found by first assuming the soil response is elastic-perfectly-plastic. Although a plateau of reasonable values is available, the software is able to identify a single optimal curve. Of note in the example given is that a much higher resolution is needed for the b parameter. Using a

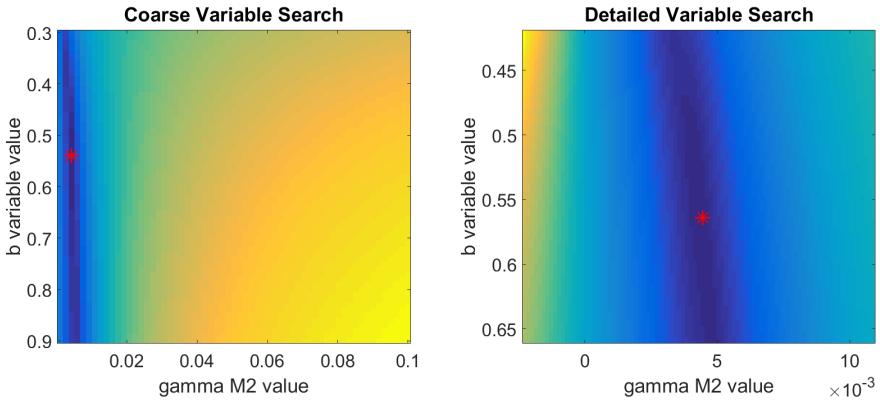

FIGURE 7.33: A set of plots showing the search area the Equation Method used for the Rotating Wall case modelled with the "Vardanega and Bolton" soil response.

coarse search followed by a detailed search has been an effective compromise in finding a good solution using this method.

It does at first appear that there are a large range of suitable values of b that are close to optimal. A side effect of the relatively large search area is that small but important differences in energy gap are hidden due to extremely high gaps that arise from very bad variable choices. To illustrate this point further Figure 7.34 shows a plot of how varying the b variable by 0.01 effects the global energy gap. All other variables were kept the same, and despite b being varied by a very small amount, it is clear that the recovered value is in fact the true optimum.

7.3.6 Simple Footing FEA dataset

The final datasets against which the Segment based and Equation based Identification Methods will be validated is the simple footing case. In these models a footing is pressed into the soil at a constant displacement rate. As well as resulting in a fairly complex strain field, these models also feature a large area in which little to no strain is present. This scenario is also most similar to the physical modelling that will be discussed in Chapter 8. Due to the increased complexity of the problem, ABAQUS assigned 31 timesteps to the solution.

Figures 7.35 and 7.36 show the comparisons in input and output stress-strain curves. Examination of the curves for the "Vardanega and Bolton" soil response show that both the Segment based approach and the Equation based approach overestimate c_u and are initially steeper. The curve for the Segment based approach also appears to have split into several straight sections as opposed to a smooth curve as has been previously observed. The observed c_u values for the two methodologies ae $104kPa$ and $103kPa$ respectively. The curves

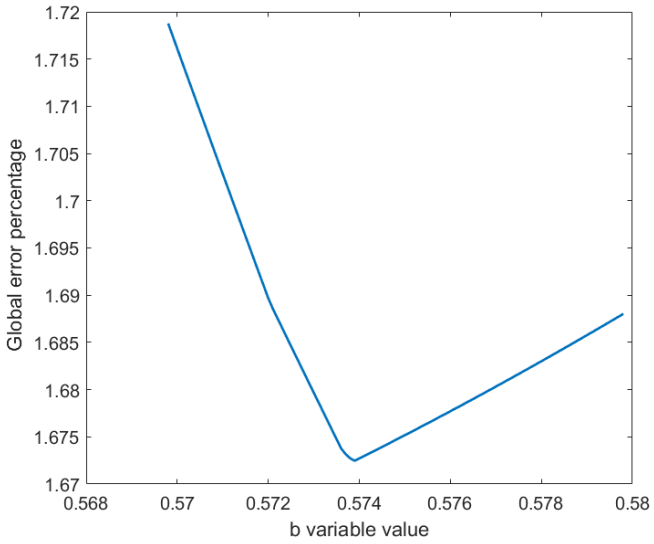

FIGURE 7.34: Global energy gap change when slighly varying b for the Equation Method used for the Rotating Wall case modelled with the "Vardanega and Bolton" soil response.

for the elastic-perfectly-plastic soil response however have found approximately the correct c_u values, with the elastic part of the curve being slightly steeper than expected. Additionally, the Segment based approach has cut the corner at the interface between elastic and plastic behaviour.

As with the previous scenarios, despite by eye the output curves not matching the input curves, the optimiser reports that an optimal solution is found for the segment method and the percentage global energy gaps are fractions of a percent. For the "Vardanega and Bolton" soil response the gaps are 3.7×10^{-2}% and 8.9×10^{-3}% for the segment and equation methods and for the elastic-perfectly-plastic soil response 2.2×10^{-1}% and 5.7×10^{-3}%. Of note is the energy gap for the segment method's attempt at the elastic-perfectly-plastic soil response. It has by far the highest energy gap observed so far. Examining the curves, it is clear that in this case the equation method has found a much more suitable possibility, despite this however, manually forcing the Segment based method to use the input curve results in a larger error gap percentage of 0.43% that is almost double the error for the recovered curve. This indicates that the recovered curves truly are the best fit for the provided datasets in terms of minimising the gap between internal and external work, even if they do not match with the curve that would be expected based on the soil response input into the FEA software.

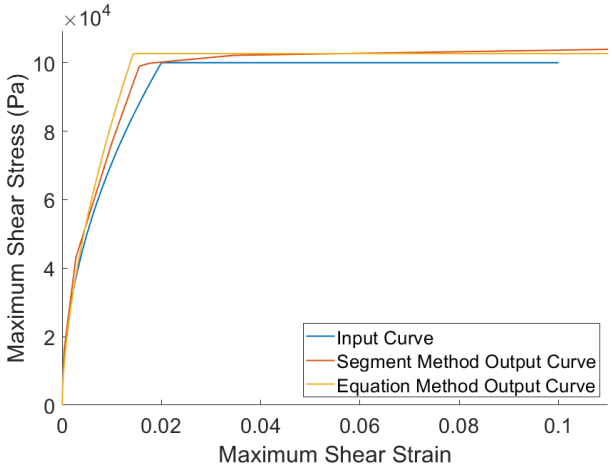

FIGURE 7.35: The input and output stress-strain curves for the FEA Unfixed y Shear case modelled with the "Vardanega and Bolton" soil response.

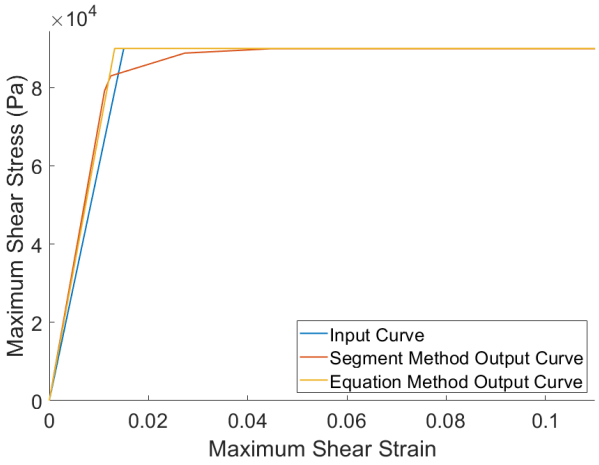

FIGURE 7.36: The input and output stress-strain curves for the FEA Unfixed y Shear case modelled with the elastic-perfectly-plastic soil response.

7.3.7 Overall Commentary on Validation Process

In the previous subsections it has been demonstrated that both the Equation based and Segment based Identification Methods are able to recover realistic stress-strain responses. In some cases, particularly for more complex examples, the stress-strain curve recovered is slightly different that the input curve. Some possible reasons for this have been identified such as the location and quantity of timesteps. This idea will be investigated in the following section.

Also to be investigated is the number of increments used in the segment method. All the examples specified use 100 segments in the output stress-strain curves but this number can be set to anything. The arrangement of the segments is chosen programmatically such that

each segment includes roughly the same amount of data. Segments in areas with lots of data, typically at low strain levels, will be very small in relation to segments in areas with less data, typically high strains. To some extent the discretisation into segments will effect the shape of the curve. If the elastic limit in reality is at 0.015 but there is a segment that starts and ends at 0.0145 and 0.0155 then the output response cannot possibly have the correct elastic limit. This is not something that can happen with the Equation based approach in which the interface between differing parts of the curve can move.

Another point raised is that the output curves are in fact the optimal shape. This is dependent on the formulation of the problem, as the correct answer to the wrong question is still a wrong answer, but as identical input and output curves are attainable for very simple cases it would appear that the problem formulation is correct. For the elastic-perfectly-plastic soil response for the simple footing, the actual input curve used in the FEA model was manually selected and the global error percentage was nearly double that of the "ugly" curve that the Segment based Identification Method recovered. There is the possibility that the recovered curves for the scenarios discussed above are just one of many possibilities that are largely the same error, or within the tolerance of the optimiser, but test such as this indicate that this is not the case. The MOSEK optimiser indicates that the outputs for the more complicated cases are the optimal answers. It was only for the simplest case, in which the output curve is by eye correct, that MOSEK reported being near optimal rather than optimal. The Equation based method is guaranteed to find the true global minimum provided that the search area is realistic and sufficient resolution is provided. The plots of search area for the "handmade" split case and the rotating wall demonstrate this.

A final possibility is that ABAQUS is behaving differently than expected. The FEA datasets were modelled assuming isotropic soil with a Poisson's ratio of 0.499 with the input stress-strain response chosen as the soil behaviour. For the simple shear case, the displacement and strain fields can be directly compared between the "handmade" and FEA datasets and they are identical. Nodal displacement, strain, and force start and end at the same values and increase linearly with the only difference being the arrangement of timesteps. This example however is pure shear strain. No volumetric strain is present. The more complex cases do feature volumetric strain with some elements increasing in size while others get smaller, with the overall volume change being approximately equal to zero. The assumption of both of the Identification Methods in their current implementation is that volumetric strains acting in such a way would lead to zero work done, and although the problem in ABAQUS has not been specified in any way that should contradict this, the internal workings of the software are opaque. Unfortunately, it is not possible to produce "handmade" datasets for comparison for the more complex cases.

A possible cause of the small discrepancies relating to the implementation in ABAQUS the

discretisation process. 6-Node triangles were used for the mesh in ABAQUS in order to generate the displacement field. Every node was taken (both corner and edge) from the array of 6-node triangles to produce a uniform grid which was then triangulated into 3-node triangles as part of the pre-processing of the Identification Method procedure. This conversion to lower order triangular elements is a potential source of error. This is either due to spurious volumetric strain being introduced at the expense of shear strain or a mismatch in internal work. In a scenario in which both stress and strain are known, the work done to a 6-node triangle could be trivially be calculated. Splitting this 6-node triangle into four lower order 3-node triangles and calculating internal work would not necessarily produce the same result.

Despite the slight discrepancies between input and output curves the results of this validation are very promissing. Of particular note is the fact that the c_u values recovered, a key parameter in geotechnical design, are always within a few percent of the expected value.

In the following sections the aforementioned investigations into the arrangement of timesteps and segment method increments will be presented, followed by the artificial degradation of this "perfect" data.

7.4 Investigation into Segment based method increments

One key variable in the Segment based Identification Method is the number of segments used in the curve. A curve with only a handful of segments will have a poor resolution and would be unable to recover stress-strain responses with any degree of nonlinearity. A curve with many thousands of segments would take a very long time to run and may provide no benefit. All the datasets used in the validation section used 100 segments. This section will vary the number of segments to see how it affects output curve shape and global error percentage. A subset of the previously described models will be used for this.

First examined will be the "handmade" split shear case. This model has a near perfect output curve for the validation case with 100 increments and as such serves as a useful benchmark. In order to investigate the effects on increment (or segment) numbers, the dataset was input into the Segment based Identification Method for a range of increment numbers. Figure 7.37 shows a comparison between a subset of the output stress-strain responses.

It is clear to see in Figure 7.37 that increasing the number of increments improves the quality of the output curve. As the soil response in question is elastic-perfectly-plastic it could theoretically be described perfectly with only two increments, one for the elastic phase and one for the plastic phase. The Segment based Identification Method however distributed the start and end points of increments based on the distribution of strains. This means that

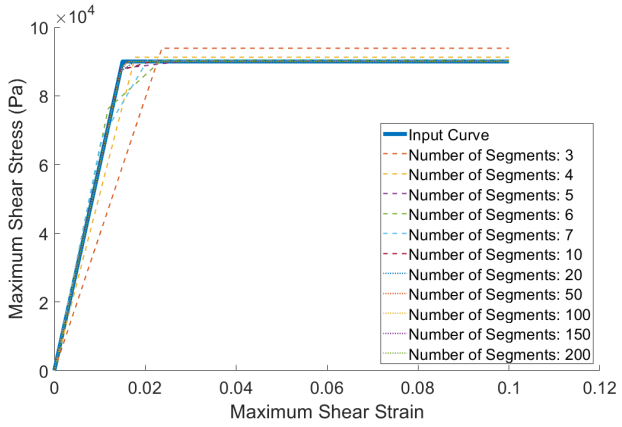

FIGURE 7.37: The stress-strain curves for the "handmade" split shear case modelled with the elastic-perfectly-plastic soil response for a range of Segment Method increment numbers.

for such a simple stress-strain response the main issue with a small number of increments is that they are unlikely to line up with the input curve.

Perhaps the biggest disadvantage of the Segment based Identification Method is that the arrangement of increments is fixed and cannot be adjusted in the strain axis. Despite this the optimiser attempts to get the best output curve even with lower resolution. Examining the curves for three and four increments it can be seen that if the limitation of few increments forces an underestimate early in the stress-strain curve, the lost energy can be made up by overestimating a later part of the curve. The areas under the curves shown however is not likely to match due to different parts of the curve being used by differing amounts in different timesteps, although for the split shear case the distribution of strains throughout the curve is more uniform than is likely to be found in more realistic datasets.

Figure 7.38 shows a plot of global error percentage against number of increments. As predicted this quickly drops as the number of increments increases. For the very worst case with only a three increments available the energy gap is 1.55%. This represents the difference between internal and external work should the soil behaviour be assumed to be the recovered curve. Despite being a seemingly small value the stress-strain response associated with it is unsatisfactory.

Of note in the plot is the fluctuations in global error percentage when single digit numbers of increments are used. This is likely due to whether the boundaries of the specified increments happen to line up with the actual elastic limit. As the number of increments increases this becomes less of an issue with there always being a relatively close increment available to capture curve features such as elastic limit. It can be seen that any increment number after 50 has roughly the same global error percentage. Increasing the number indefinitely offers

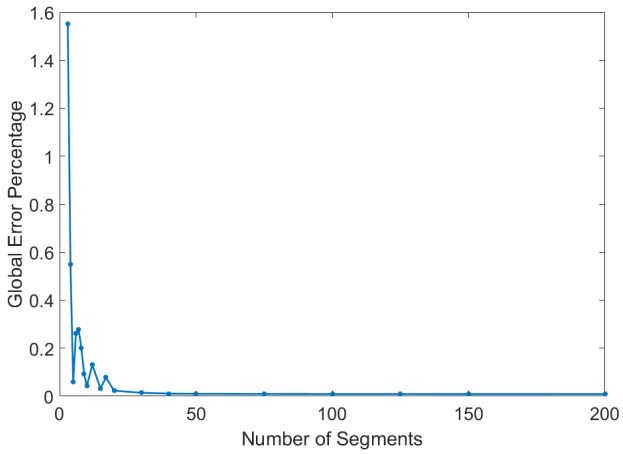

FIGURE 7.38: Global error percentage against increment number for the "handmade" split shear case modelled with the elastic-perfectly-plastic soil response.

no further improvement, and although it has no negative effects on error or curve shape, it is time consuming to have too many. 100 was chosen to ensure that there are more than enough increments while not taking an unreasonable amount of time.

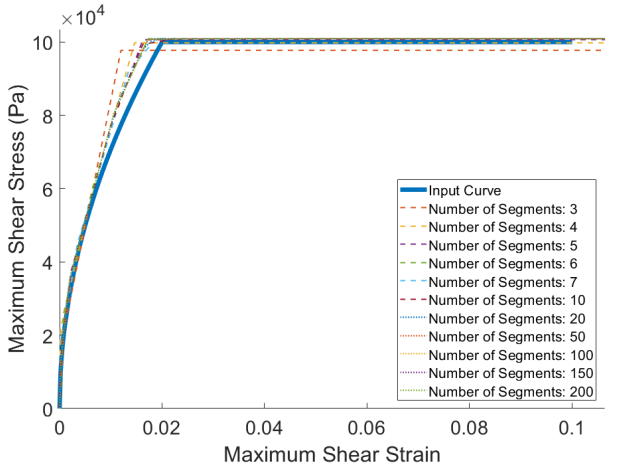

FIGURE 7.39: The stress-strain curves for the FEA rotating wall case modelled with the "Vardanega and Bolton" soil response for a range of Segment Method increment numbers.

Figure 7.39 shows the recovered stress-strain responses for the FEA derived rotating wall dataset modelled using the "Vardanega and Bolton" soil response. Although the response presented in the validation section for this dataset isn't quite as good a match with the input as the simpler "handmade" cases it still was acceptably good. This model also has a much more complicated mechanism with elements in each timestep undergoing strains at various parts of the stress-strain curve.

As before, the recovered curves become closer to the input curve as the number of segments increases. The curves in general are much better than for the elastic-perfectly-plastic case discussed previously, with even the three increment curve being of an acceptable standard. The c_u values for every number of increments is not only consistent but also approximately the same as the input curve. It appears that the rounded "Vardanega and Bolton" curve is much easier to fit a low resolution segmented curve to than the elastic-perfectly-plastic. This dataset also has the advantage that low strain elements are overrepresented in the model due to there being areas of relatively low movement, forcing the distribution of increments to mostly be in the curved part of the soil response.

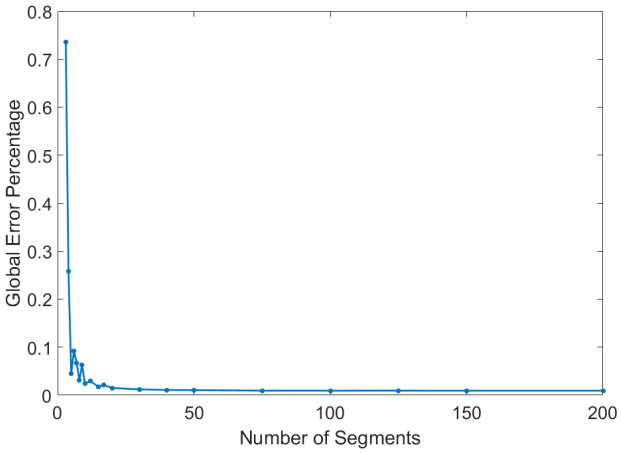

FIGURE 7.40: Global error percentage against increment number for the FEA rotating wall case modelled with the "Vardanega and Bolton" soil response.

Figure 7.40 shows how global error percentage changes with increased increment number for the rotating wall case. The insights gained via this figure are largely the same as those of the split shear case discussed previously. Of note is that the global error percentages found are generally lower than for the split shear case, with the highest value for the three increment recovered response being approximately half. As stated, due to the general higher quality of responses found this is to be expected.

This investigation into the effects of number of increments on the output of the Segment based Identification Method has a few key findings. Firstly, increasing the number of increments has a positive effect on both the quality of the recovered curve and the global error gap. Secondly, there are diminishing returns for further increasing the increment above 50 or so. The choice to use 100 increments as a standard recommended amount is reasonable with this in mind. Thirdly, the issue with low numbers of increments is that they likely do not line up with features of the stress-strain response that need to be captured such as the elastic limit. The exact shape of the true soil response and the distribution of strains will determine how pronounced this effect is. Overall, although the recovered curves are sensitive

to the number of increments used, it is straightforward to use a sufficiently high number that this isn't a major problem.

7.5 Investigation into timestep quantity and spacing

The comparison between the "handmade" simple shear datasets and the FEA simple shear datasets identified a discrepancy that investigation into could potential provide insight into the capabilities of the proposed Identification Methods. The two simple shear datasets were specified to be identical with the same linearly increasing displacement and strain, with the same force response. The only difference was the arrangement of timesteps. The "handmade" models had 50 evenly spaced timesteps across 10 seconds whereas the FEA models had 11 timesteps, with over half of them in the first 2 seconds.

As the stress-strain responses recovered from two otherwise identical scenarios differed, this phenomenon has been chosen for further experimentation. The "handmade" simple shear dataset with the "Vardanega and Bolton" soil response will be used for this as it trivially easy to specify the timesteps in an arbitrary manner and the dataset is known to otherwise present no issues.

Although the FEA datasets have highly irregular timestep arrangements, this would be hard to vary in a consistent manner such that graphs for comparison can be plotted. As such for this section the timesteps will still be evenly distributed, but simply increase in number, from 2 in which all nodes start at zero displacement in the first step and are at final displacement in the last step, to 50 as used for the validation examples. Despite this, the timesteps that the simple shear FEA model used were manually input into the "handmade" model generation script and it has been confirmed that exactly the same dataset is produced.

For very low numbers of timesteps a lot of detail will be lost for both internal and external work. For only 2 timesteps both the Force-Displacement plots and Strain-Time plots will simply be a straight line. Unfortunately the implementation of the Identification Methods does not allow for such low numbers of timesteps. 2 timesteps will simply not work due to code that interpolates data with time for cases where the internal and external timesteps do not match. The built in Matlab functions used for this process require at least 3 points. 3 timesteps is theoretically possible, however for the simple shear dataset in which all elements have the same shear strains the Segment based approach is unable to find suitable locations for the strain increments if the recommended increment number of 100 is used. Reducing the number of increments can solve this problem but for uniformity of testing the effects of changing timestep numbers, 5 will be used as the starting point.

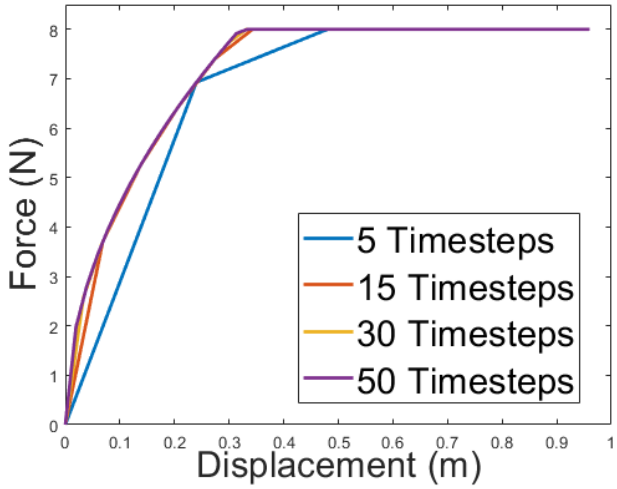

FIGURE 7.41: A plot showing how altering the number of timesteps affects the force-displacement curve for the "handmade" simple shear case modelled using the "Vardanega and Bolton" soil response.

Figure 7.41 shows the effect of reducing the temporal resolution on the force-displacement curve. Shown is a subset of the timestep numbers tested. It can be seen that the same final force and displacement are reached. Also of note is that the curves for lower numbers of timesteps are simply connecting points on the higher timestep curves. Vertices for the 5 timestep curve are clearly at points on the 50 timestep curve, as are vertices on the intermediate resolution curves.

As external work is the integral of the force-displacement plot, i.e. the area under the curve, it appears that lowering the temporal resolution in this way reduces external work. Examining by eye the area under the curve between a displacement of 0.24m and 0.48m it is obvious that the 5 timestep curve represents less external work than the 50 timestep curve. Due to this, it would be expected that recovered stress-strain responses will be altered such that less internal work is present.

Figures 7.42 and 7.43 show how the recovered stress-strain response varies with a subset of trialled timestep numbers for the Segment based Identification Method and the Equation based Identification Method respectively. As per the verification section earlier in this chapter, the 50 timestep curve is very close to the input curve which has been omitted to increase readability.

It is clear that the quality of the recovered stress-strain responses worsens with lower numbers of timesteps. For the segment method the shapes of the recovered curves have stayed suitably curved, the 5 timestep curve retains the familiar "Vardanega and Bolton" shape despite the force-displacement curve being particularly segmented. The curves with lower

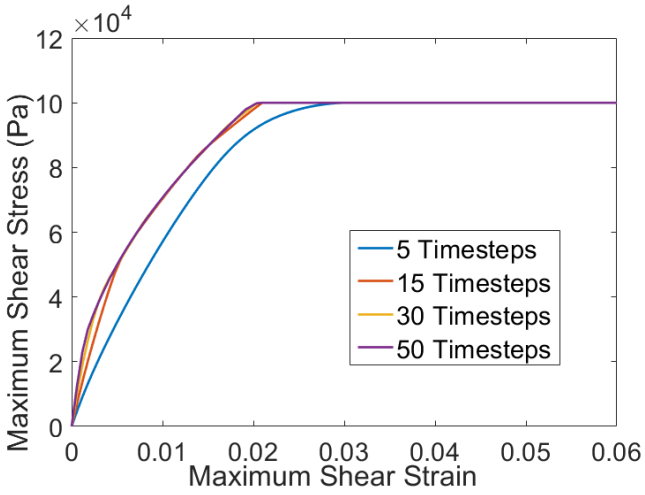

FIGURE 7.42: A plot showing how altering the number of timesteps affects the stress-strain curve recovered using the Segment based approach for the "handmade" simple shear case modelled using the "Vardanega and Bolton" soil response.

timesteps (including others trialled but not presented for clarity) are below the curves with higher numbers of timesteps. As stated previously, lowering the temporal resolution resulted in a reduction in external work, and as such an equivalent reduction in internal work is to be expected. The Equation based identification is similarly, if slightly less, effected in this manner.

Not presented, due to the plots already having several overlapping lines, were cases in which 100 and 1000 timesteps were used. Increasing the temporal resolution to such a degree has no further impact on the quality of the recovered stress-strain responses. There was however a noticeable increase in time to run the code, with the Equation based approached being extremely time-consuming for such large datasets.

A final point of consideration is that the c_u values remained unchanged regardless of temporal resolution. By eye, all recovered curves have the correct c_u value, and examination of the raw data indicated that the highest discrepancy is less than a thousandth of a percent higher that the expected value of $100kPa$. Depending on what parameters are needed for future use (e.g. design) even datasets with low numbers of timesteps could be of use.

The presented investigation has been based on the assumption that the distribution of timesteps is uniform, which wasn't the case for the FEA dataset that identified this potential issue. A thorough investigation into arbitrary timestep arrangements will not be included as there would be a near infinite amount of combinations and also that irregular arrangements are unlikely with real datasets in which data will be recorded fairly regularly by a digital camera.

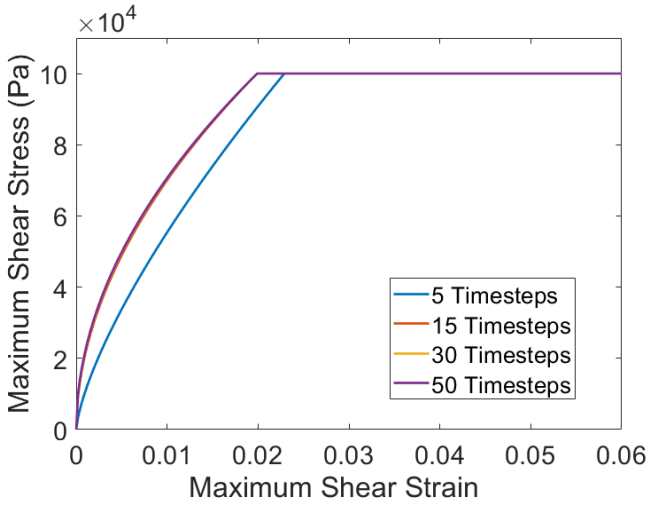

FIGURE 7.43: A plot showing how altering the number of timesteps affects the stress-strain curve recovered using the Equation based approach for the "handmade" simple shear case modelled using the "Vardanega and Bolton" soil response.

Despite these reasons, a simple trial has been carried out. Two datasets were produced, the first in which the first quarter of the time range is modelled with the resolution of the 50 timestep models, and the rest with just one timestep per quarter, and the second model with the inverse, the first quarter now has one timestep at zero, with the other $\frac{3}{4}$ of the dataset at the full resolution.

Figures 7.44 and 7.45 show comparisons between the expected and output stress-strain responses for the two scenarios, with Figure 7.44 being the case in which the first quarter is high density data with the rest being sparse, and Figure 7.45 is the case where the first quarter data is very sparse with the rest high density.

It would be possible to tell these figures apart even without labels. The Segment based approach effectively ignores parts of the stress-strain response in which there is no data. In the case where the first $\frac{1}{4}$ of the time range is dense, the output curve follows the input curve exactly, after which it cuts the corner and enters the plastic deformation phase. The case where the first $\frac{1}{4}$ is sparse simply draws a straight line from the origin to the point where the dataset has actual values again, after which the input curve is almost exactly matched.

The likely reason behind this is the same as what was proposed for the uniformly spaced timesteps. The areas with low density have effectively connected the dots for the force-displacement curve which lowers external work. Internal work must additionally be lower, however in this case this change has been applied only to a subset of the time range, with the rest of the external work being unchanged. The stress-strain curves have been affected this

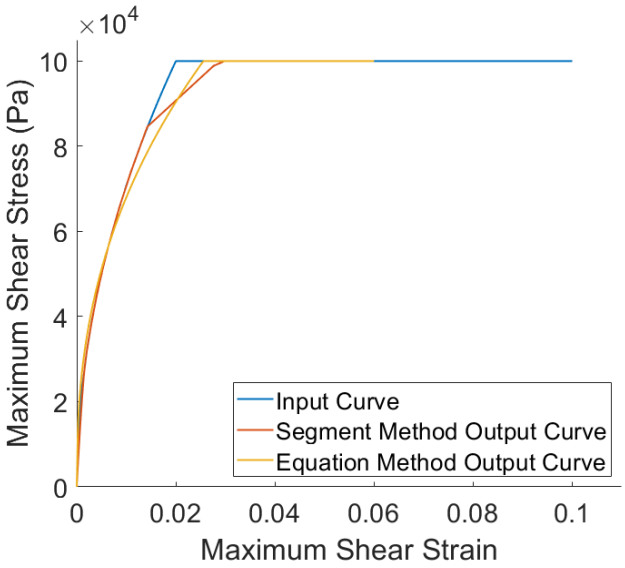

FIGURE 7.44: The recovered stress-strain curve "handmade" simple shear case modelled using the "Vardanega and Bolton" soil response in which the last $\frac{3}{4}$ of data are at a very low temporal resolution.

way to allow for energy equilibrium in all parts. The curves recovered using the Equation based approach can be seen to be slightly higher than the expected curve in the dense time ranges and lower in the sparse time ranges. The Equation based curves are a single discrete entity so a compromise has to be made between lowering them for the sparse time ranges and keeping them the same for the dense time ranges.

It is likely that what is being observed is an artefact of the special case of simple shear. In this model strain is uniform in every element and increases linearly. The data for a single timestep is fully contained within one discrete part of the stress-strain curve with no overlap. A more complex strain field would still be effected but since the stress-strain curve is a lot more self constrained the effect would depend on the dataset in question. As with what was observed with the Equation based approach, the Segment based approach would need to find a compromise to ensure the lowest energy gap.

It has been shown in this section that both proposed Identification Methods are affected by the arrangement of timesteps in the datasets. Fortunately, both the irregularity observed in the FEA models, and the extremely sparse temporal resolutions trialled in this section are unlikely in real data. A camera can be programmed to take photos regularly, and LVDTs and Load cells will have sample rates at least one order of magnitude higher that the cameras frame rate. Another finding from this section is that more timesteps is better, provided the computational time is acceptable.

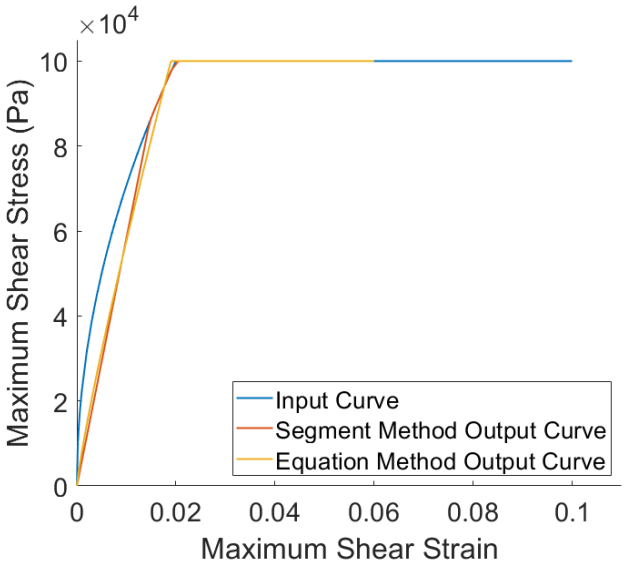

FIGURE 7.45: The recovered stress-strain curve "handmade" simple shear case modelled using the "Vardanega and Bolton" soil response in which the first $\frac{1}{4}$ of data are at a very low temporal resolution.

7.6 Artificial degredation by addition of random noise

Perfect artificial datasets are by definition perfect. Nodal displacements are known exactly to a large number of significant figures. There are no photogrammetric issues with lens distortion and no grainy images are taken and PIV is unnecessary to obtain the displacement field. Real data will have the aforementioned issues and potentially more. Many of these issues can be summed up as noise. Noise is random and unwanted variations to the dataset. A scheme by which noise can be artificially applied to the perfect FEA or "handmade" datasets was described in Chapter 5.

It was predicted in Chapter 5 that the addition of noise would affect the strain field by causing maximum shear strains to increase in general while causing no change in total volumetric strain (although some elements will change in size the sum of these changes will on average be zero). The predicted result of this general increase in maximum shear strains was that the stress-strain curves will be lowered, i.e. the observed c_u values will be lessened with increasing addition of noise.

Noise will be added in two separate ways. The first is the addition of noise as a normal distribution, and the second is the addition of noise using a uniform distribution. The first methodology will have a higher proportion of noise added be closer to zero. Noise will be added as a percentage of mean displacement with a range of values trialled. Plots will be presented showing how varying the amount of noise effects key parameters of the recovered

stress-strain curves such as c_u.

This section will present the results of this investigation. The "handmade" split shear case will be used for this analysis and will be degraded through the addition of noise, with the changes in c_u recorded and analysed.. As well as being a case that has near perfect results from the validation process, the relative uniformity facilitates adding noise in the manner discussed. Cases such as the simple footing dataset have small areas of very high displacement and vast areas with very low displacement so the addition of noise based on mean observed displacement shows no effect for low percentages of noise, and high percentages of noise effectively make the actual observed deformations irrelevant. Using the simpler split shear dataset allows for meaningful analysis of noise, with up to 7.5% of the mean displacement added, an amount that far exceeds what would likely be observed in laboratory testing. It should be noted that all testing carried out in the section used 100 segments for the Segment based approach and the full temporal resolution of 50 timesteps for both Identification Methods.

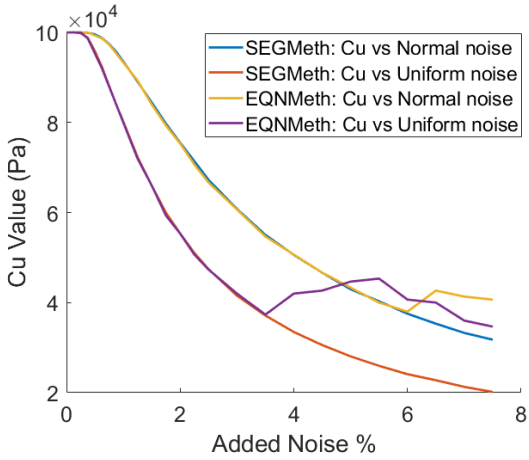

FIGURE 7.46: A plot showing how c_u varies with the addition of noise applied to the "handmade" split shear case modelled using the "Vardanega and Bolton" soil response.

Figure 7.46 shows the results of varying the amount of noise added for the "handmade" split shear case modelled with the "Vardanega and Bolton" soil response. As predicted, increasing the amounts of noise results in the observed c_u values being lower. Interestingly, the plot of c_u against noise percentage is initially fairly flat, indicating that low amounts of noise produce little effect, before dropping significantly and finally starting to level out again. This levelling out is likely when the added displacements start to significantly overwhelm the actual soil movement. Although 7.5% of the mean displacement may seem a low amount, it is of displacements across all timesteps and is applied in both the x and y directions, so data that is essentially simple shear will soon become meaningless, particularly in earlier timesteps.

With the Equation Based approach the plot soon flattens out and begins to fluctuate. This is due to the lower limit of the search area being reached. As per Chapter 4, when the Equation based approach is used in a brute force approach, limits to curve parameters must be selected. Lowering these limits would likely cause the noise plots to continue in the same pattern as those of the Segment based approach, however the same settings were used as for the validation stages. Were the method to be used in practice it would require engineering judgement to select these limits and if the user were confident that the limits selected were valid, recovering a stress-strain curve that reaches these limits would serve as a useful indicator that something has potentially gone wrong.

Also of note is that uniform noise distribution has had more of an effect. This was expected as although the mean of noise added should be equal for both methods, the mean of absolute noise added will be more for the uniform distribution.

As this section deals with randomness, the presented plots would vary every time this process is carried out. In the "handmade" split shear case there are over 1000 nodes across 50 timesteps that have had a random displacement added to them. This is enough that the chances of any significant variation between repeats of this noise investigation is negligible. Initial trials indicate that this is the case. Although only one such plot is presented it serves as a useful illustration of the effects of noise.

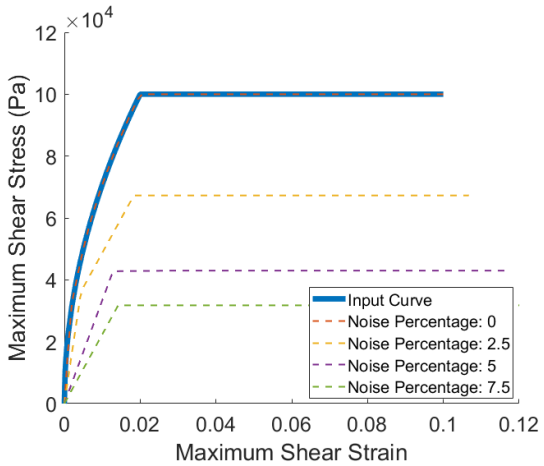

FIGURE 7.47: A plot showing how stress-strain curves recovered with the Segment based approach vary with the addition of noise applied to the "handmade" split shear case modelled using the "Vardanega and Bolton" soil response.

Figure 7.47 shows a selection of the recovered stress-strain responses obtained from the noisy datasets when using the Segment based approach. It can be seen how not only do the c_u values become lower, but the overall shape of the curves becomes worse.

Overall, it would appear that the Identification Method is resilient to small amounts of noise, however larger values, in which the signal to noise ratio is low could prevent the proposed Identification Methods from recovering suitable stress-strain curves. It is likely that preprocessing of real data will be necessary to mitigate the effects of noise.

7.7 Artificial degredation by reducing displacement field resolution

One notable downside of using FEA derived datasets for validation is that they are discrete rather than continuous as real soil is. An FEA model consists of a grid of elements with nodes, and these nodes are used as displacement points as PIV patches would be for real soil. Whereas reducing or increasing the number of PIV patches is likely to have an effect on the recovered curve due to areas of localised strain being missed, reducing the node number in an FEA model would have no such effect as there can be no detail other than that which is expressed with the available nodes. ABAQUS enforces energy equilibrium within the simulation, so despite being fewer but larger elements, recovering a stress-strain response using an Identification Method should give a similar, if not identical, result.

Although an investigation into PIV patch density will be presented in the following chapter in which real datasets will be examined, a preliminary investigation will be carried out in this section. For a subset of the presented FEA models, the effects of using only some of the available nodes will be examined. As the FEA datasets were modelled using 6-node triangles, it is straightforward to take displacements of only the three corner nodes. This will result in a simulated patch density of half that of when the full node set is used. Whereas simply running an FEA model with fewer nodes would not allow such an experiment, running a model at full density and then using only a subset of nodes as input for the Identification Method process will allow the effects of sparsity to be examined.

The FEA unfixed y shear model was examined first. Figures 7.48 and 7.49 show the strain fields, with Figure 7.48 including the full FEA nodal field in the strain calculations, and Figure 7.49 showing the strain field in which only every other node is triangulated for strain calculation. This model was tested using 100 segments for the Segment based approach and every timestep available (21) from the FEA model. No noise was added to this model for the purpose of this analysis.

As would be expected the half density grid is lower resolution but perhaps less expectedly the highest observed maximum shear strains are lower. This does not however mean that the sparser grid has undergone less straining, the mean shear strain is the same even with less nodes sampled, and summing the shear strains (adjusting for the fact one model has 4 times

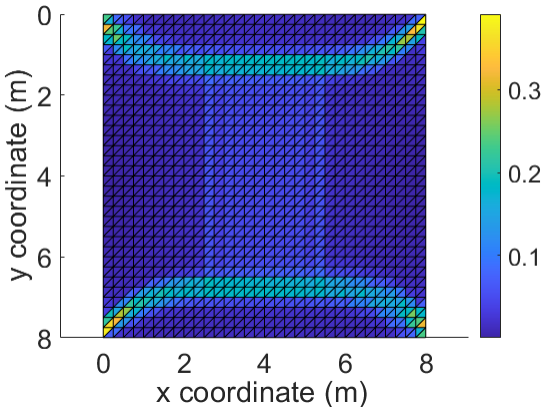

FIGURE 7.48: The strain field for the FEA unfixed y shear case modelled using the "Vardanega and Bolton" soil response with the full resolution of FEA nodes included.

as many elements) also gives the same value. These statistics indicate that the half density model hasn't ended up with smaller shear strains in the strain field, if it had the recovered stress-strain curve would be overly steep to ensure the internal work was sufficiently high.

Figures 7.50 and 7.51 show the comparison between input and output stress-strain curves for the Segment based approach and Equation based approach respectively. The first point of consideration is that although both node densities result in a different output curve, it would be hard to say that one is better than the other. The lower density model has an initially steeper response regardless of which Identification Method is used as well as a very slightly lower c_u value.

It is possible that the effects being so minimal is due to the simplicity of the problem. Although the unfixed y shear case is more complex than the true simple shear cases, as the number of sampled nodes reduces it will tend towards the simple shear case. The extreme example of sampling the four nodes in the corners of the domain for example would result in the true simple shear case. As such a more complex scenario will also be examined.

The simple footing FEA model using the "Vardanega and Bolton" soil response will similarly be examined with every other node sampled. This model features extremely high strains at small areas around the footing which will be smoothed out. The recovered stress-strain responses for the simple footing model are already of a lower quality than the curves for the simpler examples so this should be a more challenging scenario. As before, this model was tested using 100 segments for the Segment based approach with full the full temporal resulution included and no noise added.

Figures 7.52 and 7.53 show the strain field for the simple footing case at both full and halved nodal density. As before, it can be seen that the highest recorded maximum shear strain

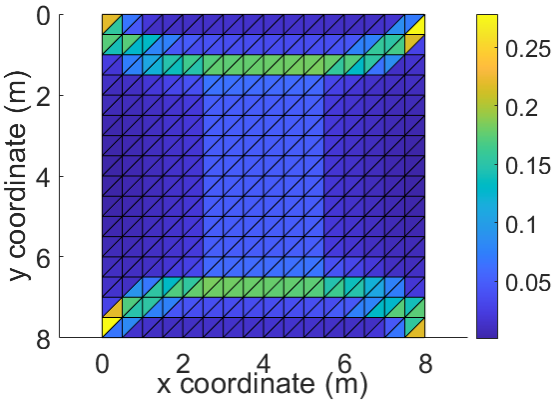

FIGURE 7.49: The strain field for the FEA unfixed y shear case modelled using the "Vardanega and Bolton" soil response with every other FEA node included.

observed is significantly lower for the model with halved nodal sampling rate. Unlike the shear case however, there is a noticeable difference in the mean maximum shear strain and the area adjusted sum of shear strains. The mean shear strain is 2.7% higher for the model using the full nodal density and the area adjusted sum of shear strains is 1.5% higher.

As there is a meaningful discrepancy between the strain fields for these two models, there will be a corresponding discrepancy between the recovered stress-strain curves. Were the same stress-strain response to be used for both cases, the sparser model with its generally lower strain values would have a lower internal work and significantly higher global energy gap. This is indeed what can be observed.

Also of note is that there is a significant increase in the values of volumetric strain measured. For the full nodal density case the sum of volumetric strains is approximately zero. This is not the case for the sparse nodal density case. As the FEA model was specified to have a Poisson's ratio of 0.5 the total volumetric strain is expected to be zero, and this is indeed the case when the full nodal density is used, however for the case in which every other node is used a total negative volumetric strain that is 4.4% of total maximum shear strains is observed. This implies the area of the soil is shrinking slightly. The most likely culprit is the soil heave at the side of the footing. By selecting every other node, what would otherwise have been a smooth curve now has had sections cut off.

Figures 7.54 and 7.55 show the comparison between stress-strain curves for the Segment based approach and Equation based approach respectively.

As the reduction in nodal sampling rate resulting in generally lower strains across the field (though the large areas of low strains are unlikely to be effected) there must be a corresponding increase in shear stresses such that energy equilibrium can be maintained. This has been

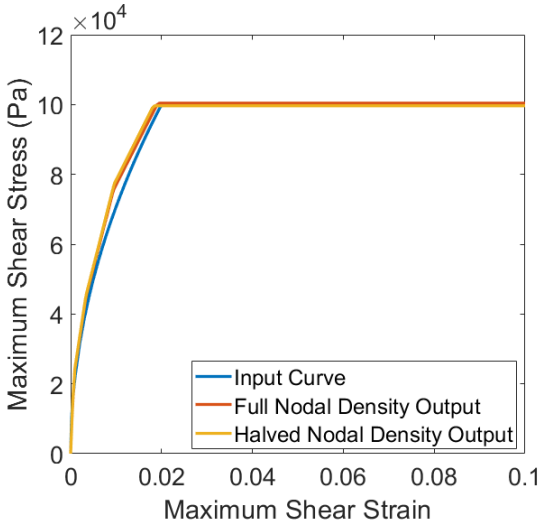

FIGURE 7.50: The stress-strain curves recovered with the Segment based approach for the FEA unfixed y shear case modelled using the "Vardanega and Bolton" soil response with varying node density.

observed for the curves recovered using both the Segment and Equation based approached. Observed c_u values were found to increase by 1.1% when reducing nodal sampling rate for the Segment based approach and by 2.2% for the Equation based approach. Further reduction in nodal sampling rate would likely cause even higher increases in c_u.

It would appear that the quality of the recovered stress-strain curves and their significant parameters such as c_u can be negatively affected should the spatial resolution be sufficiently low. As FEA models are themselves discrete there is an upper limit to spatial resolution that is guaranteed to be the best density. Doubling the nodal density by linearly interpolating new nodes for instance would be a pointless exercise. Real data however is continuous and choice must be made as to what PIV patch density to use. The findings in this section indicate that if the chosen density is low then localised features in the strain field are likely to be missed which will tend to result in lower measured shear strain values, which in turn will result in the recovered curve being either initially too steep or having an excessively high c_u value or both.

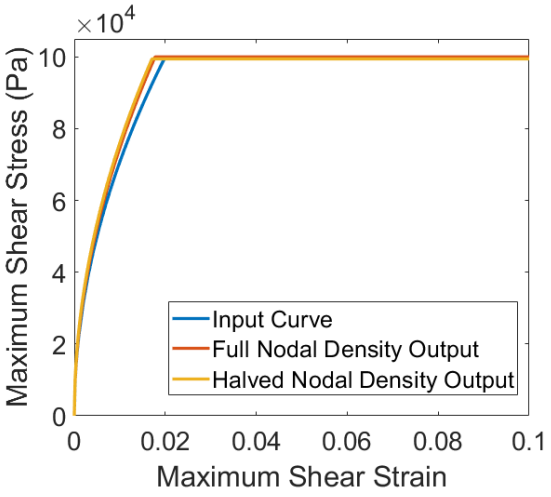

FIGURE 7.51: The stress-strain curves recovered with the Equation based approach for the FEA unfixed y shear case modelled using the "Vardanega and Bolton" soil response with varying node density.

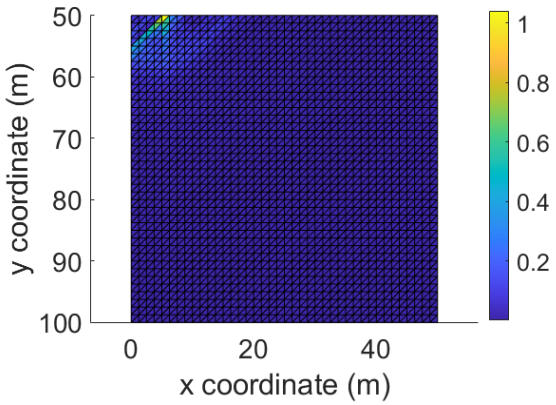

FIGURE 7.52: The strain field for the FEA simple footing case modelled using the "Vardanega and Bolton" soil response with the full resolution of FEA nodes included.

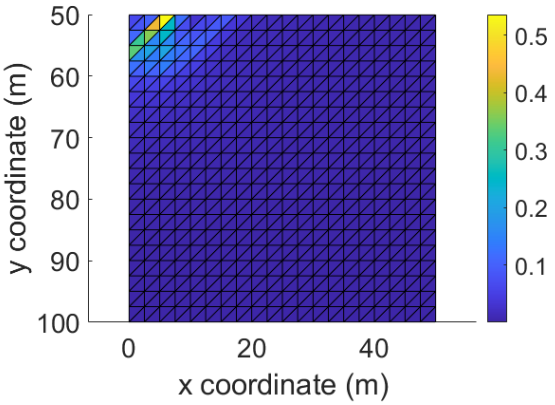

FIGURE 7.53: The strain field for the FEA simple footing case modelled using the "Vardanega and Bolton" soil response with every other FEA node included.

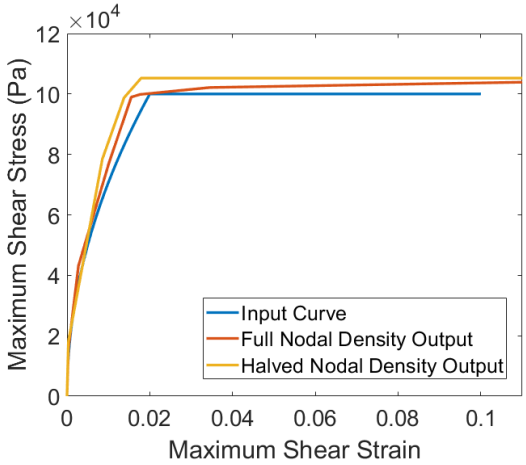

FIGURE 7.54: The stress-strain curves recovered with the Segment based approach for the FEA simple footing case modelled using the "Vardanega and Bolton" soil response with varying node density.

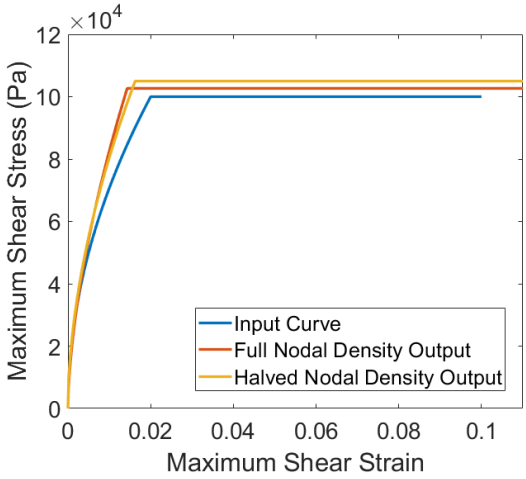

FIGURE 7.55: The stress-strain curves recovered with the Equation based approach for the FEA simple footing case modelled using the "Vardanega and Bolton" soil response with varying node density.

7.8 Conclusion

This chapter has demonstrated that both the Segment based Identification Method and the Equation based Identification Method are able to recover high quality stress-strain responses for a number of artificial datasets. Differences between different datasets were qualitatively analysed with the insights gained used to explain discrepancies in the recovered stress-strain responses. Despite slight variations, the recovered curves consistently had reasonable values of c_u which was never more than a few percent out from the expected value.

A number of supplementary investigations into the datasets were carried out, including the effects of varying the number of timesteps, where it was shown that temporal sparsity can negatively effect the quality of results. The number of increments used for the segment method was also investigated, with the key finding that more is better up to a point of diminishing returns after which unnecessary computational resources are wasted. The prediction made in Chapter 5 that increasing noise results in lower values of c_u has been confirmed. The effects of improperly trimming the datasets has also been discussed. Finally, an investigation into the effects of reducing the spatial resolution of the strain field has shown that localised features of the strain field can be smoothed out resulting in generally lower maximum shear strains and a higher c_u value.

The findings of this chapter not only demonstrate that the proposed Identification Methods function sufficiently that issues with real datasets are likely not issues of the programmatic implementation but also provides a base of knowledge by which any issues can be diagnosed and ideally solved.

Chapter 8

Analysis of Real Datasets

8.1 Introduction

This chapter will attempt to validated the proposed Identification Methods with the data derived from physical model tests. The methodology used to generate these datasets can be found in Chapter 6. The data consists of 8 simple footing tests on undrained clay, carried out at 1g with a strain based actuator. Cameras were placed on either side of the sample box, for a total of 16 sets of image data. The force and displacement of the footing was recorded using several LVDTs and a load cell.

The first section of this chapter will discuss the techniques necessary to preprocess the data into a usable form. Photogrammetric procedures will be carried out, as will PIV. PIV will have several parameters that can be adjusted, notably patch size and patch spacing. Additionally, the method by which experimental noise will be smoothed will be examined. Discussion on how the zero point of each dataset was selected will also be provided.

The second section of this chapter will present a qualitative analysis of the available data. Comparison between datasets will be given and any flaws or irregularities resulting from the laboratory processes will be identified. Initial commentary on the effects of preprocessing techniques will be given here.

Next will be the most important section of this chapter: carrying out the Identification Method processes on all 16 available datasets. The quality of the recovered curves will be analysed, with reference given to any flaws identified in the previous section. Discussion will also be provided with regards to how the preprocessing techniques used are likely to have affected the recovered curves.

After presenting the main data analysis, the assumptions made in the preprocessing stage will be analysed. An investigation into PIV patch size and spacing will presented, as will an

investigation into the effects of varying zero time. Confirmation that the smoothing scheme used is valid will also be provided.

The final section of this chapter will provide discussion and commentary on the main findings. Comparison between the artificial datasets presented in Chapters 5 and 7 and the real datasets will be given.

8.2 Dataset Preprocessing Techniques

8.2.1 GeoPIV-RG

Much of the preprocessing required for the physical modelling derived datasets has been previously discussed, either theoretically in Chapter 2 or practically in Chapter 6. A very brief summary would be that GeoPIV-RG will be used to recover movement of the soil from image data after which photogrammetric techniques will be used to remove lens distortion and refraction. Photogrammetry will be carried out as previously specified. GeoPIV-RG has a number of settings that will likely affect the quality of the results.

Many GeoPIV settings such as full field correlation tolerance and maximum number of Gauss-Newton iterations have suggested starting values with instructions in the GeoPIV documentation to gradually reduce them if the software is unable to find a satisfactory correlation. These settings will not be investigated as part of this section, instead the instructions will be followed such that the image data can be processed while keeping as close to the suggested values as possible. Table 8.1 shows the values that were used for processing the datasets. These values allowed GeoPIV-RG to find a suitable correlation in every dataset.

Parameter	**Value**
analysis_mode	2
cutoff_diffnorm	1×10^{-5}
cutoff_iteration	50
seed_zncc_tol	0.9
min_zncc_tol	0.6

TABLE 8.1: GeoPIV parameters used for processing image data.

The GeoPIV settings that will be considered are the size and spacing of the PIV patches. A patch is a region of soil that will be tracked between images through the correlation process described in Chapter 2. Small patches have less data that can be used for the correlation process but excessively large patches may have non trivial internal deformations that make finding a good correlation harder. As such it would seem apparent that there is an optimal

intermediate patch size, however this will vary depending on the expected movement and soil texture and the values used here will not necessarily be suitable for other datasets.

For the purposes of testing the proposed Identification Methods having a higher density of patches would be beneficial. It was demonstrated in Chapter 7 that reducing the resolution in artificially generated FEA datasets can cause localised features of the displacement field to be smoothed out which results in recovery of a less accurate stress-strain response. A feature of GeoPIV is that patch spacing is specified separately to patch size. This would allow for patches to be more spaced out, or much more usefully allow them to overlap. Patches sized to be large enough to allow for accurate correlation can be overlapped to provide a higher resolution displacement field. As each patch will provide a single displacement node at its centre there are no energy considerations to having an overlap. More patches however will potentially be time consuming due to the extra computational expense.

Initial informal experimentation found that patches of size 50 by 50 pixels with a spacing of 25 pixels allows for good results and this is what will be used for validation of the proposed Identification Methods. A formal investigation into the size and spacing on the outputs of the proposed Identification Methods will be presented later in this chapter for a subset of the available datasets.

8.2.2 Noise, smoothing, and spurious vectors

The PIV process can result in spurious vectors. These are nodal displacements that are by eye incorrect. An example would be a region in which most nodes are moving several millimetres to the left, amongst which there is a single node moving several centimetres to the right. These will be manually removed. The most likely location for spurious vectors is along the surface but it is possible that they could be found in the area of interest. Interpolation of missing vectors would be possible, however the Delaunay triangulation process is simply able to generate larger elements over the top of any area with missing vectors. A possible cause of these spurious vectors is regions of poor texture in which the correlation process is unable to distinguish between candidate displacements.

Another factor of preprocessing that has yet to be covered is noise. In Chapter 7 artificial datasets were deliberately degraded through the addition of noise and it was shown that doing so results in lower values of c_u being recovered. Real displacement fields are likely to have some degree of noise either resulting from the cameras or as an artefact of the PIV correlation process. As the real datasets were loaded with a monotonically increasing strain based actuation it would follow that strains should also be increasing. This is in fact an assumption made in the programming of the Identification Methods.

There would be a number of means of dealing with this such as fitting a curve or some other means of smoothing. The method that was used was to simply disallow negative differential strains. If strain at time t is less than strain at time $t-1$, strain at time t is set to be equal to strain at time $t-1$. It was found in initial experimentation that elements in which strain is a constant value (i.e. zero) were showing fairly large fluctuations such that counting them as expended energy would significantly degrade the quality of the recovered curve. Removing negative differential strain in this manner eliminates this problem and does not have the possibility of incorrectly fitting a curve to elements in which the rate of strain increase may vary throughout the test. The effects of this decision will be discussed later in this chapter.

Additionally, there are likely to be large numbers of elements around the periphery of the area of interest that have negligible strains. Images were taken to allow for the largest possible area, right up to the control points, to be recorded. As stated previously, these elements in which no strains are expected are particularly susceptible to spurious work due to a lower signal to noise ratio than that which would be found nearer to the footing. Additionally, the Segment based approach functions better with data points distributed more evenly. An overwhelming amount of low strains would e.g. effect the distribution of segments. It would be possible to simple select a smaller area of interest for the PIV process, but doing so would mean the data for these unwanted regions would not be readily available should it in fact turn out to be wanted.

As such, a programmatic means of trimming these negligible strain elements was implemented. Every element whose largest strain is lower than a specified percentage of the mean strain across the entire field can be trimmed. Choosing a threshold that is too high will of course affect the quality of the recovered curve, as well as increase the recovered c_u value due to more work being done by fewer elements, and too low a threshold will have no effect what so ever. Initial experimentation (see Appendix B) indicates that a threshold of 1% of the mean observed strain has positive impact on the recovered curves. This value had negligible impact on the recovered c_u value yet significantly improved the distribution of segments throughout the strain range. For the 20mm footing tests, this process resulted in over 50% of strain elements being trimmed. For future datasets, a good value would be one that removes as many zero strain elements as possible without having a meaningful impact on the recovered c_u value. This value was used for the validation trials presented in this chapter.

As per the equilibrium equations derived in Chapter 3 there is the possibility to include work due to gravity or soil-perspex friction. The exact density of the soil and friction coefficient were not recorded. Gravity is assumed to expend a net zero overall work due to volumetric strain being assumed to be nil; the same amount of soil should be moving up

as down. This hypothesis was tested and found to be accurate, with the data presented in Appendix B. Examining the vector plots shown in the following section, this does visually appear to be the case for all non anomalous datasets. A range of friction values were trialled, from zero to the c_u values obtained from shear vane testing. It was found that the work expended due to friction was negligible. Due to these points, along with the fact that the true coefficient of friction is unknown, friction was not included in the presented analyses. As with gravity, an investigation that demonstrates the negligibility of friction can be found in Appendix B.

8.2.3 Sensor data preprocessing

As per Chapter 6, load and displacement data of the footing test will be recorded with a load cell and a set of LVDTs. The LVDTs will be placed at either side of the footing.

The sensor data, for both the load cell and LVDTs will have noise. This is typical for sensors and light smoothing was applied as standard practice with no further investigation. The Matlab "smooth" function was used which carries out a moving average filter with a span of 5. It should be noted that loads and displacements have been sampled orders of magnitude more frequently than images have been taken and as a single value of external work is needed for each timestep much of the noise in the external sensor data will be ignored as a side effect of this sampling process.

A final and particularly important preprocessing decision is how the start of a test will be determined. The reality of the footing coming into contact with the soil provides some challenges. If the footing is not exactly level for instance, work is being done only to one side of the specimen. It was observed in some cases where this happened that negative loads were recorded on the load cell due to the footing bending away from the actuator when only one end was in contact with the soil, before increasing as expected when full contact is achieved.

It was necessary to select a point from which the test can be zeroed, both the external force-displacement data and the internal strain data. With the exception of Specimen One, in which touchdown was recorded separately to the main test, it was decided that the point at which data will be zeroed is when the image data indicates both ends of the footing are fully in contact. Picking a value too early will result in excessively large loads being recorded, particularly if the absolute load is negative at the start point, and too late would result in a load that is lower.

The location of the start of the test will therefore effect the outcome of the Identification Method. It is important that consistency is achieved for all datasets to ensure the verification

process presented in this chapter is fair but as it is a manual process to select the start image there is a possibility of error.

The effects of unrecorded (or trimmed) preloading on the soil is a further source of potential error. The Identification Method assumes that the soil starts at zero stress and zero strain, but the touchdown process brings this assumption into question. As the force-displacement curve is also assumed to start at zero and is being similarly trimmed during the touchdown, it is likely that the effects will be cancelled out. An investigation into the effects of altering the start and end points of the tests will be presented later in the chapter. The procedure specified in this section, in which the start images were manually selected, was used for the verification process and was found to mostly work satisfactorily. The raw force-displacement plots can be examined in Appendix B, along with tables indicating the start and end times selected for each test.

A final point to consider is the effects of friction between the footing and the perspex window. A lubricated rubber wiper was present at each end of each footing which was designed such that friction is minimised while preventing soil movement around the footing. The friction between the footing and window would result in additional loading recorded that isn't applied to the soil, which would result in additional external work being erroneously counted. Values for this friction were recorded but ultimately not needed. The process of zeroing load-displacement at the point of full impact has the added effect of removing this additional friction load.

8.3 Qualitative and Supplementary Analysis of Real Datasets

Four specimens were produced, each of which consists of an aluminium box of size 600 by 400 by 200mm filled with kaolin clay consolidated from slurry with a final consolidation load of 200kPa. Two footing tests were carried out on the specimen, using footings of width 20mm and 40mm with a camera observing each test from both sides resulting in two sets of PIV data per footing per specimen for a total of 16. Load and displacement data for each footing test was also recorded. Chapter 6 contains a detailed description of both the equipment used and the procedures carried out as part of this suite of tests.

Additional supplementary testing was carried out on each of the four specimens, primarily in order to recover data points though more traditional means that can be compared with the outputs of the proposed Identification Methods, but also to allow for qualitative analysis and troubleshooting of potential issues. As described in Chapter 6, each specimen underwent shear vane testing and had trixial cores taken and tested. A c_u value was also obtained

through back analysis of the load displacement data using Terzaghi's bearing capacity equation.

This section will primarily deal with analysis of these supplementary tests and any insight that can be gained into the behaviour of the soil tested from them. Observations from testing will be reported where appropriate and discussed in context of the data points available. A preliminary look at the imaging data will also be given, however the PIV process will not be discussed at this time. The following section will analyse the optimal GeoPIV parameters and processes prior to carrying out the PIV process on all datasets.

Each specimen will be analysed in turn, followed by overall comparison and commentary. For illustrative purposes, an example of the raw image data can be seen in Figure 8.1.

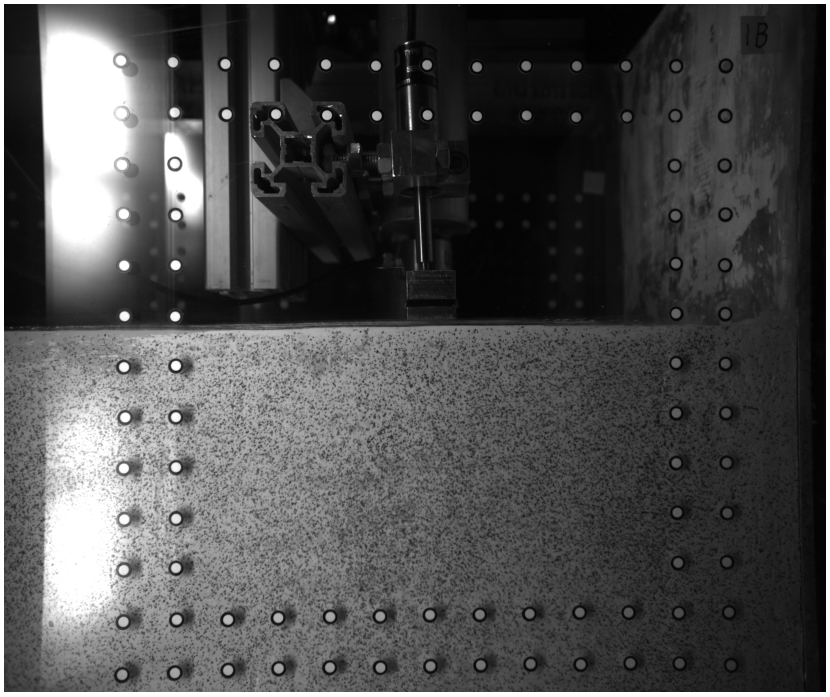

FIGURE 8.1: An example of the raw imaging data that was produced and processed using GeoPIV-RG for the purposes of this analysis.

8.3.1 Specimen One

Specimen One was the first specimen to be prepared and tested and as such had a number of issues that were ironed out with later specimens. Although this specimen is of poorer quality than the others, it is presented anyway such that the robustness of the proposed Identification Methods can be assessed when dealing with lower quality datasets.

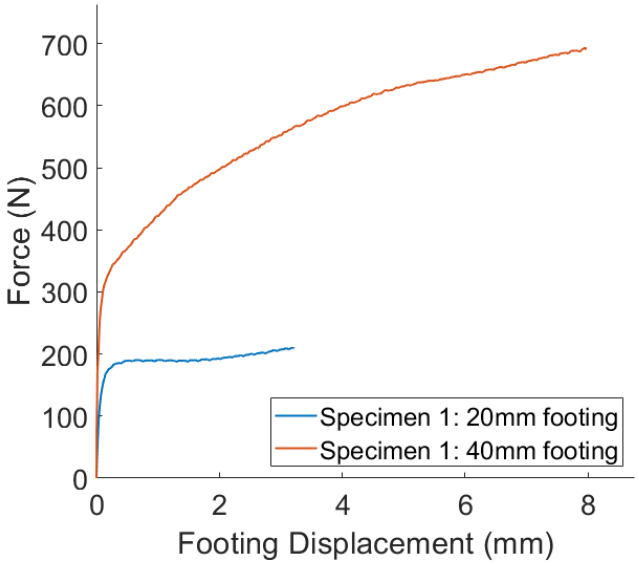

FIGURE 8.2: Central Force and Displacement for the two footing tests carried out on Specimen One.

A significant issue with this first specimen was that the consolidation top plate was slightly bent. As this plate measured 200 by 600 by 30mm and was machined from aluminium this was not expected when the plate was selected from amongst similar plates from the storage shelf. It is likely that the damage to this consolidation plate was pre-existing as it was used to consolidate clay of average strength, well within the specifications for the equipment used. Nonetheless, the top plate resulted in the final surface of the consolidated clay to not be level, with the soil at the centre of the box several millimetres lower than the edges.

This is unlikely to be meaningful in the context of the proposed Identification Methods, with the exception of possible differential consolidation which would at most be minor. One issue however is it would be difficult to begin the test with the footings properly in contact with the soil. One edge would touchdown first and would produce force and disturb the soil before the footing had made full contact. In attempt to minimise this issue, touchdown was recorded separately to the main test, with a pause before recommencing loading. Doing this enabled the loading process to be carried out with a level footing in full contact with the soil, but resulted in a degree of preloading with drainage occurring during the pause.

For later specimens in which the soil surface was level, touchdown would be recorded as part of the main test procedure, with force and displacement zeroed and the first instance the image and sensor data indicate full contact has been achieved. However in this case zeroing could be carried out only prior to starting the main test procedure which was likely later than ideal due to the unlevel surface. The outcome of this is that the forces recorded are likely to be an underestimate of what they should be, and indeed comparing Figure 8.2

with the equivalent plots for the later tests this appears to be the case.

Another issue with the first test was unexpected equipment issues resulting in a delay in testing even after the specimen was consolidated and prepared. Although the specimen was wrapped in air tight cling film, several days of midsummer heat in a non airconditioned lab potentially had a negative effect on the quality of the specimen.

Finally, floccing was insuffient to allow for the PIV process to adequatly recover the displacement field in some areas of the area of interest.

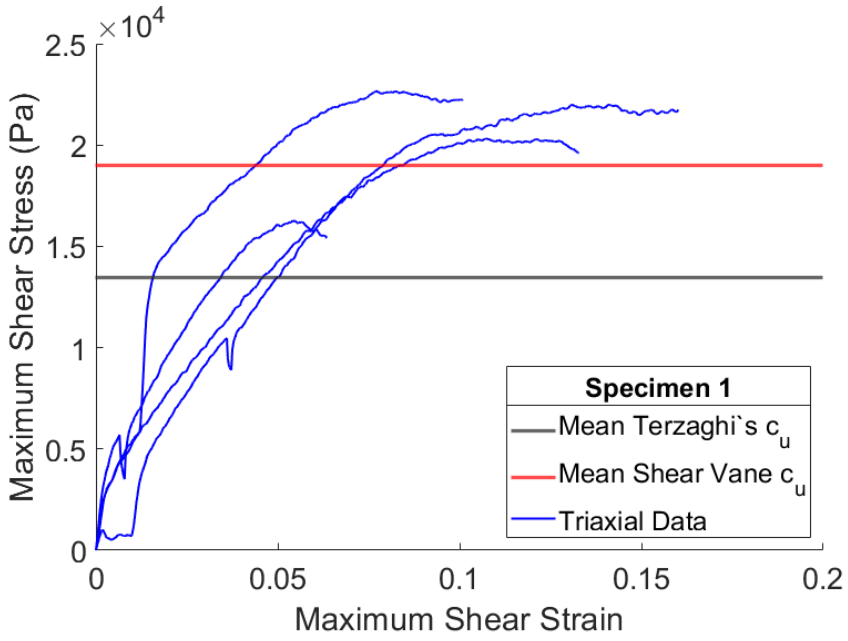

FIGURE 8.3: The triaxial and shear vane tests and Terzaghi's back analysis carried out on Specimen One.

Figure 8.3 shows the stress-strain data recovered through supplementary testing including a set of triaxial tests. Horizontal lines for the mean c_u recovered by shear vane testing is also provided, as is the mean c_u obtained by back analysis using Terzaghi's bearing capacity equation with the loading data for each of the two footings.

The intention regarding triaxial testing was that eight tests were to be carried out, with four core sample tubes used to extract soil, with each long enough to extrude two triaxial specimens. As per the figure, data for just four triaxial tests is provided. Again, a number of issues existing due to this being the first specimen were present. Two triaxial specimens were inaccessible due to one of the core tubes being several millimetres too long to fit into the extruder, which was trivially solved for future tests by selecting a different tube, and two more were destroyed by experimental error due to the soil being both softer and stickier

than the author of this work had experienced in previous triaxial testing. These issues were solved, with the full complement of triaxial tests carried out for future tests.

Several points can be made regarding Figure 8.3. Firstly, the c_u values recorded with shear vane testing are slightly lower than those of other tests. This is possibly due to variance in the consolidation process, as a particularly noisy load cell was used, or alternatively due to the specimen drying slightly as discussed earlier. Secondly, the c_u values obtained through back analysis using Terzaghi's bearing capacity equation are notably lower than both the shear vane values and the triaxial values. As previously discussed, the irregular soil and the touchdown process likely resulted in an underestimate in peak observed loading which would result in a lower c_u via Terzaghi's equation. This observation is not present to nearly the same extent in later testing with improved touchdown procedures. Finally, although there is variance between the triaxial tests, save for one lower result, three have a similar peak stress that is not dissimilar to the values obtained via shear vane testing.

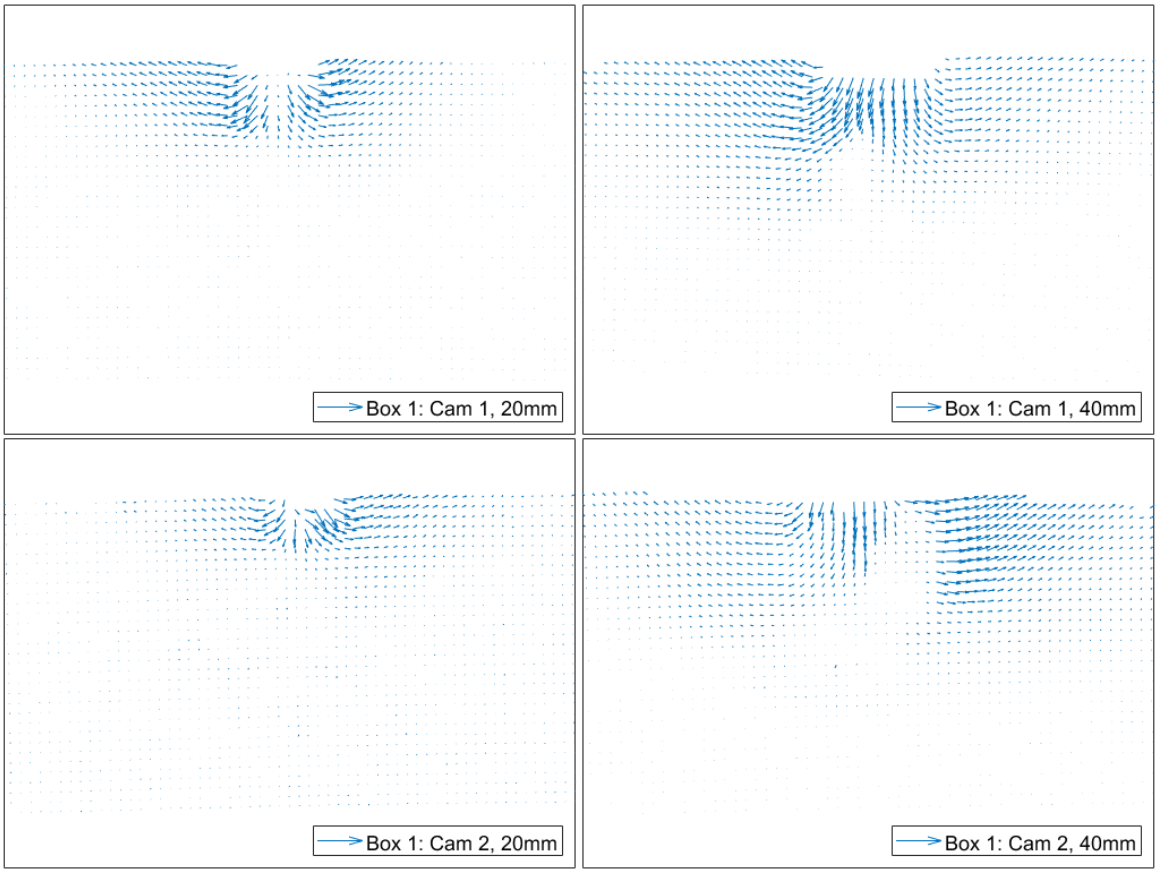

FIGURE 8.4: The PIV derived displacement fields for both cameras for each footing test carried out on Specimen One.

A plot showing vector plots representing the displacement fields obtained during testing of Specimen One can be seen in Figure 8.4. Examining the plots, it is clear to see that the

sample preparation for this first test was sub par with regards to the quality of PIV imaging data obtained.

Large areas of the field are missing from some tests, particularly for the 40mm footing in which both Camera One and Camera Two have regions with no data. Camera Two particularly is missing data in what is likely to be a key area based on the surrounding vectors. For the 20mm fields, Camera Two has some somewhat wild vectors directly under the footing. Although obvious wild vectors were removed, it was particularly difficult in this case to determine what to be removed as simply selecting all wild vectors would end up with huge amounts of data missing and as such only the most obviously unacceptable wild vectors were removed.

The effects on the stress-strain curve of having either wild vectors or missing areas will be discussed further when the results are presented, but the effects can be predicted based on knowledge of how the proposed Identification Methods function. Missing areas will have lower strain than they should, which will mean internal work that should be counted, isn't. The recovered stress-strain response will therefore have to be higher and/or steeper to make up for this. Wild vectors will have the opposite effect. They will typically cause higher strains which will introduce internal work that shouldn't be present and will result in the recovered stress-strain curve to be lower. The mechanism by which this happens is essentially the same as the randomised noise discussed in Chapter 7, albeit localised.

8.3.2 Specimen Two

Specimen 2 represented a significant procedural improvement over Specimen One. Lessons learned during the preparation and testing of the first specimen were put into practice. A new consolidation plate was assembled which resulted in a perfectly flat surface on the specimen. Floccing was carried out more thoroughly, and timing of the consolidation allowed for testing to be carried out promptly once the consolidation load was removed.

Perhaps the biggest difference is that the touchdown will now be part of the main test procedure. The footing will be lowered in one stage by strain based actuation and begin to press into the soil without pause with continuous image and sensor data recorded throughout. As described in the previous section of this chapter, for the purposes of the Identification Method the test will be considered to have commenced at the point at which both sides of the footing are in contact with the specimen. Although the surface of the specimen was flat, the floor wasn't necessarily level. A spirit level was used to manually adjust the testing box. This will be considered and discussed in the following sections of this chapter when the analysis of the datasets is presented.

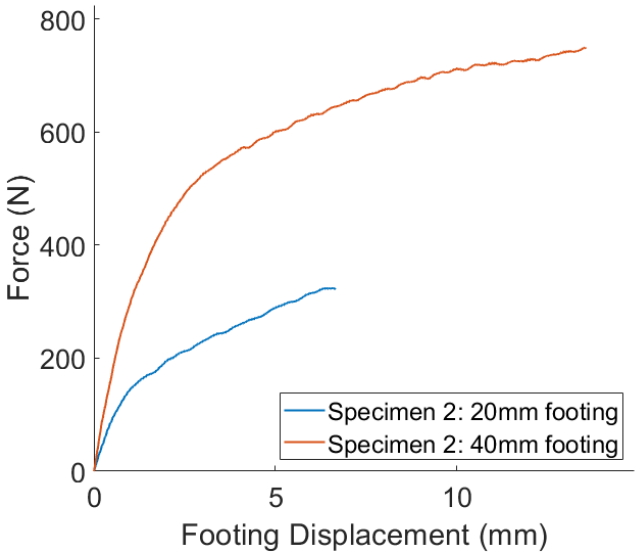

FIGURE 8.5: Central Force and Displacement for the two footing tests carried out on Specimen Two.

Figure 8.5 shows that loading is slightly higher than what was observed in specimen one. Zeroing took place at a more appropriate time without the beginning of the test essentially being missed by having a touchdown recorded separately. As would be expected, the load observed for the 40mm footing is approximately double that of the 20mm footing.

Figure 8.6 shows the supplementary data that will be used in comparison to the results of the proposed Identification Methods for Specimen Two. Both the mean shear vane c_u value and the mean Terzaghi's back analysis c_u are higher than the previous specimen and have a smaller gap between them.

Triaxial testing for Specimen Two was significantly improved over the testing carried out with Specimen One. All 8 tests were performed and, as per the figure, are mostly consistent. There was one anomalous result that was far lower and shallower than the others and has not been included.

As per Figure 8.7, the quality of the PIV data has improved compared to Specimen One for most of the datasets. Both of the displacement fields for the 20mm footing look as expected, as does Camera Two for the 40mm footing. Camera One for the 40mm footing unfortunately still has missing areas. Examining the raw images for this it can be seen that floc is sparse in the affected areas. Figure 8.8 shows a close up comparison between the floc quality of the Camera one and Camera two datasets for the 40mm footing.

It is clear to see, particularly in the 20mm datasets, that a row of vectors directly above

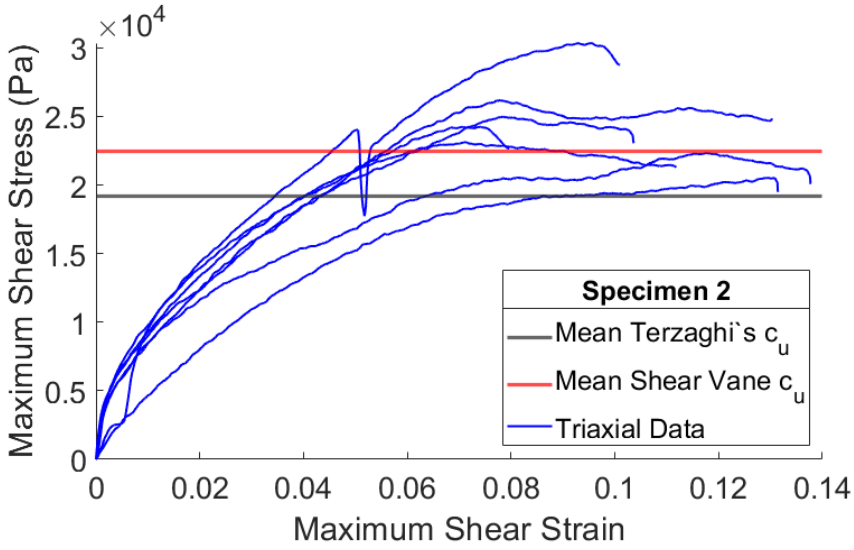

FIGURE 8.6: The triaxial and shear vane tests and Terzaghi's back analysis carried out on Specimen Two.

the footing are missing. This have been removed as wild vectors for reasons that are common throughout the four specimens. As the footing penetrates the soil, some soil moves up between the footing and the perspex window. Although there is a rubber wiper a few millimetres from the base of the footing, this few millimetres of soil movement is picked up. In some cases, upward displacement is recorded which is obviously spurious. In other cases, downward movement is recorded here, but at a lower magnitude than the row of displacement vectors immediately below, which is also incorrect but is sometimes harder to manually spot. Although the upwards movement is of only a small amount of soil, there is the potential that this would slightly increase friction between the wiper and the window.

The commentary given for the effects of missing regions or wild vectors on the displacement fields of Specimen One is also valid for this case.

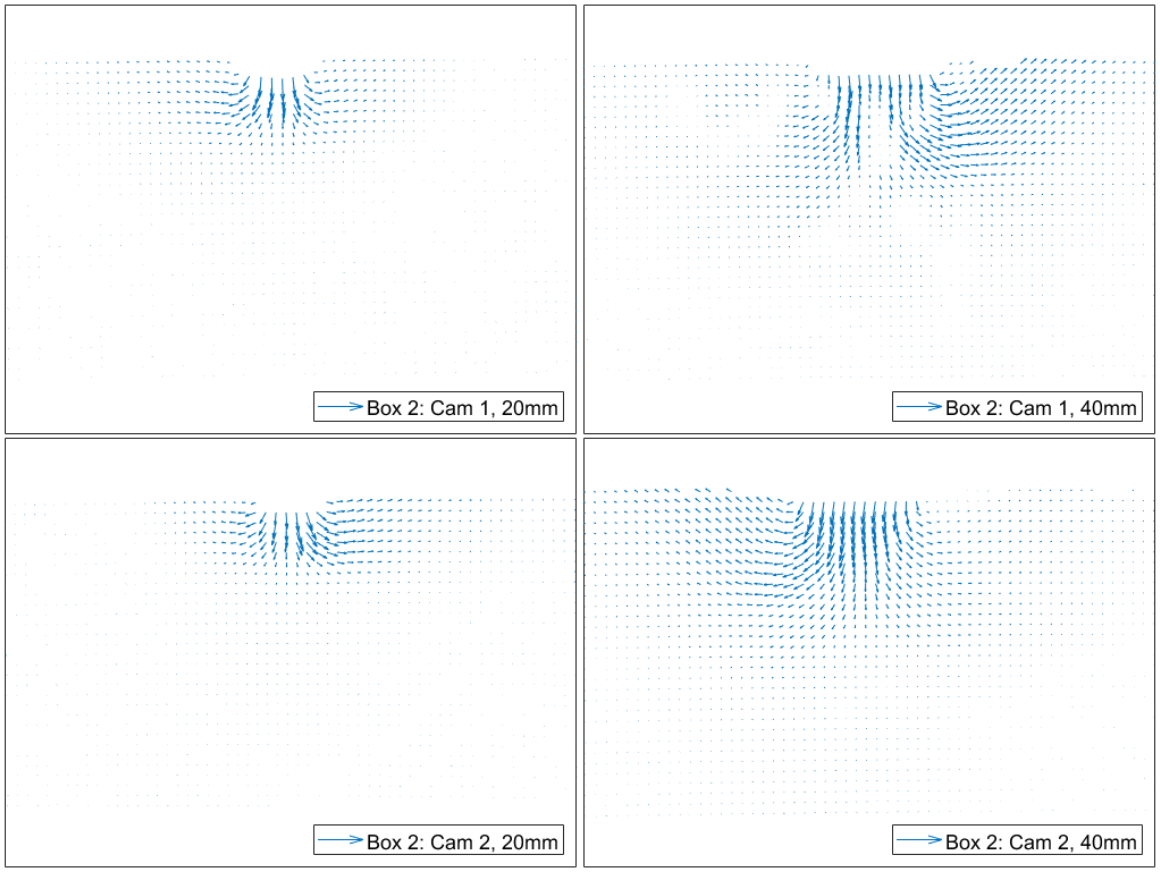

FIGURE 8.7: The PIV derived displacement fields for both cameras for each footing test carried out on Specimen Two.

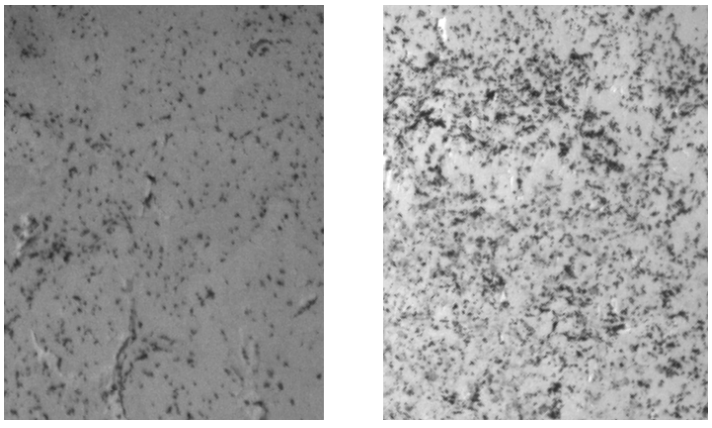

FIGURE 8.8: A comparison between floc on the Cam 1 (left) and Cam 2(right) image data for the Specimen Two 40mm footing.

8.3.3 Specimen Three

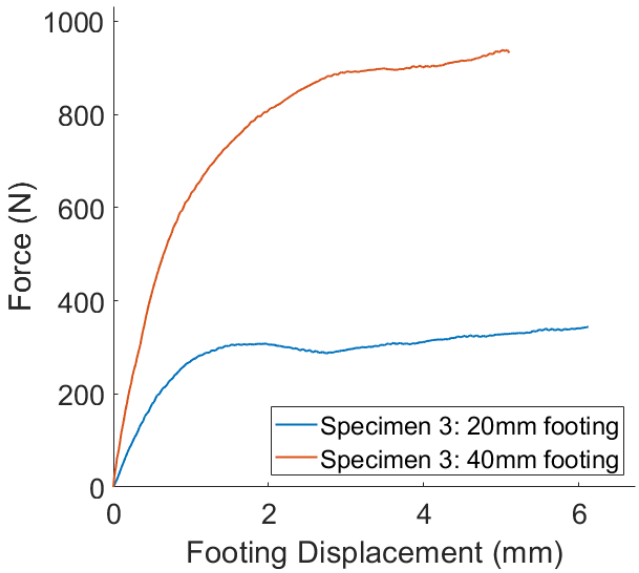

FIGURE 8.9: Central Force and Displacement for the two footing tests carried out on Specimen Three.

Specimen Three is largely the same a Specimen Two. This specimen had no noteworthy errors either during the preparation of the specimen or during testing. The only key point to raise regarding the force-displacement data presented in Figure 8.9 is that the force recorded for the 40mm footing is the highest observed by a small margin. Again, variance here is possibly due to variance in the consolidation process but is more likely due to the difficulty in knowing when to start the test for purposes of the proposed Identification Methods.

As with the other tests, zero force and displacement was chosen at the point when both sides of the footing are visually in contact with the soil. The footing tests for this specimen were the easiest in this regard as the footings were most level and came into contact much more uniformly so it is possible that the levels of force recorded in this test are a better representation than other specimens in which a slightly lower value was recorded.

Figure 8.10 shows the results of the supplementary tests carried out on Specimen Three. Triaxial tests for Specimen Three were fairly uniform, although less so than the triaxial results from Specimen Two. In this case the variance between the plotted curves is slightly higher but there are no curves that stand out as anomalies. Given the presented data it can be said with a good degree of certainty that the true c_u value for the soil in Specimen Three is around 20 to 25kPa.

The vector plots for Specimen Three, as shown in Figure 8.11, are perhaps the best obtained during the suite of tests. There are no regions of missing data, indicating the floccing process

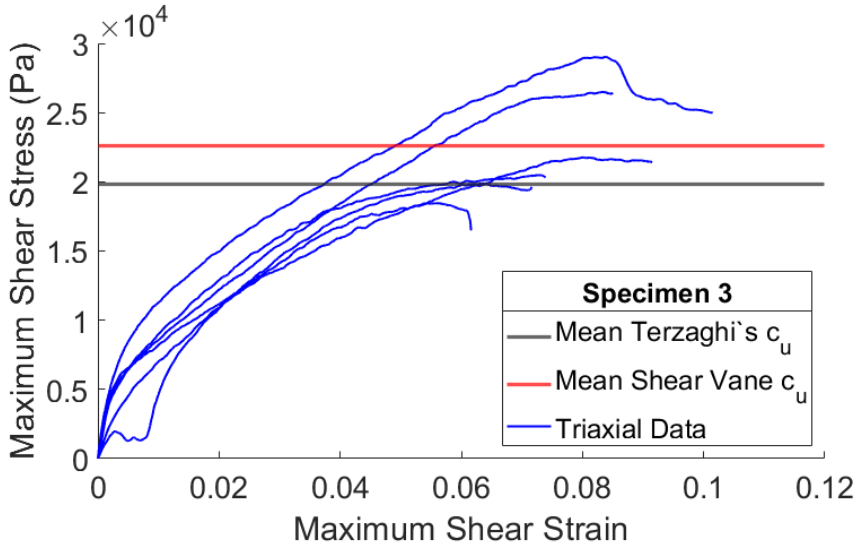

FIGURE 8.10: The triaxial and shear vane tests and Terzaghi's back analysis carried out on Specimen Three.

was successful. Lessons learned from the previous tests, such as ensuring the metal side plates of the consolidation box are sufficiently lubricated prior to filling with slurry resulted in a much higher quality specimen.

Wild vectors were not observed in the immediate vicinity of the footings for any of the datasets related to Specimen Three. A few were observed along the surface on the left hand side of Camera Two for the 40mm test. A distinct missing line of vectors can be observed here. Wild vectors in the peripheries of the dataset are much less of an issue than those in the centre.

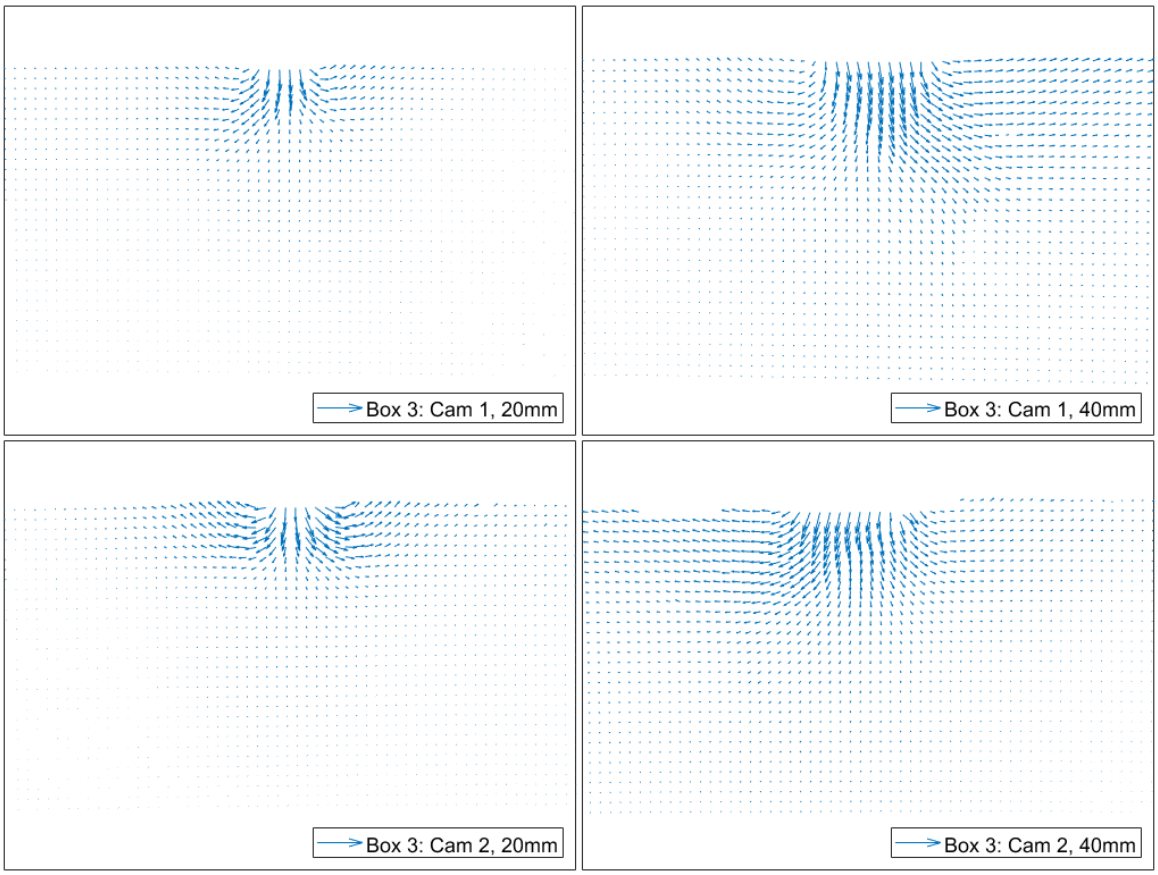

FIGURE 8.11: The PIV derived displacement fields for both cameras for each footing test carried out on Specimen Three.

8.3.4 Specimen Four

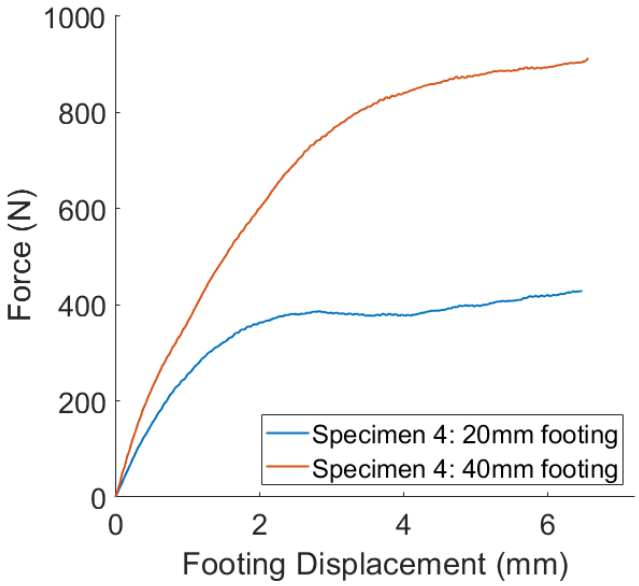

FIGURE 8.12: Central Force and Displacement for the two footing tests carried out on Specimen Four.

Specimen Four, was the final specimen to be produced and tested. A noteworthy issue occurred during the consolidation phase for this specimen. As the kaolin slurry was mixed for the same batch that was used for Specimen Three, it was left in the mixer for just over a week while Specimen Three was being prepared and tested to save the need to decant it into multiple buckets. When the time came to use this remaining slurry, it was briefly mixed to undo any separation in the mixer and then transferred to the sample box using the methodology specified in Chapter 6.

Possibly due to the slurry not being mixed enough after its week in the mixer, it proved to be highly liquid when consolidation pressure was applied with lots of slurry escaping around the top plate. Due to the load cell used to control the consolidation process being extremely noisy at low stresses it was impossible to simply use a lower consolidation pressure for a day or so. To solve this issue a vacuum pump and desiccator were attached to the drainage tubes at the bottom of the specimen box overnight with a nominal consolidation pressure applied. Overnight a small amount of water was removed and in the morning the vacuum pump and desiccator were removed and the consolidation process was carried out as normal.

As this measure was applied for only one night of an eight day consolidation process, and when a very low pressure was applied, it is unlikely to have had any effect on the final properties of the prepared specimen.

Other than this issue the specimen was the highest quality one that was produced. Specimen trimming and floccing was carried out as per the specified methodology in a well practised process.

Figure 8.12 shows the force-displacement curves observed during the footing tests carried out on this specimen. There are no comments specific to this specimen that can be made regarding this data.

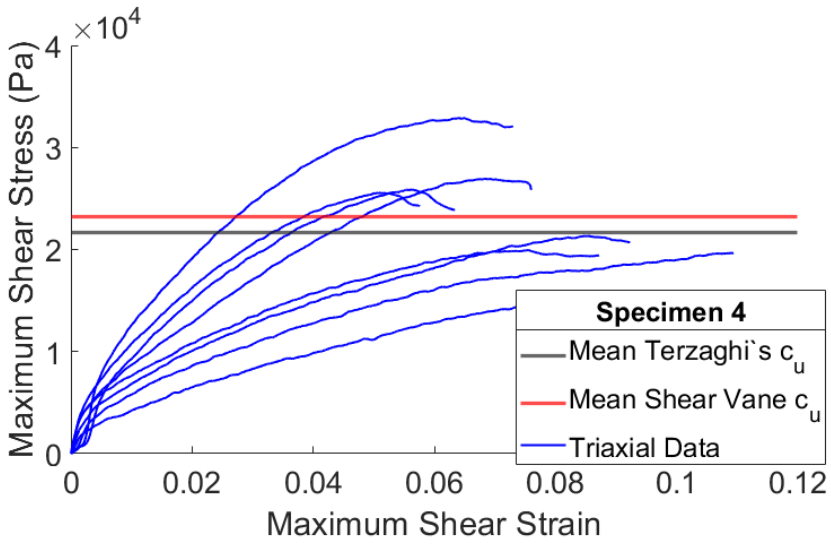

FIGURE 8.13: The triaxial and shear vane tests and Terzaghi's back analysis carried out on Specimen Four.

It can be seen in Figure 8.13 that the results from the triaxial testing of Specimen Four are much more varied than was observed in earlier specimens. Although there are no tests that can be pointed to as anomalous, there is a significant range of possible curves. Variance in triaxial test results is a reality of the method, however in this case it is much more pronounced than in some of the earlier specimens. It is unclear what the cause for this would be and it will potentially make comparisons with the outputs of the proposed Identification Methods less useful for validation.

Other than the spread in triaxial results, the mean value of shear vane tests and of back analysis using Terzaghi's bearing capacity equation are largely the same as observed for other tests. Notably, the back analysis c_u is higher than observed in previous specimens. It is likely the difficulty in correctly zeroing the footing tests that is the cause of this, as mentioned in the discussion for previous specimens.

Similar to those of Specimen Three, the displacement field vector plots, Figure 8.14, of Specimen Four are similarly high quality. Sample prep and floccing was carried out to a very high standard, as fitting for the final specimen to be produced. Trimming of wild vectors

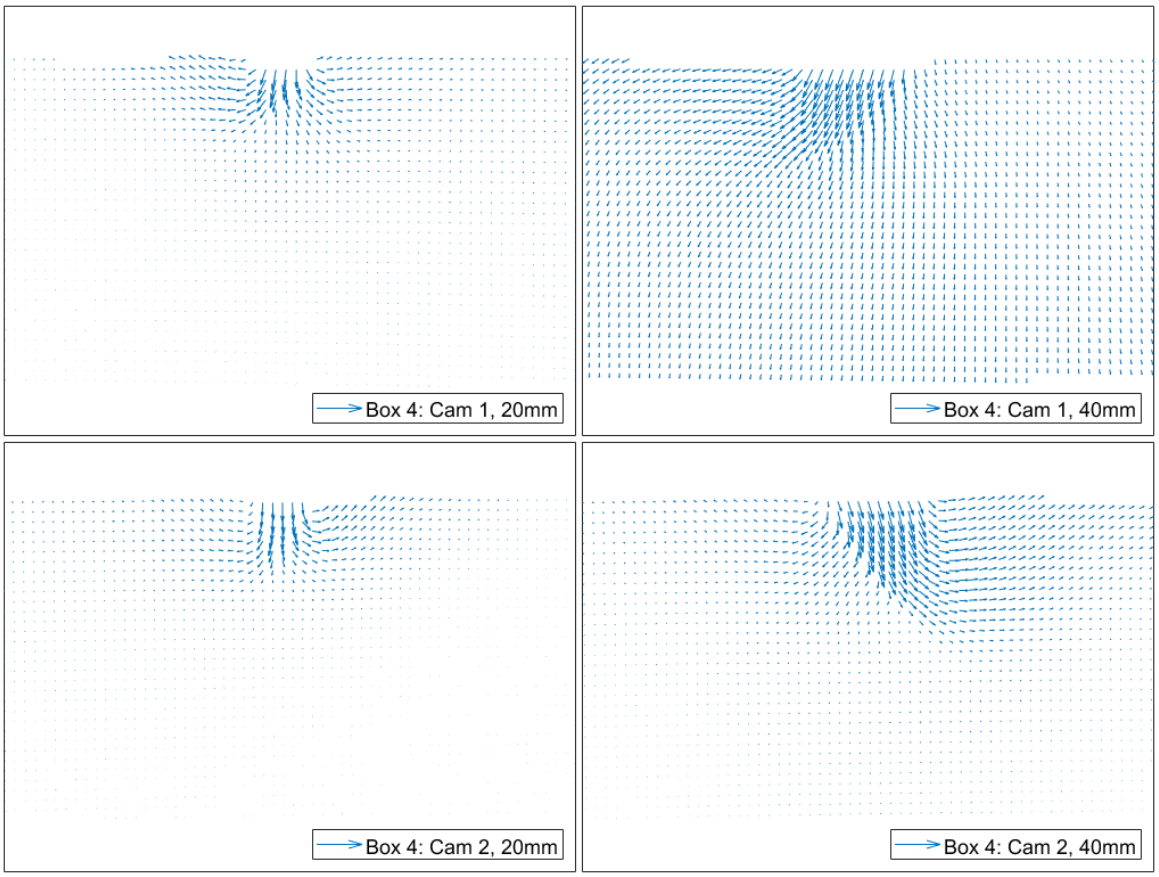

FIGURE 8.14: The PIV derived displacement fields for both cameras for each footing test carried out on Specimen Four.

was limited to either the row immediately below the footing, or to the peripheries along the surface.

Camera One of the 40mm test stands out as deserving commentary. In this dataset, significant movement can be observed throughout the field. Other specimen datasets are typically zero around the edges, with the exception of 40mm tests in which an asymmetric failure mechanism often has formed in which case sideways movement may extend to the nearest border. This dataset does have this asymmetric failure mechanism, but unlike other datasets where this can be observed (including Camera Two for the very same test) significant downwards movement can be seen across the whole field.

The possibility that this is systematic error caused by camera movement was considered, but dismissed after looking into the displacements recorded for the control points in which no such systematic movement can be observer, either numerically or by eye. Further examination was performed by simultaneously opening both the first and the last image of the dataset and rapidly flicking between them. It can be seen through this method that soil is in

fact moving out of the region of interest and past the control points in the manner shown in the displacement field vector plot.

The reasons why this would be the case are unknown. Applied footing displacement was the same as Specimen Three (save for a slight difference due to touchdown timing) and lower than Specimen Two where such movement was not observed. As stated, the other camera for the same test also does not see such a phenomenon.

The effects are likely to be similar to having missing regions of data, which is in fact what has happened. The missing regions are not however in the centre of the region of interest as observed in cases with sub par floccing, but extending outwards from the perimeter. The effects will likely be that the recovered stress-strain response will be higher as more internal work must be done by a smaller area.

Additionally, the assumption that boundary effects are not present is called into question. There is no means to include boundary effects in the current paradigm of the proposed Identification Methods and the effects of doing so are beyond the scope of this project. It is likely that energy is being expended due to soil movement towards/past the metal specimen box wall panels but not counted in the overall equilibrium process. As before, this will result in the recovered stress-strain response being higher than it should be.

8.3.5 Comparison and Commentary

Throughout the discussion of the four specimens, a number of differences were pointed out and explained, most notably due to the refinement of experimental technique after the first test. Variance between later tests is due to the touchdown process. It proved difficult to achieve simultaneous contact along the length of the footing, resulting in one end touching down before the other. The need to zero the force-displacement and displacement field at some point after this touchdown proved difficult to do consistently. Every effort was made to select the times of the very first images in which contact was observed, but even being one image too late or early can have a large effect on the peak load, should the force-displacement curve be particularly steep. Investigation into this phenomenon will be presented later in the chapter.

What hasn't been discussed to the same extent is the similarities between specimens. All specimens were consolidated to the same target pressure, with some small differences in the procedure as have been noted, and for the most part, the triaxial data, load data, and shear vane data, shows a lot of similarities between tests. Plotting the triaxial curves for the four specimens on a single plot, for instance, would make it hard to identify which curves belong together. It does seem that, after taking into account the points raised in this section, that the specimens have roughly the same material properties.

To allow for easier comparison between the qualitative analyses carried out, a table has been compiled summarising the key points. Table 8.2 presents this information. This comparison between differing c_u values adds confidence to the load zeroing process. Excepting Specimen One, the values obtained from Terzaghi's bearing capacity equation back analysis compare well with the c_u values found from both shear vane and triaxial data. This implies that the peak load values that were observed after the zeroing process are what would be expected based on the soil strength.

Variable	Specimen 1	Specimen 2	Specimen 3	Specimen 4
Peak Load 20mm (N)	209	321	341	428
Peak Load 40mm (N)	690	747	938	906
Mean Terzaghi's c_u (kPa)	13500	19200	19200	21600
Mean Shear Vane c_u (kPa)	19000	22500	22600	23300
Mean Triaxial c_u (kPa)	20300	22900	20400	24600

TABLE 8.2: Comparison between footing tests.

8.4 Verification using "real" datasets

This section will present a comparison between the recovered stress-strain responses for each dataset and the representative responses and c_u values obtained through supplementary testing. This comparison will be presented for both the Segment based Identification Method and the Equation based Identification Method.

All 16 datasets (4 specimens with two tests, each with two cameras) will be processed for the Segment based approach whereas only a subset of available datasets will be processed using the Equation based approach due to the prohibitively computational expense of the brute force process. As per the investigations on artificial datasets presented in Chapter 7, although there are differences between the recovered curves using each method, the overall quality is largely the same. It can therefore be assumed that commentary on the quality of the stress-strain curves recovered using the Segment based approach, giving reference to the qualitative analysis presented earlier in this chapter, will also be valid for stress-strain curves recovered using the Equation based approach. Additionally, the Equation based approach has very particular assumptions about the shape of the recovered curves that are unlikely to be valid for real datasets.

After the presentation of the verification of the Identification Methods the following section of this chapter will consider whether the decisions made regarding preprocessing parameters and strategies were valid.

8.4.1 Segment based approach

As per the analyses in Chapter 7, the Segment based approach was performed using 100 segments for each of the datasets. Preprocessing was uniform for every test, as per the earlier section in this chapter. Timesteps were based on availability of images, with every image utilised between the start and end time.

Specimen One

Specimen One was the first specimen produced and tested. As per the qualitative analysis on this specimen, there were a number of issues. Firstly, the specimen was allowed to dry slightly due to equipment availability delays for the actual test procedure. Secondly, the floc patterns were poor, with regions in which GeoPIV was unable to pick up displacements. Finally, touchdown was carried out separately to the main test, resulting in the data being zeroed slightly later than it should be. The effects of these factors on the final recovered stress-strain curves will be examined.

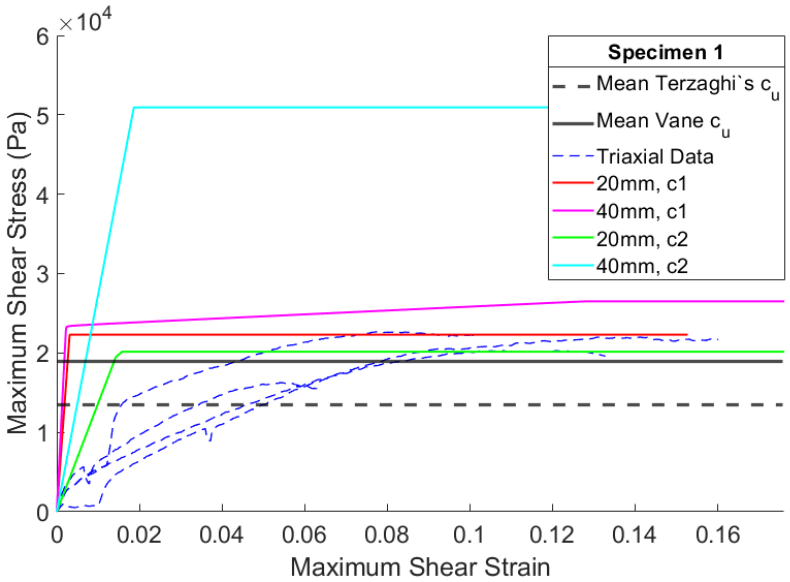

FIGURE 8.15: A comparison between the stress-strain curves recovered with the Segment based approach and the supplementary data for Specimen One.

Figure 8.15 shows the recovered stress-strain responses for the four datasets corresponding to Specimen One. The stress-strain curves are superimposed over the supplementary data that was previously presented in Figure 8.3.

What immediately stands out from the recovered stress-strain curves is that the Camera Two dataset for the 40mm footing significantly overestimates the cohesion of the soil. The

triaxial plots seem to agree on a c_u of a little over $20kPa$, whereas the aforementioned recovered curve has a c_u value that is around 2.5 times larger. As per the qualitative discussion on Specimen One, this dataset had a particularly poor displacement field, even compared to other datasets from the same specimen. Not only was a large region missing due to poor floc coverage, but it can be inferred from the field plot that it corresponds to a region with significant strain. It does appear that the prediction that such a region results in an overestimate of c_u is supported by the presented data. Although it is possible to assess image quality by eye, the future development of a tool to automatically quantify the quality of image data would potentially be of use.

Although some imaging data from Specimen One is of lower quality, the confirmation that poor PIV texture impacts the Identification Method performance in the expected way is of value. Knowledge of this issue will be of use for the design of any future tests where it is desired to use PIV data as input to an Identification Method.

The other three recovered curves have more reasonable c_u values. The Camera One data for the 40mm footing has a similar elastic region to the Camera One data for the 20mm footing, although has a higher c_u value. Although the c_u value for this data is higher than the supplementary triaxial data, this specimen only has four successful triaxial plots with variance that is lower than shown amongst the larger number of triaxial plots presented for other specimens, so it can't be said with confidence whether the Camera One data for the 40mm footing is or isn't within acceptable bounds.

The aforementioned responses are excessively steep, even if the plateau is at a reasonable value. This indicates that the optimisation process is requiring more work to be done by small strains. Throughout all datasets for all specimens, a significant majority of elements have very low strains, and although some have been filtered in the manner described in the preprossessing section, this doesn't fully rectify the situation. It can easily be seen from the relevant displacement plots that only a handful of elements will have strains in the plateaued part of the curves.

Why this would happen is not known, possibilities relating to the issues with touchdown, or poor displacement field are possible. Nonetheless, recovering c_u is still of use even if the shape of the curve is not of value. There is also the possibility that the triaxial responses plotted are not representative of a footing response.

The final recovered stress-strain response is the one resulting from the Camera Two dataset for the 20mm footing. This curve has a shape that is more similar to the triaxial data than the other curves, and has a c_u at an appropriate height.

The quality of a recovered stress-strain response in comparison to supplementary test data is useful for validation, but would not be possible in cases in which only the recovered

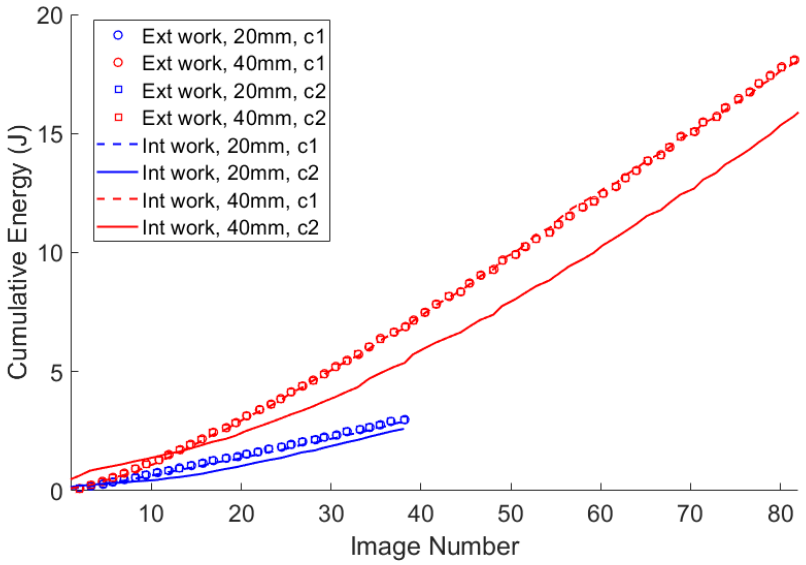

FIGURE 8.16: The difference between local internal and external energy for Specimen One.

response is available. The quality of the recovered curves can be assessed further by examining the energy gap. Although this can be expressed as a single percentage value, the global energy gap, it is more useful to look at the local gaps, of which one exists per image frame. Figure 8.16 shows plots of cumulative internal and external work for the four datasets of Specimen One.

It should be noted that for Specimen One, due to touchdown being carried out as a separate stage, footing displacement data was taken as an average of the LVDT at either end. As such, external work is identical for both cameras for this specimen.

As before, the standout dataset is Camera Two for the 40mm footing. After an initial over estimate of internal work, the curve ends up having a fairly large energy deficit. It should be noted, as per Chapter 4, that the optimiser doesn't simply sum local energy gaps to find the global energy gap, but uses the least square of the local energy gaps. The optimiser has no motivation to attempt to make up for early energy surpluses with a later energy deficit.

The recovered stress-strain curve for the 40mm/cam2 dataset is significantly higher than it should be, and one of the ways the optimiser can increase internal work is through a higher stress-strain curve. Despite the extremely high c_u value, there is still an energy deficit indicating that moving the curve further higher would not improve the energy situation but instead make it worse.

In comparison with the other datasets for this specimen, it appears that a large energy gap is indicative of a poor recovered curve. This will be analysed further in later specimens.

Specimen Two

As per the qualitative discussion, Specimen Two had an improved prep and testing process. The displacement field is poor for the 40mm/cam1 test but significantly better for the other three tests. Most notably, the touchdown process was recorded as part of the main test, with no pause after soil impact. The load, displacement, and PIV displacement data was zeroed at the earliest point where both ends of the footing can be seen to be in full contact with the soil.

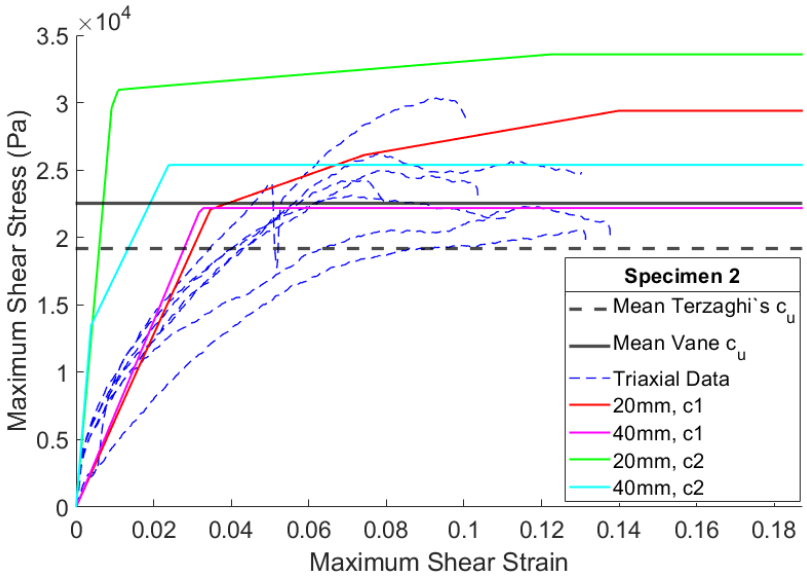

FIGURE 8.17: A comparison between the stress-strain curves recovered with the Segment based approach and the supplementary data for Specimen Two.

Figure 8.17 shows the recovered stress-strain curves for the four datasets, along with plots relating to the supplementary tests. A distinction can be drawn between the datasets collected with Camera One and those collected with Camera Two. The Camera One datasets for both footing widths are within the range that the triaxial test data would imply is acceptable, whereas the curves recovered for Camera Two are initially too steep.

The reason for this discrepancy is the touchdown process. As stated previously, the specimen box was levelled with use of a spirit level, which it to say that there is a margin of error involved. The footing was slightly off of parallel with the surface of the soil such that one end touches down first. Although all data is zeroed only when both ends are in contact, the side touching down first will already have small soil deformations whereas the side touching down second may not begin to measurably deform for a short while. The end of the footing recorded with Camera One touched down first for both footings.

It follows that the image data associated with the end that touches down first will record overall higher strains throughout the test. Table 8.3 shows the mean and maximum values of shear strain recorded for the tests carried out on Specimen Two which provides evidence to support this. It should be noted that the values in the data are after the preprocessing described in earlier sections of this chapter.

Test	**Mean** ϵ_s	**Max** ϵ_s
20mm/Cam1	0.0223	0.5943
20mm/Cam2	0.0124	0.3663
40mm/Cam1	0.0623	1.8725
40mm/Cam2	0.0325	0.7121

TABLE 8.3: A comparison between the mean and maximum observed shear strains for Specimen Two.

Based on this discrepancy in strains, a dataset in which strains are generally higher would be expected to have a lower stress-strain response, provided that in reality the soil behaviour is the same for both datasets and the external work is the same or approximately the same.

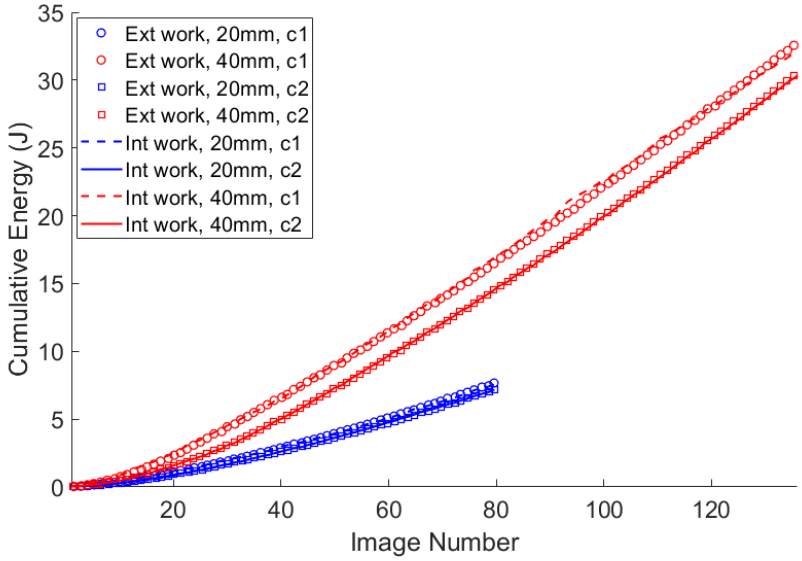

FIGURE 8.18: The difference between local internal and external energy for Specimen Two.

Figure 8.18 shows the energy plots for Specimen Two and will allow for further insight to the phenomenon observed with this specimen. Note that the external work is not equal for both cameras. Due to the touchdown process, one end of the footing was in contact before the other so there is a short time before the footing levels out. The force data used is equal for both datasets, however displacement was measured at both ends of the footing, with a different Force-displacement plot used for each dataset.

It can be seen in the cumulative energy plots that the difference is mostly in the first 30 images or so, after which the cumulative energy plots are parallel, indicating that the footing is moving down into the soil uniformly.

The difference in energy between the datasets is relatively small, and as internal work and external work are equilibrated incrementally, the difference is mostly limited to the first part of the test. Although Camera Two has lower external work at the earlier stages of the test, it is not enough to mitigate the lower strain values. The ability to accurately choose the touchdown location appears to significantly impact the quality of results, particularly in this case in which a compromise must be made due to the footing not touching down equally.

The cumulative energy plots for the 20mm footings are much closer to each other. Examining the chart closely, or indeed the numeric values, it is clear the same phenomenon can be observed but to a lesser extent due to the overall lower strains and displacements.

Other than the discrepancies due to the touchdown process, the internal work and external work are a close match for all four datasets, including the 40mm/Cam1 dataset which featured regions of missing PIV data. Examining the displacement field for this dataset (Figure 8.7) it seems that the missing regions are areas of lower strain than those of the problematic dataset from Specimen One. Also these missing regions are smaller. It is also important to understand that "missing" PIV data is not discounted, but instead has a displacement set to zero (or approximately zero). A large patch of zero displacement will of course have zero strain, but small patches surrounded by more typical non zero displacements may in fact cause higher strain. Areas of uniform movement or no movement have low strains, and areas of non uniform movement have higher strains. It is possible that a better strategy would be to delete the vectors in these areas as wild, however, for this dataset doing so would result in removing a large percentage of the displacement field. A reinterpretation scheme would be possible but would raise questions in the accuracy of the interpolation due to the size of the area.

Specimen Three

Specimen Three, as described in the qualitative analysis section, with no noteworthy issues that may effect the quality of results. The imaging data recorded with the cameras was of good quality for all four datasets.

Figure 8.19 shows the recovered stress-strain curves for Specimen Three. Comparisons can be made by splitting the datasets by both camera and footing width.

Comparing the different footing widths, both datasets for the 20mm footing have a reasonable c_u value that is within the range suggested by the triaxial data. The datasets for the

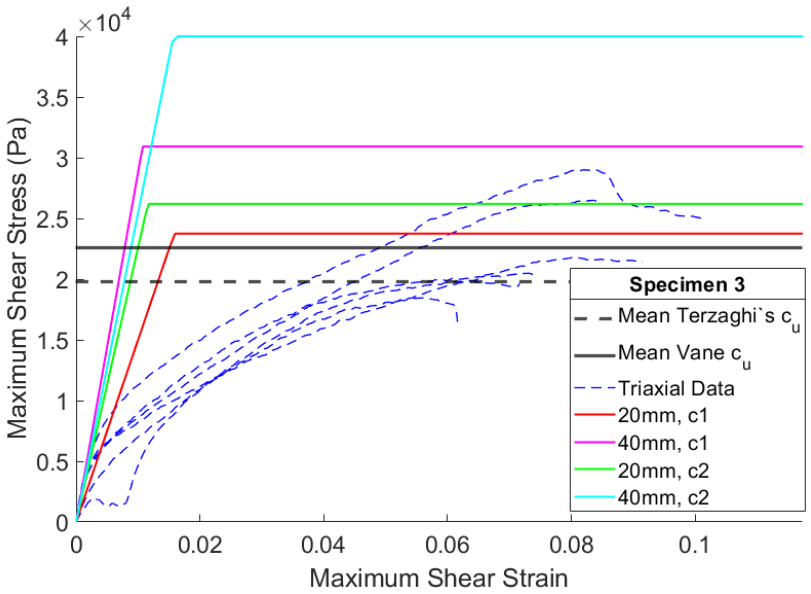

FIGURE 8.19: A comparison between the stress-strain curves recovered with the Segment based approach and the supplementary data for Specimen Three.

40mm footing have c_u values that are much higher. It was noted that the observed force for the 40mm test of Specimen Three was the highest observed across the suite of tests.

As mentioned several times before, choosing the start of the test is not an exact science, there is difficulty in either visually selecting when the footing is in full contact, or doing so based on the raw force-displacement data. The start was selected using the same methodology as all other specimens. Selecting a start point even one image earlier or later could have a meaningful impact on the observed peak strain. Although it would be possible to tweak the start position to acheive a more favourable recovered curve, this has not been done as it would be an unfair test and unrepresentative of the ability of the proposed Identification Methods to recover a curve in cases where supplementary data for comparison is unavailable.

The other comparison to be made is the phenomenon of uneven touchdown. The ends of the footing recorded by Camera One touched down first, and as with Specimen Two, have lower c_u values than the datasets recorded by Camera Two.

The plots of cumulative internal and external energy for the four datasets can be seen in Figure 8.20. It can be confirmed that just as with Specimen Two, the external work for the side of the footing that touches down first (Camera One) is higher. Much of the commentary on this is given under Specimen Two and will not be repeated here.

An additional point that can be made regarding this specimen is that there is a significant energy gap for the 40mm/Cam2 dataset. Initially there is a very large energy surplus, after

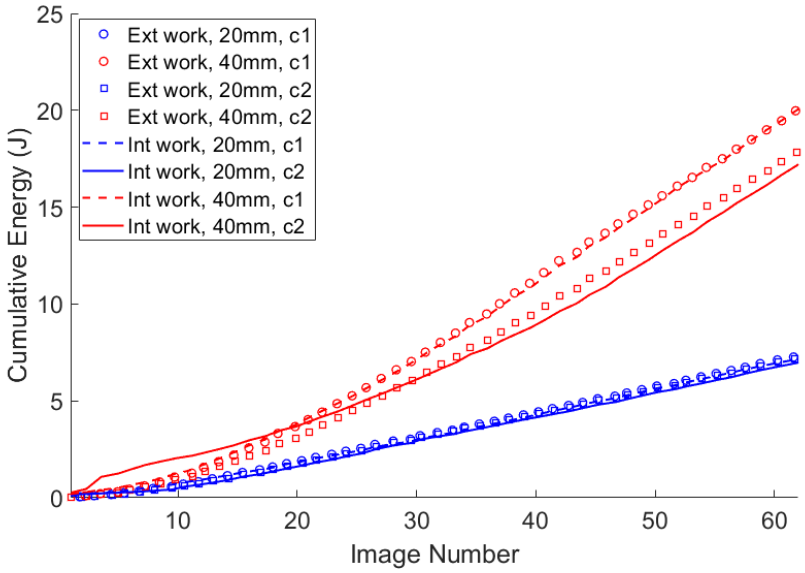

FIGURE 8.20: The difference between local internal and external energy for Specimen Three.

which there is an energy deficit in the middle of the dataset, and the final third or so has approximately equal internal and external energy as per the parallel lines.

To better illustrate the energy errors of the 40mm/Cam2 dataset, an additional figure is provided. Figure 8.21 shows the local energy gap. Each marker represents one image increment and is plotted at the time at the end of the increment. It can be seen from this that the assessment given based on the cumulative plot is correct, but this additional plot makes it clear the extent that internal energy is in surplus at the initial part of the dataset.

It should be remembered that the optimiser seeks to minimise root mean square of local energy gaps. A surplus early is not cancelled out by a later deficit. This can be thought of minimising the area between the plotted local energy gap and the x axis, with area above and below the axis counted equally.

These relatively few early timesteps with a huge local gap no doubt have an impact on the shape of the recovered curve. The possibility of refining the dataset by removing increments with significant energy gaps was considered, but found to be of little benefit. This dataset would have been a prime candidate for such refinement by simply not including the first 10 or so timesteps in the global energy gap calculation. Trials using this methodology found that although the global energy gap was reduced, there was negligible change to the recovered curve, with the c_u value still being unacceptably high.

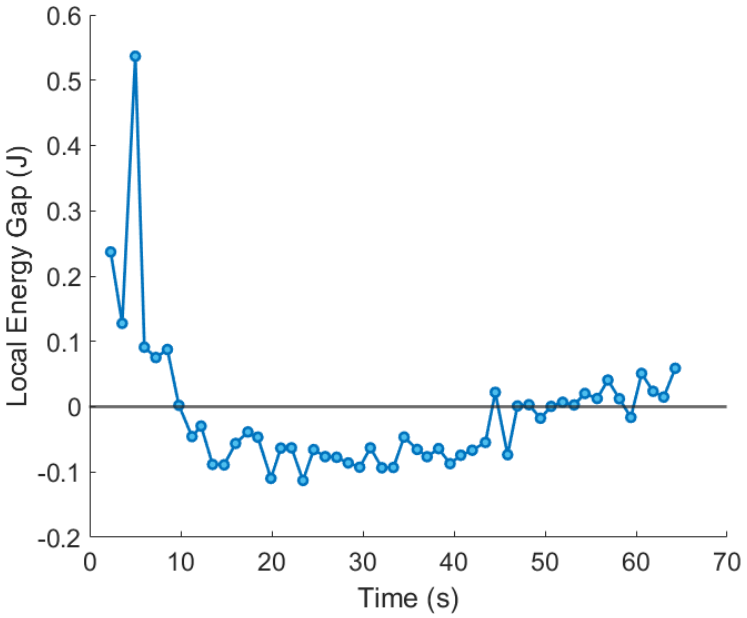

FIGURE 8.21: The local energy gaps for the 40mm footing width, Camera Two dataset of Specimen Three.

Specimen Four

The final specimen to be prepared and tested was Specimen Four. A detailed qualitative analysis of this specimen can be found earlier in the chapter. The key points however were that it was the best produced in terms of quality of the flocced surfaces and that one of the datasets had significant movement outside of the area of interest, that appears to be genuine and not simply an artefact of the photographic and/or photogrammetric processes.

The recovered stress-strain curves for Specimen Four are shown in Figure 8.22 along with the relevant supplementary data to allow for assessment of the recovered curves. As done with previous specimens, the most clearly incorrect recovered response will be discussed first.

The recovered stress-strain response for the 40mm/Cam1 dataset is significantly higher than the others with a c_u of just over $40kPa$, exceeding even the highest triaxial plot. As per the qualitative discussion presented earlier, this is the dataset that featured significant movement outside of the region of interest. It would be expected that the recovered stress-strain response would be an over estimate as significant movement and potentially strains are simply not recorded, requiring more work to be done by the elements within the area of interest. Why this has happened for this specific dataset is not known. Although small amounts of lateral movement have been observed along the borders of 40mm footings failing assymetrically, no other dataset has such movement to this extent. Even the corresponding dataset

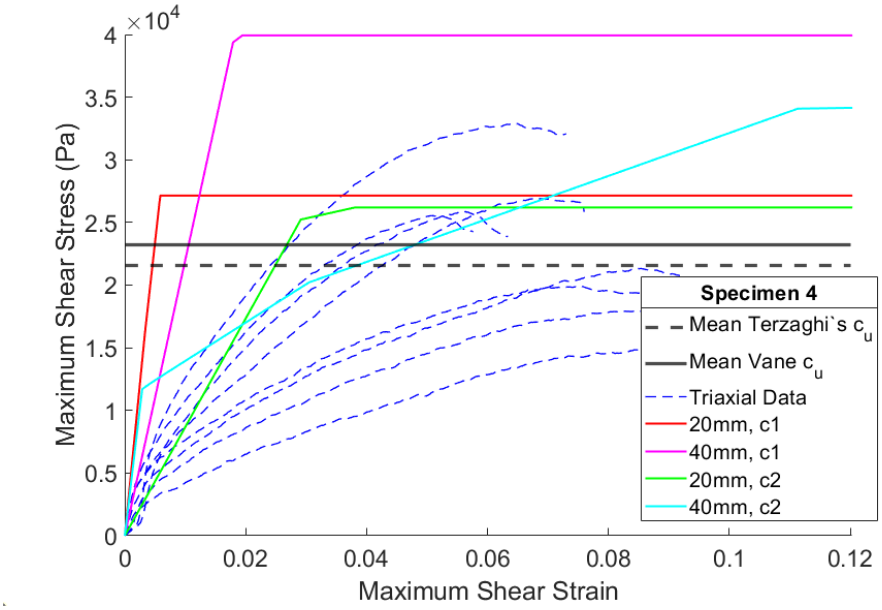

FIGURE 8.22: A comparison between the stress-strain curves recovered with the Segment based approach and the supplementary data for Specimen Four.

for Camera Two does not exhibit the same behaviour.

As with the previously discussed specimens, the curves recovered from the ends of each footing that touch down second are higher. It should be noted that for this specimen the datasets associated with Camera Two represent the ends of the footing that touched down first, the opposite of the previously discussed specimens.

This specimen also has perhaps the best example of a recovered stress-strain response. 20mm/Cam2 has both an elastic phase and a plateau that are within the area of acceptability based on the supplementary triaxial data, with even a slightly rounded transition.

Figure 8.23 shows the differences between the cumulative internal and external energy for each of the four datasets associated with Specimen Four. There is little to add that hasn't already been covered with the discussion of previous specimens.

The differences in external work based on which footing touches down first are still present (in this case Camera Two represents these datasets). Unlike previous specimens there is a meaningful gap between the two external work curves for the 20mm footing. It does appear that in this case the differences in alignment between the footing and the soil surface were larger than in earlier tests.

As expected there is a significant energy gap for the 40mm/Cam1 dataset. Like the erroneous dataset from Specimen One, despite a very high c_u being recovered with a steep curve, the internal work is still lower than the external work. If the optimiser were able to

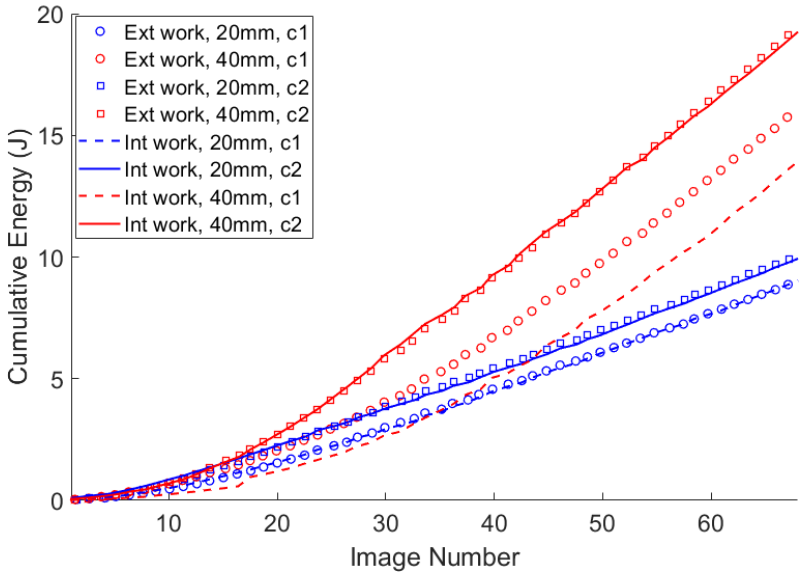

FIGURE 8.23: The difference between local internal and external energy for Specimen Four.

reduce the energy gap by further raising the curve it would have, but evidently doing so would not represent an improvement.

Validation of the Segment based approach optimisation procedure

Although the Segment based approach theoretically recovers the stress-strain response with the lowest energy gap, there is the question as to whether the recovered curve is genuinely the best possibility. The recovered curve could instead be one of many possibilities that have negligible difference in energy gap, with some of these curves being a better representation of the true soil behaviour despite being found to be technically suboptimal. An example is the bilinearity observed in many of the recovered curves. It would be potentially more useful should a smooth curve exist that is almost as optimal.

The first thing to consider is whether the optimisation problem is convex. For the MOSEK optimiser to find a global optimal solution, the optimisation problem must be convex. A non-convex problem has the possibility of local minima being found. According to the MOSEK documentation (MOSEK, 2020), there are built in checks for convexity. These checks were left on their default setting which would return an error message should non-convexity be identified. As stated in Chapter 4, conic optimisation is used. As conic optimisation uses convex cones as a constraint, the problem is by definition convex. Combined with the built in checks, it can with confidence be said that the recovered solutions are the optimal solutions in terms of energy gap.

The second consideration is a continuation of the point raised in the introductory paragraph. There is the potential that a slightly sub-optimal stress-strain response exists that would be of more practical use to a geotechnical engineer. Whereas the Equation based approach using a brute force approach allows for a contour plot to determine the existence of a near optimal plateau, the Segment based approach is essentially a black box. It is however possible to investigate the effects of altering the recovered stress-strain curve. All the relevant optimisation matrices are saved, and as such simply changing the values in the segmental maximum shear stress vector and completing the multiplication will allow for a new global energy gap value to be calculated. Although only simple variations can be made (e.g. scaling up or down all or some of the recovered curve), a brief investigation will allow for increased confidence in the Segment based approach.

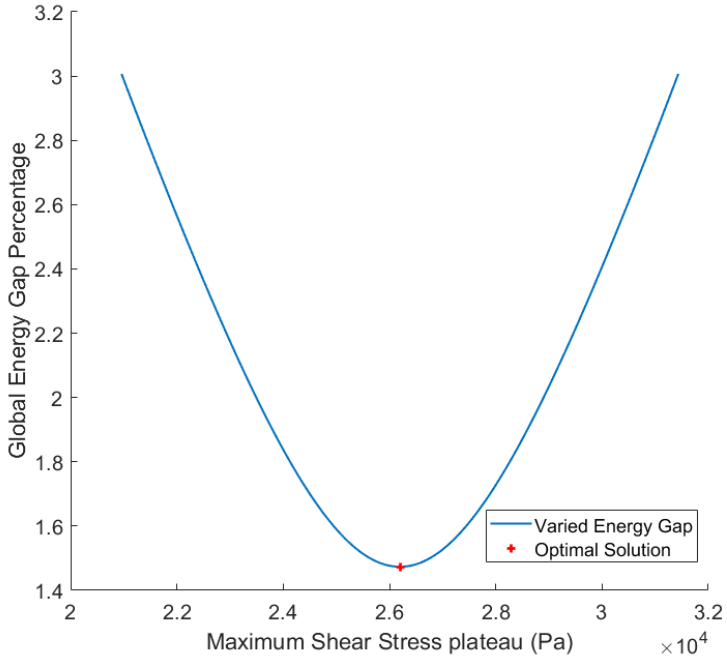

FIGURE 8.24: Scaling up and down the Cam 2, 20mm footing dataset from Specimen Four.

Figure 8.24 is a plot showing how global energy gap varies with a scaled stress-strain response. The recovered curve for Camera 2, 20mm footing, from Specimen Four was scaled up or down by up to 20%. The x axis in the figure is the peak maximum shear stress at the top of the scaled stress-strain curve. It can clearly be seen that the original curve was optimal, with global energy gap varying in the form of a parabola. It is notable that the global energy gap percentage (a percentage of external work) is changed by a relatively small amount (1.47% to 3%) despite scaling the stress-strain response by $\pm$20%. This is

likely due to the uneven distribution of work across the stress-strain response; the vast majority of elements are represented earlier on where percentage based scaling will have lower impact. It does however seem to follow that less populated portions of the stress-strain response could be varied wildly with little impact to the global energy gap provided the more populated portions are sufficiently accurate.

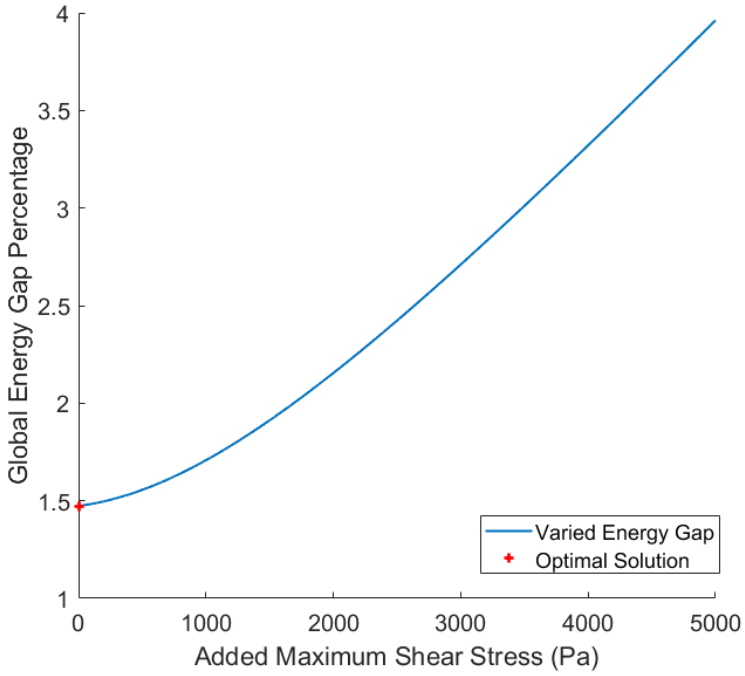

FIGURE 8.25: Adding stress uniformly to the Cam 2, 20mm footing dataset from Specimen Four.

Figure 8.25 shows a plot of global energy gap in which stress has been uniformly added to the recovered stress-strain response. The same dataset has been used as in the previous investigation. It should be noted that due to the programmatic implementation of the Segment based approach, the stress-strain response is hard-coded to pass through the origin. As such the first segment, representing 1% of elemental strain increments, has not been scaled to the same degree as the other 99. This procedure is still much more uniform than the previous investigation. It appears that the plot quickly approaches an asymptote in which any additional stress causes a linear increase in energy gap. As before, the original recovered curve is the most optimal.

A detailed investigation in which all 100 segments are manually adjusted would not be possible. This simple check does appear to confirm that the recovered stress-strain is the global minimum. Small changes to e.g. c_u are possible with negligible impact on global energy gap, however these changes quickly result in linear (or worse) impact on energy

gap. It is likely that other more localised adjustments to the recovered curves have a similar impact. The plateau of "passable" but sub-optimal curves would appear to be fairly small, as far as the checks carried out here indicate.

Having established that the recovered stress-strain response is optimal as per the problem formulation, the question is raised as to whether changes to the formulation would allow for "better" recovered curves. The Segment based approach implemented a number of constraints on the shape of the recovered curve that were intended to produce curves of more practical use. Chapter 4 details these constraints. The constraint enforcing a gradually reducing gradient stands out as worthy of investigation as a potential reason for the observed segmentation or bilinearity.

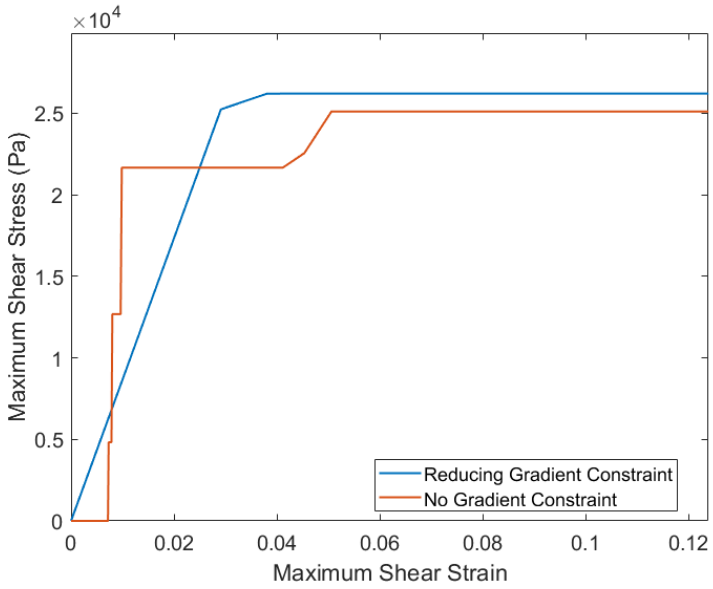

FIGURE 8.26: Recovered stress-strain responses with and without the gradient constraint activated.

Figure 8.26 shows the recovered curve for the Cam 2, 20mm footing dataset from Specimen Four with and without the gradient constraint activated. It can be seen that without this gradient based constraint the recovered curve is allowed to freely increase and decrease the gradient as it sees fit. This results in a somewhat ugly staircase shaped curve. With the constraint added, increases in gradient are disallowed and the recovered curve is forced to change. The constrained curve essentially plots a straight line through the staircase region of the unconstrained curve. As the recovered curve can never increase its gradient, if it required a certain stress value at a late stage of the curve it is necessary to ensure the recovered curve is sufficiently steep to reach that stress value. In this example, if the earlier parts of the curve were to be assigned more appropriate lower stress values, there would be no way that

later parts of the curve also could. As such, the straight line is the best possible compromise for the available data provided the reducing gradient constraint is present.

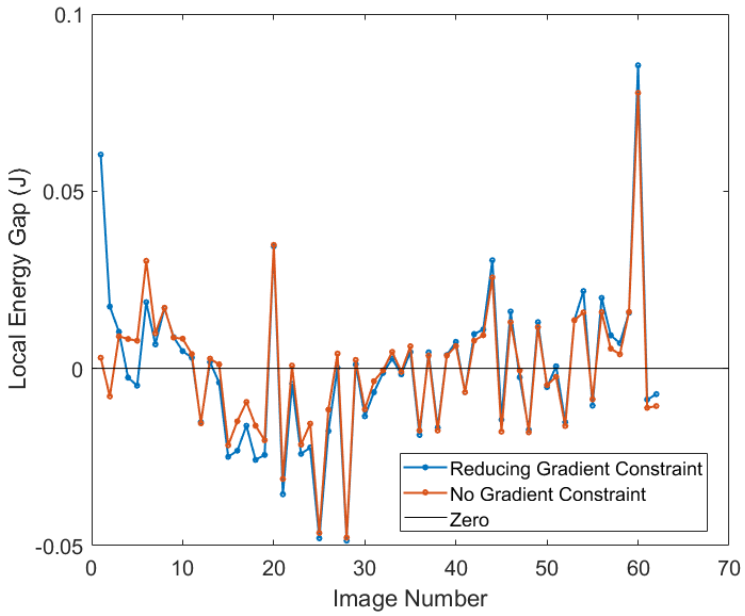

FIGURE 8.27: Local energy gap for responses with and without the gradient constraint activated.

Insight can be gained from the energy considerations of this comparison. Figure 8.27 shows the local energy gaps for the Cam 2, 20mm footing dataset from Specimen Four with and without the gradient constraint activated. In general, and as expected, the energy gap is smaller without the constraint active. Of particular note is the first three of so frames. Although strains from each frame are spread throughout the stress-strain response, the lower strains associated with the initial frames are likely to be over represented in the earlier parts of the stress strain curve. It can be seen that the local gap with the constraint is significantly higher than without the constraint for these initial frames. It appears that this is the result of the constraint forcing the recovered curve to overestimate the stress associated with the very small strains. The global energy gap matches the observation made regarding the local gaps. With the constraint, the gap (as a percentage of external work) is 1.47%, and without the constraint it is 1.27%.

Although the curve recovered without the reducing gradient constraint has a lower energy gap and a reasonable c_u value, it is clearly a less useful curve. Even if the true soil response is not the almost bilinear recovered response, the staircase is almost certainly a less representative alternative. The reducing gradient constraint appears to be beneficial in making the recovered curve more practically useful despite the slightly higher energy gap. The question can be raised as to whether there are alternative constraints that could be used in addition

or instead that may further improve the shape of the curve. The gradient could additionally be constrained such that the rate at which it reduces must always increase which would disallow sets of segments to form a straight line. Adding this, or a similar constraint, to force a smoother curve instead of the segmented curve, would incur an increased energy gap. Whether this is a worthwhile exchange would depend on the quality of the dataset. It was demonstrated in Chapter 7 that perfect datasets can recover smooth curves without any adjustment to the specified constraint.

The question is raised as to why some recovered curves are highly segmented or even bilinear, or would return a staircase without the gradient constraint. The Segment based approach was allowed to choose the locations of 100 segments, yet in many cases it is recovering a stress-strain response that could be described with two or three. It was seen in Chapter 7 that datasets of lower quality typically tend towards a more segmented recovered curve whereas higher quality datasets have no such issue. The datasets that were artificially degraded through the addition of noise tended towards bilinearity as noise was increased (along with a reduced c_u). It seems likely that this bilinearity is the result of carrying out the optimisation process on a flawed dataset, however at the current time no one property has been identified that could be pointed to as the reason for this. To pinpoint the exact cause of the issue would allow either a quantitative assessment of dataset quality or potentially the removal of the issue. Unfortunately, this is something that, if possible, will have to be undertaken as future work.

It would be possible to force the recovered curve to be smooth in the same way that it is possible to force the recovered curve to not feature a staircase pattern. Doing so when the recovery of such a curve is not optimal for the dataset, for whatever reason, would make it difficult to quantify the accuracy of the recovered stress-strain response. Any attempt to constrain the shape of the curve will result in an increase in energy gap. As it would be unknown what manner of curve is expected, writing a general constraint that has the desired impact would prove challenging. The constraints defined during this project were intended to be very general yet when faced with flawed data, unexpectedly resulted in bilinear or almost bilinear curves. The definition of additional or replacement constraints will not be carried out as part of this project but is something that would be of interest as future work.

A final check on the Segment based Identification Method is whether the number of segments can effect the recovered stress-strain response. It was demonstrated using artificial datasets in Chapter 7 that increasing the number of segments improved both the shape of the curve and the global energy gap. It was found that there are diminishing returns and after 50 segments there is no observable change. For all analyses carried out in this chapter 100 segments were used. To confirm that this decision is suitable and is not having any unintended effects, the investigation into segment number was repeated for the Cam 2, 20mm

footing dataset from Specimen Four.

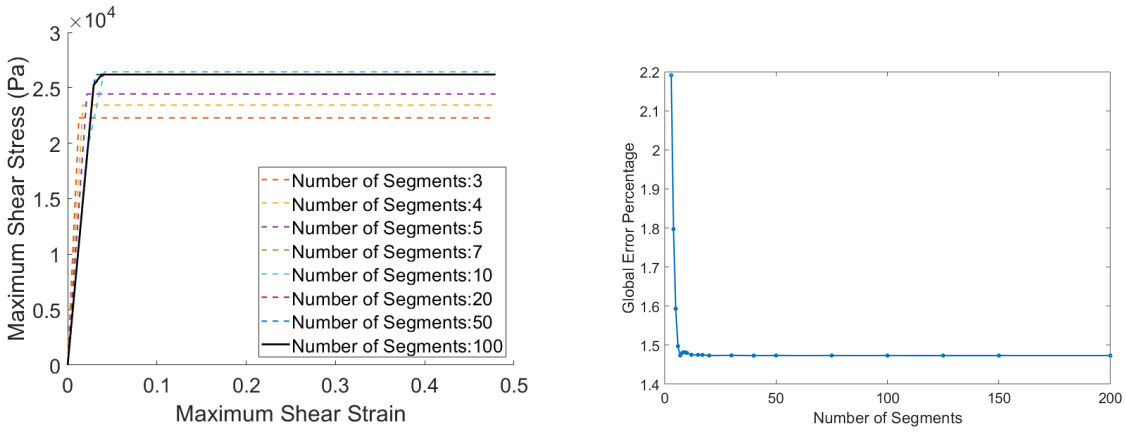

FIGURE 8.28: An investigation into number of segments using a real dataset.

Figure 8.28 shows the results of the investigation into segment number. The findings are essentially the same as with the equivalent study carried out for the artificial dataset. There is no particular change in the segmentation of the recovered curve based on segment number. Every curve plotted is made up of two or three linear sections. It does appear that c_u increases with segment number for the initial few segments, however from seven segments onwards, the c_u value recovered is essentially the same as for 100 segments. Also plotted is the variance of global energy gap with number of segments. After a few relatively poor energy gaps, this quickly plateaus to the value of 1.47% that has been observed throughout this discussion.

To conclude, it has been confirmed that the stress-strain responses recovered using the Segment based approach are optimal as per the current implementation of the optimisation problem, and that the constraints and parameters used for the Segment based approach are suitable. There is potential for improvements to be made to the curve constraints which will form potential future work. Not included in this investigation is the effects of preprocessing on the datasets. This will be covered later in the chapter.

8.4.2 Equation based approach

The Equation based approach is significantly more limited than the Segment based approach in the recovery of curves, with the shape of any recovered curve being limited to a presupposed equation. Two equations were implemented, an elastic-perfectly-plastic response and the "Vardanega and Bolton" response. The first features a straight line through the origin,

followed by a horizontal plateau. The unknown variables are ϵ_{lim} and c_u. The second equations features a power law curve followed by a horizontal plateau. More can be read about these equations and how they are used in Chapter 4.

With artificial dataset analysis, these equations were able to capture the modelled soil behaviour as the same equations had been used to generate the properties input into ABAQUS. With real datasets however, the true behaviour is unlikely to match. The elastic-perfectly-plastic equation has potential to recover curves similar to what the Segment based approach was able to achieve, with many of the presented recovered curves being approximately elastic-perfectly-plastic. The "Vardanega and Bolton" equation is unlikely to match soil behaviour. Initial experimentation found that the Equation based approach using the "Vardanega and Bolton" response chooses parameters such that the power law curve part of the recovered response is very close to a straight line. Additionally, using the "Vardanega and Bolton" equation takes a huge amount of computational time. For these reasons, only the elastic-perfectly-plastic soil response will be used for assessment of the Equation based approach.

The recovered curves using the elastic-perfectly-plastic response with the Equation based approach are typically similar to the recovered curves from the Segment based approach, and as such only a subset will be presented. Any commentary that could be given regarding reasons why some datasets perform better than others is identical to that which was presented for the Segment based approach. The same issues with touchdown timing or displacement field quality still apply. As such, commentary given here will focus on any differences between the two approaches. Specimen Four has been chosen as the dataset to be analysed.

Figure 8.29 shows the recovered stress-strain curve superimposed over the supplementary data. By eye, the curves recovered using the Equation based approach are very similar to those recovered using the Segment based approach (Figure 8.29), with a few differences that will be discussed. The Camera One datasets are very similar to what was shown previously. The exact values can be found in Table 8.4. The Camera Two datasets have some meaningful differences. The limitation of an elastic-perfectly-plastic response being presupposed is apparent here, with the 40mm/Cam2 dataset being of a radically different shape than before.

The reasons for the locations of each curve are the same as previously discussed. 40mm/Cam1 has an extremely high plateau due to uncounted internal work resulting from a significant amount of soil movement outside the area of interest. The Cam 1 data was expected to be both steeper and have higher plateaus than the Cam 2 data due to the flaws in the touchdown process. This is not in fact the case for the 20mm footing datasets, where the inverse

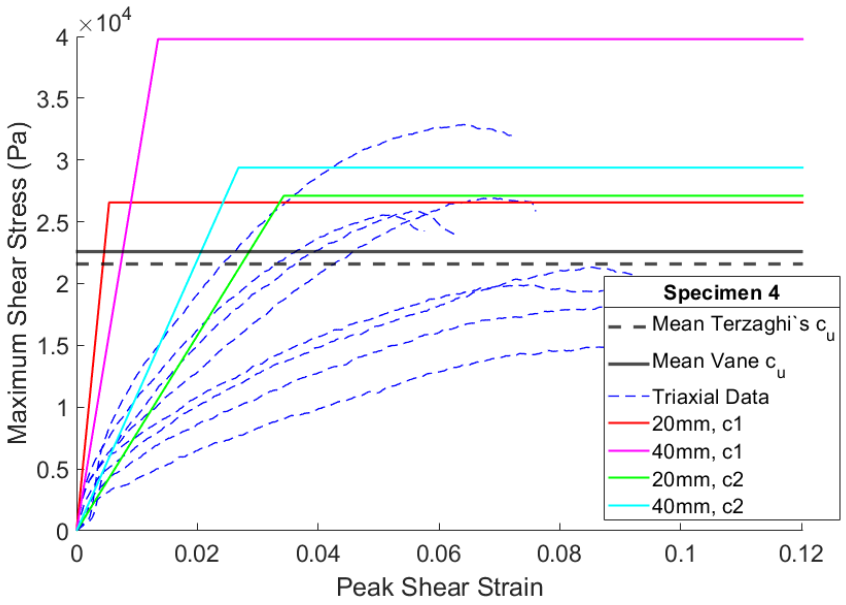

FIGURE 8.29: A comparison between the stress-strain curves recovered with the Equation based approach and the supplementary data for Specimen Four.

is observed. The cam 2 dataset has a very slightly higher c_u than the cam 1 dataset, however cam 1 is extremely steep in comparison, which would perhaps make up for this discrepancy.

It should be noted that any curve recovered by the Equation based approach is theoretically recoverable by the Segment based approach, so every curve should be a worse fit in terms of energy. This will be considered by examining the cumulative energy plots.

Plots of cumulative internal and external work can be found in Figure 8.30. By eye, there are a few points of consideration. Exact figures for global energy gap can be found in Table 8.4. The energy plots are approximately the same as before, with no significant deviations in shape. Slight differences can be found in that the 20mm datasets appear to have small energy deficits that were not present before, and the energy deficit for 40mm/Cam1 appears to be smaller. Despite this unexpected result of plotting cumulative local energy gap, the global error is worse for the Equation based approach as expected. This appears to be the case for every dataset. Table 8.4 provides key figures to allow for comparison between the two methods.

8.5 Investigation into Preprocessing techniques

In order to prepare the previously discussed datasets for use with the proposed Identification Methods, a number of preprocessing techniques were used. A thorough investigation

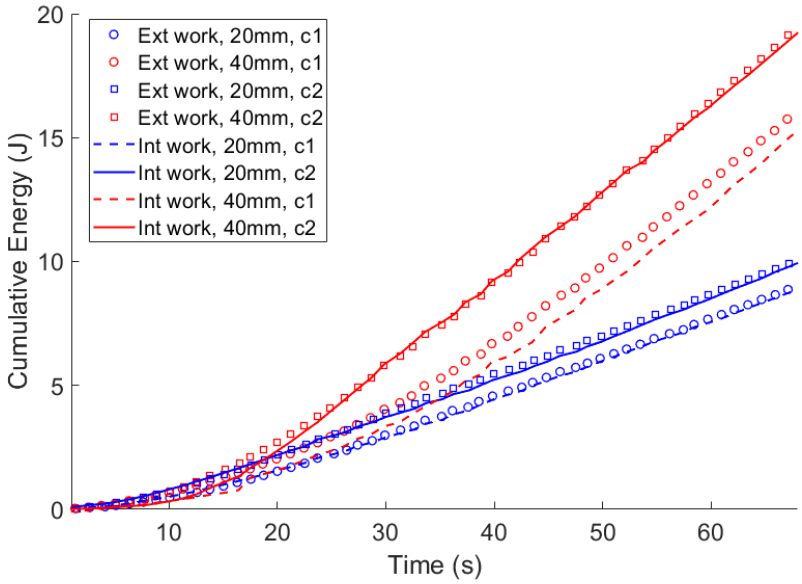

FIGURE 8.30: The difference between cumulative local internal and external energy for Specimen Four using the Equation based approach.

Test	Segment c_u	Equation c_u	Segment Energy Gap	Equation Energy Gap
20mm/Cam1	27144	26567	1.1582%	1.1815%
20mm/Cam2	26196	27108	1.4733%	1.4925%
40mm/Cam1	39925	39783	3.5079%	3.7202%
40mm/Cam2	34269	29383	1.2142%	1.4445%

TABLE 8.4: A comparison between the two Identification Method Approaches for Specimen Four.

in to how to best process the data would be a substantial challenge, due to a huge combination of different factors that interrelate in different ways, and the variance between datasets. An optimal pre-processing strategy for one dataset may be suboptimal for another.

It is for this reason that initial informal experimentation was used to determine which techniques should be used. Various combinations of preprocessing methodologies were tried with datasets as they became available, with the techniques described earlier in this chapter appearing to be best for most datasets. As supplementary data was available for comparison, it would have been possible to individually tweak the methods used for each individual dataset. One set may produce a stress-strain response closer to the triaxial data with less smoothing for instance, while another could have a c_u value closer to the shear vane data if a sparser GeoPIV patch grid is used.

Doing this however would not allow for a set of recommendations for datasets in which the "true" soil response is not known. It was decided that a single methodology of preprocessing

techniques that appeared to give the best results on average would be uniformly applied to each dataset, which is indeed what has been presented in the preceding section of this chapter.

A number of issues with the datasets were identified, some independent of preprocessing techniques such as soil movement outside of the area of interest, or areas with artificially low movement due to flocing issues. Some issues, such as the difficulty of choosing the exact start point of the test when the footing touchdown is slightly askew, are things that can be affected through preprocessing decisions.

This section of the chapter will therefore investigate the effects of the processing decisions made. Where there is little difference, or where one decision is clearly dominant, this will be stated, as will cases where the recovered curve is extremely sensitive to the decision made. A subset of datasets will be examined here. To investigate the effects of PIV patch size for example for all 16 datasets would be hugely consuming in both time and space in the thesis. The goal of this section is not to optimise the process separately for each individual dataset, but to broadly consider how such preprocessing decisions affect the proposed Identification Method such that commentary can be given on the uniform preprocessing strategy employed and potentially how it could be refined.

8.5.1 Sensor Zero Time

The point at which the test is considered to have began was not trivial to find for many of the datasets. Ideally, the point at which the footing comes into contact with the soil will immediately be followed by both loading and displacement gradually increasing. In practice, ensuring that both the footing and the soil surface were level and perfectly parallel proved to be difficult with the available equipment. An analogue bubble spirit level along with placing bolts under the feet of the specimen box proved to be insufficient and as such the footing touched down slightly unevenly for many datasets, often with the load cell recording a negative load briefly while the footing levels out.

As previously discussed, a point in time must be chosen from which the data can be zeroed, and the point at which the footing is in contact at both edges was chosen. This seemed a logical time to start, with the c_u value obtained from using the peak observed load with back analysis uses Terzaghi's bearing capacity equation being of a similar value to the c_u values obtained through shear vane testing. The downside is that the same start time was used for the datasets obtained on both sides of the box, with one undergoing small but visible distortion in the soil prior to the designated start time. There is the possibility that both sets of data could be used simultaneously, with a single curve recovered that is optimal for the combination of datasets. Exploring this is a potential area of future work.

Due to the flaws in the available data, the start time has a large impact on the recovered curve. This was one of the considerations behind ensuring uniformity in the preprocessing techniques used, particularly for the pairs of datasets obtained simultaneously. Simply zeroing the data several images earlier or later to get a better recovered curve would give an unfair impression of the procedures used.

The effects of moving the zero point forwards and backwards by up to 10 seconds will be presented for a two datasets. The recovered stress-strain responses will be provided, as will the effects on c_u value and global energy gap percentage. The data presented was generated using the Segment based Identification Method, however similar plots would be produced were this analysis carried out using the Equation based Identification Method.

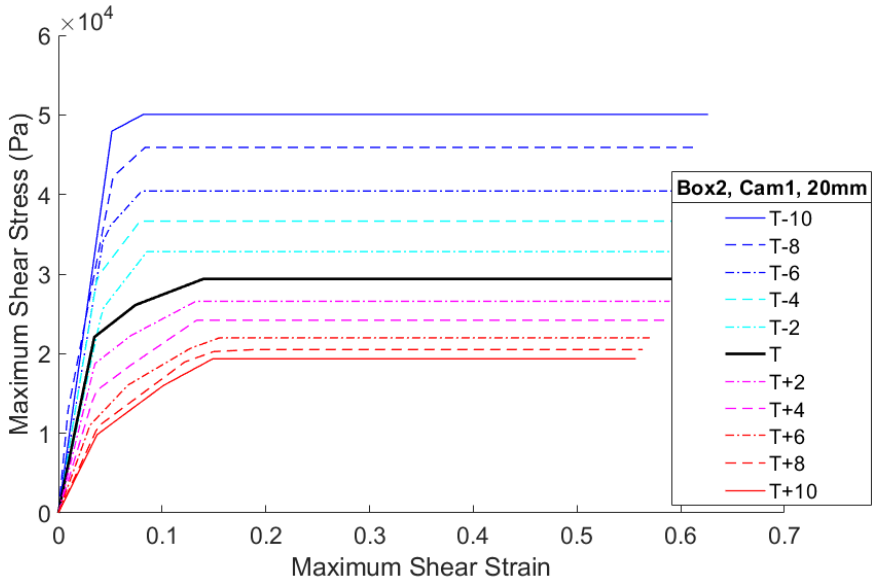

FIGURE 8.31: The effects of varying the start time of the Specimen Two, Camera One, 20mm dataset regarding the recovered stress-strain response.

Figure 8.31 shows that altering the zero time point in increments of two seconds causes the recovered stress-strain response to increase or decrease relative to the time change. Each time increment represents an average of two image frames. It is of note that the changes to the recovered stress-strain curve directly correspond to the change in zero time; there is no scenario in which starting later causes a lower stress-strain curve or starting earlier causes a higher curve.

The primary mechanism behind this observation is that external work is essentially scaled up. The load-displacement curve is initially very steep, such that two seconds is a significant amount of load. Work done early in the dataset is of minimal concern, the later stages in the dataset will see the same plateau in the load displacement curve, only now higher. Stresses will have to be scaled up by a similar proportion in pursuit of energy equilibrium. A less

significant but still present effect is that the strain field will also be altered at the earlier stages.

The overall effect observed is large. It can clearly be seen in Figure 8.31 that the c_u value from the stress-strain response is over double based on a 20 second differential in the zero time. This extreme time differential is somewhat large but unlikely in practice as it would be equivalent to being out by at least 20 images when selecting which image has full touch-down. Being out by a small handful of images is within the realm of possibility, which would correspond to the plots for $T-2$ and $T+2$. This is still not ideal, but managable provided there is awareness of the issue.

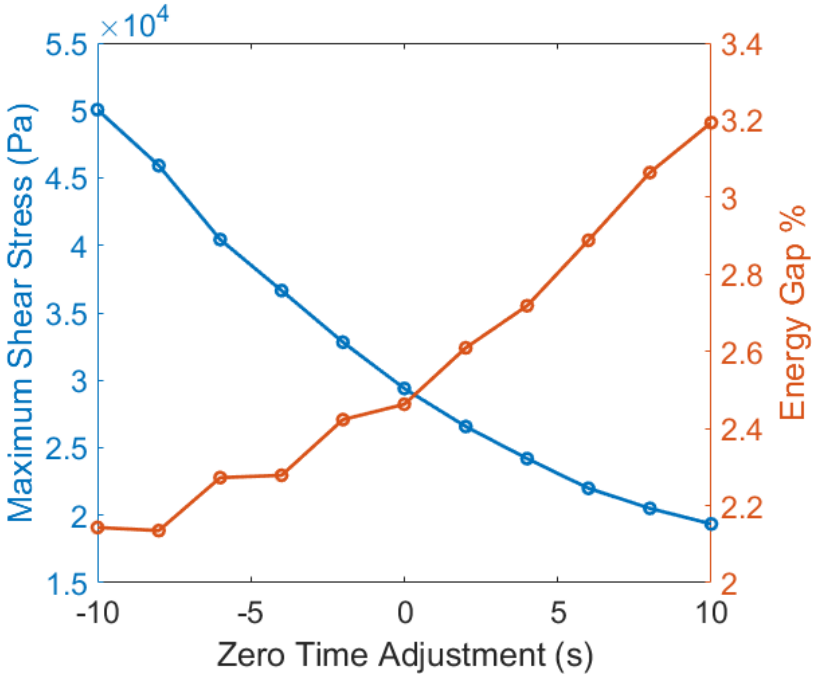

FIGURE 8.32: The effects of varying the start time of the Specimen Two, Camera One, 20mm dataset regarding peak c_u and the global energy gap.

Figure 8.32 confirms how c_u alters and also plots global energy gap percentage against the zero time adjustment. There does appear to be a correlation between energy gap and zero time, with earlier zero times resulting in a slightly lower energy gap. This does not imply that the stress-strain response for $T-10$ is better, as it clearly isn't due to far exceeding the triaxial and shear vane data. A possible explanation for the improvements in energy gap are that this dataset represents the end of the footing that touches down first. There are small strains that are observable by eye prior to $T=0$ but which are discounted due to needing to start both datasets in the pair at the same time. Were it not for the compromised external load data, it is likely that being able to include these earlier strains would be beneficial.

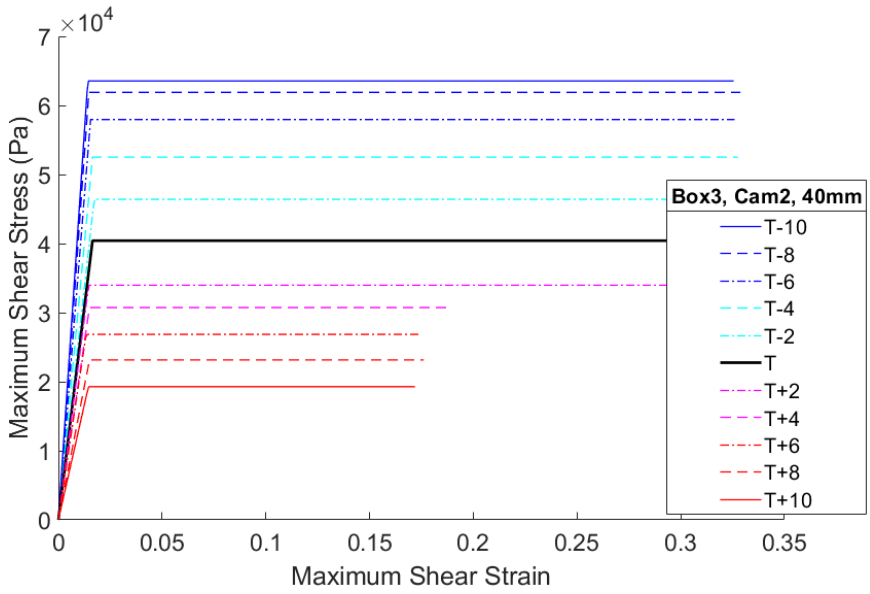

FIGURE 8.33: The effects of varying the start time of the Specimen Three, Camera Two, 40mm dataset regarding the recovered stress-strain response.

Figure 8.33 shows the recovered curves for the Specimen Three, Camera Two, 40mm dataset. The same phenomenon can be observed for this dataset as can be seen for the previous case study. Starting later lowers the recovered stress-strain curve and starting earlier raises it. Whereas the previous case study was for a relatively good dataset, in which the recovered curve at $T = 0$ was reasonable, this dataset is for a poorer dataset. This dataset was discussed previously for having a large energy gap, particularly in the first 5 seconds or so. This can be seen in Figure 8.21 presented earlier in this chapter.

It can be seen in Figure 8.34 that the energy gap against zero time adjustment is significantly different than in the previous case study. There is an overall movement towards a lower energy gap as zero time is moved later, although it is not apparent until the point is reached that the anomalous frames with a huge local gap are eliminated. This anomaly in the early parts of the dataset prevents any conclusions being drawn that would be generally applicable, but the fact that simply cutting the anomalous frames out has resulted in both a more reasonable curve in comparison to the supplementary data and an improved energy gap indicates that this is something that could be worthy of future consideration.

8.5.2 PIV Patch Spacing

Another preprocessing technique that was used was the patch spacing options in GeoPIV-RG. It was possible to vary both patch size and patch spacing (both measured in pixels), such that overlaps or gaps were possible. Having overlaps or gaps in the PIV patch set has

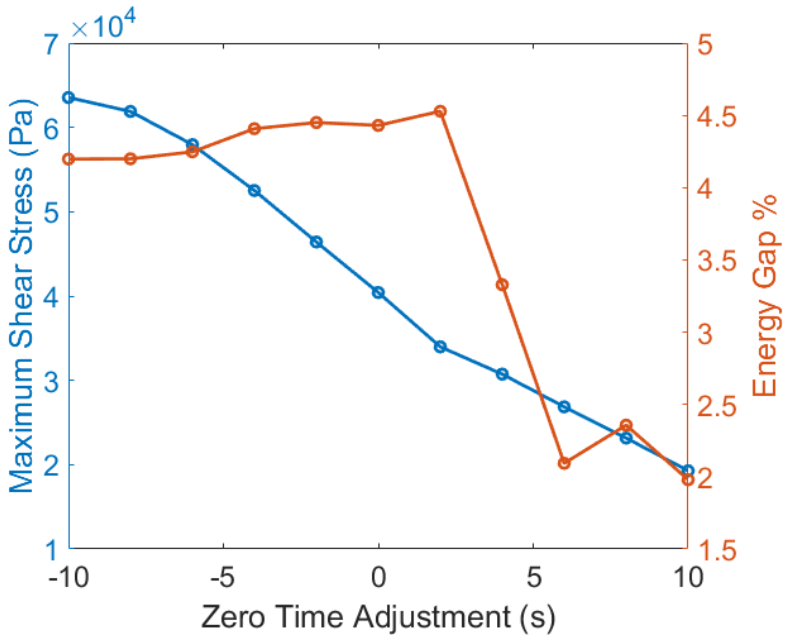

FIGURE 8.34: The effects of varying the start time of the Specimen Three, Camera Two, 40mm dataset regarding peak c_u and the global energy gap.

no energy implications in and of itself, as the displacement and strain fields are based on the central node of each patch. The means by which patch spacing or size will effect the recovered curve is in the quality of the displacement and strain fields. A combination of size and spacing has potential to cause strains to be overall higher or lower than they should be. For instance, a sparse array of patches has potential to miss out localised features of the strain field.

There is also the concern of the quality of the PIV process. Patches that are excessively large, with significant internal deformation, or too small, with little texture, are unlikely to be satisfactorily tracked using the DIC process. Incorrect sizing has the potential to cause a higher number of wild vectors, or even to simply fail, as if GeoPIV-RG finds too many patches to be below a user defined standard it will return an error without completing the process.

A patch size of 50px and a spacing of 25px was selected based on preliminary informal experimentation and this is what was used for the presented validation tests earlier in the chapter. The chosen values appear to have been a good choice, in that the displacement vector plots appear to be good representations of the expected mechanisms for a footing test. Nonetheless, this section will present a brief investigation into the effects of altering the selected size and spacing. To be able to pick a single value as a recommendation for future use of the Identification Method is not the goal here, as every dataset will be different, but instead to investigate how varying these factors could potentially impact the Identification

Methods.

To achieve this, the Box 4, Camera Two, 20mm image set was selected and GeoPIV-RG was used to extract a displacement field with every combination of patch sizes 25, 50, 75, and 100px and patch spaces 25, 50, and 75px. The datasets produced were otherwise identically preprocessed using the usual methodologies. The Segment based approach was used with 100 segments. One point to note is the removal of wild vectors. It was decided that removal of such vectors should be done as consistently as possible, however the differences between the displacement fields made this somewhat difficult. Particularly for the sparser grids, removing a single wild vector could represent an area almost as large as the footing width. It also became increasingly hard to identify wild vectors as there are significantly less "good" vectors to compare them too. As such, comparing patch sizes and spacings in the manner is somewhat flawed as there are other uncontrollable factors that are inadvertently varied.

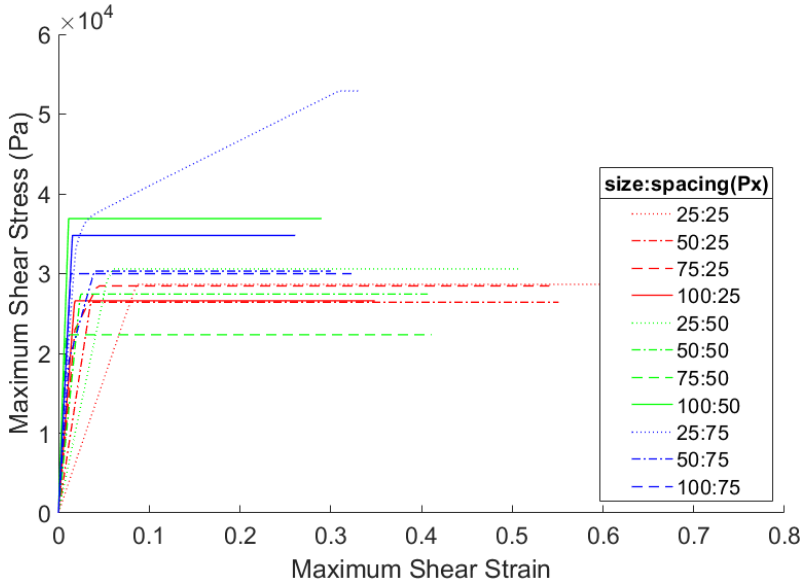

FIGURE 8.35: The effects of varying the PIV patch size and spacing of the Specimen Four, Camera Two, 20mm dataset alters the recovered stress-strain response.

Figure 8.35 shows the recovered stress-strain responses. The plot is at first somewhat messy, but a few points can be made based on the available data. The recovered curves appear at first to be very sensitive to the GeoPIV patch setup, however closer examination indicates that much of the variance is for either sparse setups, or cases in which vary small or large patches are used.

Examining only the curves recovered from datasets with a spacing of 25px (seen in red), it can be seen that the variance between the recovered curves is much smaller. The variance

between datasets with sparser spacing is much higher. Likewise, the curves for datasets with a patch size of 50px (alternating dot and dash) area also reasonably close.

8.5.3 Strain Data Processing

The displacement field has some degree of inherent noise. This noise will also affect the strain field. It was shown in Chapter 7 that the addition of noise to artificial datasets degrades the recovered curve and results in a lower value of c_u. The mechanism by which this happens is that negative incremental strains are introduced. A key assumption of the proposed Identification Methods is that the soil undergoes a monotonically increasing load and strains will similarly be increasing. Based on this assumption, the proposed Identification Methods were implemented such that negative strain gradient is simply not counted. Models to correctly deal with this would be significantly more complex than the simple curve recovery process is able to handle.

Despite negative strain not being counted, positive incremental strain is still increased by the addition of noise. There are more "uphill" sections of the strain-time plots even if the "downhill" sections are not counted for energy equilibrium purposes. Unlike the artificial data, noise doesn't need to be artificially added to real datasets as it is already present. Elements with significant strain are less affected as the signal to noise ratio is much better, however elements with negligible displacement and strain have a very poor signal to noise ratio. A zero strain element that in actual fact would contribute zero to internal work could instead contribute a substantial amount of work due only to noise. Taking into account the fact that the vase majority of elements are low or zero strain it is clear that a strategy would be required to deal with this issue.

What was ultimately decided was that negative strain increments should be removed. What would previously be a jagged strain-time plot would instead look somewhat like a stair case. Figure 8.36 shows a number of strain elements that have undergone this process, with the plot in the top left being a zero strain element, the bottom right being a high strain element, and the other two being somewhere in between. It is clear to see that from these plots the signal to noise ratio is extremely poor for the zero strain element, and gradually improves as the final strain increases. The staircase processing applied smooths out any negative movement.

A downside of this process is that noise can also involve increasing strain. Particularly in the zero strain case, a particularly high peak essentially forms the new high point of the dataset causing an overall increase in strain between the first and last increment. This will result in a small amount of spurious internal work being counted, but significantly less that were the staircase processing not applied. An additional stage of removing elements with final

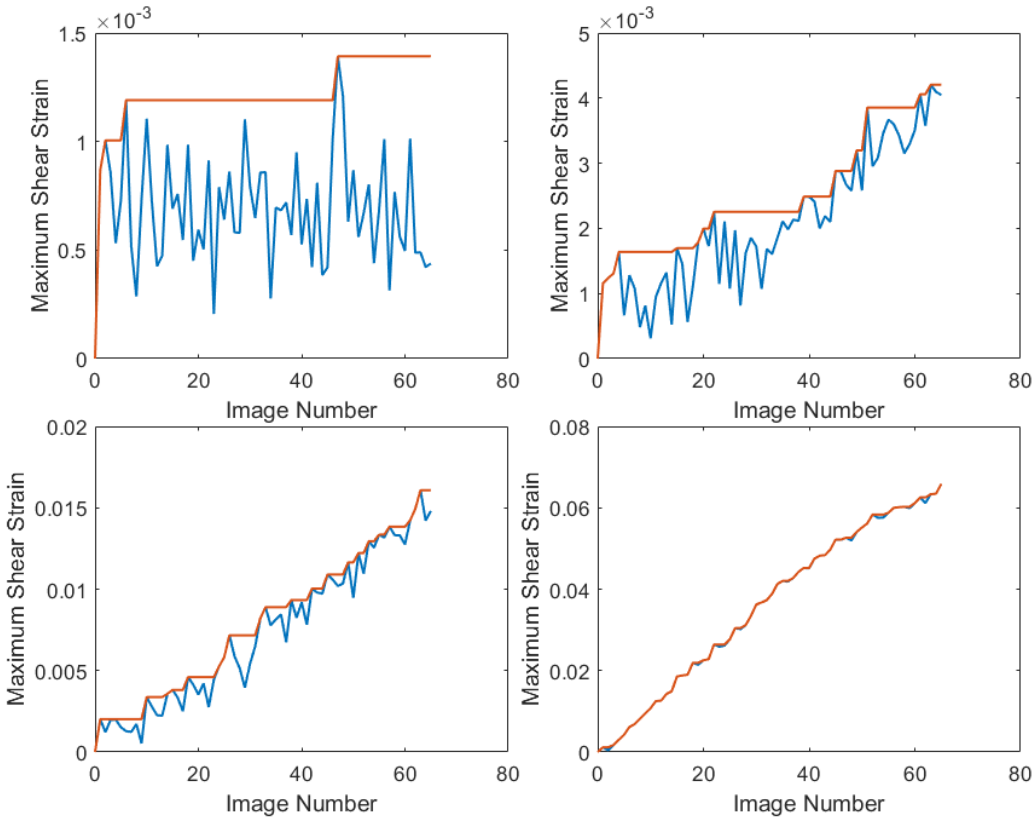

FIGURE 8.36: A set of plots showing how noisy strain data is processed into a "staircase" in which negative increments are removed.

maximum shear strains below a threshold was applied, and despite typically eliminating several tens of percent of the total number of elements, the effects on the recovered stress-strain curves were small.

Other methodologies were considered. A line of best fit could be used, but would risk ignoring a genuine change in slope for elements with actual movement. Curves of best fit are also possible, but with a polynomial order high enough to capture genuine features there is still a risk of having negative strain movement. Various smoothing algorithms also have this issue. Using techniques such as these also leads to the risk that negative shear strain could be introduced. Not incremental negative strain but absolute negative strain in which the strain-time plot would drop below the x axis. As a negative shear strain is not a physical possibility, the implementation of the proposed Identification Methods would not function correctly. The Segment based approach for instance, would be stuck in an infinite loop during the process were strains are distributed into segments; an element with below zero shear has no place on the stress-strain curve. Any methodology in which this is a possibility would require additional logic to catch and deal with such an issue.

Test	c_u	**Global Energy Gap**
Strain Preprocessed	26196	1.4733%
Strain not Preprocessed	16410	1.7795%

TABLE 8.5: The effects of the proposed strain preprocessing methodologies for the Specimen Four, Camera Two, 20mm dataset.

Table 8.5 shows how applying the described strain preprocessing techniques affects the recovered stress-strain response. Not dealing with the negative incremental shear strains causes the addition of significant spurious work, resulting in a much lower stress-strain response. The global energy gap is also marginally worse.

8.6 Discussion

This section will contain overall discussion and commentary on the validation of the proposed Identification Methods. First, key points will be drawn from the work presented relating to "real" datasets along with relevant discussion. Next, reference will be made to Chapter 7 such that differences between "real" and artificial datasets can be considered, along with the potential insights that can be drawn from such a comparison. Finally, recommendations will be given that will be of use to any reader who would seek to design physical modelling experiments such that either of the proposed Identification Methods (or similar methods) can best be utilised.

8.6.1 Overall Commentary on "Real" dataset analysis

A total of 16 datasets were produced through a series of 8 $1g$ footing tests carried out across 4 specimens of undrained kaolin clay consolidated from slurry to a final consolidation pressure of $200kPa$. Load and displacement of the footing were recorded through use of LVDTs and a load cell and the displacement field of the flocced soil was recorded on each side of the specimen through digital photography.

The quality of the prepared specimens improved throughout the test procedure based on experiences with earlier specimens. Fortunately, the slightly lower quality of earlier specimens allowed for the identification of issues that might otherwise have been missed. Of note is that should GeoPIV-RG or a similar PIV package have regions within the area of interest in which data is missing, likely due to insufficient soil texture, this will result in an internal energy deficit that must be made up by the remaining regions of soil. The 40mm width datasets from Specimen One are a good example of this phenomenon.

Other cases in which missing data can cause an energy deficit can also be identified. Soil movement outside of the specified area of interest will not be considered for purposes of energy equilibrium, requiring the difference to be assigned to the energy expended by the soil within the area of interest. In many of the 40mm footings in which an asymmetric failure mechanism formed (i.e. the displacement pattern is predominantly going in one direction) there is a small amount of movement perpendicular to a vertical edge of the area of interest. In the Specimen Four, Cam 1, 40mm dataset this effect was particularly pronounced. The reason behind this particular case was unknown, the loading and soil strength was no different than for other datasets, and systematic error due to camera movement was ruled out. The effects were significant movement outside of the area of interest in multiple directions that caused an extremely high recovered stress-strain response.

Although some sets of displacement/strain data had flaws, preprocessing was applied uniformly such that all datasets could be directly compared. GeoPIV-RG was selected as the tool to convert raw image data into a displacement field. The key decision for the PIV process is the size and spacing of DIC patches. Smaller patches would have insufficient texture to allow for accurate tracking, and overly large patches would potentially have large internal deformations similarly preventing accurate tracking, as well as possibly smoothing out localised displacement field features. Patch spacing is essentially denser the better. Patch overlaps are not a concern regarding energy eqilibrium and a sparse patch would potentially miss details, so the only downside of an overly dense grid or patches is increased computational time.

A patch size of 50px and a spacing of 25px was chosen through informal experimentation and was used for the validation analysis process. This patch size and spacing was later varied as part of a more formal investigation into the effects of changing parameters and it was found that a size of 50px and a spacing of 25px was a reasonably good choice. The investigation into size and spacing however had issues that lower the value of direct comparison. Consistency was hard as different combinations of size and spacing would give different grids with different wild vectors needing to be removed such that it is difficult to know if the differences between recovered curves are truly due to the different sizes and spacings.

Despite this concern, it was found that the variations between cases with a size of 50px and between cases with a spacing of 25px were lower, indicating that the chosen parameters were indeed suitable. A much more thorough investigation into the optimal GeoPIV-RG settings would be possible but is beyond the scope of this work. To judge PIV parameters by the outputs of the proposed Identification Methods requires the Identification Method process to be fully validated, which is the purpose of this work. Having PIV parameters that are "good enough" is sufficient for the purposes here and a patch size of 50px and a spacing of 25px certainly appears to be just that. Further refinement of the PIV process for

use with an Identification Method would however be a possibility for future work.

The remaining preprocessing of the strain fields is much less controversial. Wild vectors were removed, as is standard practice for PIV analysis. Whereas in qualitative PIV a wild vector is essentially an annoyance that makes vector plots ugly, for the purposes of the proposed Identification Methods a wild vector represents spurious internal work. After removal of such vectors, strains were calculated. The displacement field was triangulated using Delaunay triangulation, a process that is resilient to irregular grids due to photogrammetry or missing nodes due to wild vector removal. Strains were calculated based on the three noded triangular element methodology described in Chapter 3. Noise in the strain data was removed by converting the elemental strain-time data into staircases, replacing any negative incremental shear strain with zero. Elements with very low strain were also trimmed, allowing large areas of interest to be chosen for PIV with no ill consequences.

One important issue is the decision of when to consider a test to have started. As the footing touches down it is not necessarily going to do so simultaneously across the entire length. This could happen due to the surface of the soil not being level, or in this case due to the footing simply not being parallel. The footing was rigidly fixed to a large robotic actuator which was immobile and assumed to be level. The specimen box was levelled using a spirit level and by placing bolts or other miscellanea under the feet of the box such that it was level. This process was somewhat less than precise and resulted in uneven touchdowns for some datasets.

When the footing touched down unevenly, there was enough soil strength that it wasn't simply driven in but instead caused the footing to flex, applying a moment to the rigidly connected load cell which recorded a negative load. Zeroing the dataset at such a time would result in the loading data recorded after full contact being excessively high. It was chosen that the zero time would be when both sides of the footing were visibly in contact which would be determined by manual examination of the imaging data. The peak loads observed when zeroing in this manner compare reasonably well with what would be expected when entering shear vane data into Terzaghi's bearing capacity equation, or certainly better than zeroing when nominal load is negative.

Unfortunately, the proposed Identification Methods were demonstrated to be highly sensitive to changing the start time. An investigation was presented that showed that moving the start time forwards or back, and hence decreasing or increasing external work, would have a corresponding impact on the recovered stress-strain curve. Error in selecting the start point would potentially cause an incorrect curve to be recovered. As supplementary data was also collected, it would be possible to simply pick a start time that causes the recovered stress-strain curve to most closely match the available triaxial data. This was not done however, as individually tweaking each dataset rather than using a consistent approach would make the

validation process meaningless, and would not be possible for any future use were supplementary data was not available for comparison. Instead the approach of selecting the start time was carried out as consistently as possible, such that pairs of datasets (e.g. both camera views of a footing test) have exactly the same start time despite one end of the footing coming in contact first.

The uneven touchdown process did have an identifiable effect on the recovered stress-strain curves from such pairs of datasets. It was found that the dataset corresponding to the end that touches down first has overall higher recorded strains, both average and maximum, as although the displacement field is zeroed small deformations are already underway from the very start. The opposite is true for the dataset corresponding to the second end to touch down, in which strains are generally lower. This causes the recovered curves to be higher and steeper. This was observed across all datasets with the touchdown discrepancy.

Discounting datasets in which flaws were identified, reasonable stress-strain responses were recovered for the datasets corresponding to the end of the footing that touches down first. c_u values were typically within the range suggested by the supplementary triaxial or shear vane data, and in many cases the earlier stages of the recovered stress-strain response prior to the plateau were also within the region suggested by triaxial data. Most curves recovered by the Segment based approach were of the form of an elastic-perfectly-plastic response which is unlikely to be the true soil behaviour and instead the form that the proposed Identification Method returns with less perfect data (as seen in Chapter 7 where artificial datasets are artificially degraded). Some recovered curves however have much smoother interfaces between the elastic and plastic regions of the curve.

Although many datasets were able to be analysed successfully, some were not. In all these cases the reasons were identified and were typically due to flaws in the data, such as PIV issues, or the touchdown issue. This is both a point for and against the proposed Identification Methods. On one hand, being able to deal with "good" datasets is promising, but on the other hand, the resilience to less "good" datasets appears to be low. The most likely solution is additional pre-processing rather than changes to the Identification Methods themselves. An interpolation scheme, for example, could be used to fill in empty regions in the PIV outputs, but this mitigation would only work for small empty regions.

Other issues such as the touchdown issue, will best be removed by designing experiments where these issues simply aren't present. There is not much to be done with the currently available datasets, but any future research where there are plans to utilise an Identification Method will no doubt be able to take into account lessons learned during this work.

In terms of the comparison between the two proposed Identification Methods, it appears that the Segment based approach is superior for several reasons. Firstly, the Segment based

approach is able to recover suitable curves for a wider range of soil behaviours than the Equation based approach. As the equations that were programmed in, the "Vardanega and Bolton" curve and the elastic perfectly-plastic curve, did not closely match the true soil behaviour the Equation based approach struggled to find a satisfactory output. The Equation based approach, relying on a brute force methodology, also took much longer to run.

The following subsections will look at the differences between the "real" datasets analysed in this chapter and the "artificial" datasets analysed in the preceding chapter, which lacked many of the issues identified here, followed by recommendations that will allow physical modelling to best be optimised for use with the proposed methodologies.

8.6.2 Comparison between "Real" and Artificial datasets

The artificial datasets produced and analysed in Chapter 7 facilitated the recovery of overall better stress-strain curves. This is of course expected. Artificial datasets have very few avenues by which the proposed Identification Methods could perform poorly.

It was found that the recovered curves would be of lower quality as the "perfect" artificial datasets were moved closer to real datasets, either by modelling increasingly complex scenarios or by deliberately degrading the datasets by adding noise or reducing spatial or temporal resolution.

There were a number of factors that were not considered when testing the artificial datasets. Degradation by simply removing a region of the displacement field was not attempted. Doing so would simulate the effects of missing regions of PIV data, but the effects are predictable and would closely match the commentary regarding this phenomenon earlier in this chapter. Wild vectors are not present in artificial datasets. Extreme amounts of noise added to a handful of elements would be the equivalent. The investigation into the effects of the addition of noise however would be broadly applicable, although likely to a different degree depending on the exact values used.

Noise was present in the "real" datasets but was dealt with rather painlessly. Singular anomalies were simply deleted, and random noise was removed throgh the staircase process. The exact signal to noise ratio varies between elements. Some, elements in the peripheries of the real dataset would be expected to have zero shear strain, but instead were recorded to have a very noisy strain-time plot rather than a simple straight line along the axis. Elements with lots of strain however had much better signal to noise ratios and required essentially no smoothing.

The touchdown issue was not present in the artificial datasets. Artificial datasets are discrete sets of data, there is no before and there is no after. The model runs for exactly the time

specified and starts at zero. This is not the case for real datasets in which the specimen has been consolidating in the sample box for a week, moved around on a forklift, and has been trimmed, flocced, and otherwise processed.

There is no discrepancy with an artificial dataset, the test starts at the point of contact with a perfectly undisturbed 2D plane of soil. With much additional complexity, it would be possible to create a 3D model of a footing test, including edge effects and an irregular touchdown. It would also be possible to take the existing artificial datasets and desynchronise the times for the internal and external components, or simply scale up external work. The expected outcome would likely confirm the findings presented in this chapter regarding the touchdown process.

A final difference is the quality of the comparison data. For artificial datasets, the true soil behaviour is known exactly as it is used as an input for the ABAQUS model. Not only that, but it is known to be of the same form as the equations specified for the Equation based approach. There is no such luxury for the real datasets. The true behaviour is unknown. Insight can be gained through supplementary testing, but this provides a fairly large range of possibilities. There is of course no guarantee that the specified equations used in the Equation based approach will be valid for real data, as was found in this chapter.

Knowing how the differences between real and artificial datasets affect the proposed Identification Methods, it would certainly be possible to further degrade artificial datasets to be more representative, but there is no guarantee that the resilience of the proposed methods could be improved to deal with this. A much better approach would be to ensure future physical models are designed to best take advantage of the Identification Methods, should a modeller plan to utilise them.

8.6.3 Recommendations for future Physical Models that are to utilise an Identification Method

This subsection will identify means by which physical models can be best designed to utilise the proposed Identification Methods. Some will be based on parts of the presented experimental program that causes issues, but also parts that went well. Many of these points will be generally good experimental technique but will be identified due to particular relevance to Identification Methods.

1. Displacement field quality. In cases were PIV is used qualitatively to provide a rough overview of mechanisms with a body of soil, patch size and spacing are not overly important. The numeric values for the vectors may not be used in any way, save perhaps for plotting a strain field that is for illustrative purposes. It is imperative that

the quality of the PIV derived displacement field is as high as possible. Gaps due to poor texture have a meaningful effect on the recovered curve.

2. Inclusion of all work. All work that is done to the specimen must be measured and included. This primarily requires PIV to be carried out anywhere where there is soil movement. Overly conservative regions of interest potentially will miss interesting data. Other factors such as boundary effects or friction should either be quantified and included or the model should be designed such that these can be safely ignored.

3. Consideration of the test start. In the presented datasets, the touchdown process caused issues as it became difficult to determine the time at which energy should be measured from. Ideally there should be no ambiguity. Loading and Displacement should begin to increase simultaneously. For the presented work, the footing could have been placed on the soil surface with the actuation arm contacting via a ball bearing when it lowers into contact. There are pros and cons to any methodology, including the suggestion just given. Understanding the impacts of the start of the test is simply another aspect to consider. Other tests such as a pipe rising through the soil or a slope failing under its own weight (possibly due to increasing gravity during a centrifuge test) could potentially eliminate this issue.

8.7 Conclusion

This chapter has provided proof of concept that the proposed Identification Methods have potential to successfully recover stress-strain responses from datasets produced through physical modelling. The datasets were qualitatively analysed and contrasted, with flaws and special considerations identified. A number of issues with some datasets such as insufficient PIV texture and footing touchdown irregularities were discussed, along with their effects on the recovered curves.

The proposed Identification Methods can consistently recover soil strength of a reasonable value when compared to supplementary testing results provided the available image and footing data is of sufficient quality. For higher quality datasets, the recovery of a stress-strain response that compares well with triaxial responses was demonstrated. Although there is work still to be done in perfecting the Identification Methods such that they could be used as a general purpose research tool, the potential of such a tool has been clearly established.

A preprocessing methodology regarding PIV parameters, strain smoothing, and zero time selection was identified and justified. After using the methodology to prepare and run 16 datasets, the key assumptions and decisions were tested and found to be acceptable with some caveats. It was found that the Identification Method is particularly sensitive to zero

time selection, and although the starts of tests were selected appropriately there is a possibility of human error negatively impacting the recovered curves. The effects of the irregular touchdown were also considered in context of this finding.

Finally, overall discussion and commentary was given including identifying key differences between the "real" datasets analysed in this chapter and the artificial datasets analysed in Chapter 7 and key points that would be of use in the design of future physical models that facilitate the utilisation of the proposed Identification Methods were given.

Chapter 9

Conclusions and Future Work

This chapter contains list of the objectives of this project with commentary discussing to what extent they have been achived. Additional findings that were made in the course of completing these objectives have also been identified. Commentary on future work that could be carried out, either by the author of this thesis or by others, will be provided.

9.1 Commentary on Objectives

The primary aim of this project was to develop, test, and validate one or more Identification Method suitable for extracting the stress-strain response geotechnical physical models using full field PIV-derived displacement data. This aim has been met. Two different approaches have been developed, the Segment based approach which is built upon previous work with significant improvements and additions, and the Equation based approach which is a novel algorithm developed during this project. These Identification Methods have been validated and tested with both artificial datasets and real datasets and have been shown to be generally functional. Commentary on the objectives identified in Chapter 1 is as follows:

1. An investigation into the existing techniques used by material scientists has been carried out. It was found that existing methods are typically used for unit testing and typically use linear constitutive models with nothing comparable to geotechnics. The existing work in this field by Gueguin et al. (2015) was inspired by the Virtual Field Method but removed some requirements such as kinematic admissibility in order to allow for measurements of materials with significantly more deformation.

2. Literature relating to physical modelling techniques was examined. Of note was an investigation into several possible PIV packages that could be potentially used, with GeoPIV chosen as the most appropriate. Photogrammetric techniques were researched with bespoke code developed to carry out the procedure. Existing methods by which soil behaviour is measured were examined.

3. The method proposed by Gueguin et al. (2015) and the associated codebase were analysed. A new algorithm for the Segment based approach was developed that allowed for improved calculation of the area under the unknown stress-strain curve with regard to differing timesteps and increments. Changes were made allowing for minimising of absolute energy difference rather than relative energy difference and to use incremental internal and external work rather than cumulative.

4. While allowing for reuse of code relating to data management, an additional Identification Method was derived. The Equation based approach defines the unknown stress-strain response in terms of an equation with only a few parameters. Although allowing for less freedom in the recovered curve shape, this method allows for the user to use their judgement to presuppose the curve shape.

5. A suite of artificial datasets were generated to allow for validation of the two proposed Identification Methods. Matlab was used to produce "handmade" simple shear and split shear datasets, with FEA used to produce two differing shear cases along with a rotating wall model and a simple footing model. Each dataset was modelled using both an elastic-perfectly-plastic response and the "Vardanega and Bolton" curve as described by Vardanega and Bolton (2011). The datasets were degraded by adding noise and by reducing the resolution of the displacement field.

6. A series of laboratory physical model tests were designed and carried out. The tests were a set of 8 simple footing tests on undrained clay with two different footing widths. PIV was used to recover the displacement fields. Supplementary testing including shear vane and triaxial testing was carried out to provide comparison between the proposed Identification Methods and existing techniques.

7. Both the artificial and real datasets were used to test and validate both of the proposed Identification Methods. The artificial datasets were degraded with noise to find the limits to the robustness of the methods, with the finding that addition of noise reduces the recovered soil strength. It was found that the Segment based approach functions well with 50 or more segments. Commentary was given on the benefits and drawbacks of each method, with the Segment based approach being more adaptable to unexpected soil behaviours whereas the Equation based approach is useful if the used already has a good estimate. The Identification Methods were found to be overall promising and able to recover reasonable soil responses, depending on the quality of the input data. The methods functioned very well for artificial datasets, and typically recovered good values for peak stress for real datasets, although with real data the recovered curves were often bilinear rather than smooth.

8. The software used for this project was written using Matlab. Although measures to

increase the usability of the code have been made, particularly with functionality to allow for more automation, it is still fundamentally a piece of research software with all the usual associated drawbacks. Rewriting the software, possibly in C++ with multithreading or potentially GPU support would be possible and beneficial, as would adding a graphical interface.

9.2 Additional Findings

The key result of this work is the derivation, implementation, and validation of the two proposed Identification Methods. Details of the overarching aims and objectives have been given in the preceding section. A number of additional findings were made during the course of analysing both the artificial and real datasets that were produced. These will be listed as follows:

1. **The effects of noise.** It was theorised that adding random noise to a displacement field would result in a general increase in observed shear strains, proportional to the added noise, which would in turn result in lower stresses being required to meet the required internal energy expenditure, with a final outcome of a lower recovered stress-strain response. This was demonstrated through experimentation with artificial datasets in which increasing degrees of both normal and uniformly distributed noise was added. To further confirm the theory, the inverse was demonstrated with real datasets, which naturally have noise. Smoothing the noise results in the opposite effect, and the recovered stress-strain curve being raised such that it is in a location that is supported with supplementary data.
2. **The effects of start time.** During the physical modelling tests that were carried out, the footing often did not come into contact with the soil surface simultaneously which causes ambiguity in selecting a start time from which data can be zeroed. It was demonstrated that adjusting this start time forwards or backwards can have a large effect on the recovered stress-strain curve, obviating a need to strategise a means of dealing with this. Selecting a start time at the first point where both sides of the footing are visibly in contact was chosen and provided promising results. The effects of this on pairs of datasets using the same footing was identified, as were methodologies by which future experimentation may avoid this issue.

9.3 Future Work

Future work can be split into four main areas:

1. Carry out further testing of the existing techniques. Currently, the physical models used to test the Identification Methods are limited to simple footing tests on undrained clay. Carrying out further testing with more variety would allow for increased confidence in and further improvements of the proposed Identification Methods. Designing testing that eliminates the issues identified regarding touchdown would allow for further confidence in the validitiy of the proposed methodologies. Fortunately, many researchers in geotechnics carry out physical model testing with many models producing datasets that would potentially be suitable for analysis with the Identification Methods so further validation would likely be possible without carrying out laboratory tests explicitly for this purpose. Work on novel load cases may be necessary for some problems, for instance a slope failing under gravity with a weighted block at the peak of the slope will require a very different energy equilibrium than a simple footing problem. Adapting the proposed Identification Methods to work for datasets produced during centrifuge testing is another logical step. Scaling internal work with depth based on a varying gravity field would facilitate this addition.

2. Add additional features to the Identification Method pre/post processing stages. Allowing for strains to be formulated in terms of 6-node triangles for instance would allow for the higher order displacement field data output by GeoPIV-RG to be fully utilised. Another possible improvement is allowing several datasets to be used simultaneously. A stress-strain response could be recovered that is the best fit for image data recorded on both sides of the specimen box would potentially produce improved results.

3. Improve the range of soil responses that can be recovered. As per Chapter 3 a number of assumptions were made to simplify the problem for the purposes of this project. Soil was assumed to be isotropic undrained clay with associative flow and unchanged volume. Many of these assumptions can be removed by reformulating the equilibrium equation to include variables relating to these concepts. Work done by volumetric strain and mean stress could be incorporated, however measures would have to be taken such that the recovered mean stress is compatible with the recovered maximum shear stress that corresponds to maximum shear strain.

4. The final piece of future work is related to the last objective that was only partially completed. Although the current codebase is functional it is not particularly user friendly and some large datasets may be time-consuming to run depending on the level of detail required. As the software was written and changed over time with new

functions added it would likely be necessary to completely rewrite the code before it would be suitable for sharing with other researchers. This opportunity could be used to refactor many of the internal workings to allow for future development. Using as faster language such as C++ and incorporating technologies such as multithreading would also be worthwhile. Additionally, the Equation based approach currently uses a brute force approach to recovering the stress-strain response. Investigating whether nonlinear optimisation could be implemented could potentially allow for rapid increases in speed, however this would depend on which equation is being optimised. Parallelisation of the brute force search, possibly using graphics card based processing would be a good alternative.

Appendix A

Reformulating Internal Work to use "Geotechnical" Parameters

In Chapter 3 internal work was derived in terms of the stress componants σ_x, σ_y, τ_{xy}, and the strain componants ϵ_x, ϵ_y, γ_{xy}. The final internal work equation using these terms is reproduced here, in Equation A.1.

$$W = [\underline{\sigma} : \underline{\epsilon}] \cdot V = \begin{pmatrix} \sigma_x & \tau_{xy} \\ \tau_{xy} & \sigma_y \end{pmatrix} : \begin{pmatrix} \epsilon_x & \frac{\gamma_{xy}}{2} \\ \frac{\gamma_{xy}}{2} & \epsilon_y \end{pmatrix} \cdot V = \begin{pmatrix} \sigma_x & \tau_{xy} \\ \tau_{xy} & \sigma_y \end{pmatrix} : \begin{pmatrix} \epsilon_x & \epsilon_{xy} \\ \epsilon_{xy} & \epsilon_y \end{pmatrix} \cdot V \tag{A.1}$$

It is useful to express internal work due to deformation with terms such as maximum shear stress t and maximum shear strain ϵ_s, as these are more commonly used in constitutive models and found as the result of laboratory testing. This appendix contains the derivation for expressing work in such a way. What is presented is a very generalised case that has multiple simplifications that are be discussed in Chapter 3.

The significant complexity of the following derivation is due to the fact that the principal angles for stress and strain $\theta_{p\sigma}$ and $\theta_{p\epsilon}$ are not necessarily the same. It should be noted that the equations given in this section assume that stress is constant. This assumption has been made for readability, as having multiple integral symbols per equation would make this derivation somewhat harder to follow. Upon completion of the derivation, the final form can simply be converted to the more general case in which stress varies with time.

Internal work due to deformation is found by taking the double dot product of the stress tensor and strain tensor. In 2D this is stated as follows:

$$W_{\text{int}} = \underline{\sigma} : \underline{\epsilon} \cdot V \tag{A.2}$$

Which is the equivalent to:

$$W_{\text{int}} = (\sigma_x \cdot \epsilon_{xx} + \sigma_y \cdot \epsilon_{yy} + 2\tau_{xy} \cdot \epsilon_{xy}) \cdot V \tag{A.3}$$

Firstly, define the principal stress and strain tensors in terms of the known tensors and rotation matrices corresponding to both the stress and strain Mohr's circles.

$$\underline{\sigma}_p = R_\sigma \cdot \underline{\sigma} \cdot R_\sigma^T \tag{A.4}$$

$$\underline{\epsilon}_p = R_\epsilon \cdot \underline{\epsilon} \cdot R_\epsilon^T \tag{A.5}$$

It is now possible to rearrange the above equations such that the principal tensors are in terms of the known tensors:

$$R_\sigma^T \cdot \underline{\sigma}_p \cdot R_\sigma = R_\sigma^T \cdot \ R_\sigma \cdot \underline{\sigma} \cdot R_\sigma^T \cdot \ R_\sigma = \underline{\sigma} \tag{A.6}$$

$$R_\epsilon^T \cdot \underline{\epsilon}_p \cdot R_\epsilon = R_\epsilon^T \cdot R_\epsilon \cdot \underline{\epsilon} \cdot R_\epsilon^T \cdot R_\epsilon = \underline{\epsilon} \tag{A.7}$$

As such, internal work can be redefined based on the principal stress and strain tensors and associated rotation matrices:

$$W_{\text{int}} = (R_\sigma^T \cdot \underline{\sigma}_p \cdot R_\sigma : \ R_\epsilon^T \cdot \underline{\epsilon}_p \cdot R_\epsilon) \cdot V \tag{A.8}$$

Carrying out matrix multiplication results in the following expansion:

$$\begin{aligned} W_{\text{int}} = &\begin{pmatrix} \cos\theta_\sigma & \sin\theta_\sigma \\ -\sin\theta_\sigma & \cos\theta_\sigma \end{pmatrix} \begin{pmatrix} \sigma_1 & 0 \\ 0 & \sigma_2 \end{pmatrix} \begin{pmatrix} \cos\theta_\sigma & -\sin\theta_\sigma \\ \sin\theta_\sigma & \cos\theta_\sigma \end{pmatrix} : \\ &\begin{pmatrix} \cos\theta_\epsilon & \sin\theta_\epsilon \\ -\sin\theta_\epsilon & \cos\theta_\epsilon \end{pmatrix} \begin{pmatrix} \epsilon_1 & 0 \\ 0 & \epsilon_2 \end{pmatrix} \begin{pmatrix} \cos\theta_\epsilon & -\sin\theta_\epsilon \\ \sin\theta_\epsilon & \cos\theta_\epsilon \end{pmatrix} \cdot V \end{aligned} \tag{A.9}$$

$$\begin{aligned} W_{\text{int}} = &\begin{pmatrix} \sigma_1 \cos^2\theta_\sigma + \sigma_2 \sin^2\theta_\sigma & (\sigma_2 - \sigma_1)\cos\theta_\sigma \sin\theta_\sigma \\ (\sigma_2 - \sigma_1)\cos\theta_\sigma \sin\theta_\sigma & \sigma_1 \sin^2\theta_\sigma + \sigma_2 \cos^2\theta_\sigma \end{pmatrix} : \\ &\begin{pmatrix} \epsilon_1 \cos^2\theta_\epsilon + \epsilon_2 \sin^2\theta_\epsilon & (\epsilon_2 - \epsilon_1)\cos\theta_\epsilon \sin\theta_\epsilon \\ (\epsilon_2 - \epsilon_1)\cos\theta_\epsilon \sin\theta_\epsilon & \epsilon_1 \sin^2\theta_\epsilon + \epsilon_2 \cos^2\theta_\epsilon \end{pmatrix} \cdot V \end{aligned} \tag{A.10}$$

Carrying out the double dot product, i.e. multiplying each element with the corresponding element in the second matrix, as shown above gives the following equation for internal work:

$$\begin{aligned} W_{\text{int}} = [&(\sigma_1 \cos^2\theta_\sigma + \sigma_2 \sin^2\theta_\sigma)(\epsilon_1 \cos^2\theta_\epsilon + \epsilon_2 \sin^2\theta_\epsilon) \\ &+(\sigma_1 \sin^2\theta_\sigma + \sigma_2 \cos^2\theta_\sigma)(\epsilon_1 \sin^2\theta_\epsilon + \epsilon_2 \cos^2\theta_\epsilon) \\ &+2((\sigma_2 - \sigma_1)\cos\theta_\sigma \sin\theta_\sigma)((\epsilon_2 - \epsilon_1)\cos\theta_\epsilon \sin\theta_\epsilon)] \cdot V \end{aligned} \tag{A.11}$$

Expanding the brackets results in Equation A.12 which can be factorised to give Equation A.13.

$$\begin{aligned} W_{\text{int}} = [&\sigma_1\epsilon_1(\cos^2\theta_\sigma \cos^2\theta_\epsilon + \sin^2\theta_\sigma \sin^2\theta_\epsilon) + \sigma_2\epsilon_2(\sin^2\theta_\sigma \sin^2\theta_\epsilon + \cos^2\theta_\sigma \cos^2\theta_\epsilon) + \\ &\sigma_1\epsilon_2(\cos^2\theta_\sigma \sin^2\theta_\epsilon + \sin^2\theta_\sigma \cos^2\theta_\epsilon) + \sigma_2\epsilon_1(\sin^2\theta_\sigma \cos^2\theta_\epsilon + \cos^2\theta_\sigma \sin^2\theta_\epsilon) + \\ &2(\sigma_2 - \sigma_1)(\epsilon_2 - \epsilon_1)\cos\theta_\sigma \sin\theta_\sigma \cos\theta_\epsilon \sin\theta_\epsilon] \cdot V \end{aligned} \tag{A.12}$$

$$\begin{aligned} W_{\text{int}} = [&(\sigma_1\epsilon_1 + \sigma_2\epsilon_2)(\cos^2\theta_\sigma \cos^2\theta_\epsilon + \sin^2\theta_\sigma \sin^2\theta_\epsilon) \\ &+(\sigma_1\epsilon_2 + \sigma_2\epsilon_1)(\cos^2\theta_\sigma \sin^2\theta_\epsilon + \cos^2\theta_\epsilon \sin^2\theta_\sigma) \\ &+2(\sigma_2 - \sigma_1)(\epsilon_2 - \epsilon_1)\cos\theta_\sigma \sin\theta_\sigma \cos\theta_\epsilon \sin\theta_\epsilon] \cdot V \end{aligned} \tag{A.13}$$

In order to simplify further, the Pythagorian identity relating to the squared trigonometric terms should be noted. The intention of this stage is to find a common factor.

$$\begin{aligned} &(\cos^2\theta_\sigma \cos^2\theta_\epsilon + \sin^2\theta_\sigma \sin^2\theta_\epsilon) + (\cos^2\theta_\sigma \sin^2\theta_\epsilon + \cos^2\theta_\epsilon \sin^2\theta_\sigma) = \\ &(\cos^2\theta_\sigma + \sin^2\theta_\sigma)(\cos^2\theta_\epsilon + \sin^2\theta_\epsilon) = (1)(1) = 1 \end{aligned} \tag{A.14}$$

Therefore:

$$(\cos^2\theta_\sigma \cos^2\theta_\epsilon + \sin^2\theta_\sigma \sin^2\theta_\epsilon) = 1 - (\cos^2\theta_\sigma \sin^2\theta_\epsilon + \cos^2\theta_\epsilon \sin^2\theta_\sigma) \tag{A.15}$$

Equation A.15 allows for a substitution resulting in a common factor. Minor adjustment to signs within the third term has been carried out, with the contents of each bracket multiplied by -1. These adjustments allow internal work to be expressed as Equation A.16.

$$\begin{aligned} W_{\text{int}} = [&(\sigma_1\epsilon_1 + \sigma_2\epsilon_2)(1 - (\cos^2\theta_\sigma \sin^2\theta_\epsilon + \cos^2\theta_\epsilon \sin^2\theta_\sigma)) \\ &+(\sigma_1\epsilon_2 + \sigma_2\epsilon_1)(\cos^2\theta_\sigma \sin^2\theta_\epsilon + \cos^2\theta_\epsilon \sin^2\theta_\sigma) \\ &+2(\sigma_1 - \sigma_2)(\epsilon_1 - \epsilon_2)\cos\theta_\sigma \sin\theta_\sigma \cos\theta_\epsilon \sin\theta_\epsilon] \cdot V \end{aligned} \tag{A.16}$$

Next, expansion results in Equation A.17, which in turn can be simplified to Equation A.18.

$$\begin{aligned} W_{\text{int}} = [&\sigma_1\epsilon_1 + \sigma_2\epsilon_2 \\ &+(\cos^2\theta_\sigma \sin^2\theta_\epsilon + \cos^2\theta_\epsilon \sin^2\theta_\sigma)(\sigma_1\epsilon_2 + \sigma_2\epsilon_1 - \sigma_1\epsilon_1 - \sigma_2\epsilon_{2)} \\ &+2(\sigma_1 - \sigma_2)(\epsilon_1 - \epsilon_2)\cos\theta_\sigma \sin\theta_\sigma \cos\theta_\epsilon \sin\theta_\epsilon] \cdot V \end{aligned} \tag{A.17}$$

$$\begin{aligned} W_{\text{int}} = [&\sigma_1\epsilon_1 + \sigma_2\epsilon_2 \\ &+(\cos^2\theta_\sigma \sin^2\theta_\epsilon + \cos^2\theta_\epsilon \sin^2\theta_\sigma)(\sigma_1 - \sigma_2)(\epsilon_2 - \epsilon_1) \\ &+2(\sigma_1 - \sigma_2)(\epsilon_1 - \epsilon_2)\cos\theta_\sigma \sin\theta_\sigma \cos\theta_\epsilon \sin\theta_\epsilon] \cdot V \end{aligned} \tag{A.18}$$

The terms within the $(\epsilon_2 - \epsilon_1)$ bracket can be reversed by taking a factor of -1, allowing for more factorisation and simplification.

$$\begin{aligned} W_{\text{int}} = &[\sigma_1\epsilon_1 + \sigma_2\epsilon_2 \\ &+(\sigma_1 - \sigma_2)(\epsilon_1 - \epsilon_2)(2\cos\theta_\sigma \sin\theta_\sigma \cos\theta_\epsilon \sin\theta_\epsilon - \cos^2\theta_\sigma \sin^2\theta_\epsilon - \cos^2\theta_\epsilon \sin^2\theta_\sigma)] \cdot V \end{aligned} \tag{A.19}$$

$$\begin{aligned} W_{\text{int}} = &[\sigma_1\epsilon_1 + \sigma_2\epsilon_2 \\ &-(\sigma_1 - \sigma_2)(\epsilon_1 - \epsilon_2)(\cos^2\theta_\sigma \sin^2\theta_\epsilon + \cos^2\theta_\epsilon \sin^2\theta_\sigma - 2\cos\theta_\sigma \sin\theta_\sigma \cos\theta_\epsilon \sin\theta_\epsilon)] \cdot V \end{aligned} \tag{A.20}$$

The complex series of trigonometric terms at the end of Equation A.20 can be factorised by finding the square root, as shown in Equation A.21, with the trigonometric terms further simplified via the angle sum/difference formula.

$$\begin{aligned} W_{\text{int}} = &[\sigma_1\epsilon_1 + \sigma_2\epsilon_2 \\ &-(\sigma_1 - \sigma_2)(\epsilon_1 - \epsilon_2)(\cos\theta_\epsilon \sin\theta_\sigma - \cos\theta_\sigma \sin\theta_\epsilon)^2] \cdot V \end{aligned} \tag{A.21}$$

$$W_{\text{int}} = [\sigma_1\epsilon_1 + \sigma_2\epsilon_2 - (\sigma_1 - \sigma_2)(\epsilon_1 - \epsilon_2)(\sin^2(\theta_\sigma - \theta_\epsilon))] \cdot V \tag{A.22}$$

The penultimate stage is dealing with the $\sigma_1\epsilon_1 + \sigma_2\epsilon_2$ term, which can be achieved with the following steps.

$$(\sigma_1\epsilon_1 + \sigma_2\epsilon_2) = (\sigma_1 + \sigma_2)(\epsilon_1 + \epsilon_2) - (\sigma_1\epsilon_2 + \sigma_2\epsilon_1) \tag{A.23}$$

The final term in Equation A.23 can be expressed as follows:

$$(\sigma_1\epsilon_2 + \sigma_2\epsilon_1) = (\sigma_1\epsilon_1 + \sigma_2\epsilon_2) - (\sigma_1 - \sigma_2)(\epsilon_1 - \epsilon_2) \tag{A.24}$$

Substituting Equation A.24 back into Equation A.23 results in Equation A.25. Rearangement of this equation is shown in Equations A.26 and A.27.

$$(\sigma_1\epsilon_1 + \sigma_2\epsilon_2) = (\sigma_1 + \sigma_2)(\epsilon_1 + \epsilon_2) + [(\sigma_1\epsilon_1 + \sigma_2\epsilon_2) - (\sigma_1 - \sigma_2)(\epsilon_1 - \epsilon_2)] \tag{A.25}$$

$$2(\sigma_1\epsilon_1 + \sigma_2\epsilon_2) = (\sigma_1 + \sigma_2)(\epsilon_1 + \epsilon_2) - (\sigma_1 - \sigma_2)(\epsilon_1 - \epsilon_2) \tag{A.26}$$

$$(\sigma_1\epsilon_1 + \sigma_2\epsilon_2) = \frac{1}{2}(\sigma_1 + \sigma_2)(\epsilon_1 + \epsilon_2) - \frac{1}{2}(\sigma_1 - \sigma_2)(\epsilon_1 - \epsilon_2) \tag{A.27}$$

Substituting Equation A.27 into Equation A.22 gives the following:

$$\begin{aligned} W_{\text{int}} = \Bigg[&\frac{1}{2}(\sigma_1 + \sigma_2)(\epsilon_1 + \epsilon_2) + \\ &\frac{1}{2}(\sigma_1 - \sigma_2)(\epsilon_1 - \epsilon_2) - (\sigma_1 - \sigma_2)(\epsilon_1 - \epsilon_2)(\sin^2(\theta_\sigma - \theta_\epsilon))\Bigg] \cdot V \end{aligned} \tag{A.28}$$

$$W_{\text{int}} = \left[\frac{1}{2}(\sigma_1 + \sigma_2)(\epsilon_1 + \epsilon_2) + (\sigma_1 - \sigma_2)(\epsilon_1 - \epsilon_2)(\frac{1}{2} - \sin^2(\theta_\sigma - \theta_\epsilon))\right] \cdot V \tag{A.29}$$

Finally, substitute in the terms of mean stress s, maximum shear stress t, volumetric strain ϵ_v, and shear strain ϵ_s.

$$W_{\text{int}} = \left[\frac{1}{2} \cdot 2s\epsilon_v + 2t2\epsilon_s(\frac{1}{2} - \sin^2(\theta_\sigma - \theta_\epsilon))\right] \cdot V \tag{A.30}$$

Simplifying to a final internal work equation of:

$$W_{\text{int}} = \left[s\epsilon_v + 2t\epsilon_s(1 - 2\sin^2(\theta_\sigma - \theta_\epsilon))\right] \cdot V \tag{A.31}$$

Appendix B

Additional Data

B.1 Small strain trimming investigation

A preprocessing function was developed that trims small strain elements from the optimisation problem. Due to the relatively large areas of interest recorded via GeoPIV-RG, there are many strain elements with approximately zero strain. Elements were trimmed when there strain, as a percentage of the maximum observed strain, falls below a threshold. Eliminating more elements will cause the recovered c_u value to increase by a small amount, but having too many unnecessary small strains elements will negatively impact the distribution of Segment method segments. Figure B.1 shows a plot of how c_u is altered by increasing the threshold along with how many elements are trimmed. For reference, 1% was selected as a compromise value, however this is largely arbitrary as altering this has only a small impact. This investigation was carried out on the Specimen 2, 40mm, cam 1 dataset and uses 100 segments.

B.2 Gravity investigation

The assumption was made that during the physical model tests an approximately equal quantity of soil moves up as down due to the assumption of nil volumetric strain. To determine whether this was valid, the work done due to gravity was calculated as a percentage of external work for each dataset. A unit weight of 23kNm^{-3} was taken from a soil mechanics textbook using the upper value suggested for stiff clay (Barnes, 2010). Additionally, a factor of 1.5 was applied to this unit weight to further demonstrate the negligibility of gravity.

Table B.1 shows work done (positive) or work imparted (negative) by gravity as a percentage of external work. With the exception of the anomalous result in which large vertical movement was observed (marked with an asterisk), work due to gravity is never more than two tenths of a percent of external work and in many cases is far less than this.

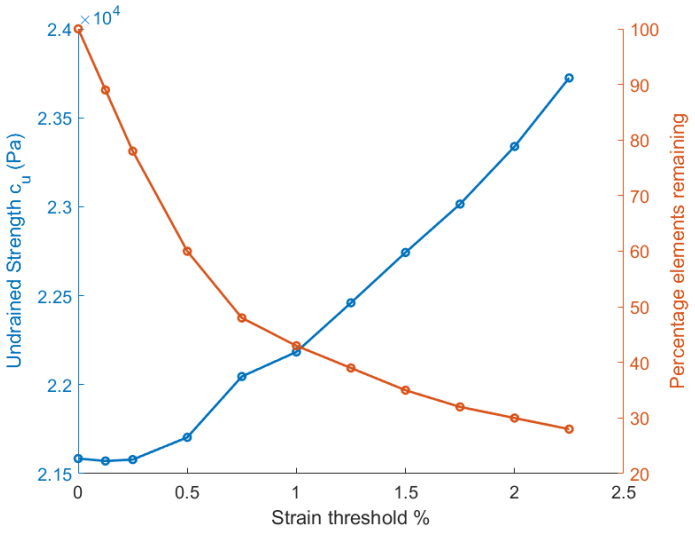

FIGURE B.1: The impact of changing the small strain trim threshold.

B.3 Friction investigation

As values for friction or adhesion between the clay and glass were not available, an investigation into the possible effects of friction was carried out. Work due to friction as a percentage of external work was calculated for every specimen. Values were found both with and without trimming of small strain elements. A threshold of 1% was used for the small strain trimming process. Friction between the clay and window was conservatively assumed to be the full c_u value as recorded by shear vane, which is likely to be a large overestimate in reality. Table B.2 presents this data. Elemental displacements were smoothed using a moving average filter with a window of 5.

It can be seen that work expended due to friction is typically very low, typically of the order of 1% of external work or lower. As stated, c_u was taken to be the adhesive stress between the window and clay which is a large overestimate. A more realistic value would make the contribution of friction even more trivial. The decision to ignore friction appears to be of little importance. It should be noted that the cam 2, 40mm footing for specimen 4 dataset features very large vertical movement which in turn results in large amounts of frictional work.

B.4 Raw sensor data

As discussed in Chapter 8, choosing the correct start time of each test proved to be difficult. Footing touchdown was not level, resulting in one side of the footing touching down first.

Test	**Gravity work %**
Specimen 1; 20mm, cam 1	−0.0114
Specimen 1; 20mm, cam 2	0.0175
Specimen 1; 40mm, cam 1	0.0301
Specimen 1; 40mm, cam 2	−0.0126
Specimen 2; 20mm, cam 1	0.0975
Specimen 2; 20mm, cam 2	0.0772
Specimen 2; 40mm, cam 1	0.0604
Specimen 2; 40mm, cam 2	0.129
Specimen 3; 20mm, cam 1	0.150
Specimen 3; 20mm, cam 2	0.0338
Specimen 3; 40mm, cam 1	0.192
Specimen 3; 40mm, cam 2	0.143
Specimen 4; 20mm, cam 1	0.119
Specimen 4; 20mm, cam 2	0.0447
Specimen 4; 40mm, cam 1	0.835*
Specimen 4; 40mm, cam 2	0.124

TABLE B.1: Work due to gravity as a percentage of external work.

This caused the inline load cell to flex and record negative force prior to full contact. Due to this ambiguity, it was decided that all data would be zeroed based on the time when both ends of the footing can be observed to be in contact via the imaging data. This manual process is not an exact science and was a potential source of error. Table B.3 shows the start, end, and LVDT used. As one LVDT was present on either end of the footing, each LVDT was matched with the corresponding set of image data. Note that similar start times are coincidental due to a similar "no movement" pause being recorded prior to commencing actuation.

The untrimmed sensor data can be found in Figures B.2, B.3, B.4, and B.5. Plotted is Displacement against time and Force against time. This data has been calibrated. Downsampling and basic moving average smoothing has been applied in the same manner as used for the final datasets.

Test	Friction work %: no trimming	Friction work %: with trimming
Specimen 1; 20mm, cam 1	0.863	0.712
Specimen 1; 20mm, cam 2	1.130	0.839
Specimen 1; 40mm, cam 1	1.161	0.977
Specimen 1; 40mm, cam 2	0.583	0.542
Specimen 2; 20mm, cam 1	1.054	0.754
Specimen 2; 20mm, cam 2	0.707	0.558
Specimen 2; 40mm, cam 1	0.889	0.762
Specimen 2; 40mm, cam 2	1.132	1.081
Specimen 3; 20mm, cam 1	1.263	1.032
Specimen 3; 20mm, cam 2	0.969	0.824
Specimen 3; 40mm, cam 1	1.349	1.312
Specimen 3; 40mm, cam 2	1.089	1.011
Specimen 4; 20mm, cam 1	1.241	0.888
Specimen 4; 20mm, cam 2	1.127	0.941
Specimen 4; 40mm, cam 1	9.171*	8.059*
Specimen 4; 40mm, cam 2	1.371	1.183

TABLE B.2: Work due to friction as a percentage of external work.

Test	Start time (s)	End time (s)	LVDT used
Specimen 1; 20mm, cam 1	28.2	68.2	*avg*
Specimen 1; 20mm, cam 2	28.2	68.2	*avg*
Specimen 1; 40mm, cam 1	28.21	127	*avg*
Specimen 1; 40mm, cam 2	28.21	127	*avg*
Specimen 2; 20mm, cam 1	84.5	166	4
Specimen 2; 20mm, cam 2	84.5	166	3
Specimen 2; 40mm, cam 1	84.5	250	3
Specimen 2; 40mm, cam 2	84.5	250	4
Specimen 3; 20mm, cam 1	52.08	126.17	4
Specimen 3; 20mm, cam 2	52.08	126.17	3
Specimen 3; 40mm, cam 1	50.37	115.16	4
Specimen 3; 40mm, cam 2	50.37	115.16	3
Specimen 4; 20mm, cam 1	63.55	141.8	4
Specimen 4; 20mm, cam 2	63.55	141.8	3
Specimen 4; 40mm, cam 1	64.79	146.01	3
Specimen 4; 40mm, cam 2	64.79	146.01	4

TABLE B.3: Start, end, and sensor selection parameters.

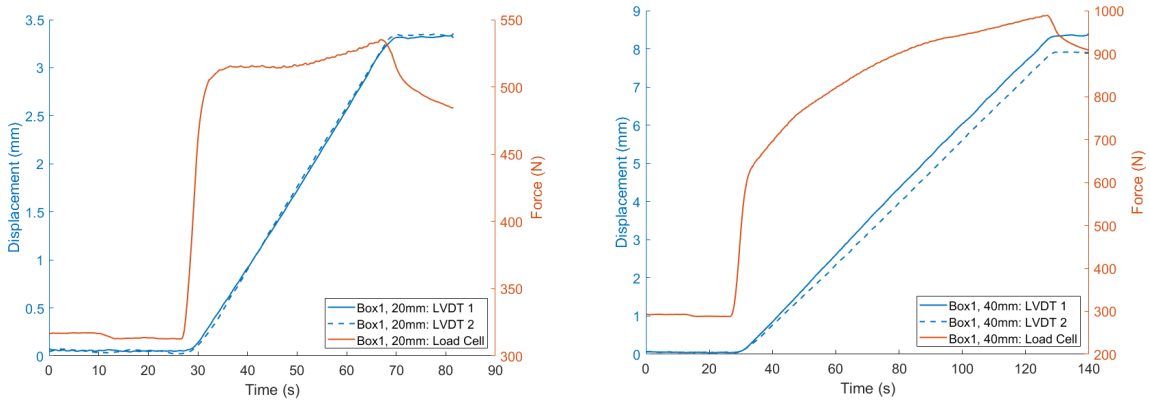

FIGURE B.2: The untrimmed sensor data for Specimen One.

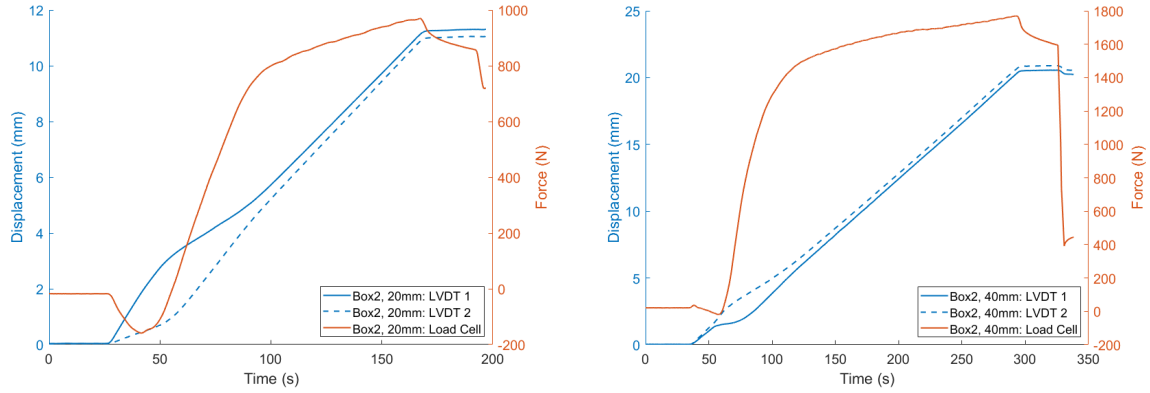

FIGURE B.3: The untrimmed sensor data for Specimen Two.

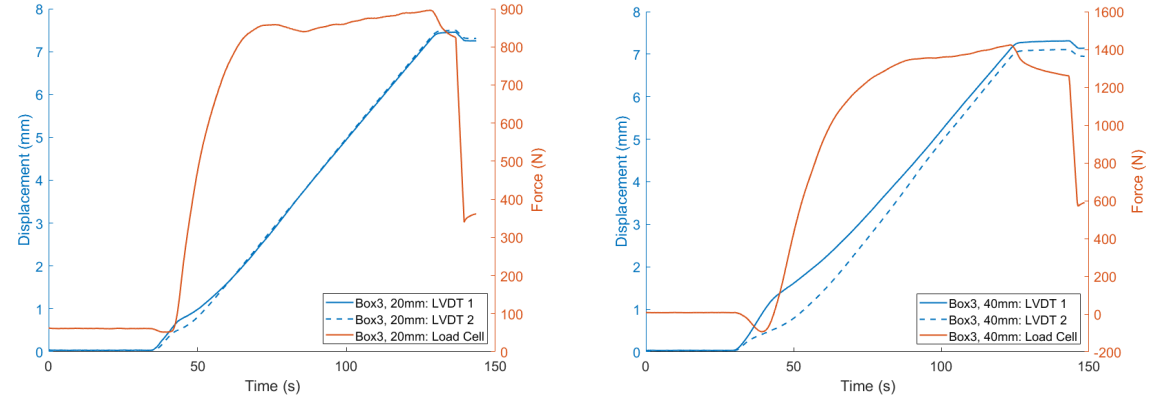

FIGURE B.4: The untrimmed sensor data for Specimen Three.

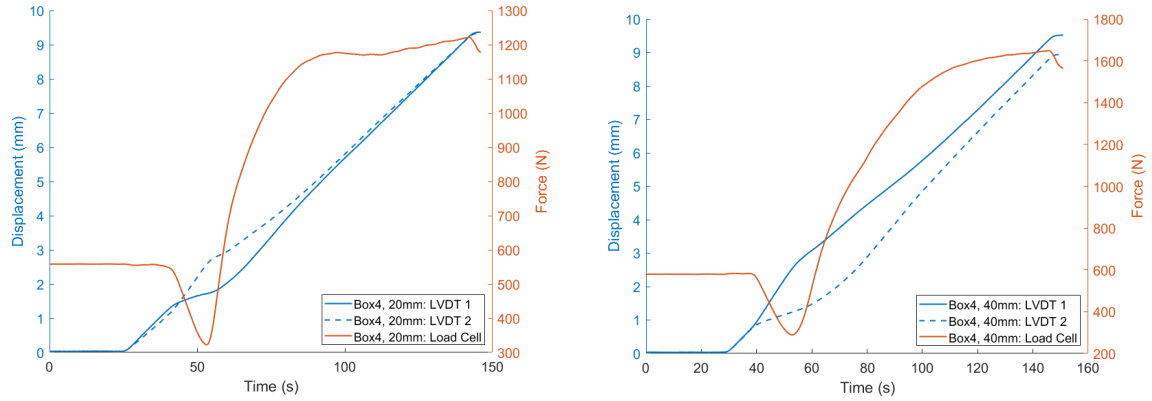

FIGURE B.5: The untrimmed sensor data for Specimen Four.

Bibliography

Adrian, Ronald J (1991). "Particle-Imaging techniques for experimental fluid mechanics". In: *Annu. Rev. Fluid Mech.* 23, pp. 261–304.

Adrian, Ronald J and Jerry Westerweel (2011). *Particle Image Velocimetry*. Cambridge University Press. ISBN: 978-0-521-44008-0.

Albertz, J (2001). "Albrecht Meydenbauer - Pioneer of Photogrammetric Documentation of the Cultural Heritage". In: *Proceedings 18th International Symposium CIPA 2001*, pp. 19–25. URL: http://www.theulegium.de/fileadmin/user_upload/Texte/Meydenb.pdf.

Andrieux, S., A. B. Abda, and H. D. Bui (1999). "Reciprocity principle and crack identification". In: *Inverse problems* 15.1, p. 59. DOI: 10.1088/0266-5611/15/1/010.

AppliedImage (2017). *ACCU-PLACE Dot Distortion Target (AP-DD)*. https://www.appliedimage.com/products/robotics-and-machine-vision-standards/robotic-machine-vision-standards/accu-place-dot-distortion-target-ap-dd.

ASPRS (2019). *What is ASPRS?* URL: https://www.asprs.org/organization/what-is-asprs.html.

Avril, S. and F. Pierron (2007). "General framework for the identification of constitutive parameters from full-field measurements in linear elasticity". In: *International Journal of Solids and Structures* 44.14-15, pp. 4978–5002. ISSN: 00207683. DOI: 10.1016/j.ijsolstr.2006.12.018.

Avril, Stéphane et al. (2008a). "Overview of identification methods of mechanical parameters based on full-field measurements". In: *Experimental Mechanics* 48.4, pp. 381–402. ISSN: 00144851. DOI: 10.1007/s11340-008-9148-y.

Avril, Stephane et al. (2008b). "Stress reconstruction and constitutive parameter identification in plane-stress elasto-plastic problems using surface measurements of deformation fields". In: *Experimental Mechanics* 48.4, pp. 403–419. ISSN: 17412765. DOI: 10.1007/s11340-007-9084-2.

Barnes, Graham (2010). *Soil Mechanics; Principles and practice*. Palgrave Macmillan. ISBN: 978-0-230-57980-4.

Bhavikatti, S. S (2005). *Finite element analysis [electronic resource]*. eng. New Delhi: New Age International (P) Ltd., Publishers. ISBN: 1-281-78893-7.

British Standards Institution (1990a). "Methods of test for soils for civil engineering purposes — Part 2". In: *British Standard* 2.1.

British Standards Institution (1990b). "Methods of test for soils for civil engineering purposes — Part 5". In: *British Standard* 5.1.

– (1990c). "Methods of test for soils for civil engineering purposes — Part 7". In: *British Standard* 7.1.

– (1990d). "Methods of test for soils for civil engineering purposes — Part 9". In: *British Standard* 9.1.

– (2012). "ISO 22476-1:2012 Geotechnical investigation and testing — Field testing — Part 1: Electrical cone and piezocone penetration test". In: *British Standard* 1.1.

Brown, DC (1966). "Decentering Distortion of Lenses". In: *Photometric Engineering* 32.3, pp. 444–462.

Bui, Huy Duong, Andrei Constantinescu, and Hubert Maigre (2004). "Numerical identification of linear cracks in 2D elastodynamics using the instantaneous reciprocity gap". In: *Inverse Problems* 20.4, pp. 993–1001. ISSN: 02665611. DOI: 10.1088/0266-5611/20/4/001.

Calderón, A. P. (2006). "Inverse Boundary Value Problems". In: *Computational & Applied Mathematics* 25.2-3, pp. 133–138. ISSN: 2238-3603.

Charles, J A, C C Smith, and J A Black (2018a). "Evaluating the effects of noise on full field displacement data used for the identification of soil stress-strain response". In: *Numerical Methods in Geotechnical Engineering IX, Volume 1: Proceedings of the 9th European Conference on Numerical Methods in Geotechnical Engineering (NUMGE 2018), June 25-27, 2018, Porto, Portugal*. CRC Press, pp. 221–226. DOI: 10.1201/9780429446931.

– (2018b). "Identification of soil stress-strain response from full field displacement measurements in plane strain model tests". In: *Physical Modelling in Geotechnics, Volume 2: Proceedings of the 9th International Conference on Physical Modelling in Geotechnics (ICPMG 2018), July 17-20, 2018, London, United Kingdom*. CRC Press, pp. 835–840. DOI: 10.1201/9780429438646.

– (2019). "Automated reconstruction of soil stress-strain response from full field displacement measurements and loading data using optimisation". In: *Proceedings of the XVII ECSMGE-2019, Geotechnical Engineering foundation of the future*. IGS, pp. 1–8. DOI: 10.32075/17ECSMGE-2019-0343.

Chen, J et al. (1996). "An evaluation of three different image capture methods for measurement and analysis of deformation within a geotechnical centrifuge". In: *International archives of photogrammetry and remote sensing* XXXI, B5, 70–75.

Claire, D., F. Hild, and S. Roux (2004). "A finite element formulation to identify damage fields: The equilibrium gap method". In: *International Journal for Numerical Methods in Engineering* 61.2, pp. 189–208. ISSN: 00295981. DOI: 10.1002/nme.1057.

Dassault Systèmes (2014). *ABAQUS CAE 6.14*. URL: https://www.3ds.com/products-services/simulia/products/abaqus/abaquscae/.

Davies, E.R. (2012). *Computer and Machine Vision*. Elsevier Inc. ISBN: 9780123869081.

Delaunay, Boris et al. (1934). "Sur la sphere vide". In: *Izv. Akad. Nauk SSSR, Otdelenie Matematicheskii i Estestvennyka Nauk* 7.793-800, pp. 1–2.

Doyle, F (1964). "The historical development of analytical photogrammetry". In: *Photogrammetric Engineering* 30.2, pp. 259–265. ISSN: 00318663.

Effendi, Rustam (2007). "Modelling of the settlement interaction of neighbouring buildings on soft ground". PhD thesis.

Florentin, Eric and Gilles Lubineau (2010). "Identification of the parameters of an elastic material model using the constitutive equation gap method". In: *Computational Mechanics* 46.4, pp. 521–531. ISSN: 01787675. DOI: 10.1007/s00466-010-0496-y.

Florio, D Di, F Di Felice, and G P Romano (2002). "Windowing, re-shaping and re-orientation interrogation windows in particle image velocimetry for the investigation of shear flows". In: *Measurement Science and Technology* 13.7, p. 301. ISSN: 09570233. DOI: 10.1088/0957-0233/13/7/301. URL: http://stacks.iop.org/0957-0233/13/i=7/a=301?key=crossref.52a33aef5d227b713cbfe456f4b8eceb.

Forsyth, David (2012). *Computer vision : a modern approach*. eng. 2nd ed., International ed. contributions by Soumen Mukherjee, Arub Kumar Bhattacharjee. Boston, [Mass.] ; London: Pearson. ISBN: 9780273764144.

Genovese, Katia, Luciano Lamberti, and Carmine Pappalettere (2006). "Mechanical characterization of hyperelastic materials with fringe projection and optimization techniques". In: *Optics and Lasers in Engineering* 44.5, pp. 423–442. ISSN: 01438166. DOI: 10.1016/j.optlaseng.2005.06.003.

Gerber, E (1929). "Untersuchungen uber die Druckverteilung im Oertlick Belasteten Sand". In: *Dissertation Technische Hochschule, Zurich*.

Geymonat, Giuseppe, François Hild, and Stéphane Pagano (2002). "Identification of elastic parameters by displacement field measurement". In: *Comptes Rendus Mecanique* 330, pp. 403–408.

Giraudeau, Alain and Fabrice Pierron (2003). "Simultaneous identification of stiffness and damping properties of isotropic materials from forced vibrating plates". In: *Comptes Rendus - Mecanique* 331.4, pp. 259–264. ISSN: 16310721. DOI: 10.1016/S1631-0721(03)00061-5.

Grédiac, M. and F. Pierron (1998). "A T-shaped specimen for the direct characterization of orthotropic materials". In: *International Journal for Numerical Methods in Engineering* 41.September 1996, pp. 293–309. ISSN: 00295981. DOI: 10.1002/(SICI)1097-0207(19980130)41:2<293::AID-NME284>3.0.CO;2-Y. URL: http://eprints.soton.ac.uk/210699/.

Grédiac, Michel and Fabrice Pierron (2006). "Applying the Virtual Fields Method to the identification of elasto-plastic constitutive parameters". In: *International Journal of Plasticity* 22.4, pp. 602–627. ISSN: 07496419. DOI: 10.1016/j.ijplas.2005.04.007.

Grédiac, Michel, Evelyne Toussaint, and Fabrice Pierron (2002). "Special virtual fields for the direct determination of material parameters with the virtual fields method. 2 - Application to in-plane properties". In: *International Journal of Solids and Structures* 39.10, pp. 2707–2730. ISSN: 00207683. DOI: 10.1016/S0020-7683(02)00128-2.

Gueguin, M., C.C. Smith, and M. Gilbert (2015). "Use of digital image correlation to directly derive soil stress-strain response from physical model test data". In: *Geotechnical Engineering for Infrastructure and Development*, pp. 3881–3886. DOI: 10.1680/ecsmge.60678.vol7.612. eprint: http://www.icevirtuallibrary.com/doi/pdf/10.1680/ecsmge.60678.vol7.612. URL: http://www.icevirtuallibrary.com/doi/abs/10.1680/ecsmge.60678.vol7.612.

Hakhamaneshi, M et al. (2016). "Development of a 25ton consolidation press at the Centre for Energy and Infrastructure Ground Research". In: *Proceedings of the 3rd European Conference on Physical Modelling in Geotechnics (EUROFUGE 2016)*.

Head, K H (1984). *Manual of Soil laboratory testing, Volume 1, Soil classification and compaction tests*. Pentech Press. ISBN: 0-7273-1302-7.

– (1986). *Manual of Soil laboratory testing, Volume 3, Effective stress tests*. Pentech Press. ISBN: 0-7273-1306-1.

– (1994). *Manual of Soil laboratory testing, Volume 2, Permiability, shear strength and compressibility tests*. Pentech Press. ISBN: 0-470-23362-1.

Heikkila, J. and O. Silven (1997). "A four-step camera calibration procedure with implicit image correction". In: *Proceedings of IEEE Computer Society Conference on Computer Vision and Pattern Recognition*, pp. 1106–1112. ISSN: 1063-6919. DOI: 10.1109/CVPR.1997.609468. URL: http://ieeexplore.ieee.org/lpdocs/epic03/wrapper.htm?arnumber=609468.

Heikkilä, Janne (2000). "Geometric camera calibration using circular control points". In: *IEEE Transactions on Pattern Analysis and Machine Intelligence* 22.10, pp. 1066–1077. ISSN: 01628828. DOI: 10.1109/34.879788.

Hook, E. (2013). *The Ultimate Guide to Learning how to use Your first DSLR*. /urlhttps://digital-photography-school.com/megapost-learning-how-to-use-your-first-dslr/.

House, A.R., J.R.M.S. Oliveira, and M.F. Randolph (2001). "Evaluating the coefficient of consolidation using penetration tests". In: *International Journal of Physical Modelling in Geotechnics* 1.3, pp. 17–26. ISSN: 1346-213X. DOI: 10.1680/ijpmg.2001.010302.

Huang, H, D Dabiri, and M Gharib (1997). "On errors of digital particle image velocimetry". In: *Meas. Sci. Technol.* 8.

Imerys (2018). *Speswhite*. URL: https://imerys-kaolin.com/product-finder/en/products/speswhite/.

J. de Villiers et al. (2008). "Centi-pixel accurate real-time inverse distortion correction". In: *SPIE Optomechatronic Technologies* 7266.1, pp. 726611–726618. ISSN: 0277786X. DOI: 10.1117/12.804771.

Karmarkar, N. (1984). "A new polynomial-time algorithm for linear programming". In: *Proceedings of the Annual ACM Symposium on Theory of Computing* 4.April, pp. 302–311. ISSN: 07378017. DOI: 10.1145/800057.808695.

Kavanagh, Kenneth T. and Ray W. Clough (1971). "Finite element applications in the characterization of elastic solids". In: *International Journal of Solids and Structures* 7.1, pp. 11–23. ISSN: 00207683. DOI: 10.1016/0020-7683(71)90015-1. URL: http://dx.doi.org/10.1016/0020-7683(71)90015-1.

Kramer, Sharlotte L B and William M Scherzinger (2014). "Implementation and Evaluation of the Virtual Fields Method: Determining Constitutive Model Parameters From Full-Field Deformation Data". In: September, pp. 1–80.

Latourte, Felix et al. (2009). "Local energy analysis of HCF fatigue using DIC & IRT". In: *SEM 2009*. Albuquerque, United States, Cd–Rom. URL: https://hal.archives-ouvertes.fr/hal-00836156.

Lehane, B. M. et al. (2008). "Rate effects on the vertical uplift capacity of footings founded in clay". In: *Geotechnique* 58.1, pp. 13–21. ISSN: 00168505. DOI: 10.1680/geot.2008.58.1.13.

MathWorks (2017). *Matlab Single Camera Calibration App*. https://uk.mathworks.com/help/vision/ug/single-camera-calibrator-app.html.

Meuwissen, M.H.H et al. (1998). "Determination of the elasto-plastic properties of aluminium using a mixed numerical–experimental method". In: *Journal of Materials Processing Technology* 75.1-3, pp. 204–211. ISSN: 09240136. DOI: 10.1016/S0924-0136(97)00366-X.

Meyerhof, GG (1956). "Penetration tests and bearing capacity of cohesionless soils". In: *Journal of the Soil Mechanics and Foundations Division* 82.1, pp. 1–19.

MOSEK (2020). *MOSEK Optimization Toolbox for MATLAB, Release 9.1.13, Documentation*. Mosek.

Nogueira, J, A Lecuona, and P A Rodriguez (1997). "Data validation, false vectors correction and derived magnitudes calculation on PIV data". In: *Measurement Science Technology* 8, pp. 1493–1501.

Pagnacco, E. et al. (2005). "Inverse strategy from displacement field measurement and distributed forces using FEA". In: *Proceedings of the 2005 SEM Annual Conference and Exposition on Experimental and Applied Mechanics*, pp. 1079–1088. URL: http://www.scopus.com/inward/record.url?eid=2-s2.0-32044455297{\&}partnerID=tZOtx3y1.

Pan, Bing et al. (2008). "Study on subset size selection in digital image correlation for speckle patterns". In: *Optics Express* 16.10, p. 7037. ISSN: 1094-4087. DOI: 10.1364/oe.16.007037.

Pan, Bing, Zixing Lu, and Huimin Xie (2010). "Mean intensity gradient : An effective global parameter for quality assessment of the speckle patterns used in digital image correlation". In: *Optics and Lasers in Engineering* 48.4, pp. 469–477. ISSN: 0143-8166. DOI: 10.1016/j.optlaseng.2009.08.010. URL: http://dx.doi.org/10.1016/j.optlaseng.2009.08.010.

Pearse, R.S. (1994). *What Size is It - The evolution of photogrammetry within CIA*. URL: https://www.cia.gov/library/center-for-the-study-of-intelligence/kent-csi/vol15no1/html/v15i1a03p_0001.htm.

Pierron, Fabrice (2012). *The virtual fields method [electronic resource] : extracting constitutive mechanical parameters from full-field deformation measurements*. eng. New York: Springer. ISBN: 9781461418245.

Prasad, Ajay K. (2000). "Particle image velocimetry". In: *Current Science* 79.

Randolph, Mark (2004). "Characterisation of soft sediments for offshore applications". English. In: *Proceedings of the 2nd International Conference on Site Characterization*. Ed. by A.V. Da Fonseca and P.W. Mayne. Vol. 1. Millpress Science, pp. 209–232. ISBN: 90 5966 009 9.

Rémai, Zsolt (2013). "Correlation of undrained shear strength and CPT resistance". In: *Periodica Polytechnica Civil Engineering* 57.1, pp. 39–44. ISSN: 15873773. DOI: 10.3311/PPci.2140.

Ricoh (2018). *2 Megapixel Lens*. URL: https://industry.ricoh.com/en/fa_camera_lens/lens/2m/.

Roscoe, K.H., J.R.F Arthur, and R.G. James (1963). "The determination of strains in soils by an X-ray method". In: *Civil Engineering & Public Works Review* 58, pp. 873–876.

Simek, K (2013). *Dissecting the Camera Matrix, Part 3: The Intrinsic Matrix*. URL: https://ksimek.github.io/2013/08/13/intrinsic/.

Slama, C (1980). *Manual of photogrammetry*. eng. 4th ed. Falls Church, Va: American Society of Photogrammetry. ISBN: 0937294012.

SodaVision (2018). *BASLER pilot piA2400-17gc*. URL: https://www.sodavision.com/product/pia2400-17gc/.

Stanier, S A (2011). "Modelling the Behaviour of Helical Screw Piles". PhD thesis.

Stanier, S A et al. (2015). "Improved image-based deformation measurement for geotechnical applications". In: *Canadian Geotechnical Journal* 13.October 2015, pp. 1–35. ISSN: 12086010. DOI: 10.1139/cgj-2015-0253. URL: http://www.nrcresearchpress.com/doi/10.1139/cgj-2015-0253.

Take, W A (2014). "Thirty-Sixth Canadian Geotechnical Colloquium: Advances in visualization of geotechnical processes through digital image correlation". In: *Canadian Geotechnical Journal* 52.9, pp. 1199–1220. ISSN: 12086010. DOI: 10.1139/cgj-2014-0080. URL: http://www.nrcresearchpress.com/doi/10.1139/cgj-2014-0080.

Taylor, Z. J. et al. (2010). "Long-duration time-resolved PIV to study unsteady aerodynamics". In: *IEEE Transactions on Instrumentation and Measurement* 59.12, pp. 3262–3269.

Thielicke, William and Eize J. Stamhuis (2014). "PIVlab – Towards User-friendly, Affordable and Accurate Digital Particle Image Velocimetry in MATLAB". In: *Journal of Open Research Software* 2.1. ISSN: 2049-9647. DOI: 10.5334/jors.bl. URL: http://openresearchsoftware.metajnl.com/articles/10.5334/jors.bl/.

Toussaint, Evelyne, Michel Grédiac, and Fabrice Pierron (2006). "The virtual fields method with piecewise virtual fields". In: *International Journal of Mechanical Sciences* 48.3, pp. 256–264. ISSN: 00207403. DOI: 10.1016/j.ijmecsci.2005.10.002.

Vardanega, P.J. and M.D. Bolton (2011). "Practical methods to estimate the non-linear shear stiffness of fine grained soils". In: *International Symposium on Deformation Charateristics of Geomaterials* 1972, pp. 372–379. URL: http://www-civ.eng.cam.ac.uk/geotech{_}new/people/bolton/mdb{_}pub/214.pdf.

Westerweel, J (1993). "Digital particle image velocimetry: Theory and application". PhD thesis. Delft University Press.

– (1999). "Fundamentals of digital particle image velocimetry". In: *Measurement Science and Technology*.

Westerweel, J and F Scarano (2005). "Universal outlier detection for PIV data". In: *Experiments in Fluids* 39, pp. 1096–1100.

White, D. J. and W A Take (2002). "GeoPIV: Particle Image Velocimetry (PIV) software for use in geotechnical testing". In: *Cambridge University Engineering Department Technical Report* 322.October, p. 15.

White, D. J., W A Take, and M.D. Bolton (2001). "Measuring soil deformation in geotechnical models using digital images and PIV analysis". In: *10th International Conference on Computer Methods and Advances in Geomechanics*, pp. 997–1002. URL: http://www-civ.eng.cam.ac.uk/geotech{_}new/people/bolton/mdb{_}pub/99{_}IACMAG{_}2001{_}Proc{_}997{_}1002.pdf.

White, David John (2002). "An investigation into the behaviour of pressed-in piles". PhD thesis, pp. 1–390. URL: http://publications.eng.cam.ac.uk/328467/.

Willert, C E and M Gharib (1991). "Digital particle image velocimetry". In: *Experiments in Fluids* 10, pp. 181–193.

Zhengyou, Z (2000). "A Flexible New Technique for Camera Calibration". In: *IEEE transactions on pattern analysis and machine intelligence* 22.11, pp. 1330–1334. URL: https://www.microsoft.com/en-us/research/publication/a-flexible-new-technique-for-camera-calibration/.